

**STRUCTURE AND PROPERTIES OF SELF-ASSEMBLED
SUB-MICRON THIN NAFION[®] FILMS**

by

Devproshad K. Paul

A thesis submitted to the Department of Chemical Engineering

In conformity with the requirements for

the degree of Doctor of Philosophy

Queen's University

Kingston, Ontario, Canada

(September, 2013)

Copyright ©Devproshad K. Paul, 2013

Abstract

This thesis is concerned with the study of morphology and properties of sub-micron thin Nafion® films. The motivation of the work arises from the need to characterize the 4 -10 nm thin ionomer films in the catalyst layer of polymer electrolyte fuel cell (PEFC).

A protocol for the fabrication of self-assembled ultra-thin Nafion® films on planar substrates was successfully developed. Films of thickness ranging 4 nm-300 nm, determined by three different techniques - variable angle spectroscopy ellipsometry (VASE), atomic force microscope (AFM) and x-ray photo-electron spectroscopy (XPS), could be reproducibly generated on SiO₂/Si wafer. The 4 nm thin film is one of the *thinnest, continuous film* of Nafion® ever reported. This is the first time that the structure/properties of such thin Nafion® film have been investigated.

An interesting finding is the thickness-dependent structure and property of these films. Films with thickness <55 nm exhibited hydrophilic-free surface but thicker films (>55 nm) had hydrophobic surface. Similarly, sub-55 nm films had a lower and thickness-independent protonic conductivity compared to thicker films that exhibited thickness-dependent conductivity. Anomalously high water uptake (by quartz crystal microbalance) and swelling (by ellipsometry) of sub-55nm films indicate that low conductivity is not due to low water content. However, differences in surface morphology were observed by the AFM phase contrast analysis. The lack of ionic domain was also observed in the thinner films (4-30 nm) from the grazing incidence small x-ray scattering (GISAXS) experiments.

Thermal annealing over a range of temperature (110-160 °C) revealed a dramatic switching of the film surface from hydrophilic to hydrophobic was observed for sub-55 nm films with lower thickness film requiring higher annealing temperature. Bulk proton conductivity was significantly reduced after annealing for all films. An interesting finding was the regeneration of conductivity after to prolonged liquid water exposure and a corresponding switching back of the

surface to hydrophilic. The thickness-dependent structure/property of ultra-thin Nafion® films is attributed to substrate induced confinement effect.

Self-assembly of Nafion® on various substrates (SiO₂, carbon, Pt and Au) was studied. The ionomer/substrate interaction and resulting film morphology followed a trend with respect to substrate surface energies and Nafion® dispersion compositions.

Co-Authorship

List of Publications

(Main author in bold; corresponding author is underlined)

1. **Devproshad K. Paul**, Kunal Karan, Javier Giorgi, Aris Docoslis, and Joshua Pearce, Characteristics of Self-Assembled Ultra-thin Nafion® Films, *Macromolecules* 2013, 46 (9), 3461–3475
2. **Devproshad K. Paul**, Javier Giorgi, and Kunal Karan, Chemical and Ionic Conductivity Degradation of Ultra-Thin Ionomer Film by X-ray Beam Exposure, *Journal of The Electrochemical Society* 2013, 160 (4), F464-F469.
3. **Devproshad K. Paul**, and Kunal Karan, Effect of Thermal Treatment on the Properties of Ultra-Thin Nafion® Film, *ECS Transactions* 2013, 50 (2), 951-959.
4. **Devproshad K. Paul**, Andrew Fraser, and Kunal Karan, Towards the understanding of proton conduction mechanism in PEMFC catalyst layer: Conductivity of adsorbed Nafion® films *Electrochemistry Communications* 2011, 13 (8), 774-777.
5. **Devproshad K. Paul**, Andrew Fraser, Joshua Pearce, and Kunal Karan, Understanding the Ionomer Structure and the Proton Conduction Mechanism in PEFC Catalyst Layer: Adsorbed Nafion® on Model Substrate, *ECS Transactions* 2011, 41 (1), 1393-1406.
6. Miguel Modestino, **Devproshad K. Paul**, Shudipto Dishari, Stephanie A Petrina, Frances I Allen, Michael A Hickner, Kunal Karan, Rachel A Segalman, Adam Z Weber, Self-Assembly and Transport Limitations in Confined Nafion® Films, *Macromolecules*, 2013, 46 (3), 867–873. [included with proper acknowledgement and reference]
7. **Devproshad K. Paul** and Kunal Karan, Conductivity and wettability changes of ultra-thin Nafion® films subjected to thermal annealing and liquid water exposure, *Journal of Physical Chemistry C* (ready for submission).
8. **Devproshad K. Paul**, and Kunal Karan, Javier Giorgi, Aris Docoslis, Thickness-dependent ionomer confinement in self-assembled ultrathin ionomer films, *Macromolecules* (in preparation).
9. **Devproshad K. Paul**, and Kunal Karan, Thickness-dependent proton transport of self-assembled ultrathin Nafion® films: details of the measurement and interpretation by impedance spectroscopy, *Journal of Physical Chemistry C* (in preparation)
10. **Devproshad K. Paul**, and Kunal Karan, Controlling morphology and properties of the Nafion® ultrathin film via substrate energy and wetting interactions, *ACS Macro Letters*, (in preparation)

Acknowledgements

At first, I would like to thank and express my sincere gratitude to my supervisor, Prof. Kunal Karan. The thesis could not have been accomplished without his unlimited support, continuous encouragement, guidance, leadership, expertise and patience throughout the thesis work. I would like to thank my co-supervisor, Prof. Aris Docoslis for his support, valuable inputs and discussions in my research work. I am grateful to Prof. Brant Peppley (Director FCRC) for his valuable input/suggestion to my research and also for providing me the opportunity to work at internationally recognized Queen's-RMC Fuel Cell Research Centre (FCRC) and its facilities.

I would like to thank past and present students and researchers of FCRC, especially, the members of PEFC research group. In particular, I am thankful to Dr. Madhu Saha (at present, research scientist of AFCC) for his initial help and encouragement in the laboratory experiments and also for giving me a homely atmosphere at Kingston. I am thankful to Dr. Dzmitry Malevich and Dr. Ruhul Amin (at present, research fellow at MIT) for technical scientific discussion and help in the laboratory experiments. I also thank other colleagues at FCRC, especially, Barath Jayasankar (PhD student) for useful scientific discussions from time to time. I would like to thank numerous people in the Department of Chemical Engineering and Department of Chemistry, Queen's University for helping me in my experiments.

I am very grateful to a number of collaborators for their support and discussion in my research projects. I am thankful to Prof. Javier Giorgi (University of Ottawa) for hosting me at the University of Ottawa and giving me the access to the XPS measurement in his lab. I am thankful to Prof. Joshua Pearce (Queen's University) for giving me direct access to his lab for using ellipsometry. I am grateful to Prof. Mike Hickner (Penn State University, USA) for the collaborative project and cross-checking of the experimental findings. I am also thankful to Dr.

Adam Weber (Laurence Berkley National Lab, USA) for his interest in collaborating on my research and providing the GISAXS experimental support.

I thank my wife, Surmita Paul, who has given continuous inspiration to my work and unconditional supports to achieve my goals. I am always grateful to my Parents for their encouragement and blessings and also for keeping faith on me. Finally, I must have to thank the members of Queen's Bangladeshi Student Association (QBSA) and my friends in Queens University for their constant support and affections which made my stay in Kingston lively and enjoyable. Above all, I thank to God for giving me the highest opportunity and capability to perform this work.

Table of Contents

| | |
|--|-----|
| Abstract..... | ii |
| Co-Authorship | iv |
| Acknowledgements..... | v |
| List of Figures | xi |
| List of Tables | xix |
| List of Abbreviations | xx |
| Chapter 1 General Introduction | 1 |
| 1.1 The approach of this thesis | 5 |
| 1.2 Thesis Structure | 5 |
| Chapter 2 Literature Review and Research Objectives..... | 9 |
| 2.1 Introduction..... | 9 |
| 2.2 PEFC Catalyst layer..... | 10 |
| 2.2.1 Fundamental aspects of PEFC CL | 10 |
| 2.2.2 Catalyst layer fabrication and microstructure | 12 |
| 2.2.3 CL wettability and ionomer behavior | 15 |
| 2.3 Nafion® Ionomer | 17 |
| 2.3.1 Fundamental of Nafion® ionomer | 17 |
| 2.3.2 Nafion® as polymer electrolyte membrane (PEM) | 18 |
| 2.3.3 Nafion® in dispersion..... | 25 |
| 2.3.4 Nafion®-substrate interactions and reorganization | 30 |
| 2.3.5 Nafion® ionomer thin film | 31 |
| 2.4 Existing gaps in the knowledge of ionomer thin films | 37 |
| 2.5 Research Objectives..... | 38 |
| Chapter 3 Experimental Techniques: Theory and Application..... | 40 |
| 3.1 Introduction..... | 40 |
| 3.2 Characterization techniques | 40 |
| 3.2.1 Variable Angle Spectroscopy Ellipsometry (VASE)..... | 40 |
| 3.2.2 Atomic Force Microscopy (AFM) | 43 |
| 3.2.3 X-Ray Photoelectron Spectroscopy (XPS) | 46 |
| 3.2.4 Contact angle measurement | 49 |
| 3.2.5 Electrochemical Impedance Spectroscopy (EIS) | 52 |
| 3.2.6 Dynamic Light Scattering (DLS)..... | 54 |

| | |
|--|-----|
| 3.3 Conclusions..... | 57 |
| Chapter 4 Fabrication and Characterization of Self-Assembled Ultrathin Films | 58 |
| 4.1 Introduction..... | 58 |
| 4.2 Experimental | 60 |
| 4.2.1 Film Preparation..... | 60 |
| 4.2.2 Film Characterization..... | 62 |
| 4.2.3 Dispersion characterization..... | 64 |
| 4.3 Results and Discussions | 65 |
| 4.3.1 Surface characterization of films generated by varying immersion times | 65 |
| 4.3.2 Effect of dispersion medium composition (IPA/water) on self-assembled Nafion® films. | 71 |
| 4.3.3 Thickness of films self-assembled from Nafion® dispersion of varying concentration | 83 |
| 4.3.4 Surface characterization..... | 95 |
| 4.3.5 Influence of the solvent/dispersion media on self-assembled films..... | 105 |
| 4.3.6 Proposed nanostructure of self-assembled Nafion® films..... | 112 |
| 4.4 Conclusions..... | 114 |
| Chapter 5 Protonic Conductivity of Ultra-Thin Nafion® Films | 116 |
| 5.1 Introduction..... | 116 |
| 5.2 Experimental | 118 |
| 5.2.1 Materials | 118 |
| 5.2.2 The design and fabrication of Interdigitated array (IDA) of Au electrode | 118 |
| 5.2.3 Preparation of self-assembled thin films on IDA..... | 119 |
| 5.2.4 Treatment of self-assembled thin films..... | 120 |
| 5.2.5 Impedance measurement of the self-assembled thin films | 121 |
| 5.2.6 Water-uptake measurements | 123 |
| 5.2.7 Grazing-incidence small-angle X-ray scattering measurements..... | 125 |
| 5.3 Results and discussions..... | 126 |
| 5.3.1 Impedance responses | 126 |
| 5.3.2 Equivalent circuit design..... | 133 |
| 5.3.3 Impedance response and data fitting..... | 140 |
| 5.3.4 Capacitance behavior of the Nafion® thin films | 143 |
| 5.3.5 Proton conductivity of the Nafion® thin films | 146 |
| 5.3.6 Aging effect on the proton conductivity of Nafion® thin film. | 153 |

| | |
|---|-----|
| 5.3.7 Effect of inter electrode gap on the proton conductivity of the thin films | 154 |
| 5.3.8 Effect of electrode design and materials on the proton conductivity of the thin films | 156 |
| 5.3.9 Activation energy of the proton conduction in Nafion® thin films. | 159 |
| 5.3.10 Water uptake and swelling behavior of Nafion® thin films | 164 |
| 5.3.11 Internal structure of the Nafion® thin films by GISAXS | 166 |
| 5.4 Conclusions..... | 168 |
| Chapter 6 Effect of Thermal Annealing and Liquid Water Exposure on Surface and Bulk Characteristics of Ultrathin Nafion® Films | 170 |
| 6.1 Introduction..... | 170 |
| 6.2 Experimental | 173 |
| 6.2.1 Thermal annealing protocol of the Nafion® thin films..... | 173 |
| 6.2.2 Characterization of Nafion® thin films | 174 |
| 6.3 Results and discussions | 176 |
| 6.3.1 Characterization of surface properties of the annealed thin films..... | 176 |
| 6.3.2 Characterization of bulk proton conductivity of annealed thin films..... | 194 |
| 6.3.3 Effect of Treatment Temperature on Surface and bulk properties of Nafion® thin film | 199 |
| 6.3.4 Effect of external environments on the annealed Nafion® thin films. | 204 |
| 6.3.5 Activation energy for ionic conduction | 216 |
| 6.4 Conclusions..... | 219 |
| Chapter 7 Substrate Effect on Ultrathin Nafion® Films..... | 221 |
| 7.1 Introduction..... | 221 |
| 7.2 Experimental | 222 |
| 7.2.1 Materials | 222 |
| 7.2.2 Substrate cleaning | 226 |
| 7.2.3 Film preparation and treatment | 226 |
| 7.2.4 Film characterization | 227 |
| 7.3 Results and Discussions | 227 |
| 7.3.1 Dispersion medium effect on Nafion®/carbon interaction | 227 |
| 7.3.2 Substrate surface characterization..... | 229 |
| 7.3.3 Substrate effect on the morphology of the Nafion® thin films..... | 231 |
| 7.3.4 Substrate effect on thin film wettability..... | 233 |
| 7.3.5 Thickness dependent morphology of films on Carbon and Au substrates..... | 236 |
| 7.3.6 Thickness-dependent surface wettability | 239 |

| | |
|---|-----|
| 7.3.7 Substrate influence on water uptake | 240 |
| 7.4 Conclusions..... | 242 |
| Chapter 8 X-ray Beam Damage of Ultra-Thin Nafion® Films | 244 |
| 8.1 Introduction..... | 245 |
| 8.2 Experimental | 248 |
| 8.2.1 Materials and sample preparation | 248 |
| 8.2.2 Electrochemical Impedance Spectroscopy..... | 248 |
| 8.2.3 X-ray Photoelectron Spectroscopy..... | 249 |
| 8.3 Results and Discussion | 250 |
| 8.3.1 Film degradation | 250 |
| 8.3.2 Degradation extent and mechanism | 258 |
| 8.3.3 Proton conductivity of 10 nm thin film before and after X-ray exposure..... | 260 |
| 8.4 Conclusions..... | 263 |
| Chapter 9 Conclusions and Recommendations..... | 265 |
| 9.1 Conclusions..... | 265 |
| 9.2 Recommendations..... | 270 |
| Bibliography (or References)..... | 272 |

List of Figures

| | |
|--|----|
| Figure 1.1: (a) Membrane Electrode Assembly (MEA) (b) CLs microstructure (c) CL transport and reactions. | 2 |
| Figure 2.1: TEM image showing the structure of Pt/ionomer/C microstructure [1]. | 15 |
| Figure 2.2: Molecular Structure of Perfluorosulfonic acid ionomer (Nafion®) | 18 |
| Figure 2.3: SAXS experimental data showing ionomer peak of Nafion® ionomer membrane. Figure is taken from the reference [64]. | 19 |
| Figure 2.4: Structural models of Nafion® ionomer membrane. The Figures are re-printed from the references [60-64] | 20 |
| Figure 2.5: Nafion® dispersion state as described and reported by different group in the literature. Figures are re-printed from Aldebert <i>et al.</i> 99], Pietek <i>et al.</i> 104], Jiang <i>et al.</i> 105]. | 28 |
| Figure 3.1: Typical Ellipsometry configuration [140]. | 41 |
| Figure 3.2: Flowchart of Ellipsometry data analysis [140]. | 42 |
| Figure 3.3: Interatomic force variation versus distance between AFM tip and sample [141]. | 44 |
| Figure 3.4: Phase imaging uses the Extender Electronics Module to measure the phase lag of the cantilever oscillation (solid wave) relative to the piezo drive (dashed wave). The amplitude signal is used simultaneously by the NanoScope III controller for Tapping Mode feedback. Spatial variations in sample properties cause shifts in the cantilever phase (bottom) which are mapped to produce the phase images shown here [142]. | 45 |
| Figure 3.5: XPS instrumentation, image taken from Wikipedia (wikipedia.org/wiki/X-ray_photoelectron_spectroscopy). | 46 |
| Figure 3.6: Instrumentation of Goniometer (contact angle measurement set up) | 49 |
| Figure 3.7: Impedance presentation (a) Nyquist Plot (b) Equivalent circuit (c) Bode Plot [152]. .. | 54 |
| Figure 3.8: Instrumentation of DLS technique, image taken from the website [153]. | 55 |
| Figure 4.1: Self-assembled Nafion® thin film preparation on SiO ₂ terminated Si wafer substrate | 60 |
| Figure 4.2: 3-D AFM height images of Blank SiO ₂ surface (top row left) and of SiO ₂ surface after immersion in 0.1 wt% Nafion® dispersion for 30 mins (top row right), 1 h (bottom row left) and 12 h (bottom row left). | 66 |
| Figure 4.3: 2-D height images with section analysis. Blank SiO ₂ surface (top row) and SiO ₂ surface after immersion in 0.1 wt% Nafion® dispersion for 30 mins (2nd top row), 1 h (3rd row), 12 h (bottom row). | 68 |

| | |
|--|-----|
| Figure 4.4: Mean roughness of blank SiO ₂ surface and SiO ₂ surface immersed in 0.1 wt% Nafion® dispersion for different time. | 70 |
| Figure 4.5: (a) AFM image and (b) line analysis showing height distribution of scratched surface of film deposited from immersion in 0.1 wt% Nafion® dispersion for 12 h. | 70 |
| Figure 4.6: AFM height, section analysis and phase of films prepared from 0.1 wt% Nafion® dispersion in different water/IPA composition. Top row (height images), middle row (section analysis) and bottom row (corresponding phase images). | 72 |
| Figure 4.7: AFM height image and section analysis of Nafion® thin film prepared from 0.1 wt% dispersion (left) and 0.05 wt% dispersion (right) in IPA. | 75 |
| Figure 4.8: Representative size distribution of Nafion® in 0.1wt% dispersion in various Water/IPA composition termed as 100%, 80%, 50%, 20% and 0.4% water. | 76 |
| Figure 4.9: The volume fraction of Nafion® aggregates in 0.1wt% dispersion at three categories varying Water/IPA composition termed as 100%, 80%, 50%, 20% and 0.4% water. | 77 |
| Figure 4.10: AFM image showing Nafion® particles deposited by spray drying of 0.1 wt% dispersion from various Water/IPA compositions. | 79 |
| Figure 4.11: ψ (a) and Δ (b) spectra for the variation of blank SiO ₂ thickness 25 nm to 2000 nm at incident angle 75° | 84 |
| Figure 4.12: Three-layer model used for fitting Ellipsometry data, (a) Cauchy model and (b) EMA model. | 85 |
| Figure 4.13: ψ and Δ spectra obtained from variable angle spectroscopic ellipsometry of 4 different films at 65° incident angle and corresponding fits with a Cauchy model. | 87 |
| Figure 4.14: X-ray photoelectron spectra of the 10 nm Nafion® film as a function of electron take-off angle. a) 90°, b) 45°, and c) 10°. Spectra have been off-set for clarity. Insert shows the normalized XPS intensity for silicon (solid triangles) and sulfur (solid square) peaks at normal take-off angle as a function of film thickness. | 92 |
| Figure 4.15: Water contact angle of Ultra-thin and thin Nafion® films varying film thickness. [Open Circles: Films from IPA-diluted dispersions; Open Diamond: films from Nafion® in water dispersions] | 96 |
| Figure 4.16: Height and corresponding phase images with section analysis of 4 nm film (a, b, c, d), 10 nm film (e, f, g, h), 55 nm film (I, j, k, l), 160 nm film (m, n, o, p), and 300 nm film (q, r, s, t). [Films prepared from IPA-diluted Nafion® dispersions]. | 99 |
| Figure 4.17: Morphologies and section analysis of self-assembled ultra-thin Nafion® film prepared from different Nafion® concentration in water. | 107 |

| | |
|--|-----|
| Figure 4.18: Comparative raw data of ψ spectra obtained from variable angle spectroscopic ellipsometry of three different corresponding films at 75° incident angle..... | 108 |
| Figure 4.19: Refractive index of the films prepared from IPA diluted Nafion® dispersion and Nafion®-water dispersion in terms of thicknesses. | 109 |
| Figure 4.20: Size distribution of various Nafion® in water dispersions..... | 110 |
| Figure 4.21: Thickness –dependent proposed nanostructure of ultra-thin and thin Nafion® films | 112 |
| Figure 5.1: IDA of Au electrode supported by SiO ₂ terminated wafer. Gray color represents SiO ₂ , golden color represents Au electrode. The electrodes were fabricated in the National Institute for Nanotechnology (NINT) lab, Alberta. | 119 |
| Figure 5.2: Impedance measurement setup inside the environmental chamber. Nafion® film on IDA of Au electrode has been connected by two probes to the impedance analyzer coupled with dielectric interface..... | 122 |
| Figure 5.3: Impedance monitoring at a single frequency of 100 Hz for film subjected to RH change from 40 % to 50% at 50 °C..... | 123 |
| Figure 5.4: Typical impedance response of ultra-thin Nafion® film presented as a Nyquist plot. | 127 |
| Figure 5.5: Nyquist impedance plots for 10 nm ultrathin Nafion® film at 60 °C and different RH. The data for 80, 60 and 40% RH have been reduced 3, 12 and 100 times respectively to fit into the scale..... | 128 |
| Figure 5.6: Nyquist impedance plot for 55 nm ultrathin Nafion® film at 80% RH and different temperature. | 130 |
| Figure 5.7: Nyquist impedance plots for ultrathin Nafion® film varying thicknesses at 60% RH and 60 °C. The data for 55, 10 and 4 nm film have been reduced 5, 20 and 60 times respectively to fit into the scale..... | 131 |
| Figure 5.8: Nyquist impedance plots for 55 nm ultrathin Nafion® film at 25 °C and 70% RH varying local measurement atmosphere of the film. | 133 |
| Figure 5.9: Equivalent circuit model – (a) possible impedance and capacitance components in the Nafion® thin film on SiO ₂ supported IDA gold electrode. Gray color, yellow color and sky color represent SiO ₂ , Au and Nafion® thin film respectively, (b) simplified equivalent circuit. | 134 |
| Figure 5.10: Typical impedance plot of ultra-thin Nafion® film and the fitting with three different equivalent circuits - (a) EC-1 (b) EC-2 and (c) EC-3 (inset) | 136 |
| Figure 5.11: Nyquist plot for self-assembled Nafion® thin film at 60 °C and 96% RH. Experimental data (open circle) and fitted data with EC-2 (solid line) | 139 |

| | |
|--|-----|
| Figure 5.12: Nyquist plots – experimental data of 55 nm film (open circle), data fitting with EC-2 (solid black line) and simulated data according the EC equation 5.5. | 141 |
| Figure 5.13: Nyquist plots – experimental data of the 4 nm film (open circle), data fitting with EC-2 (solid black line) and simulated data according the EC equation 5.5 (dotted red and green line). | 142 |
| Figure 5.14: Capacitance of Nafion® thin films with different thicknesses as a function of relative humidity at 60 °C. | 143 |
| Figure 5.15: Capacitance of Nafion® thin films in terms of thickness at 20 to 96% RH and 60 °C. | 144 |
| Figure 5.16: Normalized capacitance of the Nafion® thin films as a function of film thickness for various temperatures (30-60 °C) at 96% RH (Top) and 40% RH (Bottom). | 145 |
| Figure 5.17: Proton conductivity of the Nafion® thin films varying thicknesses 4 to 300 nm at 25 °C as a function of RH | 147 |
| Figure 5.18: Proton conductivity of the Nafion® thin films as a function of film thickness at 25 °C. | 148 |
| Figure 5.19: Proton conductivity of the Nafion® thin films with different film thickness in terms of relative humidity ranging 20 to 96% RH at 60 °C. | 149 |
| Figure 5.20: Proton conductivity in terms of film thickness at 60 °C for both low – 40 %, RH and high – 95 %, RH. | 150 |
| Figure 5.21: Comparative proton conductivity at 25 °C in between treated and un-treated films, for (a) the 10 nm film and (b) the 160 nm film. | 152 |
| Figure 5.22: Proton conductivity of the 160 nm Nafion® thin film in terms of relative humidity at 60 °C symbolized as (●) 0 months, (◇) 8 months and (■) 12 months. | 154 |
| Figure 5.23: Proton conductivity of the 10 nm film in terms of inter-teeth distance of IDA electrode at 60 °C and three different RH conditions. | 155 |
| Figure 5.24: The normalized capacitance of the 10 nm film in terms of inter-teeth distance of IDA electrode at 60 °C and three different RH conditions. | 156 |
| Figure 5.25: Image of Pt electrode design (left) and SEM image of center electrodes (right) and the corresponding distance between electrodes. Lighter color indicates platinum metal, darker color indicates silicon wafer in SEM image. [The electrode was designed and fabricated at the Penn State nanofabrication clean room facility by Stephanie Petrina from Dr. Mike Hickner group, Penn State University, USA]. | 157 |
| Figure 5.26: Proton conductivity of the 55 nm film measured on Pt and Au IDA electrode system at 25 °C in terms of relative humidity | 158 |

| | |
|--|-----|
| Figure 5.27: Arrhenius plots for conductivity of the 10 nm and the 160 nm Nafion® thin films. | 161 |
| Figure 5.28: Activation energy of the proton conductivity varying film thickness in terms of relative humidity ranging 20 to 96% RH. | 162 |
| Figure 5.29: Activation energy of the proton conductivity in terms of Nafion® thin film thickness at both high (96%) and low (40 %) RH. | 163 |
| Figure 5.30: Thickness changes upon water uptake (left) and λ_w values (moles of H ₂ O/mol of sulfonic acid group) (right) show that thinner films uptake significantly more water than thicker and even saturated-vapor-equilibrated bulk Nafion® 117 (dotted line) at all humidity levels. [The measurements were performed by Stephanie Patrino from Dr.Mike Hickner group, Penn State University, but the films were prepared in Queen's laboratory by Author]. | 165 |
| Figure 5.31: 2D GISAXS patterns from Nafion® films of (a) 4, (b) 10, (c) 50 and (d) 160 nm in thickness equilibrated at 100% RH. The patterns presented only show scattering arising from periodic ionic domains for films of 50 and 160 nm in thickness. Thinner films do not show any appreciable scattering, suggesting a loss in correlations between ionic domains in the polymer. (q_p refers to the in-plane scattering vector, and q_z corresponds to the out-of-plane scattering vector) [The measurements were performed at Lawrence Berkeley National Laboratory by Weber group, but the films were prepared by the author]. | 167 |
| Figure 5.32: Line cuts from the GISAXS patterns for q_p at the specular position only show an intensity decay for 4 and 10 nm films and no indication of order in the films, while 50 and 160 nm films present a typical ionomer peak resulting from correlations between conducting domains. [The measurements were performed at Lawrence Berkeley National Laboratory by Weber group, but the films were prepared by the author]. | 167 |
| Figure 6.1: Images of water sessile drop on films of various thicknesses and annealed/thermally treated at 40, 110, 146 and 160 °C. | 177 |
| Figure 6.2: Water contact angles on the 10, 30 and 55 nm ultra-thin Nafion® films with time when the films were treated at 110 °C. | 180 |
| Figure 6.3: AFM height and phase image (1000 nm X 1000 nm) of 4 nm film; (a) height (b) section analysis (c) phase at 40 °C treatment; (d) height (e) section analysis (f) phase at 146 °C treatment; (g) height (h) section analysis (i) phase at 160 °C treatment | 186 |
| Figure 6.4: AFM height and phase image (650 nm X 650 nm) of the 10 nm film; (a) height (b) section analysis (c) phase at 40 °C treatment; (d) height (e) section analysis (f) phase at 146 °C treatment. | 187 |

| | |
|--|-----|
| Figure 6.5: AFM height and phase image (650 nm X 650 nm) of 55 nm film; (a) height (b) section analysis (c) phase at 40 °C treatment; (d) height (e) section analysis (f) phase at 146 °C treatment. | 188 |
| Figure 6.6: AFM height and phase image (650 nm X 650 nm) of 300 nm film; (a) height (b) section analysis (c) phase at 40 °C treatment; (d) height (e) section analysis (f) phase at 146 °C treatment. | 189 |
| Figure 6.7: Thickness dependent surface roughness of thin Nafion® films (a) unannealed (b) annealed at 146 °C. | 190 |
| Figure 6.8: Thickness dependent surface roughness in phase of thin Nafion® films (a) unannealed (b) annealed at 146 °C..... | 191 |
| Figure 6.9: Silicon signal increase as the 4 nm film is annealed. Si _{2p} peak region, normal incidence. Black line before annealing, red line after annealing. | 193 |
| Figure 6.10. XPS carbon region. a) C _{1s} region for the 4 nm film; b) C _{1s} region for the 30 nm film. Black line before annealing, red line after annealing..... | 194 |
| Figure 6.11: Impedance response of the 10 nm films – unannealed (black line) and annealed (red line). Nyquist plot (left hand side) and Bode plot (right hand side) | 195 |
| Figure 6.12: Impedance response of the 55 nm films – unannealed (black line) and annealed (red line). Nyquist plot (left hand side) and Bode plot (right hand side). | 196 |
| Figure 6.13: Proton conductivity of annealed Nafion® thin films with different thicknesses in terms of relative humidity at 60 °C. | 197 |
| Figure 6.14: Proton conductivity at 60 °C of both unannealed and annealed Nafion® thin films as a function of film thickness (a) at 40% RH, (b) 96% RH. | 199 |
| Figure 6.15: Surface wettability of heat-treated (annealed) ultra-thin (10 nm) Nafion® film. (Solid lines are only guides for eye). Error bar represents standard deviation of results obtained from four different points of each of triplicate samples..... | 200 |
| Figure 6.16: Proton conductivity of treated ultra-thin Nafion® film with different film treatment temperature at 95 % RH and 60 °C. | 203 |
| Figure 6.17: Water contact angle of Nafion thin films - Annealed (red open circle) and water vapor exposed for a week (black open circle), at ambient measurement condition..... | 206 |
| Figure 6.18: Impedance response of 10 nm Nafion® film exposed to 95% RH at 30 °C over 18 hours (a) fixed frequency (100 Hz) impedance monitored over 360 mins (6 h) periods of 0-6h, 6-12h, 12-18 h. (b) impedance spectroscopy data (10 MHz-1 Hz) after 6, 12 and 18 h exposure. | 207 |
| Figure 6.19: Water contact angle and time effect on liquid water treated films with the thicknesses (a) 10 nm (b) 30 nm and (c) 55 nm. | 209 |

| | |
|--|-----|
| Figure 6.20: Switchability of surface wettability of the 10 nm ultra-thin film subjected to thermal annealing (annealed film) and liquid water exposure (regenerated film). | 211 |
| Figure 6.21: Impedance response of 55 nm films – unannealed (black open circle), annealed (red open square), 24 h water treated (blue open triangle), 24 h-repeat water treated (purple open diamond) and 96 h water treated (green open triangle). | 212 |
| Figure 6.22: Conductivity vs relative humidity of the 55 nm films at 60 °C and different treatment condition – unannealed (black open circle), annealed (red open square), 24 h water treated (blue closed triangle) and 96 h water treated (green closed diamond). | 213 |
| Figure 6.23: Impedance response of 10 nm films – unannealed (black open circle), annealed (red open square), 24 h water treated (green open triangle). | 214 |
| Figure 6.24: Proton conductivity for 10 nm Nafion® film subjected to the various treatments.. | 215 |
| Figure 6.25: Arrhenius plots of annealed and water treated films – (a) 55 nm (annealed), (b) 10 nm (annealed) and (c) 10 nm (water treated). | 217 |
| Figure 6.26: Activation energy of 55 nm film as a function of RH for untreated (●), and annealed (■). | 218 |
| Figure 6.27: Activation energy of the 10 nm film as a function of RH for untreated (●), annealed (■) and water treated (▲) films. | 219 |
| Figure 7.1: Cauchy model for ellipsometry data fitting to extract OTS layer thickness. | 224 |
| Figure 7.2: Variation of OTS layer thickness (black circle) and refractive index (red diamond) with reaction time. | 225 |
| Figure 7.3: AFM height images (1 μm X 1 μm) of the self-assembled films on carbon substrate obtained from 0.1wt% Nafion® dispersion in different dispersion medium compositions. | 228 |
| Figure 7.4: Contact angles of water, diiodomethane and formamide for different substrates. | 230 |
| Figure 7.5: AFM height images (1 μm X 1 μm) of the self-assembled thin films from 0.1wt% Nafion® dispersion in 0.4 % water. The film morphologies have been presented in terms of substrate surface energies. | 232 |
| Figure 7.6: AFM height images (1 μm X 1 μm) of the self-assembled films from 0.1wt% Nafion® dispersion in 20 % water. The film morphologies have been presented in terms of acid base component of substrate surface energies. | 233 |
| Figure 7.7: Water contact angles on and surface AFM images of Nafion® thin films (4 to 6 nm) on substrates of different wettabilities - SiO ₂ (left), Carbon (middle) and Au (right). | 234 |
| Figure 7.8: The morphologies, section analysis and contact angles of annealed Nafion® thin films (4 to 6 nm) at different substrate wettabilities – Film on SiO ₂ (left), film on Carbon (middle) and film on Au (right). | 236 |

| | |
|--|-----|
| Figure 7.9: AFM height images (1 μm X 1 μm) and roughness of the self-assembled films on Carbon. Both un-annealed and annealed film morphologies have been presented with increasing thickness (left to right). | 237 |
| Figure 7.10: AFM height images (1 μm X 1 μm) and roughness of the self-assembled films on Au. Both un-annealed and annealed film morphologies have been presented with increasing thickness (left to right). | 238 |
| Figure 7.11: Contact angles of both un-annealed and annealed Nafion® thin films on carbon, Au and Pt with the variation of Nafion® concentration correspond to the thickness. | 240 |
| Figure 7.12: Water uptake of self-assembled Nafion® thin film on Au in terms of relative humidity. The measurement was conducted in Penn State University but the films were prepared by the author at Queen's. | 241 |
| Figure 8.1: Film thinning observed by the increase in Si _{2s} intensity as a function of irradiation time. X-ray source power: (■) 300W, (▲) 200W, and (●) 100W. | 252 |
| Figure 8.2: Film degradation under 300 W X-ray source. S _{2p} region at times 0 (■), 15 (●), 30 (▲) and 45 (□) minutes exposure. a) S _{2p} peak; b) F _{1s} peak. Traces have been offset for clarity. | 253 |
| Figure 8.3: Change in intensity of the XPS signal as a function of exposure time. Solid lines indicate sulfur and dashed lines indicate fluorine intensities for exposure at 300 W (■), 200 W (●), and 100 W (▲). | 254 |
| Figure 8.4: Nafion® molecule (EW=1100; x=6, y=1) molecule. Sulfur and oxygen are present only on the side chain. Fluorine ratio is 27:10 (backbone:side chain). | 255 |
| Figure 8.5: Oxygen degradation under 300 W X-ray source. O _{1s} region at times 0 (■), 15 (●), 30 (▲) and 45 (□) minutes exposure. Traces have been offset for clarity. | 256 |
| Figure 8.6: Change in C _{1s} signal under 300 W X-ray source. Spectra at times 0 (■), 15 (●), 30 (▲) and 45 (□) minutes exposure. Traces have been offset for clarity. Four fitted components and the resulting envelope are shown as solid lines for the 45 minute exposure spectrum. | 257 |
| Figure 8.7: Changes in XPS intensity for the components of Nafion® upon irradiation during 15 minutes. | 259 |
| Figure 8.8: Impedance plots of three samples (10 nm ultra-thin Nafion® films) before X-ray exposure at 94% RH and 60 °C. | 261 |
| Figure 8.9: Proton conductivity of 10 nm films before (termed as 0 W) and after X-ray exposure (Sample-1, Sample-2 and Sample-3 were exposed to 300, 200 and 100 W X-ray power, respectively) for 45 mins (impedance measurement conducted at both 60 % & 94% RH and 60 °C). | 262 |

List of Tables

| | |
|---|-----|
| Table 2.1: Summary of nano-structural model of Nafion® membrane | 21 |
| Table 2.2: Summary of literature on Nafion® thin films..... | 32 |
| Table 4.1: Solubility parameter (at 25 °C) and dielectric constant of different water/IPA composition..... | 81 |
| Table 4.2: Summarized data for Nafion® film prepared from IPA diluted Nafion® dispersion. . | 89 |
| Table 4.3: Fitting results according to model in Figure 4.12(b). | 90 |
| Table 4.4: Thicknesses of Nafion® films generated from different dispersions and concentrations. | 95 |
| Table 4.5: Angle-Resolved XPS Data for 3 different films | 102 |
| Table 4.6: Calculated surface energy of the adsorbed thin Nafion® films according to the XDLVO theory. | 104 |
| Table 4.7: Summarized data for Nafion® film prepared from Nafion® -water dispersion..... | 106 |
| Table 5.1: Summarized equivalent circuit fitting parameters with three equivalent circuit considerations. | 137 |
| Table 5.2: Summarized equivalent circuit fitting parameters with EC-2 for the 4 and 55 nm films. | 142 |
| Table 5.3: The conductivity and capacitance of the 55 nm film on Pt electrode at 95% RH and 25 °C in terms of inter electrode gap distance..... | 159 |
| Table 6.1: Interfacial energy parameters..... | 182 |
| Table 6.2: Calculated hydrophilic fraction (%) of both un-annealed and annealed films..... | 183 |
| Table 6.3: Surface energy parameters of unannealed and annealed ultra-thin Nafion® films | 184 |
| Table 7.1: Reaction condition of OTS modified silica substrate preparation | 223 |
| Table 7.2: The summarized parameters of OTS layer on SiO ₂ with the variation of reaction time. | 224 |
| Table 7.3: The calculated surface energies of different substrates | 231 |
| Table 8.1: Atomic % of different elements of Nafion® [®] in the Ultra-thin films..... | 251 |

List of Abbreviations

| | |
|--------|---|
| AFM | Atomic force microscope |
| BE | Binding energy |
| CCM | Catalyst coated membrane |
| CL | Catalyst layer |
| CPE | Constant phase element |
| CV | Cyclic voltammetry |
| DLS | Dynamic light scattering |
| DLVO | Derjaguin, Landau, Verwey and Overbeek |
| DMAc | Dimethylacetamide |
| DMF | Dimethylformamide |
| EC | Equivalent circuit |
| EDX | Energy dispersive x-ray |
| EIS | Electrochemical impedance spectroscopy |
| EMA | Effective medium approximation |
| EW | Equivalent weight |
| ESR | Electron spin resonance |
| FWHM | Full width at half maximum |
| GDE | Diffusion electrode |
| GDL | Gas diffusion layer |
| GISAXS | Grazing incident small angle x-ray scattering |
| HOPG | Highly ordered pyrolytic graphite |
| HOR | Hydrogen oxidation reaction |
| IDA | Inter-digitated array |
| IEC | Ion exchange capacity |
| IEV | Ion-exchange voltammetry |
| IPA | Isopropyl alcohol |
| IR | Infrared spectroscopy |
| ITO | Indium Tin Oxide |
| MEA | Membrane electrode assembly |
| MPL | Micro-porous layer |

| | |
|----------|--|
| MSE | Mean squared error |
| NMF | N-Methylformamide |
| NR | Neutron reflectometry |
| ORR | Oxygen reduction reaction |
| OTS | Octadecyltrichlorosilane |
| PEFC | Polymer electrolyte fuel cell |
| PEM | Polymer electrolyte membrane |
| PM-IRRAS | Polarization-modulation infrared reflection–absorption spectroscopy |
| PTFE | Polytetrafluoroethylene |
| PZT | Lead Zirconium Titanate |
| QCM | Quartz crystal microbalance |
| RI | Refractive index |
| R_g | Radius of gyration |
| RMS | Root mean square |
| SANS | Small angle neutron scattering |
| SAXS | Small angle x-ray scattering |
| SEM | Scanning electron microscope |
| SFGS | Sum-frequency generation spectroscopy |
| SR | Synchrotron radiation |
| STM | Scanning tunneling microscope |
| SXR | Specular x-ray reflectometry |
| TEM | Transmission electron microscope |
| T_g | Glass transition temperature |
| UHV | Ultra-high vacuum |
| UV | Ultraviolet-visible spectroscopy |
| VASE | Variable angle spectroscopy ellipsometry |
| XPS | X-ray photoelectron spectroscopy |
| XRD | X-ray diffraction |
| XTM | X-ray topographic microscop |

Chapter 1

General Introduction

Polymer electrolyte fuel cell (PEFC) is an energy conversion device that directly converts chemical energy into electricity. The two main barriers for the widespread commercialization of PEFC technology are cost and durability. These two are largely related to the catalyst layer of a PEFC. The high cost is largely attributed to the precious platinum employed as the catalyst. The durability of a PEFC is linked to the degradations of carbon supported Platinum (Pt) and the polymer electrolyte membrane. The extent of accessibility and the *in operando* utilization of Pt in the catalyst layer has direct implications on the PEFC stack cost. By improving the accessibility of catalyst to the reactants (electrons, protons and molecular species) of the half-cell reactions, acceptable performance could be realized with lower amount of catalyst, which would translate into lower cost. As elaborated below, the ion-conducting polymer (ionomer) in the PEFC electrode is thought to be one of the key material components affecting the accessibility and effective utilization of expensive Pt catalyst. This thesis is concerned with this ionomer material.

The key components of a PEFC are shown in Figure 2.1. The electrochemically functional components - anode and cathode - are separated by a proton-conducting polymer electrolyte after which the fuel cell is named as PEFC. The membrane electrode assembly (MEA) is heart of a PEFC. It consists of a solid polymer electrolyte membrane (PEM), an anode catalyst layer, a cathode catalyst layer and carbon based porous transport layers (PTL). The PTL is commonly referred to as the gas diffusion layer (GDL) in the literature. The main electrochemical reaction takes place in the catalyst layers (CLs). PTLs are placed next to the CLs and serve multiple functions including the media for the transport of electrons, heat, reactant/product gases

and liquid water. In recent years, a thin micro-porous layer (MPL) has been introduced between the CL and the PTL for improved water management and electrochemical performance. The Teflon-coated, highly porous structure of MPL is thought to be highly effective in removal of water generated at cathode CL. However, the exact mechanism by which this occurs is still not resolved.

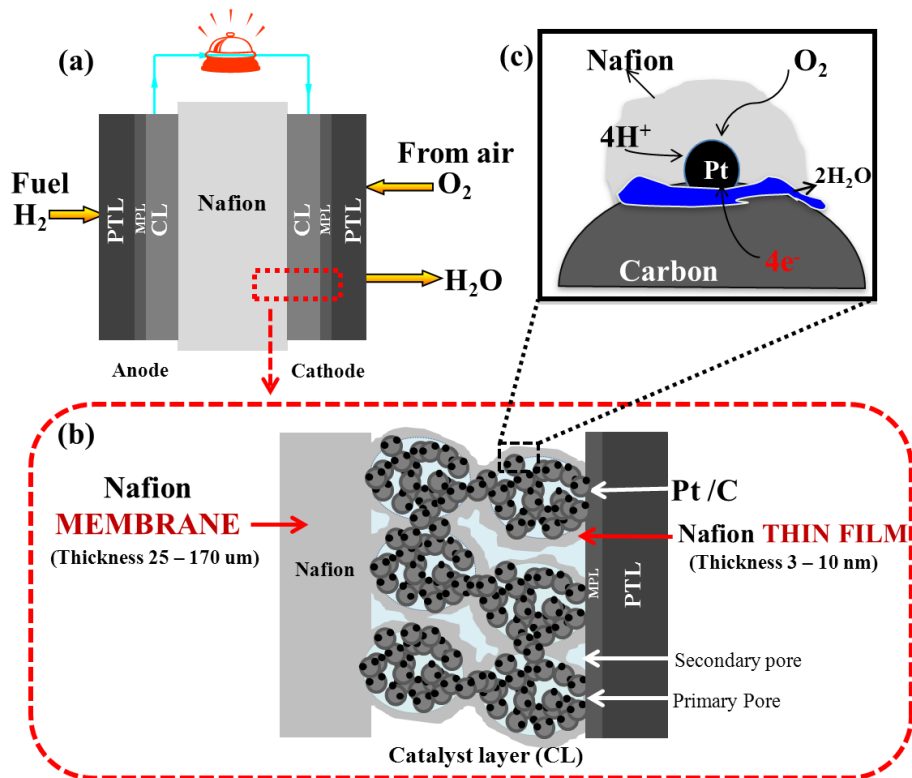


Figure 2.1: (a) Membrane Electrode Assembly (MEA) (b) CLs microstructure (c) CL transport and reactions.

The conventional catalyst layers (CLs) of PEFCs are porous composite of ionomer and Pt/C catalysts. The ionomer in the CL exists as a thin film covering the Pt/C aggregates as shown in Figure 2.1b. The thickness of the ionomer thin film has been reported to be 3-10 nm [1]. The primary role of the ionomer (typically a perfluoro-sulfonic acid, e.g. Nafion®) in the CLs is that

of a proton conductor. However, it also affects the local transport of neutral species (O_2 or H_2) to the catalyst sites. Moreover, the interfacial properties of the thin ionomer film play a significant role in the diffusion, uptake and removal of water, i.e., the water management, inside the CLs. It is obvious that the ionomer structure and property will affect both the proton and mass transport, which in turn will impact the local electrochemical reaction rate and, thereby, the overall PEFC performance. In fact, researchers of electrochemical energy research laboratory at General Motors (GM) [2] examined the electrode performance as a function of catalyst loading and found that low-Pt loading catalyst layers exhibited higher transport losses, which they attributed to local oxygen mass transport effect. They defined the ‘local’ transport effect as the oxygen transport to Pt crystals, which are thought to be covered by ionomer thin films. It was hypothesized that one of the reasons for high local mass transfer resistance could be caused by low oxygen diffusivity in ionomer thin films. In other words, the observed mass transfer resistance could not be explained by considering the thin ionomer film to have the same oxygen diffusivity as that of the membrane. This thesis is concerned with the investigation of properties and structure of ultra-thin ionomer films and, where possible, comparison to the membrane form.

Although the ionomer material has been well studied in the free-standing membrane form, there is a limited understanding of structure and properties of such nanometer thin ionomer films. This includes a limited knowledge of its nano-structure as well as surface (surface wettability) and bulk properties (water uptake, proton conductivity) of ultra-thin Nafion® films. Therefore, it is vital to establish the ionomer film characteristics and, more importantly, to establish what factors influence the ionomer film structure and property. Knowing how different factors control the properties of the ionomer film will permit a rational method for designing high performance PEFC electrodes and other electrochemical devices such as sensor, where thin ionomer films serve one or more critical functionality.

It is recognized that substrates induce the polymer molecules in thin films in such a way that can affect the polymer structure, properties and dynamics [3-6]. The differences have been attributed to polymer confinement, which can be influenced by wetting interaction of polymers with the substrate. For example, it has been reported that depending on the substrate nature or wetting interaction, the glass transition temperature of polystyrene can either decrease or increase compared to its bulk form [6]. The transport properties of polymer thin films can be thickness-dependent. For example, the diffusion coefficient of water in poly(4-ammonium styrenesulfonic acid) has been reported to decrease with a decrease in thickness for films studied as thin as 3 nm [7]. Thus, it can be expected that Nafion thin films can also possess thickness-dependent structure and properties. Further, the nature of substrate may have a strong influence on Nafion thin films because of the expected differences in the interaction between the substrate and the hydrophobic backbone and hydrophilic side chains. It can be hypothesized that Nafion thin films can have structure and properties significantly different than its well-studied membrane form.

However, direct investigation of the structure and properties of the ionomer films in the CLs is challenging because of the porous, non-uniform, composite nature of the CL microstructure. The ionomer may not be uniformly distributed within the CL. Moreover, the physical characteristics of the ionomer film such as local coverage and thickness may vary. One approach is to fabricate these ionomer films on well-defined planar substrates such that the films are uniformly distributed and of uniform thickness. Recent studies on Nafion® ionomer have been carried on films generated on such planar substrates. From these recent studies, there is already emerging evidence [8-16] that the structure/properties of these supported films are distinct from the extensively studied free-standing films or the membrane form of Nafion®. It has also been found that the substrate can play an important role in determining the morphology and

properties of the film [8-11,16]. Even with these studies, only a little is known about the properties and the nanostructure of the films. A review of the literature, presented in the next chapter, was undertaken to establish the current state of knowledge regarding the thin Nafion® ionomer films and also summarize the state of understanding of Nafion® membrane and Nafion® dispersion. This critical review identifies the key gaps in the understanding of ionomer thin film structure and properties.

1.1 The approach of this thesis

The main goal of this PhD thesis is to investigate nano-scale morphology and properties of *self-assembled* Nafion® thin film. One of the main targets was to develop a protocol for fabrication of ultra-thin Nafion® films and ideally to attain film thickness that are relevant to PEFC CLs, i.e. 4-10 nm. In addition to fabricating the Nafion® thin films, the research is aimed at understanding whether and how the morphology and properties of the films are dependent on physical characteristics such as film thickness, fabrication variables such as substrate type and thermal treatment, and local environmental variables such as relative humidity, presence of liquid water, and temperature.

1.2 Thesis Structure

Chapter 1: General Introduction

This chapter provides the motivation for undertaking the thesis work on the study of Nafion® thin films. The role of such ionomer thin films in the PEFC catalyst layer is introduced.

Chapter 2: Literature Review and Research Objectives

The goal of this chapter is to provide the background knowledge of Nafion® ionomer both in the membrane and the thin film forms in PEFC. Thus, a short review on the structure and properties of Nafion® membrane has been included. A review of the existing literature as it relates to the state of Nafion® in dispersion and the Nafion®/substrate interactions has also been presented. Finally, an extensive literature review on Nafion® thin film nano-structure and properties has been included to identify the existing research gap and challenges.

Chapter 3: Experimental Techniques: Theory and Application

In this chapter, the experimental techniques adopted in this study have been described. The theory and main application features are described to provide a practical sense about the applicability of these instruments.

Chapter 4: Fabrication and Characterization of Self-Assembled Ultrathin Films

This chapter presents the fabrication details of the self-assembled Nafion® thin film on planar substrate and the subsequent physical characterization of the prepared films for thickness, surface morphology and free surface wettability. The effect of time of immersion and the influence of dispersion medium composition on the self-assembly behavior of Nafion® and the characteristics morphology have been illustrated. Chapters 4 through 6 are restricted to the Nafion® thin films on SiO₂/Si substrate.

Chapter 5: Protonic Conductivity of Ultra-Thin Nafion® Films

In this chapter, proton transport property of the ultrathin Nafion® film is explored. Electrochemical impedance spectroscopy (EIS) was employed to determine the protonic resistivity of the film. A detailed protocol, experimental methodology, data collection and data interpretation are described. The design and interpretation of the equivalent circuit (the key

element of EIS) employed for impedance data fitting is also described. In addition, complementary property of water uptake by Quartz Crystal Microbalance (QCM) and relevant structural information (ionic domain) probed by Grazing Incident Small Angle X-ray Scattering (GISAXS) has been presented.

Chapter 6: Effect of Thermal Annealing and Liquid Water Exposure on Surface and Bulk Characteristics of Ultrathin Nafion® Films

This chapter deals with effect of thermal treatment (annealing) on the surface and bulk characteristics of the ultra-thin Nafion® films. The surface morphology, wettability and bulk proton conductivity of the annealed films have been investigated in terms of thickness and annealing temperature. The thickness dependent characteristics of annealed films upon the subsequent prolonged exposure to the two different external atmospheres i.e., water vapor and liquid water atmospheres, have also been described.

Chapter 7: Substrate Effect on Ultrathin Nafion® Films

In this chapter, the knowledge gathered from the aforementioned study on the Nafion® film supported by SiO₂ is extended on the other substrates including Gold (Au), Platinum (Pt), Carbon (C) and Octadecyltrichlorosilane (OTS) modified silica (OTS/SiO₂/Si). Self-assembly behavior of Nafion®, the resulting morphology and the wettability of film free surface are described in terms of the nature (hydrophilicity to hydrophobicity) and surface energy of the substrate. In addition, the thickness-dependent film morphology and surface wettability both before and after annealing have been described. Moreover, differences in water uptake of the Nafion® films as a function of substrate type is discussed.

Chapter 8: X-ray Beam Damage of Ultra-Thin Nafion® Films

The goal of this chapter was to investigate the damage of Nafion® thin films by X-ray irradiation. X-ray based techniques have been adopted by many researchers as a diagnostic tool for both *ex-situ* and *in-situ* material characterization techniques in PEFC. This chapter discusses the degradation of thin films in terms of the x-ray power and exposure time. The structural damage is further confirmed by measuring the loss in proton conductivity after x-ray exposure. A mechanism of x-ray irradiation damage is also proposed.

Chapter 9: Conclusions and Recommendations

The chapter summarizes the overall findings and its implication in the PEFC CL.

Chapter 2

Literature Review and Research Objectives

2.1 Introduction

This chapter provides a general idea about the PEFC working principle and presents a microscopic view of the PEFC CL where the main electrochemical reactions take place. The importance of thin ionomer film in CLs as a limiting factor for electrochemical activity is discussed. Moreover, the CL fabrication method and the post-fabrication treatment conditions as well as the nano/micro-scale structure and properties of the CL and its material components are briefly discussed to help a reader understand both the research goals and some specific experiments.

It is noted that in a PEFC, Nafion® (ionomer) is employed as the membrane and as the proton-conducting binder in the CL. In the latter, Nafion® is present as a thin film coating the Pt/C catalyst aggregate as shown in Figure 1.1 (b). Whereas the Nafion® membrane has been extensively studied and reported in literature [17], the knowledge on thin Nafion® films has only begun to emerge in recent years [8-16]. Unlike self-standing Nafion® membrane, supported thin film might be distinct in both the structure and properties due to high interfacial area to volume ratio. Therefore, a brief literature review on Nafion® membrane structure and properties has been carried out to help understand the distinct features of Nafion® thin film.

Two key factors – the state of Nafion® in dispersion and the Nafion®-substrate interaction are dominant in determining the morphology of the thin film. As Nafion® thin film is fabricated from its dispersion, one of the foci of the literature review is to provide an overview of

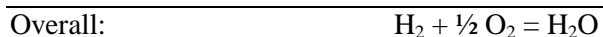
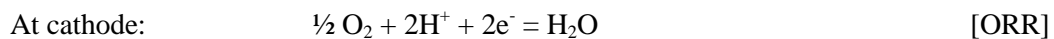
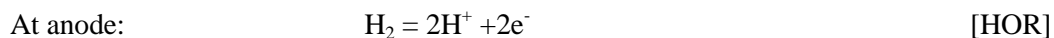
the aggregation and self-interaction behavior in different dispersion media. A knowledge regarding substrate-induced restructuring and re-organization help to understand the ultimate morphology and properties of the thin ionomer films.

Finally, a key target is to provide the state-of-the-art knowledge on Nafion® thin films which have been investigated so far. The critical review of the existing literature and a comparative and combined discussion has helped to define the scope of research for this thesis.

2.2 PEFC Catalyst layer

2.2.1 Fundamental aspects of PEFC CL

PEFC has already been introduced in Chapter 1. Membrane electrode assembly (MEA) is the heart of the PEFC which consists of PTLs, two electrodes (anode and cathode) and polymer electrolyte membrane. The electrodes are typically known as catalyst layers (CLs), which is a porous composite structure. Conventional CLs have typical thickness of 10-20 μm and are made of Pt catalyst supported on carbon and Nafion® ionomer, which serves as the proton conductor and a binder. The main electrochemical reactions take place on the Pt catalyst surface. The basic fuel cell reactions are:



Hydrogen oxidation reaction (HOR) and oxygen reduction reaction (ORR) take place at anode and cathode, respectively. Both HOR and ORR reactions occur on the catalyst surface and

the complex reaction kinetics or mechanism have been described in many fundamental steps in the literature [18,19]. In addition to the above-mentioned reactions, several side reactions can also take place. The intrinsic reaction kinetics depends on the catalyst activity and the reactant. The actual rate of the reaction depends on the relevant potentials associated with the three reactant types – local chemical potential or concentration of neutral species (H_2 and O_2) and the electrical potentials of the ion-conducting and electron-conducting material phases. The species concentration and the electrical potentials can vary across the thickness and in the plane of the catalyst layer due to transport effects. The transport of these species is a function of the intrinsic transport coefficients (diffusivity and conductivity) and the microstructure of the CL.

Thus, the local concentration of the neutral species differs from the bulk concentration of reactants being fed to the cell because finite gradients in concentration are needed to transport the reactant molecules through the porous PTL and CL and locally through the thin ionomer film covering the Pt catalyst. The wettability of the ionomer film on catalyst surface, further influences on the reactant transport. A hydrophilic film surface would promote flooding of the pore with liquid water, which could severely restrict transport of the reactant to the Pt sites [20]. The local potential/overpotential is controlled by both the electron conduction through the carbon phase and the proton conduction through the ionomer phase. The electronic conductivity of the carbon is several orders of magnitude higher than the protonic conductivity of the ionomer. Thus, proton conduction in the CL may be the limiting transport process. More importantly, as pointed out above, higher protonic resistance would translate into increased overpotential/loss to generate a given amount of current.

Both the intrinsic properties of the constituent materials of the CL and the microstructure of the CL, i.e. shape, size, distribution and connectivity of the material phases, ultimately control

the effective property and thereby the electrochemical performance of the CL [21]. The microstructure and resulting effective properties are influenced by the CL fabrication process. In this regard, the catalyst ink plays an important role. In particular, the interaction of the ionomer and Pt/C aggregates in the catalyst ink has been proposed to control the microstructure of the CL [22-24]. The interaction of the ionomer with the other solid phase of the CL (Pt/C) will depend on several factors including the dispersion media, carbon type, and ionomer type. The aggregation state of both the ionomer and Pt/C will also be dependent on the dispersion media type as well as the concentration. Furthermore, the polymers (including ionomers) have local mobility and may undergo reorganization/reorientation due to the different fabrication techniques and post treatments.

2.2.2 Catalyst layer fabrication and microstructure

As stated above, the microstructure of the CL will depend on several factors including the catalyst ink composition, the method of fabrication techniques, and the post-treatment. Lister *et al.* [25] have reviewed the various methods for CL/MEA fabrication. The discussion here is limited to the aspects of the aforementioned factors that directly affect the ionomer structure and property in the CL.

Catalyst ink: Depending on the Nafion® dispersion state in solvent, catalyst ink has been classified into two broad categories (i) solution ink and (ii) colloidal ink. Solution ink is formed from the solvent with dielectric constant greater than 10 whereas colloidal ink is formulated from the solvent group with dielectric constant between 3 to 10 [22-24]. It has been reported in the literature that colloidal ink form a network structure and solution ink form a agglomerate structure where an aggregate of Pt/C is covered by an ionomer thin film.

CL fabrication techniques: A number of fabrication techniques have been reported including spraying, brushing, rolling method, printing method and decal transfer method [26-29]. Depending on how the catalyst layer is applied to the MEA component, the electrode is referred to as the catalyst coated membrane (CCM) or gas diffusion electrode. The dominant methods for CL fabrication is the application of a catalyst ink suspension directly to the membrane resulting in CCM [30] and as a less commonly employed art of applying the ink to the porous carbon support resulting in gas diffusion electrode (GDE) [31,32]. It is pertinent to track the history of ionomer in the CL. The first step is the creating the formulation for the catalyst ink. Typically, the catalyst ink is made by adding the dry catalyst powder to the ionomer solution/dispersion. The state or the nanostructure of the ionomer in the starting dispersion may largely dictate the ionomer film that form as a result of ionomer self-assembly upon the catalysts [22]. Some rearrangement during removal of volatiles during ink application/drying on the membrane can be expected or the ionomer may remain unaltered in a kinetically frozen state. In preparing an MEA, a hot pressing step is often employed to improve the physical contact between the CCM and porous transport layer or the GDE and the membrane. The sandwiched electrode assembly is simultaneously pressed and heat-treated at temperatures ranging 120-195 °C [33-35]. One of the catalyst layer fabrication method e.g., decal transfer technique involves high temperature (usually 150-210 °C) transferring process [36,37] where catalyst layer is prepared on a separate substrate and then transferred to the membrane resulting in a CCM. The transfer step involves high temperature and pressure. These high temperatures exceed the glass transition temperature of bulk Nafion® and likely that of thin Nafion® films. Thus, structural changes in ionomer can be expected after the high temperature treatment step.

CL microstructure: Although the exact microstructure of the CL is a topic of intense investigation, an idealized representation based on the agglomerate structure has been considered

in the literature. Two types of agglomerate structures have been considered for PEFC CL modeling: (i) ionomer filled agglomerate [38,39] and (ii) water filled agglomerate [40]. There are unresolved questions about both types of agglomerate models. For ionomer filled model, it has been shown that the accessibility of reactant molecules (H_2 and O_2) to the Pt at the core of the agglomerate are restricted at high current density, which results in reduced utilization of Pt. On the other hand, proton accessibility to the core of the agglomerate is always a limiting factor for the water filled agglomerate model. In both type of agglomerate models, ionomer exists on the surface of Pt/C agglomerate as a thin layer through which the O_2 on cathode side H_2 on anode side must diffuse through. The ionomer thin film covering the agglomerate and ionomer phase in the ionomer filled agglomerate is the primary proton-conducting phase. The transport properties of the ionomer can be expected to play a critical role in determining the local electrochemical reaction rate. Existing agglomerate models have considered the transport properties of the ionomer to be the same as that of the membrane. However, the intrinsic transport properties of the ionomer thin film in CL has not been independently studied. In addition to the transport properties, it will be important to understand the nanostructure/morphology of the thin film in CL.

Ionomer might be distributed as a continuous or semi continuous film within the CL. It is difficult to determine whether the ionomer exists as a homogeneous or non-homogeneous distributed phase in CL. Irrespective of the distribution, the ionomer (usually, Nafion®) covers the aggregate of catalyst/support in the CL. More *et al.* [1] employed transmission electron microscope (TEM) to investigate CL microstructure and reported that Nafion® ionomer exists as a 3-10 nm thin film on the C/Pt surface as shown in the Figure 2.1. They also observed that ionomer strands hold the carbon agglomerates together providing a path for proton conduction through the rod-like fibrils bridging in between Pt/carbon agglomerates. Moreover, a layer of

ionomer of ~4–10 nm thickness with well-packed morphology around Pt/C clusters was evident based on molecular dynamic simulation [41].

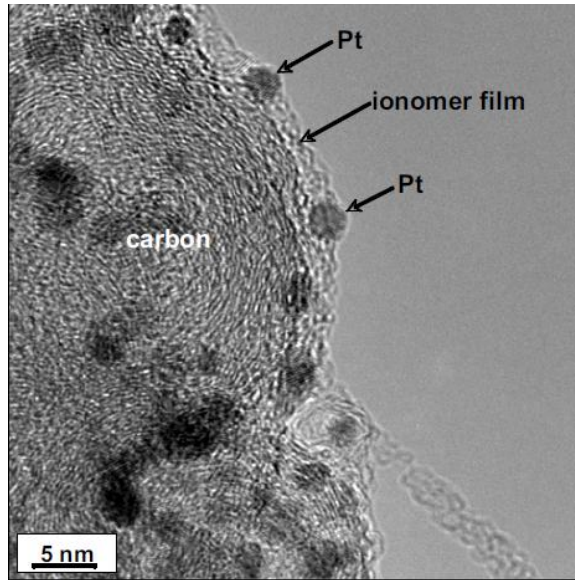


Figure 2.1: TEM image showing the structure of Pt/ionomer/C microstructure [1].

2.2.3 CL wettability and ionomer behavior

Water management inside the CL is controlled by its wettability (hydrophilicity or hydrophobicity). Local water is generated during ORR in the catalyst surface which should be properly managed to let the fuel cell functioning. Highly hydrophilic CL retain water, as a result, mass transport might be hindered. On the other hand, highly hydrophobic CL might lower the water content, which could greatly impede the water-mediated proton conduction. Therefore, water is critical for enhancing the proton mobility/diffusivity on one hand but also responsible for mass transport loss. Moreover, water transport is critical as it involves both Pt dissolution and carbon corrosion [42].

A few recent studies [43-46] have been reported on the investigation of the wettability of carbon/ionomer composites as found in CL. The wettability of CL is determined by the pore size, functional group of carbon and carbon/ionomer ratio. In general, the hydrophilic side chain of Nafion® ionomer moves toward the polar carbon surface resulting the external (film/air) interface hydrophobic. Li *et al.* [46] elaborated the wetting behavior in terms of carbon/Nafion® ratio. At low carbon content, a significant water droplet contact angle hysteresis, similar to pure Nafion® films (advancing contact angle 110° and receding contact angle 30°, hysteresis ~80°) [10,47] was observed. The composite became hydrophobic and even super-hydrophobic with changing the carbon content 30 to 80%. At >80% carbon content, the composite became wettable again as due to insufficient surface coverage by ionomer. The selection of carbon type is also a dominating factor to maintain CL wettability [48]. However, the wettability may change from hydrophobic to hydrophilic during the fuel cell operation as due to the ionomer mobility and restructuring in the presence of local water generated from the ORR reaction. Other important factors that can influence wetting property of the CL are the carbon degradation and the inherent surface roughness.

However, the thickness and distribution of the ionomer on the catalyst surface in CL is directly related to the ionomer loading. Further, it is known that the amount of ionomer loading significantly impacts the CL performance. At low Nafion® loading, the proton transport may be a limiting factor. In contrast, at high Nafion® loading, electron conductivity and oxygen diffusivity might be hindered and act as the limiting steps. High Nafion® loadings also cause flooding in the CL due to poor water management, which is further responsible for mass transport losses [42]. Therefore, an optimum ionomer loading is the key for the performance of cathode CL. Many studies [49,50] have focused on the optimization of Nafion® ionomer loading and the maximization of the CL performance. Lee *et al.* [49] investigated that an initial increase in activity

with increase in loading of up to 1.3 mg/cm^2 followed by a more gradual change with a maximum at 1.9 mg/cm^2 (~33 mass%) for CL with Pt loading of 0.4 mg/cm^2 . For the same catalyst loading, Li *et al.* [50] found that that 30% Nafion® loading resulted in highest CL performance. However, the reason for drop in CL performance is not understood at least at the microscopic level, i.e. how the Nafion® ionomer in the CL impacts the mass transport; does it affect the pore structure and property resulting in a reduced “gas-phase” mass transport or does it form a thicker layer covering the Pt crystal resulting in increased diffusional resistance through the ionomer film.

2.3 Nafion® Ionomer

2.3.1 Fundamental of Nafion® ionomer

The most extensively employed ionomer in polymer electrolyte fuel cells is a DuPont product – Nafion® because of its high chemical and thermal stability in the acidic environment. Nafion® is a copolymer with comb-like structure made of fluorocarbon monomer as a backbone upon which the sulfonic acid terminated perfluorovinyl ether monomers are decorated as pendants as shown in Figure 2.2. The exact molecular mass of a single chain Nafion® molecule is generally not reported; although, values ranging 1×10^5 - 1×10^6 g have been stated [51]. Instead, the average molecular mass (in grams) per sulfonic group referred to as the Equivalent Weight (EW) has been employed as an identifier. An EW of 1100 would correspond to $x=6$ and $y=1$ in the polymer chain shown in Figure 2.2. It is instructive to recognize some of the length scales associated with the molecular structure. From the typical bond lengths, the extended side chain length can be estimated to be of the order of 0.8 nm and the extended backbone spacing between two side chains, uniformly distributed along the backbone, can be estimated to be of the order of 0.6-1.2 nm for Nafion® of EW of 1100 [52].

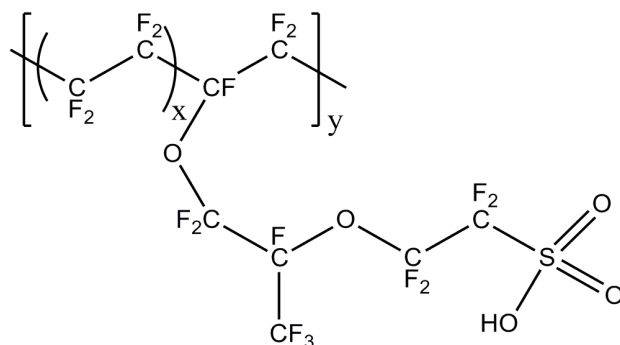


Figure 2.2: Molecular Structure of Perfluorosulfonic acid ionomer (Nafion®)

Self-standing, thick (>25 microns) films of Nafion® are considered to be the benchmark electrolyte membrane for PEFCs and also find applications in chlor-alkali and water electrolyzers [53,54]. Much thinner, supported films of Nafion® are finding increasing applications in sensors and actuators [55]. An interesting thin-film structure, not yet fully understood, arises during the self-assembly of Nafion® on aggregated Pt/C catalyst during the catalyst ink formulation stage of PEFC electrode fabrication resulting in ultra-thin, discontinuous films on non-planar, heterogeneous substrate [1].

2.3.2 Nafion® as polymer electrolyte membrane (PEM)

Nano-structure/morphology of Nafion® membrane: Different models for the Nafion® nano-structure discussed in the literature have been summarized in the Table 2.1. Most of the models have been proposed based on x-ray scattering or diffraction techniques, all those models capture the commonly observed maximum peak intensity that appears at the q values in between 1 to 2 nm^{-1} with $q=4\pi \sin\theta/\lambda$ as shown in Figure 2.3. It has been well studied that the peak in the scattering intensity vs wave vector q plot appear due to ion clustering, the peak has been termed as the ionomer peak

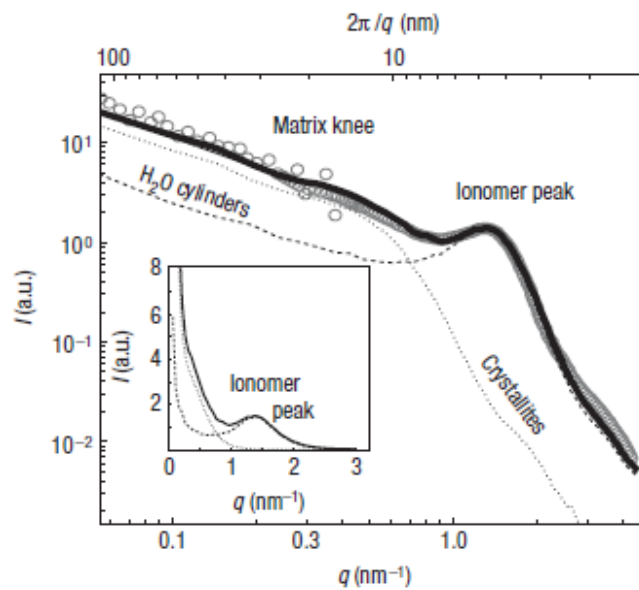


Figure 2.3: SAXS experimental data showing ionomer peak of Nafion® ionomer membrane. Figure is taken from the reference [64].

Gierke's Cluster Network model (Figure 2.4) was popular for a long period, although the 1 nm-diameter channels has been questioned. Rod-like or Fibrillar structure model is highly correlated with the ionomer solution state and aggregation behavior. Although the small angle x-ray scattering (SAXS) scattering patterns from various studies are very similar, different structural models can adequately fit selected data raising the issue of ambiguity of the models. To resolve this issue, Schmidt-Rohr *et al.* [64] came up with the independent evidence where they tried different models to fit a variety of SAXS data in the literature. Dozens of models failed to match all key features of the experimental scattering data. They proposed a new model to describe the transport properties that has been termed as the water-channel model (Figure 2.4). Besides the scattering technique, some other techniques like TEM [56,57] and atomic force microscope (AFM) [58,59] have provided visual evidence of nano-scale structure of the surface of Nafion® membrane. These images also support the existence of ionic cluster of sulfonic acid groups.

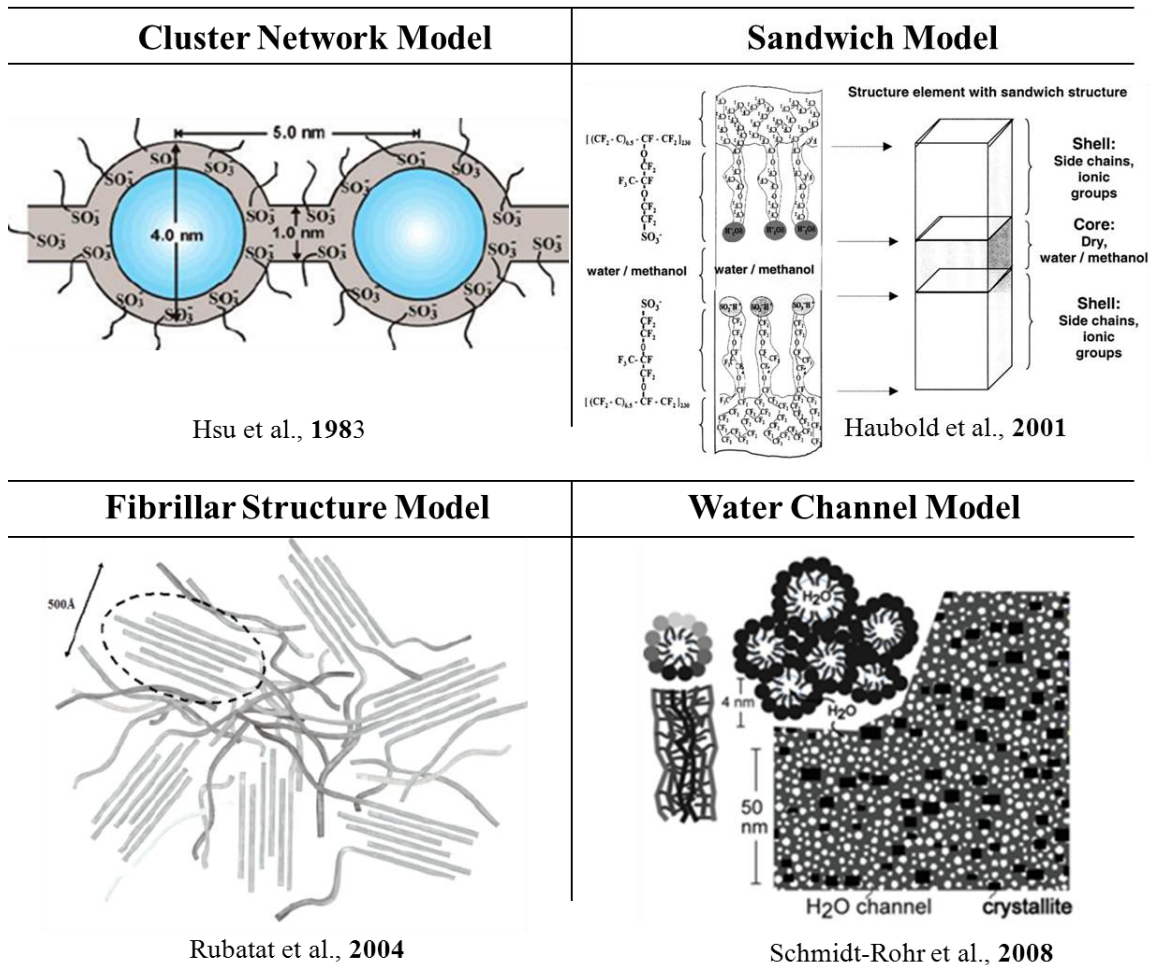


Figure 2.4: Structural models of Nafion® ionomer membrane. The Figures are re-printed from the references [60-64]

Table 2.1: Summary of nano-structural model of Nafion® membrane

| Group | Model | Description | Techniques |
|---|--|---|--|
| Gierke <i>et al.</i> 1981 [60] | Cluster- Network Model | It can be described as a 3-5 nm diameter of ionic cluster which are inter connected by narrow 1 nm channels, long range proton conduction occur through the channel | WAXD, SAXD |
| Haubold <i>et al.</i> 2001 [61] | Sandwich Model | It consist of a shell region (sulfonic acid group and side chain) and embedded core region, the core can be empty or flooded by water to facilitate proton conductivity. | SAXS with SR |
| Rubatat <i>et al.</i> 2002 [62] | Elongated polymeric bundles or rod like model | Elongated polymer bundles with a diameter of 4 nm and length larger than 100 nm can be made by the aggregation of ionomer chains. Those aggregates are surrounded by ionic group in a orderly fashion. | SAXS and SANS |
| Rubatat <i>et al.</i> 2004 [63] | Fibrillar structure model | Fibrils consist of elongated polymeric aggregates surrounded with the ionic charges, | SAXS, SANS, TEM, AFM |
| Schmidt- Rhor <i>et al.</i> 2007 [64] | Water channel model | Inverted-Micellar cylindrical water channel with the diameters in between 1.8 to 3.5 nm surrounded by partially hydrophilic side branches. Those channels are oriented in parallel in the polymer matrix. | Quantitativ e analysis of published SAXS curves |

In SAXS scattering pattern of Nafion®, in addition to the ionomer peak, another peak appear at q values at $\sim 0.05 \text{ nm}^{-1}$, which corresponds to the long-range period of lamellar crystallites to the cristanility of Nafion® membrane [65]. Although this peak is very common for Nafion® membrane indicating certain amount of crystallinity in the membrane, completely absence in the recast film (prepared from Nafion® dispersion by solvent evaporation) is noted.

The peak appears when the recast film is heat treated or annealed at elevated temperatures [65-68]. Therefore, it is clear that the crystalline order develops with thermal annealing. However, it is important to note that regardless of the source of Nafion® film, the ionomer peak at q values between 1 and 2 nm^{-1} is always present.

Water uptake in Nafion® membrane: Water uptake is one of the key factors that has a direct influence on the morphological change, proton conductivity and mechanical properties of the membrane. In a majority of the literature, water content has been presented in the terms of λ_w , number of water molecule per sulfonate group. There is a discrepancy in water uptake based on the membrane equilibration in saturated water vapor or in liquid water. Upon equilibration in pure liquid water, membrane λ_w values has been found to be ~ 23 whereas upon equilibration in saturated water λ_w values of ~ 14 have been found [69-76]. This phenomenon is known as Schroeder's paradox [77]. Proton conductivity largely depends on the state of water, which may be linked to the total amount uptake. Differential scanning calorimetry (DSC), nuclear magnetic resonance (NMR) and fourier transform infrared spectroscopy (FTIR) have been employed to identify the state of water. The state of water has been classified into three types: (i) bound water that has strong interaction with the polymer, (ii) loosely bound water that has weak interaction with the polymer and (iii) free water that behaves like bulk water. Bound water in either form can together be called as surface water.

Proton conductivity of Nafion® membrane: Several studies have reported proton conductivity values of Nafion® membrane measured mostly by AC impedance spectroscopy technique. There is a substantial discrepancy in the proton conductivity for membrane that has been exposed to liquid water versus that exposed to highly saturated water atmosphere (100% RH). Similar to water uptake behavior of membrane, liquid water saturated Nafion® membrane

show higher proton conductivity than that of water vapor saturated membrane. It was found that proton conductivity varies from 80 to 100 mScm⁻¹ at ambient temperature (20-30 °C) in the presence of liquid water [78-80]. At elevated temperature of 90 °C [81], a significant increase in conductivity of up to 190 mS.cm⁻¹ has been reported although a drastic depression in the proton conductivity 25 mS/cm at 95 °C [82] has also been reported. In a fully humidified environment, the proton conductivity varying from 50 to 80 mScm⁻¹ at ambient temperature/room temperature (20 to 30 °C) has been reported [82-84]. With increasing temperature, proton conductivity increased; values of 140 mScm⁻¹ at 65 °C [85] while 81 mS/cm at 95 °C [86] have been reported. As expected, the proton conductivity is independent of the membrane thickness.

Proton conduction mechanism in Nafion® membrane: In Nafion®, proton conduction can be described in terms of the surface diffusion, Grotthuss (hopping) mechanism and vehicular/en-mass diffusion [87-90]. At low water activity, surface conduction mechanism dominates in a layer of around 1 nm from the pore wall. Grotthuss mechanism involves proton transfer through the hydrogen bonding with the active participation of water molecules. In bulk water, proton exists as a hydronium ion and may further hydrate itself to form H₉O₄⁺ and H₅O₂⁺ are called Eigen cation [90] and Zundel cation [91], respectively. Therefore, proton can be transferred/transported through the continuous dynamic exchange of Eigen cation and Zundel cation. On the other hand, certain proton conduction contribution might come from the self-diffusion of hydronium ion through water as water has high self-diffusion coefficients which termed as vehicular or en-mass diffusion mechanism. Grotthuss mechanism is the fastest as the transport is determined by the rate of hydrogen bond exchange between a hydronium ion and water molecule instead of the slower rate of hydronium ion diffusion.

Thermal annealing effect on membrane: The ionomer properties, including proton conductivity and mass permeability, are linked to the nanostructure. The later one also depends on film thickness and density. However, the nano-structure of the ionomer films is modified through morphological changes when the films are heated above the glass transition temperature (T_g). Bulk Nafion® has a T_g of 109 °C [92]. Usually, ionomer stays as a normal micelle with outward sulfonate group in the cast membrane where annealing might reorient the structure into inverted micelle with inward sulfonate group. In literature [93-98], a wide variety of annealing temperature (100 °C to 200 °C) and annealing time (30 min to 12 h) have been employed.

Hensley *et al.* [94] found that the annealing of Nafion® membrane of different thicknesses at 165 °C for 3 h resulted in a significant improvement in the proton conductivity, the water permeability and the self-diffusion coefficient of water and protons, with the greatest improvement in the thinner films (<50 µm). It was argued and correlated with the findings of wide-angle x-ray scattering (WAXS) measurement that the crystallinity of thick films decreased whereas the crystallinity of thin films increased due to annealing [94]. Jung *et al.* [95] reported that the annealing of DMFC MEA at 130 °C provided the highest proton conductivity of Nafion® in the catalyst layer. Conversely, ionomer treated in such a high temperature, achieved sufficient mobility such that the ionomer covered the catalyst particles and blocked the primary pore of the CL. Therefore, the overall electrochemical performance of the cell decreased. Ding *et al.* [96] also showed that the cast membrane shows similar performance to commercial membrane upon annealing at 130 °C for 10 min in dry oven or 30 min in a humid oven.

In contrast, Kwon *et al.* [97] showed two-step changes in proton channel network due to annealing. Firstly, the ionic domains on the membrane surface changes from cluster-like (perpendicular to the membrane surface) to chain-like (parallel to the membrane surface) with an

accompanying increase in the proton conductivity of the membrane. Secondly, as the annealing continues, the chain-like configuration of the proton channels persist but the conductance of the membrane decreases. No significant changes were observed due to annealing at 80 °C or lower temperatures but significant changes were observed upon annealing at 100 °C or higher temperatures for a few hours. Further, when annealing temperature approaches the glass transition temperature (T_g), the mobility of sulfonic acid groups increase which may encounter and react with each other more easily forming sulfonic anhydride. Park *et al.* [98] studied sulfonated polysulfone (SPSU) ionomer membrane and found that annealing reduced the proton conductivity, the water content and the mass permeability. They concluded that the reason behind this behaviour is the compactness and densification of the structure of the membrane upon heat treatment at sub- T_g .

2.3.3 Nafion® in dispersion

Nafion® in a liquid can exist in one of the following states: i) solvated ii) colloid iii) precipitated, depending on the dielectric constant of the liquid. In the solvent with $\epsilon > 10$, Nafion® exist in a solvated state, in a solvent with $3 < \epsilon < 10$, Nafion® is colloid, and in a solvent with $\epsilon < 3$, Nafion® precipitates [22,23]. This would suggest that Nafion® forms a solution when mixed with most of the alcohol (polar solvent) types whereas it will precipitate in liquid hydrocarbon media (non-polar solvent). The structure of Nafion® consisting of a polar sulfonate group containing side-chain and a non-polar backbone is directly linked to the three states in a liquid medium. In a medium with $\epsilon > 10$, the polar side chain of Nafion® may be stabilized energetically and orient outwards in the polar solvent resulting in a solvated Nafion®. In a medium with $3 < \epsilon < 10$, the side chains become insoluble and form a reversed micelle structure resulting in a colloidal state. In contrast, Nafion® precipitates in a medium with $\epsilon < 3$ due to coagulation of the

colloidal particles. Dielectric constant of the medium also plays a great role of ion exchange capacity (IEC) of sulfonate group where IEC increases with increasing dielectric constant.

Several studies have been conducted to understand state of Nafion® in its dispersions of alcohols, water and water/alcohol mixture. Small angle neutron scattering (SANS) and small angle x-ray scattering (SAXS) techniques reveal that Nafion® exists as rod-like structure [99-103]. A diameter of 4 to 5 nm for the rod has been proposed with the core of rod made of hydrophobic Nafion® backbone and the sulfonic acid containing side-chain extending outwards of the rod surface. The diameter of the rod depends on the surface tension rather than on the dielectric constant of the dispersion media. As a result, the diameter is determined by balancing elastic and interfacial energy [99]. The elastic energy can be defined by the energy required to form rod-like structure whereas the interfacial energy corresponds to the hydrophobicity of side chain to the solvent. Therefore, at low interfacial energy the diameter of rod is independent of the dispersion media. On the other hand, at high interfacial energy, the diameter increases to minimize the surface tension.

From an electron spin resonance (ESR) study, a fringed-rod model of Nafion® was proposed. In this model, at low Nafion® concentrations in the dispersion, a part of the Nafion® chain segments is incorporated in a rod while other parts are outside of the rods and this is termed as the primary aggregated Nafion® bundle [104]. At higher Nafion® concentrations, the chains outside of the rods become incorporated in to other rods and primarily make a hexagonal structure, termed as secondary aggregated Nafion®. With further increase in the concentration, the incorporation of outside chains continues and eventually entire polymer becomes connected. That also explains how rod-like micelles in dispersions of the ionomer make a transition to reverse micelles in the swollen membrane.

Studies employing dynamic light scattering (DLS) technique propose a microgel model based on fringed rod model [105-107]. It explains that isolated rod cannot exist even at very low Nafion® concentration due to strong hydrophobic effect of Nafion® backbone. At higher concentration, one or several of the Nafion® chains form fringed rods, which further interconnect with each other through the incorporation of the dangling chain segments at their ends to form large Nafion® aggregates. Unlike the secondary aggregates of the fringed-rod model, in the microgel model, one rod in the aggregate might connect to two or more rod-like units acting as a crosslinking point. Based on the DLS measurements, it was also found that there are two types of aggregation of Nafion® in methanol/water, 4/1 wt ratio. The primary aggregated Nafion® (particle size $\sim 10^3$) can be attributed to hydrophobic interaction in the dispersion whereas the secondary aggregated Nafion® (particle size $\sim 10^4$) can be attributed to the ionic aggregation through electrostatic attraction of Nafion® side chain of the primary aggregated particles.

Moore and Martin [108] conducted concentration dependent viscosity measurement of Nafion® dispersion in 50/50 water/ethanol mixture and found an interesting behavior of Nafion®. Unlike most of the other polymer characteristics, a dramatic increase in the reduced viscosity upon dilution was observed; this phenomenon was termed as polyelectrolyte effect. Eight years later, Aldebert *et al.* [99] found a correlation between polyelectrolyte behavior and dielectric constant of solvents. They showed that the viscosity of Nafion® (EW=1100 and Li⁺ form) increases with decreasing Nafion® concentration below 0.5 g/dl to 0.01 g/dl in dispersion media like methanol ($\epsilon=17.51$), ethanol ($\epsilon=19.92$), 2-propanol ($\epsilon=124.55$), 1-propanol ($\epsilon=32.70$), and water ($\epsilon=78.39$). No effect was observed in dispersion media such as formamide ($\epsilon=111$) and N-Methylformamide ($\epsilon=182.40$). It was hypothesized that polyelectrolyte effect increases with an increase in the dielectric constant of up to $\epsilon\sim 30$ but was constant for $\epsilon\sim 30-80$ except for N,N-dimethylacetamide ($\epsilon=37.78$) and above that (i.e, $\epsilon > 100$) it disappeared. This phenomenon

was interpreted in terms of persistent length theory, where a transition of worm-like chain to a rigid chain happens with decreasing concentration. However, the effect in the high dielectric constant medium could not be explained.

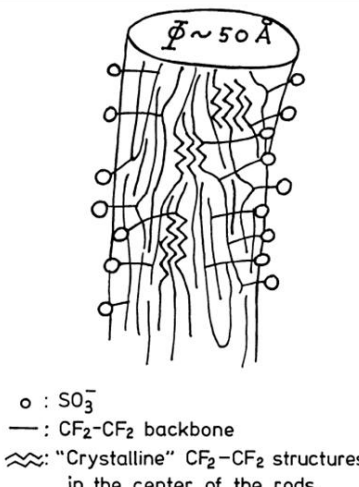
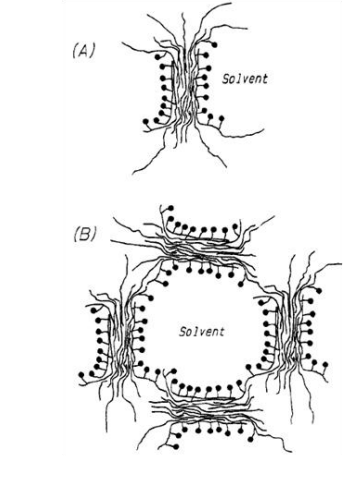
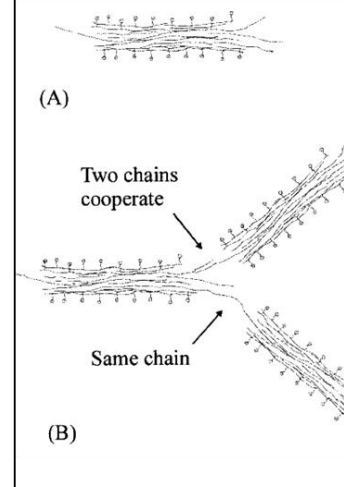
| Rod model | Fringed-rod model | Microgel model |
|---|---|--|
|  <p> \circ : SO_3^- — : $\text{CF}_2\text{-CF}_2$ backbone \sim : "Crystalline" $\text{CF}_2\text{-CF}_2$ structures in the center of the rods </p> |  <p>(A)</p> <p>(B)</p> |  <p>(A)</p> <p>Two chains cooperate</p> <p>Same chain</p> <p>(B)</p> |
| Aldebert <i>et al.</i> 1988 | Pietek <i>et al.</i> 1988 | Jiang <i>et al.</i> 2001 |

Figure 2.5: Nafion® dispersion state as described and reported by different group in the literature. Figures are re-printed from Aldebert *et al.* 99], Pietek *et al.* 104], Jiang *et al.* 105].

Recently, based on cryo-TEM study [109], it was found that solubility parameter and dielectric constant of solvent and solvent mixture have great influence on Nafion® state in dispersion. In the early year, Yeo *et al.* reported that there are two different solubility parameter of Nafion®, where δ_1 ($=9.7 \text{ cal/cm}^3$) is attributed to perfluorocarbon backbone and δ_2 ($=17.3 \text{ cal/cm}^3$) is attributed to the sulfonated vinyl ether side chains. Therefore, the solubility and dispersion state of Nafion® depend on the compatibility of solubility parameter of solvents. Nafion® in medium with solubility parameter close to δ_1 may result in isolated structure and in those with solubility parameter close to δ_2 may form a more aggregated structure. However, the

dielectric constant has a great influence on sulfonic acid dissociation and corresponding charge formation where the dissociation of sulfonic acid group increased with increasing dielectric constant. Overall, the aggregation behavior of Nafion® in different media may be explained as a balance of effect between both solubility parameter and dielectric constant. For example, in a medium with low solubility parameter close to $\delta_t=9.7$ cal/cm³ such as Dimethylacetamide (DMAc) ($\delta_t=10.8$) and Dimethylformamide (DMF) ($\delta_t=12.2$), Nafion® exists as single chain coiled structure with sulfonic acid group buried inside in dilute dispersions. On the other hand, Nafion® in N-Methylformamide (NMF) which has solubility parameter ($\delta=16.1$) very close to $\delta_t=17.3$ is found as a normal micellar structure. In media with intermediate solubility parameter, that would be apply for most of water/alcohol 4/1 mixture, a micellar structure of Nafion® has been noted and the aggregate size is thought to be determined by balancing the effect of both δ and ϵ . It was stated that the size of aggregated Nafion® particle decreases sequentially as following: MeOH-H₂O ($\delta_t=16.3$, $\epsilon=40.3$) > EtOH-H₂O ($\delta_t=15.0$, $\epsilon=32.2$) ~ isopropyl alcohol (IPA)-H₂O ($\delta_t=14.4$, $\epsilon=28.5$) > NMF ($\delta_t=16.1$, $\epsilon=182.4$) > DMAc ($\delta_t=10.8$, $\epsilon=37.8$) > DMF ($\delta_t=12.2$, $\epsilon=36.7$). Very recently, another study [110] focused on Nafion® state with varying IPA/water composition in 0.6 mg/ml Nafion® dispersion. It was reported that with an increasing IPA composition, both δ and ϵ increase resulting in an isolated coil structure of Nafion® in 80 to 70% IPA, primary aggregated rod-like structure in 60 to 50% IPA and inter-sulfonic ionic aggregation in 45 to 20% IPA. This finding is contradictory to the previous report by Ma *et al* [109], where rod-like Nafion® with aggregation was reported in 80% IPA at same 0.6 mg/ml concentration.

2.3.4 Nafion®-substrate interactions and reorganization

It is important to understand to Nafion® interaction and reorientation which are the dominating factor in determining the nano-structure of the thin films. Koestner *et al.* [111,112] employed *in-situ* AFM scanning to study Nafion® adsorption phenomenon in a liquid environment. They reported segmented rod-like aggregates with 1 nm diameter to adsorb on HOPG surface in liquid medium. With time, the height of the aggregates increases from 3 to 9 nm. The adsorption process is highly regulated by pH, where no adsorption occurred above pH 3. Nafion® structure also depends on the deposition technique. Instead of spontaneous adsorption, when rapid deposition technique like spin coating was adopted, 1- 8 nm single compact globular structure was found. It gives a direct evidence of structural variation based on deposition technique.

Masuda *et al.* [113] also employed AFM to investigate the structure of the adsorbed Nafion®. They found that the adsorbed aggregates reoriented under the influence of atomic arrangements of highly ordered pyrolytic graphite (HOPG) and two-dimensionally ordered domains were formed. Ma *et al.* [114] studied adsorption of Nafion® ionomer on various carbon types and Pt by analyzing the Nafion® dispersion before and after adsorption using ^{19}F - NMR. They found that there was a stronger interaction of Nafion® with carbon rather than with Pt. They suggested that the adsorption is achieved via hydrophilic bonding or hydrogen bonding. Zeng *et al.* [116] pointed out that Nafion® adsorbed on Pt and Au through sulfonate group as evident by Raman and cyclic voltammetry (CV) study.

2.3.5 Nafion® ionomer thin film

The membrane form of Nafion® (>25 μm) has been studied extensively over the past several decades [17], although, the nano-structure of Nafion® membrane still remains a topic of debate [64,117]. In contrast, only a few studies on ultra-thin and thin films (mostly 50 nm to several hundreds of nanometer) of Nafion® have been reported [9-16,118-129]. The structure and properties of the thin and ultra-thin Nafion® films are even less understood. Here the terminology [130] adopted for polymer films has been employed. Thus, films of less than 100 nm thickness are deemed to be ultra-thin, and those with thickness greater than 100 nm but less than a micron are deemed to be thin film. For Nafion® ionomer, an emerging body of knowledge indicates [8,10-14,131] that the properties of the ultra-thin and thin films may differ significantly from those of the membrane form of Nafion®. This is not unique to Nafion® and it is well known that as the polymer films become thinner, the interfacial characteristics dominate its bulk and surface properties [132]. In thin films of non-ionic block copolymer, it is known that the surface-block interactions (e.g. due to preferential attraction for one block) and confinement effects give rise to a variety of surface-segregated and thickness-dependent morphologies, which differ in orientation and ordering of micro-domains with respect to the surface [133-134]. The presence of an ionic moiety in the mobile side chain of Nafion® is expected to contribute to more complicated surface-ionomer interactions including electrostatic interactions. A summary of key studies in the literature on thin/ultra-thin Nafion® films is provided in Table 2.2. The studies differ in the choice of dispersion/dispersion media characteristics, the type of substrate used and the film fabrication/processing methods – all of which may impact the film properties.

Table 2.2: Summary of literature on Nafion® thin films

| References | Solution Properties | Substrates | Preparation Methods | Thicknesses | Diagnostic tools |
|---------------------------------|---|---|--|------------------------------|----------------------------|
| Blanchard <i>et al.</i> [118] | 5 wt% Nafion® (EW=1100) | ZnSe (IR-transparent) | Spin coating | 100 nm | IR |
| Krttil <i>et al.</i> [119] | 5 wt% Nafion® diluted 40 times by methanol (EW=1000) | Silver electrode of QCM | Drop casting | 20 nm, 80 nm | AFM, QCM |
| Hill <i>et al.</i> [120] | 1 wt% Nafion® in 1:1 C ₂ H ₅ OH:H ₂ O mixture (EW=800) | SiO ₂ /Si wafer | Self-assembly by immersion for 5 minutes | 200 nm, 400 nm | AFM, STM |
| Bertencello <i>et al.</i> [122] | 5 wt% Nafion® diluted by 9:1 CH ₃ OH:H ₂ O, Filtered through 0.5 mm membrane filter (EW=1100) | ITO, Quartz slides, Mica, Au | Langmuir-Schaefer | 1.3 -16 nm | UV-Vis, QCM, CV |
| Siroma <i>et al.</i> [121] | 5 wt% Nafion® diluted by 10-20 times by ethanol (EW=1000) | Si substrate with Pt band electrode | Drop casting | 70 nm | EIS |
| Ugo <i>et al.</i> [123] | 5 wt% Nafion® diluted by methanol (EW 1100) | Silanized ITO, Thiolated Au | Langmuir-Blodgett | 5.25-11.3 ug/cm ² | IEV, QCM |
| Bartencello <i>et al.</i> [124] | Dilution of commercial Nafion® by methanol to 0.85 mg/mL (EW=1100) | SiO ₂ | Langmuir-Schaefer | 16 nm | SEM, CV, AFM |
| Umemura <i>et al.</i> [125] | 5 wt% Nafion® (EW=1100) | Metal (unspecified) disk | Drop casting | 230 nm | AFM |
| Murthi <i>et al.</i> [8,126] | 20-22 wt% Nafion® diluted 16:1 by anhydrous C ₂ H ₅ OH (EW=1000) | Native SiO ₂ , Thermal SiO ₂ , Au, Pt | Spin coating, Annealing at 60 °C | 50 nm | NR |
| Wood <i>et al.</i> [9] | Nafion® dispersion-concentration not specified (EW=1100) | Glassy Carbon (GC), Pt-coated GC, Si wafer | Spin coating, Either cured at 140 °C or annealed at 210 °C | 60 nm | NR, Voltammetry |
| Noguchi <i>et al.</i> [20]127 | Nafion® (EW=1020) | Quartz prism | Spray deposition | 500 nm | SFGS |
| Siroma <i>et al.</i> [14] | 5 wt% Nafion® diluted by 10-20 times by ethanol (EW=1000) | Si substrate with Pt band electrode | Drop casting | 14-1121 nm | AFM, EIS |
| Bass <i>et al.</i> [128] | 5wt% Nafion® (EW=1100) | Si wafer | Spin coating, Annealed at 200 °C overnight | 100 nm | GISAXS, Contact Angle, AFM |
| Bass <i>et al.</i> [10] | 5 wt% Nafion® (EW=1100) | OTS-modified Si wafer | Spin coating, Annealed at 160 °C for 3-5 days | 100 nm | GISAXS, AFM |

| | | | | | |
|-------------------------------|--|---|-----------------------------------|----------------------------|--------------------------------------|
| Kongkanand [12] | 21 wt% Nafion® DE2020 diluted to 0.03-3 wt% (EW=950) | Au, Pt | Drop cast, Annealed at 80 °C | 30-300 nm | QCM |
| Ahmed <i>et al.</i> [129] | 5 wt% Nafion® diluted by a factor of 1000 with ultrapure water. (EW=1100) | Pt (111, 311, 511 & 711) | Adsorption | 3.3 nm | CV, XPS |
| Dishari <i>et al.</i> [13] | 20 wt% Nafion® diluted by ethanol into 2, 5 and 10 wt% (EW=1100) | Si-wafer | Spin coating | 70-600 nm | QCM |
| Modestino <i>et al.</i> [11] | 5 wt% Nafion® diluted by isopropanol into 2% Nafion® dispersion. (EW=1100) | SiO ₂ /Si wafer, OTS-modified Si wafer | Spin cast, Annealing at 200 °C | 100 nm (approx.) | GISAXS, Ellipsometer |
| Eastman <i>et al.</i> [15] | 20% Nafion was diluted to varied extents with anhydrous ethanol (1:20 to 1:4 by volume) | Si-wafer | Spin coating | Approximately 20–222 nm | GISAXS, QCM, NR, PM-IRRAS, SXR |

IR: Infrared spectroscopy, AFM: Atomic force microscopy, QCM: Quartz crystal microbalance, NR: Neutron reflectometry, CV: Cyclic voltammetry, EIS: Electrochemical impedance Spectroscopy, SFGS: Sum-Frequency Generation Spectroscopy, UV: Ultraviolet-visible spectroscopy, STM: Scanning tunneling microscope, SEM: Scanning electron microscope, GISAXS: Grazing incidence small angle x-ray scattering, IEV: Ion-exchange voltammetry, PM-IRRAS: Polarization-modulation infrared reflection–absorption spectroscopy, SXR: Specular x-ray reflectometry, ITO: Indium Tin Oxide.

Preparation method: Spin coating and drop casting appear to be the most common methods for film preparation resulting in film thickness typically greater than 50 nm although films as thin as 14 nm have also been reported [14]. Using Langmuir-Scahefer and Langmuir-Blodgett methods, [118,122,124] fabrication of even thinner films has been attempted. A variety of substrates have been used for film preparation including SiO₂-terminated silicon wafers, [8-15,120,121,124,126] modified silica, [10,11] metals, [8,12,118,119,125,129] and carbonaceous substrates [9].

Substrate effect/nano-structure: So far, few studies have focused on surface-induced orientation of the ionomer. Based on neutron reflectometry (NR) study, Dura *et al.* [8] found that multi-lamellar or ordering of ribbon-like aggregates of Nafion® were formed. They described

into water rich and Nafion® rich layer up to a certain thickness. No multilayer structure on Au and Pt surfaces was observed instead partially hydrated single interfacial layer was found. Wood *et al.* [9] employed same NR technique and came up with same conclusion for Pt where the interfacial layer was termed as a hydrophobic Nafion® region. While Pt turn into hydrophilic PtO by electrochemical technique long range restructuring of ionomer causing hydrophilic interface instead. Unlike metal surface, three layers of Nafion® structure were observed on glassy carbon. Based on GISAXS study, opposite view in nanostructure of ionomer on hydrophobic OTS modified wafer surface was reported where perpendicular and parallel orientation were proposed by Bass *et al.* [10] and Modestino *et al.* [11] respectively. Most recently, Page and co-workers [15] reported properties of sub-micron thin films prepared by spin-coating on SiO₂. Films of different thicknesses were generated by spin coating from Nafion® dispersions of varying concentrations prepared by dilution of stock solution by addition of ethanol. A very interesting aspect of their study was the finding that the swelling ratio, volumetric water fraction, and effective diffusivity of films are relatively constant for spin-coated films thicker than ca. 60 nm but were different for the thinner films.

Water uptake: In few studies, Quartz Crystal Microbalance (QCM) has been employed to determine water uptake of ionomer thin film. Krtil *et al.* [119] found similar water uptake in both thin film (20-80 nm) on silicon wafer and bulk membrane. In contrast, Hickner group [13] found overall lower λ_w (number of water molecules per sulfonic acid group) in thin film on silicon wafer over bulk membrane where 70 nm films has higher water uptake compare to 600 nm film. For Pt and Au substrates, totally opposite finding was reported by Kongkanand *et al.* [12] where film up to 500 nm film has similar water uptake to bulk membrane but slight depression of water content was observed in 33 nm film. In a recent study, [16] it has been showed that Nafion® films, 80 to 1000 nm on hydrophilic substrate (Si, glass) has higher water uptake than that of the films on

hydrophobic substrate (graphite, Au, ITO), though overall uptake in thin film is less than bulk membrane. It indicates that substrate has a big role but information along the ionomer thickness associated in CLs of PEFC is missing. Moreover, contradictory findings are making further complexity.

Proton conductivity: Siroma *et al.* [14,121] reported proton conductivity of Nafion® thin films prepared by drop casing method on platinum microelectrode supported by SiO₂. Thin films had significantly suppressed conductivity compared to the membrane form. Further thickness-dependent proton conductivity was observed. Both proton conductivity and activation energy decreased with a decrease in film thickness. They assumed that these phenomena may be due to the intrinsic change in the material or due to the hindrance of water adsorption in thin film. However, no details of impedance measurement and interpretation have been reported.

Thermal annealing effect on thin film: There are very few studies of annealing effect on thin ionomer film. It may be assumed that the mobility of ionomer in thin film is greater than that in thick membrane due to annealing. Maeda *et al.* [135] prepared thin film on patterned glass substrate by dropping 50 μ L of Nafion® dispersion onto the front side and dried in air. When the film was heated at 130 °C with a hot plate for 5 mins, the movement of Nafion® molecules at the surface caused by the annealing destroyed the nanostructures that were several nanometers in vertical size. Hill *et al.* [120] studied effect of thermal treatment on self-assembled thin ionomer film (200 nm and 400 nm) supported by silicon wafer. AFM revealed that even prolonged (more than 20 days) heat treatment at the temperature above T_g , did not dewet or break up the thin film which is not very common to other thin diblock copolymer films. STM study showed that ionomer exists as 3-5 nm diameter nano-aggregated structure inside of 20 nm diameter hexagonally packed cluster which led to form 200 nm circular domain but 200-nm bundles start

to break up into individual micelles with temperature annealing. Recently, Modestino *et al.* [11] characterized spin cast 100 nm film (annealed at 200 °C) properties both on SiO₂ and OTS modified substrate by GISAXS. They found that with thermal annealing of thin film, the crystalline domains were formed within the film matrix and restricted water uptake and anticipated a reduction in conductivity as well. However, the anticipation has not been validated by probing direct proton conductivity measurement of such annealed films.

Regeneration: As Nafion® consists of a hydrophilic side chain and hydrophobic backbone, the interfacial property might be hydrophilic or hydrophobic depending on the nano-orientation/organization of the polymer molecule. Freestanding Nafion® membrane has been reported to be hydrophobic with a water contact angle of 106-108° [128, 136-137]. Saturated water vapor equilibration does not make the membrane interfacial properties much difference in terms of surface wettability. In contrast, the surface of Nafion® membrane surface switches from hydrophobic to hydrophilic when water vapor replaced by liquid water onto the surface. This phenomenon has been supported by lower contact angle (~25°), [128] large contact angle hysteresis (>70°) and higher interfacial adhesion energy measurement [47]. No evidence has been reported regarding the existence of hydrophilicity of the surface in the dry condition once it has been switched from hydrophobic. Based on molecular dynamic simulation, Malek *et al.* [41] showed that thin film in the catalyst layer has a switchable behavior depending on the position of water. Unfortunately, no experimental approach has been undertaken to investigate the phenomenon.

2.4 Existing gaps in the knowledge of ionomer thin films

From the literature review, it is concluded that although a number of studies on ionomer thin films have been reported, there are still several gaps in the understanding of its structure and properties including those identified below.

- A majority of the thin Nafion® film studies have examined films of thickness (>50 nm) significantly greater than those of the ionomer in the CLs of PEFC. The structure and property of 4-10 nm thin Nafion® films do not exist in the literature. This is primarily due to the difficulty in fabricating such thin films by commonly employed methods such as spin-coating and drop-casting.
- Whereas thickness-dependent structure of block copolymers thin films has been studied, very little is known about such behavior in Nafion® thin films.
- Only one previous study (Siroma *et al.* 14]) has reported conductivity of thin Nafion® films. A strict measurement protocol and comprehensive data set on the effect of RH and temperature on protonic conductivity is missing.
- Complementary data on water uptake and swelling has not been reported.
- No systematic study has been carried out to examine the influence of thermal annealing on the behavior of Nafion® ultra-thin films.
- Many factors including dispersion characteristics and nature of substrate are expected to affect Nafion® thin structure and properties. A systematic study of these two variables has not been carried out.

2.5 Research Objectives

The overall goal of the research is to study the structure and properties of Nafion® thin films of thickness as low as 4-10 nm such as those of ionomers in the PEFC catalyst layer. The main idea was to understand and quantify if the ionomer films in the PEFC CL have characteristics different than those of the free-standing membrane form of Nafion®. At the onset of the research project, the experimental tools/techniques available were limited and the specific structure/properties to be investigated were not definitive. During the course of the thesis, the following specific goals outlined below evolved.

- To develop a protocol for the fabrication of ultra-thin Nafion® films simulating the self-assembly process occurring in the catalyst ink formulation.
- To characterize film surface in terms of surface wettability and surface morphology as a function of film thickness.
- To characterize the ionomer films for a key functional property – protonic conductivity – over a wide range of humidity and temperature and to correlate it with complementary properties of water uptake and swelling.
- To investigate the influence of thermal treatment on the properties of ultra-thin Nafion® film so as to simulate any changes in the ionomer during the hot pressing step of MEA fabrication.
- To investigate changes in surface wettability and proton conductivity of annealed films exposed to liquid water. This was to simulate the presence of liquid water in the PEFC catalyst layer during operation and motivated by the reported study (Bass *et al.* **10**) on surface wettability differences in 100 nm film exposed to water vapor versus liquid water.

- To investigate the influence of nature of substrate and dispersion medium composition on film morphology/structure and properties. This was motivated by reports on the differences in nanostructure of ionomer in different dispersion media.
- To investigate damage caused to Nafion® structure/property by x-ray exposure. This was motivated by the need to understand whether the increasing use of x-ray based diagnostic tools could be altering the structure and thereby, the properties of the ionomer in PEFC electrodes.

Chapter 3

Experimental Techniques: Theory and Application

3.1 Introduction

A number of experimental techniques have been employed to characterize the ionomer thin films. This chapter presents the basic principle of the underlying methods and the details of the instruments and specifics of the measurements.

3.2 Characterization techniques

3.2.1 Variable Angle Spectroscopy Ellipsometry (VASE)

Ellipsometry is a useful tool for the determination of thickness and optical constants of sub-nanometers to few microns thin films. It measures the change in polarization of light that is reflected or transmitted from a material. The Ellipsometer consists of a light source, polarization generator, polarization analyzer and detector as shown in Figure 3.1. The polarization generator and analyzer are built of optical components such as, polarizer, compensators and phase modulators. In principle, a light source generates electromagnetic wave with random orientation and phase, terms as unpolarized light. When light pass through a polarizer, it converts light into linear polarized where both parallel (p) and perpendicular (s) components of light are in same phase. Upon irradiation of linearly polarized light on the sample, the reflected light undergoes amplitude and phase changes for both p- and s-polarized light. Ellipsometry measures the electromagnetic wave with an arbitrary amplitude and phase resulting ‘elliptical’ polarized light

as shown in Figure 3.1. Hence, Ellipsometry term has come from the associated elliptical polarization.

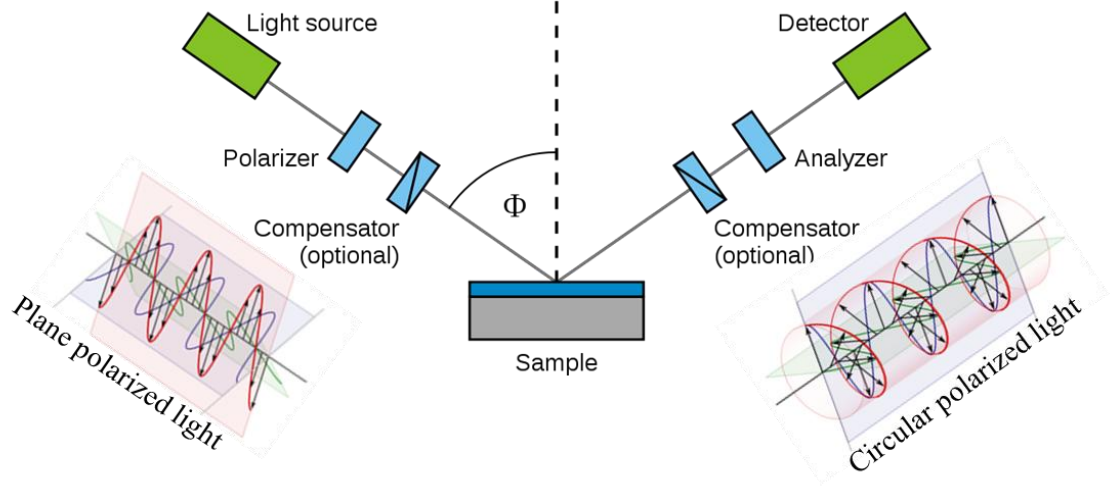


Figure 3.1: Typical Ellipsometry configuration [140].

However, VASE does not give the thickness and optical contents directly. It only provides the complex reflectance ratio, ρ , of a system, which is parameterized by Ψ and Δ in Equation 3.1.

$$\rho = \frac{r_p}{r_s} = \tan(\Psi)e^{i\Delta} \quad (3.1)$$

where, r_p is the light polarized in the plane, r_s is polarized perpendicular to the plane, $\tan(\Psi)$ is the amplitude ratio upon reflection, and Δ is the phase shift (difference). The thickness and other physical parameters can be obtained by fitting the Ψ and Δ data over a range of wavelengths with models using the WVASE32 software in the number of data analysis steps as shown in Figure 3.2. The model is used to calculate a prediction of response based on Fresnel's equations. For primary calculation estimation is given where Fresnel's equation describes each material with

thickness and optical constants. The calculated values are compared with experimental data and an estimator like Mean Squared Error (MSE) is set to quantify the quality of fit. A number of unknown parameters such as thickness, roughness, uniformity and refractive index (optical parameters) can be obtained.

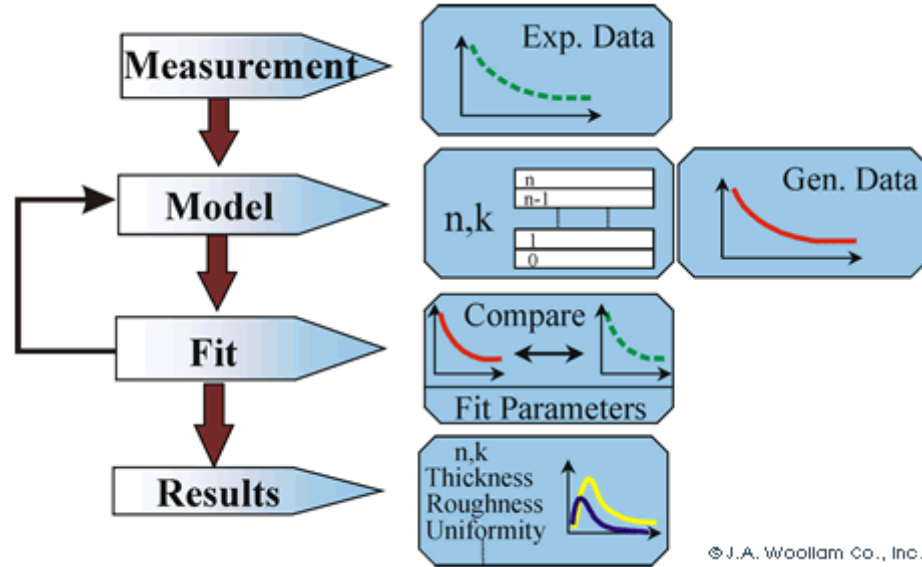


Figure 3.2: Flowchart of Ellipsometry data analysis [140].

Ellipsometry measurement for this thesis: Ellipsometry has been employed to investigate primarily, thickness of the films. Moreover, the optical parameters, homogeneity and roughness of the films have also been investigated. Ellipsometry measurements were carried out using a VASE Ellipsometer (J. A. Woollam Co., Inc., USA). The resulting Ψ and Δ spectrum was fitted with different physical model using the WVASE32 software setting a number of fitting parameters including thickness, surface roughness, optical constant, non-uniformity and void fraction. The fitting details have been described in Chapter 4.

3.2.2 Atomic Force Microscopy (AFM)

Atomic force microscopy belongs to the general class of scanning probe microscopy. A conventional AFM consists of a micro cantilever probe with sharp tip mounted on it, a piezoelectric driver and a position sensitive photo-detector. In principle, the tip scans the sample surface and PZT (Lead Zirconium Titanate) scanner maintains the tip at constant force or constant height above the sample. During the scanning, a laser beam is reflected back from the top of the cantilever and the deflected beam is recorded by the photo detector. The scanning tip movement, i.e. an up and down motion following the surface contour, creates differences in light intensities. The deflection pattern might be recorded as height deviation or deflection force by maintaining either a constant force or constant height by the PZT.

Generally, AFM can be operated in three modes (i) non-contact mode, (ii) contact mode and (iii) tapping mode. The three operational modes can be distinguishable based on interaction force difference between the tip and the sample as depicted by the force-displacement curve in Figure 3.3. Contact mode lies in the repulsive force region because the tip is in direct contact with the sample. Non-contact mode operates in the attractive force region where tip does not contact the sample at all. Tapping mode is operated both the combination contact and non-contact mode where the cantilever tip is allowed to impact the sample for a minimal amount of time.

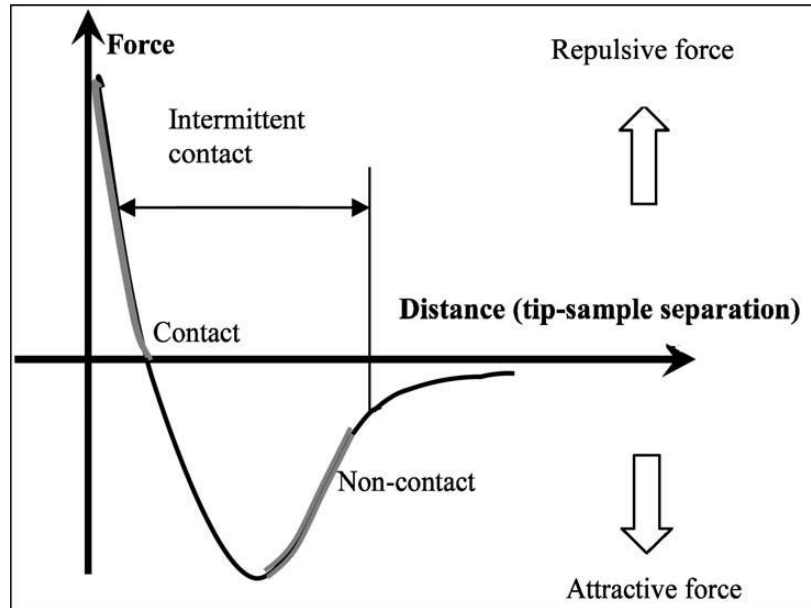


Figure 3.3: Interatomic force variation versus distance between AFM tip and sample [141].

Topographical imaging: Tapping mode of AFM is widely used for morphological or topographical study of polymer materials including block copolymers, bulk polymers, thin-film polymer and polymer composites. Topographic mapping is done by measuring the oscillation amplitude as a feedback signal where the amplitude varies due to moving the scanner up or down based on surface morphology.

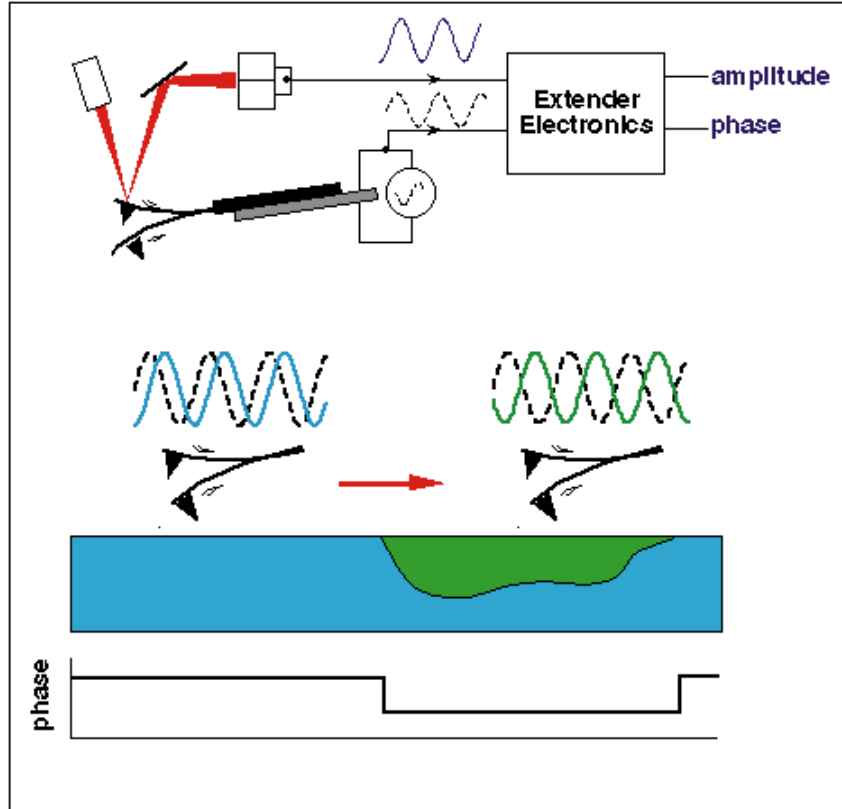


Figure 3.4: Phase imaging uses the Extender Electronics Module to measure the phase lag of the cantilever oscillation (solid wave) relative to the piezo drive (dashed wave). The amplitude signal is used simultaneously by the NanoScope III controller for Tapping Mode feedback. Spatial variations in sample properties cause shifts in the cantilever phase (bottom) which are mapped to produce the phase images shown here [142].

Phase imaging: Phase imaging is extension of tapping mode AFM which provides nano-meter scale information of surface structure. During tapping mode scan, phase image goes beyond the topographical/morphological mapping of the surface to identify surface inhomogeneity in terms of variation of composition, modulus, adhesion, friction, viscoelasticity and other properties. Phase image is done by monitoring the phase lag of the cantilever oscillation relative to the signal sent to the cantilever's piezo driver.

AFM measurement for this thesis: AFM has been employed to investigate the surface features (morphology, roughness and phase contrast) of the blank substrate and the Nafion® thin films. In addition, the film thickness has also been measured by AFM. The instrument, Nanoscope IIIa system (Digital Instruments) with a silicon tip (tip radius < 10 nm) mounted on the cantilever, has been used for the measurement.

3.2.3 X-Ray Photoelectron Spectroscopy (XPS)

XPS is a useful technique for the determination of the elemental composition and thickness of thin film up to few nano meters. XPS consists of monochromatised x-ray source, electron detector and energy analyzer. The instrumentation of XPS technique has been shown below in Figure 3.5.

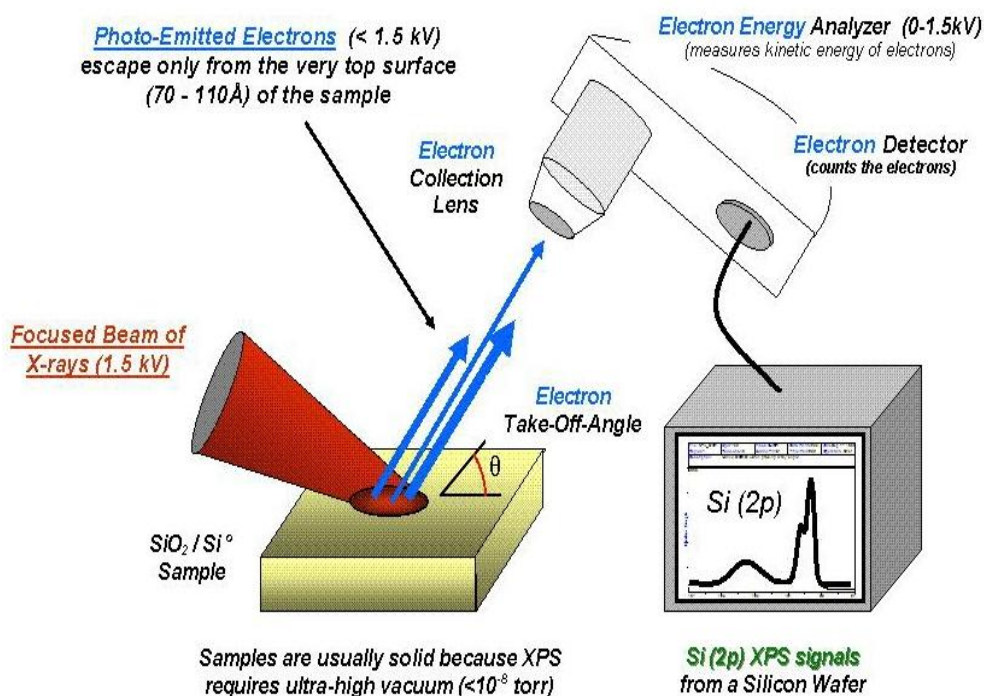


Figure 3.5: XPS instrumentation, image taken from Wikipedia (wikipedia.org/wiki/X-ray_photoelectron_spectroscopy).

In principle, irradiation of mono-energetic X-rays causes the emission of photoelectron from the sample surface. The incident X-ray photon energy (E_{photon}) and kinetic energy of ejected electron energy (E_{kinetic}) can be interrelated by the following Equation 3.2.

$$E_{\text{binding}} = E_{\text{photon}} - (E_{\text{kinetic}} + \phi) \quad (3.2)$$

Where, E_{binding} is the binding energy (BE) of the electron and Φ is the work function. As output response, XPS plots intensity of the electron (counts) in terms of BE. Knowing the BE and intensity or peak area in the spectrum, elemental identity and quantity can be determined respectively. It is noted that every element has a characteristic BE.

Film thickness measurement: Evaluation of film thickness can be performed using two methodologies to account for potential inconsistencies or non-homogeneities in the film. Starting from the general expression that describes the intensity of photoelectron lines (Equation 3.3) as a function of position of the atom and the electron take-off angle, one can consider the relationship between different species in the thin film and the underlying substrate.

$$I_i = \int_{z=0}^Z G_i^0 \cdot \exp\left(-\frac{z}{\lambda \sin(\alpha)}\right) \cdot dz \quad (3.3)$$

In the above expression, I_i is the integrated area of a peak of interest normalized by its sensitivity factor and the instrument's transmission function, G_i^0 contains the photoemission cross section and atomic density for the element, λ is the electron inelastic mean free path, α is the take-off angle and z is the position of the emitting electron within the sample (where $z=0$ corresponds

to the film-air or film-vacuum interface). The simplest approach to calculate the film thickness is to consider the attenuation of a substrate peak due to the presence of the film. Integration of Equation 3.3 between d (the film thickness) and infinity yields Equation 3.4.

$$\frac{I_{Si}}{I_{Si,bulk}} = \sin(\alpha) \cdot \exp\left(-\frac{d}{\lambda \sin(\alpha)}\right) \quad (3.4)$$

where, $I_{Si,bulk}$ is the photoelectron intensity produced by a clean silica substrate. At normal take-off angle ($\alpha=90^\circ$), this expression is similar to a Beer-Lambert absorption equation, where the electrons produced by the silica substrate are attenuated by the film.

A second method can also be used to crosscheck the film thickness. Again, starting from Equation 3.3, one can consider the intensities of Si_{2p} as the underlying substrate and another element which originates solely from the film. After integration, one can then consider the ratio of these intensities to calculate the film thickness. This methodology works well when the kinetic energies of the electrons considered is similar, and therefore the value of λ can be considered the same for both peaks (Equation 3.5). For a particular polymer, Nafion®, the equation can be written as

$$\frac{I_S}{I_{Si}} = \frac{I_{S,thick}}{I_{Si,bulk}} \left(e^{\left(\frac{d}{\lambda \sin \alpha}\right)^{-1}} \right) \quad (3.5)$$

In this case, $I_{S,thick}$ is the intensity of sulfur in bulk Nafion®.

XPS measurement for this thesis: XPS was employed to measure the elemental composition, homogeneity and thickness of the films. X-ray photoelectron spectra were obtained

on a Kratos AXIS UltraDLD 39-3061 instrument using a monochromated Al source (1486.6 eV). For data analysis CasaXPS software [146] was used.

3.2.4 Contact angle measurement

Contact angle measurement provides useful information of the wetting properties of the materials with respect to a particular solvent. The instrumentation of contact angle measurement set up (Goniometer) has been shown in Figure 3.6. It consists of a light source (usually, sodium light source), a sample stage, a micro-syringe and a camera.

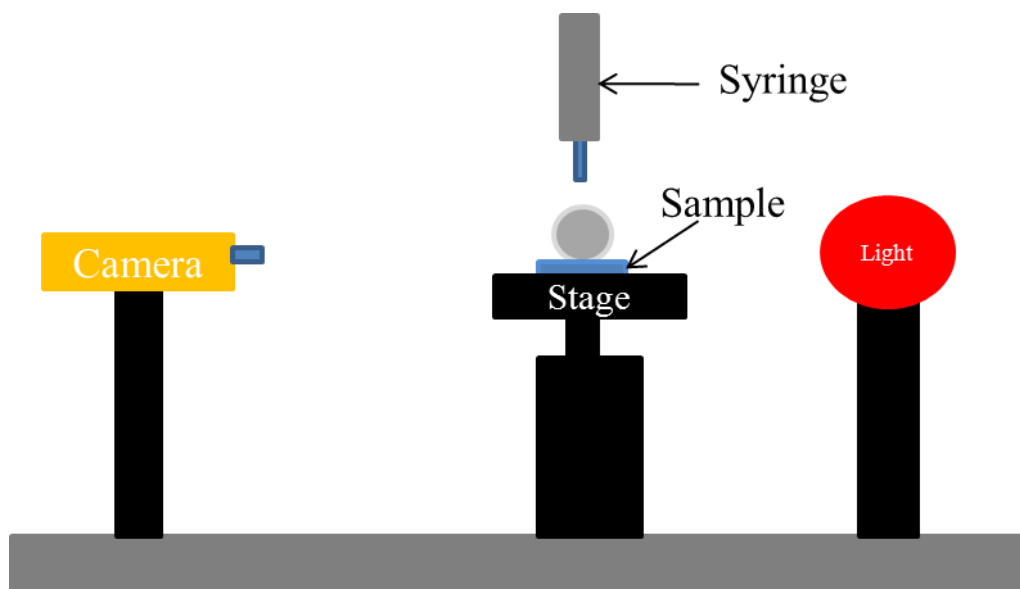


Figure 3.6: Instrumentation of Goniometer (contact angle measurement set up)

Contact angle quantifies the wettability of a solid surface by a liquid via the Young equation. Theoretically, contact angle arises from the thermodynamic equilibration between three phases including liquid, solid and gas/vapor phases. Usually, if the contact angle is less than 90° ,

the wetting is favorable and if it is more than 90° , wetting is not favorable. The equilibrium contact angle can be determined from the Young's equation.

$$\gamma_{SG} = \gamma_{SL} + \gamma_{LG} \cos \theta \quad (3.6)$$

Where, γ_{SG} , γ_{SL} , γ_{LG} are solid-vapor, solid-liquid and liquid-vapor interfacial energies respectively. Another useful parameter to quantify wetting is the spreading parameter (S). S can be defined as

$$S = \gamma_{SG} - (\gamma_{SL} + \gamma_{LG}) \quad (3.7)$$

When $S > 0$, the liquid wets the surface completely (complete wetting). When $S < 0$, there is partial wetting.

Cassie-Baxter model: When the surface is rough and associated heterogeneity, the surface can be explained and quantified the degree of heterogeneity by Cassie-Baxter equation.

$$f_1 = \frac{\gamma_{aw} \cos \theta - (\gamma_{2a} - \gamma_{2w})}{(\gamma_{1a} - \gamma_{1w}) - (\gamma_{2a} - \gamma_{2w})} \quad (3.8)$$

Where γ 's are the interfacial energy between different phases and subscripts "1", "2", "a", and "w" designate phase 1, phase 2, air (vapor), and water, respectively. For a particular polymer, Nafion® [128], surface might be divided into two distinct behaviour, water like hydrophilic (phase 1) and Teflon like hydrophobic (phase 2). Considering the associated interfacial energy, fraction of hydrophilic or hydrophobic surface can be quantified.

Surface energy calculation: Surface energy of the films can be a useful data for understanding and modeling of interaction between the thin film surface and other fluids and solids. Such information may also be useful to characterizing the interaction between polymer in dispersion and a substrate. An appropriate technique is extended DLVO (Derjaguin, Landau, Verwey and Overbeek) theory (or XDLVO for brevity) for the determination of surface energy.

In the XDLVO or the Lewis Acid-Base model, introduced by R.J. Good, C.J. van Oss and M. Chaudhury [147] the surface energy components of a solid surface can be obtained from measuring the contact angles made by liquid triplets on that surface. Usually, two polar liquids (e.g., water, ethylene glycol) and one apolar liquid (e.g., diiodomethane, α -bromonaphthalene) are used. Conceptually, [148,149] the total surface energy (γ_s^{Tot}) is the sum of a Lifshitz-van der Waals (γ_s^{LW}) component and an acid-base component (γ_s^{AB}). The acid-base component can be further defined by an electron-donating (γ_s^-) and an electron accepting parameter (γ_s^+), expressed as follows

$$\gamma_s^{Tot} = \gamma_s^{LW} + \gamma_s^{AB} \quad (3.9)$$

where,

$$\gamma_s^{AB} = 2 \cdot \sqrt{\gamma_s^+ \gamma_s^-} \quad (3.10)$$

It is useful to point out that the both the Lewis acid-base (electron donating/accepting) as well as Bronsted acid-base (proton donating/accepting) interactions are lumped in the acid-base (AB) component of the surface energy parameters. For Nafion®, these parameters may be better understood in terms of proton donating/accepting properties. Using liquids of known surface energy parameters (here, water, ethylene glycol and diiodomethane) and measuring the contact angles they make on the Nafion® film surface, the surface energy parameters of the latter can be calculated through regression of the measured contact angle data according to the following model Equation 3.11 [150].

$$1 + \cos \theta \quad \gamma_L^{Tot} = 2 \cdot \sqrt{\gamma_L^{LW} \gamma_s^{LW}} + \sqrt{\gamma_L^+ \gamma_s^-} + \sqrt{\gamma_L^- \gamma_s^+} \quad (3.11)$$

Contact angle measurement for this thesis: Contact angle measurement technique has been employed for the wettability and surface energy for both blank substrate and Nafion® thin

films. Dynamic Surface Analysis system (VCA Optima, AST Products INC.), equipped with a video camera has been used. The software (winvca32) has been used for image analysis.

3.2.5 Electrochemical Impedance Spectroscopy (EIS)

Impedance is a measure of ability of circuit to impede the current follow through the circuit, which is not limited by the simplifying properties of an ideal capacitor. Ideal capacitor follows (i) Ohm's law at all current and voltage (ii) frequency independent resistance (iii) Ac current and voltage signals through an ideal resistor are in phase with each other.

In electrochemical impedance spectroscopy [151], a single-frequency voltage is applied to an electrochemical cell or interface. In response, phase shift and amplitude or real and imaginary parts of the resulting current are measured at that frequency using either analog circuit or fast Fourier transform analysis of the response. The transform is only valid when applied voltage is sufficiently small so that system response is linear or pseudo linear. Impedance spectroscopy (IS) is used to study any intrinsic properties which influence the conductivity of an electrode materials system. The application can be categorized into two sub sections. First, those pertinent only to Materials (i) Conductivity (ii) Dielectric constant (iii) Mobility of charges (iv) Equilibrium concentrations. Second, those pertinent to an electrode material interface (i) Adsorption reaction rate constant (ii) Capacitance of interface (iii) Diffusion coefficient of neutral species.

Mathematical derivation of impedance: The applied voltage can be expressed as

$$E_t = E_o \sin(\omega t) \quad (3.12)$$

Where E_t is the voltage at a time t , E_o is the amplitude of the response, ω is the radial frequency $\omega=2\pi f$. In a linear system or pseudo linear system, the current response can be different by a phase and amplitude

$$I_t = I_o \sin(\omega t + \phi) \quad (3.13)$$

Therefore impedance can be calculated as

$$Z = \frac{E}{I} = Z_o \frac{\sin(\omega t)}{\sin(\omega t + \phi)} \quad (3.14)$$

It is also possible to express impedance as a complex function. The potential can be defined as

$$E_t = E_o \exp(j\omega t) \quad (3.15)$$

And current can be defined as

$$I_t = I_o \exp(j\omega t - \phi) \quad (3.16)$$

Hence, impedance can be express as a complex number

$$Z(\omega) = \frac{E}{I} = Z_o \exp(j\phi) = Z_o (\cos \phi + j \sin \phi) \quad (3.17)$$

Where according to Euler's relationship

$$\exp(j\phi) = \cos \phi + j \sin \phi \quad (3.18)$$

Impedance presentation: Impedance data can be presented as a Nyquist plot where the real part of $Z(\omega)$ is plotted in the x-axis and imaginary part is plotted in y-axis. Each point of Nyquist Plot is the impedance at one frequency. High frequency impedance starts from the origin of the plot and data goes far from the origin with decreasing frequency. The semi-circle can be defined by the simple equivalent circuit where an ideal capacitor is in parallel to the resistor. Another way of impedance presentation is the Bode Plot. The impedance is plotted with log frequency on x-axis and absolute value of impedance $|Z|$ or phase-shift in y-axis.

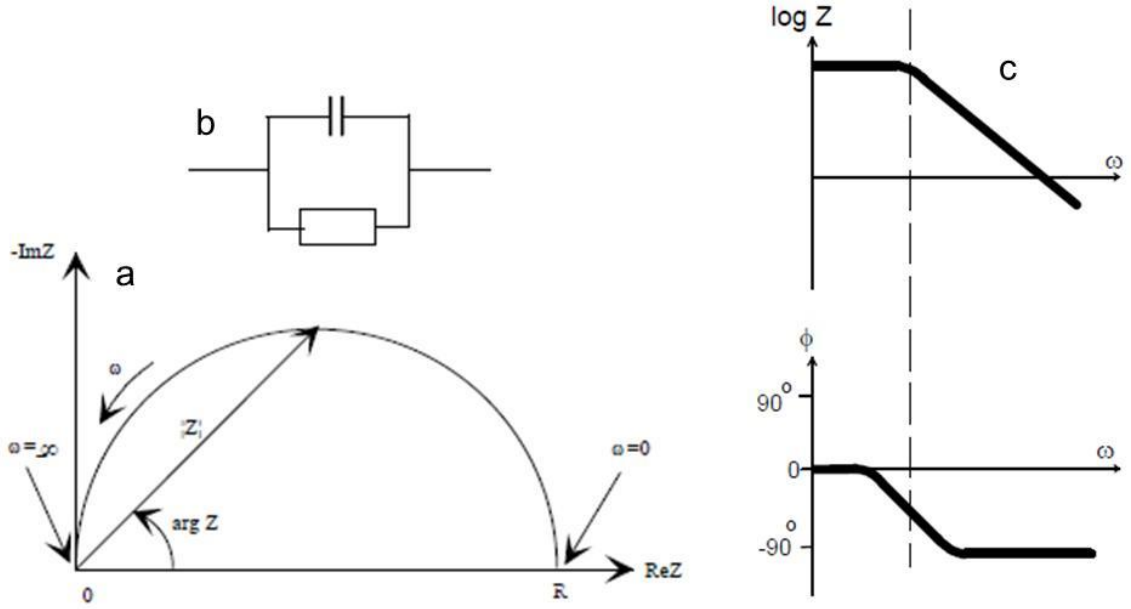


Figure 3.7: Impedance presentation (a) Nyquist Plot (b) Equivalent circuit (c) Bode Plot [152]

Impedance measurement for this thesis: In this thesis, EIS was employed for film proton conductivity and capacitance measurement. A two micro-probe setup connected with a Solartron 1260 frequency-response analyzer coupled to a Solartron 1296 dielectric interface has been used for impedance measurement. SMART software and Z view software have been used for data collection and data interpretation respectively.

3.2.6 Dynamic Light Scattering (DLS)

DLS, also known as photon correlation spectroscopy or quasi-elastic light scattering, is very useful technique for measuring particle size down to 1 nm in solution or dispersion. The instrument mainly, consists of a laser light source, sample holder and a photon detector as shown in Figure 3.8.

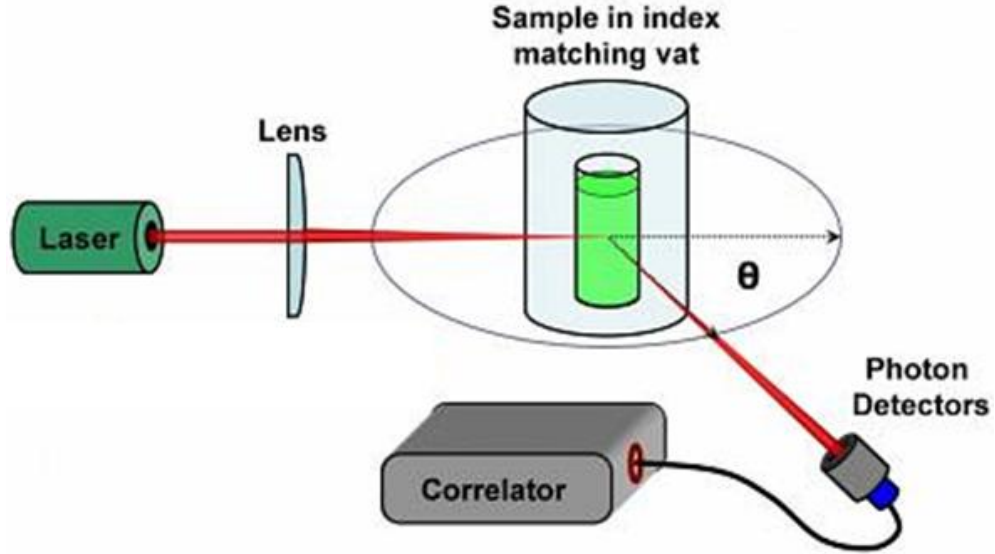


Figure 3.8: Instrumentation of DLS technique, image taken from the website [153]

The principle of DLS is very simple. When the monochromatic light hits the small particles, a time dependent fluctuation of the scattered light is detected by the photon detector. The fluctuation is originated because of the Brownian motion of small particles where the distance between particles are constantly changing with time. This motion creates randomness to the phase of the scattered light, such that the scattered light undergoes either destructive or constructive interference by the scattering contribution of surrounding two or more particles. This leads to time-dependent fluctuations in the intensity of the scattered light. The fluctuations can be analyzed for obtaining hydrodynamic diameter of the particles.

The dynamic information of the particles can be derived by the autocorrelation of intensity during the measurement. The second order correlation function is given by,

$$g^2(q, \tau) = \frac{\langle I(t)I(t+\tau) \rangle}{\langle I(t) \rangle^2} \quad (3.19)$$

where $g^2(q, \tau)$ is the autocorrelation function at a particular wave vector (q), and delay time (τ), $I(t)$ is the intensity of the scattered light at time t , and the brackets indicate averaging over all t .

If the sample is monodispersed, then the decay is simply a single exponential. The Siegert equation relates the second-order autocorrelation function with the first-order autocorrelation function $g^1(q, \tau)$ as follows:

$$g^2(q, \tau) = 1 + \beta \left[g^1(q, \tau) \right]^2 \quad (3.20)$$

The simplest approach is to treat the first order autocorrelation function as a single exponential decay.

$$g^1(q, \tau) = \exp(-\Gamma \tau) \quad (3.21)$$

where Γ is the decay rate.

From this point, Γ can be converted to the diffusion constant D for the particle via the following relation

$$D = \frac{\Gamma}{q^2} \quad (3.22)$$

Here, q is the magnitude of the scattering vector, and is given by

$$q = \frac{4\pi n_o}{\lambda_o} \sin\left(\frac{\theta}{2}\right) \quad (3.23)$$

where n_o is the sample index of refraction, λ_o is the vacuum wavelength of the incident laser light, and θ is angle at which the detector is located with respect to the sample cell.

Finally, the hydrodynamic radius r_h of the particle can be derived as a function of the diffusion constant via the Stokes-Einstein equation in the following

$$r_h = \frac{\kappa T}{6\pi\eta D} \quad (3.24)$$

where k is Boltzmann's constant, T is the temperature in K, and η is the solvent viscosity.

Dynamic Light Scattering (DLS) measurement for this thesis: The aggregate/particle size distributions of prepared samples and sample mixtures were measured by the Zetasizer Nano ZS system (Malvern Instrument Ltd), equipped with a 633 nm He-Ne laser. The instrument is capable to measure the particle size in the range 0.3 nm to 10 μ m. In the experiments, all measurement results were analyzed by Dispersion Technology Software 5.03 (Malvern Instrument Ltd).

3.3 Conclusions

The instrumentation, fundamental principles and the specific information of the particular instrument used in the thesis have been described. The detailed experimental procedure and measurement protocols have been included in the experimental sections of each of the chapters 4 to 8.

Chapter 4

Fabrication and Characterization of Self-Assembled Ultrathin Films

4.1 Introduction

Fabrication of a few nanometers to few microns thin polymer film inevitably employs solution-based technique such as drop casting, spin-casting, and Langmuir-Blodgett methods [8,12,122]. On one hand, it was of interest to generate films of thickness ranging 4-10 nm that would be representative of ionomer film thicknesses observed for CLs [1]. On the other hand, there was also a want to mimic the adsorption/self-assembly of ionomer that occurs in the catalyst ink formulation stage. Based on the prior studies [105-107], suggesting the aggregation state of ionomer is dependent on ionomer concentration in the dispersion, it was hypothesized that adsorption/self-assembly from Nafion® dispersion of varying concentrations would result in films of varying thicknesses. Spin-coating would allow control of the film thickness by varying the spin speed, ionomer concentration and amount of dispersion used. However, solvent evaporation during the spinning stage may also result in molecular rearrangement prior to allowing the completion of equilibration of ionomer-substrate interaction. On this basis, adsorption/self-assembly method for ionomer film fabrication was adopted.

The substrate chosen was Silicon wafer because it also allowed for proton conductivity to be measured for films generated on SiO₂-terminated silicon wafer with arrays of gold electrodes. The proton conductivity measurement is discussed in the next chapter.

In this chapter, self-assembled Nafion® films on SiO₂ surface generated by extended immersion in Nafion® dispersions of different concentrations were generated and characterized

by a number of techniques. To probe whether the films are generated by an adsorption type process or by simple adherence of the dispersion as in the case of dip coating, the effect on immersion time has been investigated. The nature of dispersion media affects the ionomer state in the dispersion, which in turn may affect the ionomer film characteristics. The effect of dispersion media type was probed by two sets of experiments. In one set, IPA/water composition effect on Nafion® state both in liquid dispersion media and in solid self-assembled thin film have been characterized. Later, two different Nafion® dispersion types were employed to probe the effect of dispersing media. One set of dispersion was prepared by diluting the 5 wt% Nafion® stock dispersion with iso-propyl alcohol where Nafion® to water ratio is same regardless of dilution concentration. The second set of dispersion was varying Nafion® concentration in water, which was achieved by following the solvent switching technique involving successive distillation.

A majority of the results are presented for films made from IPA-diluted dispersions. The thickness of the films was ascertained from three different techniques – AFM analysis of scratched film, Variable Angle Spectroscopic Ellipsometry (VASE) and X-ray Photoelectron Spectroscopy (XPS). The wettability of films was assessed through water contact angle. The surface energies of the film were calculated by application of extended-DLVO (XDLVO) theory by using contact angle measurements with two additional liquids varying in polarity. The surface morphology of the films were examined by AFM in the tapping mode and analyzed in terms of height and phase contrast. Angle-Resolved XPS measurements were conducted to investigate whether any differences in S/F ratio exists in between thinner hydrophilic films and thicker hydrophobic films.

4.2 Experimental

4.2.1 Film Preparation

The ultra-thin Nafion® films in this study were prepared by self-assembly process following the steps shown in Figure 4.1 below. The dispersion media of known Nafion® concentration was prepared/equilibrated and substrate was cleaned following a strict protocol. The specific of the experimental method is provided below.

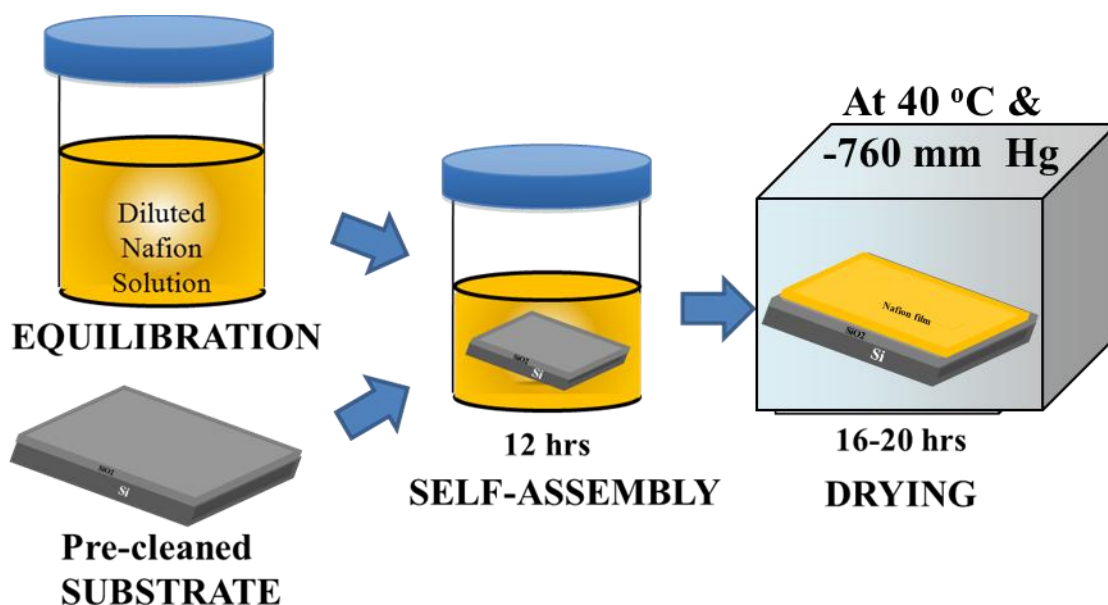


Figure 4.1: Self-assembled Nafion® thin film preparation on SiO₂ terminated Si wafer substrate

Nafion® dispersion preparation: Commercially available 5 wt% Nafion® (EW 1100) solution in water-alcohol mixture (75/20 w/w alcohol to water) acquired from Ion Power (USA) was used. Nafion® dispersions of concentration 0.1 wt%, 0.25 wt%, 0.5 wt%, 1 wt%, 1.5 wt%, 2

wt% and 3.0 wt% were prepared by adding appropriate amount of isopropyl alcohol (IPA) (Sigma Aldrich) to the stock 5 wt% Nafion® dispersion.

For second set of dispersion, 5 wt% Nafion® stock dispersion in water was prepared by evaporating alcohol at 90 °C from 5 wt% Nafion® dispersion (Nafion®: water: alcohol; 5:20:75) as similar procedure has been described by Moore *et al.* [138] and Jiang *et al.* [139] for switching solvent in Nafion® dispersion. It was considered that most of the alcohol was removed by 4 times repeated evaporation up to half of water weight of the dispersion (equivalent to 90% reduction in weight) and adjusting the total weight by adding water. Assuming equal rate of evaporation of water and alcohol, a conservative estimate of alcohol content in the final 5 wt% dispersion in water-based media is 0.0006 wt%. Significantly lower alcohol content is expected because alcohol is more volatile than water and more alcohol would be lost during evaporation. Different concentration of Nafion® in water was prepared by adding Millipore water to the 5 wt% stock dispersion.

To investigate the dispersion medium composition effect, a number of 0.1 wt% Nafion® dispersion varying the composition of IPA:Water; 0:100, 20:80, 50:50, and 80:20 were also prepared using 5wt% Nafion® dispersion in water. For all three cases, the diluted solutions were equilibrated at least 24 h after initial 5 min sonication. Dilution followed by long equilibration time was allowed to bring the presumed high aggregation state to its lower aggregation state.

Substrate cleaning: Silicon wafer with a ~300 nm thermally grown SiO₂ layer (MTI, USA) was selected as a model substrate. The cleaning of SiO₂/Si wafers involved multiple steps. First, the wafer was exposed to a Piranha solution (H₂SO₄:H₂O₂ ; 7:3) at 80 - 90 °C for 1 h to remove surface contamination. Next, the wafer was rinsed with Millipore water and dried under

flow of compressed air. Subsequently, the wafer was placed into an RCA (Radio Corporation of America) cleaning solution mixture (DI H₂O: NH₄OH: H₂O₂; 5:1:1) at 70 - 80 °C for 30 min to remove organic contaminants from the surface. Finally, the wafer was washed by Millipore water several times and dried again under flow of compressed air. The cleanness of the wafer was confirmed by AFM and XPS analyses.

Self-assembly: Thin films of Nafion® were generated by self-assembly of Nafion® onto the cleaned SiO₂/Si substrate. The cleaned substrate was immersed in the Nafion® dispersion of known concentration contained in a capped beaker. The substrate was exposed to Nafion® dispersions for 12 h or otherwise specified time as shown in Figure 4.1. After carefully removing the substrate from the solution it was dried under a flow of dry air. Vacuum drying was carried out in low vacuum at 40 °C for 16 - 20 h.

4.2.2 Film Characterization

Ellipsometry measurement for Nafion® thin film: Ellipsometry measurements at three different angles (55, 65, 75 degrees) over the wavelength range of 3000–8000 Angstroms were carried out using a VASE Ellipsometer (J. A. Woollam Co., Inc., USA). Then the resulting Ψ and Δ spectrum was fitted with different physical model using the WVASE32 software setting a number of fitting parameters including thickness, surface roughness, optical constant, non-uniformity and void fraction. The fitting details have been described in the later part of this chapter.

AFM measurement of thin film: AFM was used to investigate the surface features (morphology, roughness and phase contrast) of the blank substrate and the Nafion® thin films.

The film thickness was determined by AFM using a line analysis of the film that was scratched all the way through to the SiO₂ substrate. The AFM measurements were performed at ambient conditions in tapping mode using a Nanoscope IIIa system (Digital Instruments) with a silicon tip (tip radius < 10 nm) mounted on the cantilever.

XPS measurement of Nafion® thin film: X-ray photoelectron spectra were obtained on a Kratos AXIS UltraDLD 39-3061 instrument using a monochromated Al source (1486.6 eV). All the spectra were obtained with constant pass energy of 80 and an energy step of 200 meV. The pressure of the vacuum system was maintained at $\sim 2 \times 10^{-10}$ torr. Samples were introduced into the vacuum system immediately before measurement, minimizing the time in vacuum (atmosphere to measurement ~ 40 mins), which might change the film's morphology. To prevent excessive charging, a charge neutralizer was used. The binding energy scale was further calibrated by setting the Si_{2p} peak to 103.4 eV [143,144]. This value is well within the range for SiO₂ and silicon-supported SiO₂ films (103-104 eV from NIST X-ray Photoelectron Spectroscopy Database, 2011 [145]), and results in an adventitious carbon peak at ~ 284.8 eV. The carbon peak is not used directly because the multiple contributions of the Nafion® film produce slight shifts in this peak. Calibration of the instrumental behavior (intensity dependence of the collection solid angle) during angle-resolved measurements was performed using a freshly sputtered copper sample. Elemental quantification of the Nafion® films and the underlying silica was determined using the Si_{2p}, S_{2p}, C_{1s}, O_{1s} and F_{1s} peaks with a Shirley background subtraction in the CasaXPS software [146].

Contact angle measurement of thin film: The contact angles (θ) of sessile drops deposited on Nafion® films were measured using a Dynamic Surface Analysis system (VCA Optima, AST Products INC.), equipped with a video camera and software (winvca32) for image analysis. To

assess hydrophobic or hydrophilic characteristics, Millipore water was used as the liquid. For surface energy calculations, in addition to water, contact angle measurements with another polar liquid (ethylene glycol) and an apolar liquid (diiodomethane) were carried out. For all contact angle measurements, a sessile drop of liquid using a micro syringe was placed on the surface of a vacuum dried thin film. Several images were captured starting at 5 s after dispensing each sessile drop for up to 5 min. The relative humidity of the environment was not controlled but varied in the 40-50% range. In this study, the reported contact angles are the values obtained 5 s after the placement of the sessile drop and the average of four replicates on the film surface.

4.2.3 Dispersion characterization

Dynamic Light Scattering (DLS) measurement of dispersions: The aggregate/particle size distributions of prepared samples and sample mixtures were measured by the Zetasizer Nano ZS system (Malvern Instrument Ltd), equipped with a 633nm He-Ne laser. The dispersion was placed in a sample holder, which is a glass cuvette with a square aperture. To obtain best optical measurement, the sample height was maintained in between 10 to 15 mm. The measurement temperature was set 25 °C for all samples and allowed to be equilibration for at least 5 mins at the set temperature. In the experiments, all measurement results were analyzed by Dispersion Technology Software 5.03 (Malvern Instrument Ltd).

4.3 Results and Discussions

4.3.1 Surface characterization of films generated by varying immersion times

To investigate structural evolution of the Nafion® self-assembly, SiO₂ substrates were exposed to 0.1 wt% Nafion® dispersion (IPA diluted) for different periods of time - 0.5, 1.0, 3.0 and 12.0 h – and the surface of Nafion® covered substrate were examined by AFM. The samples were subjected to a washing step soon after withdrawal of the substrate from the Nafion® dispersion to ensure that any adhering liquid and weakly held Nafion® molecules were removed. The washing step consisted of instantaneously dipping the solution-exposed substrate into a beaker containing the same solvent that made up the Nafion® dispersion. The washed substrate was then dried in a stream of compressed air. The surface features of the films can be gleaned from the 3D representation of the topography as presented in Figure 4.2.

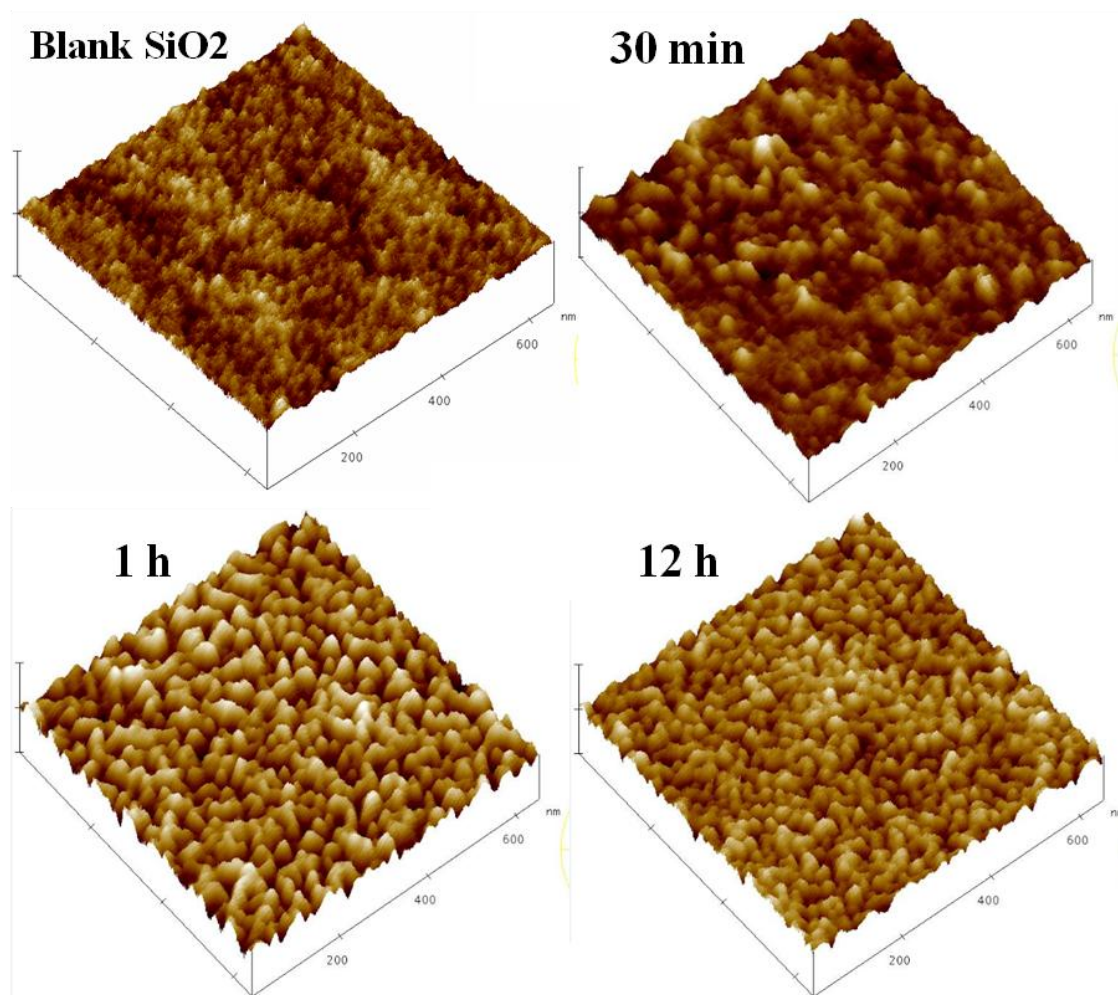


Figure 4.2: 3-D AFM height images of Blank SiO₂ surface (top row left) and of SiO₂ surface after immersion in 0.1 wt% Nafion® dispersion for 30 mins (top row right), 1 h (bottom row left) and 12 h (bottom row left).

Each image represents the surface of dimension 650 nm \times 650 nm. The bar on the left hand corner of each image represents a scale of 5 nm. From Figure 4.2, differences in the film surface morphology can be noted. The substrate exposed for 0.5 h in the Nafion® dispersion appears to be partially covered by Nafion®. On the other hand, the AFM image of substrate exposed for 1 h and 12 h indicates more Nafion® on the surface. Sample line analyses of the film

topographical images are presented in Figure 4.3 and allow us to draw further conclusions about the changing characteristics of the films generated after immersion in Nafion® dispersion for different times. Comparing films generated after 0.5 h and 1 h exposure, 1 h film exhibits a periodic feature width (20 to 30 nm) and height (~3 nm) whereas the periodicity is less clear for the 0.5 h film. Both films can be thought to be corrugated surfaces. The 12 h film showed lower feature height (1.4 nm) compared to the 1 h film. This would indicate smoothening of surface due either to restructuring of the pre-existing adsorbed Nafion® or to filling of the corrugations by further adsorption of Nafion®. Regardless of what the actual process is, it can be deduced that the surface characteristics changes with increased immersion time, indicating that the process of film formation is a self-assembly type phenomenon. It is also useful to mention that repeat measurements on new samples have shown similar results of ~3 nm feature heights in the low exposure time films and much smoother surface with feature heights in the order of 1 nm for 12 h exposure time films.

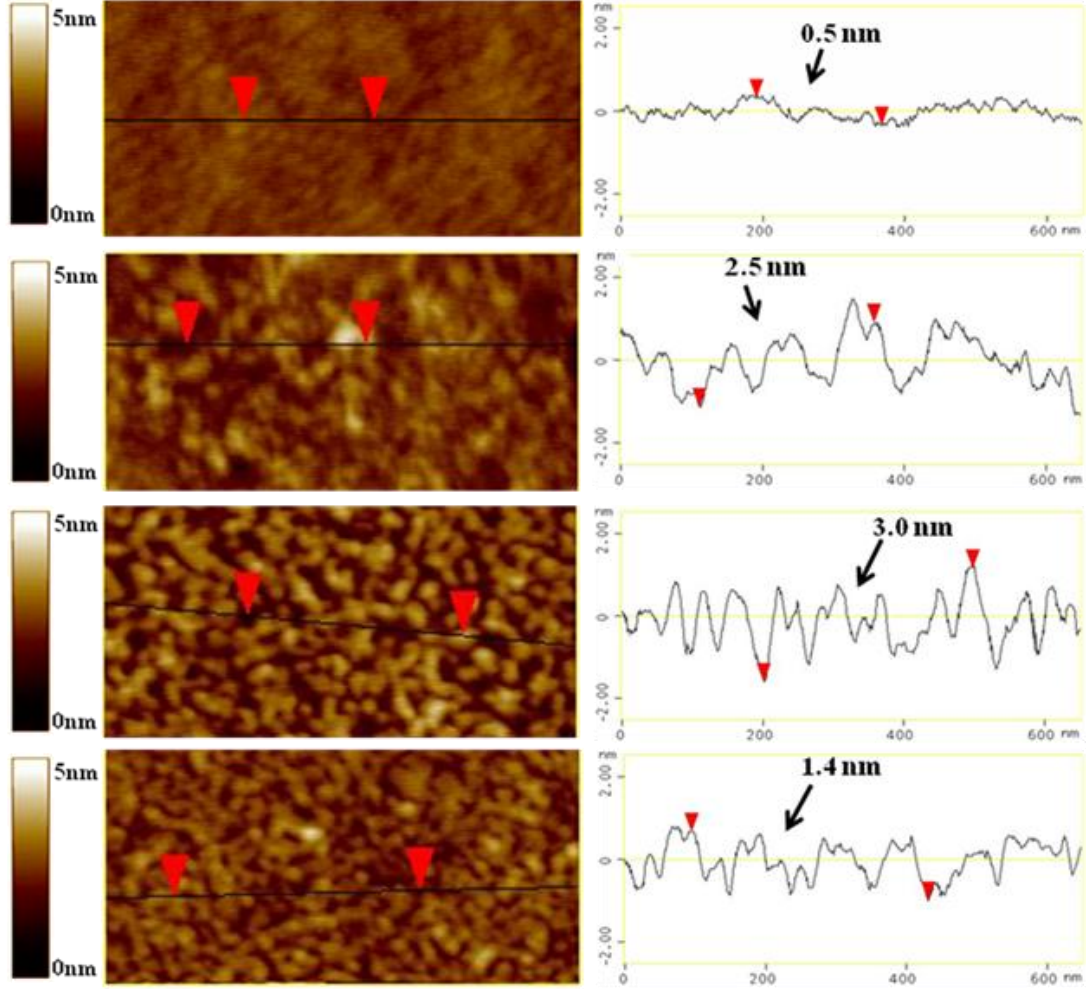


Figure 4.3: 2-D height images with section analysis. Blank SiO₂ surface (top row) and SiO₂ surface after immersion in 0.1 wt% Nafion® dispersion for 30 mins (2nd top row), 1 h (3rd row), 12 h (bottom row).

To quantify the roughness of the blank and Nafion®-covered (partial or full) substrate, the film mean roughness is presented in Figure 4.4. Surface uniformity and roughness of both substrate and films have been parameterized by the mean roughness and root mean square (RMS) roughness calculation by the following two formulae in Equation 4.1.

$$R_m = \frac{1}{NM} \cdot \sum_{x=1}^{N-1} \sum_{y=1}^{M-1} |Z_{x,y}| \quad R_{rms} = \sqrt{\frac{1}{NM} \cdot \sum_{x=1}^{N-1} \sum_{y=1}^{M-1} Z_{x,y}^2} \quad (4.1)$$

where, $Z_{x,y}$ is the difference of height from the mean height, N and M are the number of points in x and y directions. It can be noted that the mean roughness of the films increases from 0.32 nm to nearly 0.5 nm and then decreases to 0.28 nm as the immersion increases from 0.5 h to 1 h to 12 h, respectively. The observed trend for mean roughness can be explained by considering the surface coverage and the contribution of the uncovered, covered and edges of the covered regions. Thus, for 0.5 h exposed film, if we consider the substrate is not completely covered, then the mean roughness would be dominated by the bare substrate roughness with additional corrugation due to isolated Nafion® molecules. For the 1 h exposed film, the increased roughness can be explained by considering that the number of Nafion® molecules on the surface increases, almost completely covering the surface. The 12 h exposed surface shows a reduced roughness due likely to assembly/adsorption of more material. The thickness of 12 h film was measured by scratching the film followed by AFM imaging as shown in Figure 4.5. The resulting thickness (~4 nm) was more than two times the maximum surface corrugations, which would imply full surface coverage of the Nafion®. From the AFM images and line scan data shown in Figure 4.3, it can be surmised that the 1 h film does not fully cover the substrate. However, no attempts were made to quantify the surface coverage of the films

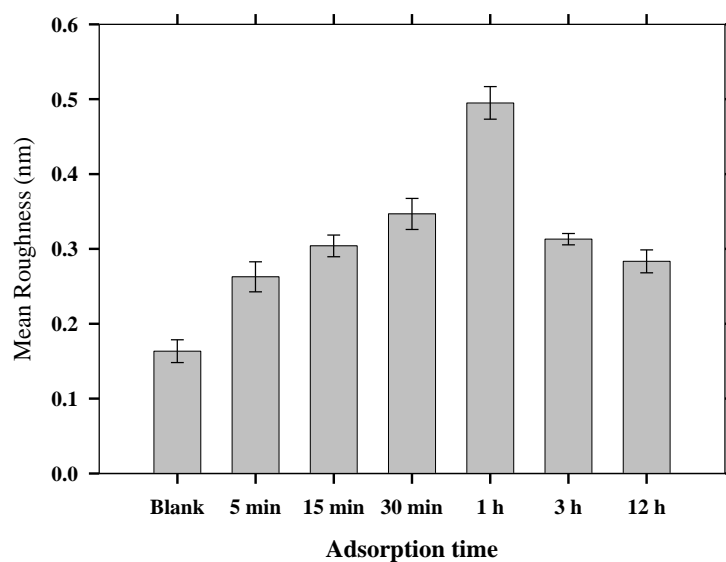


Figure 4.4: Mean roughness of blank SiO₂ surface and SiO₂ surface immersed in 0.1 wt% Nafion® dispersion for different time.

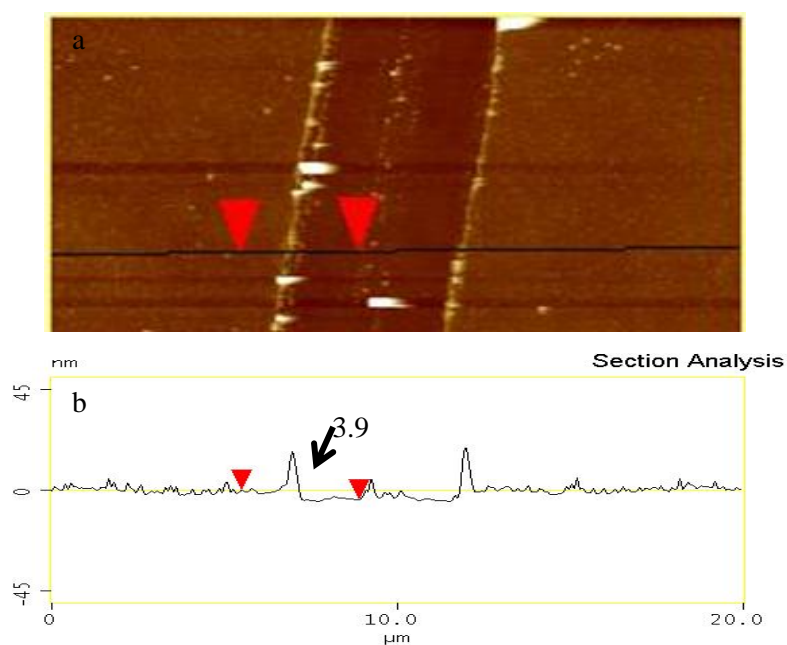


Figure 4.5: (a) AFM image and (b) line analysis showing height distribution of scratched surface of film deposited from immersion in 0.1 wt% Nafion® dispersion for 12 h.

In summary, it was found that Nafion® film preparation on SiO₂ from its dispersion state is a time dependent self-assembly phenomenon. It takes 12 h to prepare a fully covered homogeneous film. In the rest of our study, 12 h immersion time has been considered to be sufficient for homogeneous self-assembled film preparation. In the next section, the effect of solvent mixture (water/IPA) composition on self-assembly phenomenon is discussed when the Nafion® concentration is 0.1 wt% constant.

4.3.2 Effect of dispersion medium composition (IPA/water) on self-assembled Nafion® films.

Characteristics of self-assembled films obtained from 0.1 wt% Nafion® dispersion in different IPA/Water composition: To investigate dispersion medium composition effect on self-assembly of Nafion®, five dispersions of 0.1 wt% Nafion® in IPA/water mixture were prepared by adding appropriate amount of IPA and Millipore water to the 5 wt% stock Nafion® dispersion in water. Those have been termed as the percentage of water presence in the dispersion, such as 100% water, 80% water, 50% water, 20% water and 0.4% water. In the sample preparation stage, the film was dried out by nitrogen blow immediately after taking out the substrate from dispersion after 12 h immersion; no solvent washing was conducted contrary to the immersion time study as described in the section 4.3.1.

Top row of the Figure 4.6 represents height image of the films prepared from 0.1 wt% Nafion® dispersion in IPA/water mixture of composition varying water content from 100 wt% to 20% (left to right). It was observed that regardless of the composition of dispersion medium, films were discontinuous and Nafion® was scattered deposited on the silica substrate. For films generated from Nafion® dispersion in ~100% water, the self-assembled film is regular with

homogeneous structural features. Both cylindrical and globular features with 20 to 30 nm diameter were observed. For films generated from Nafion® dispersion in 80% water, mostly cylindrical and extended cylindrical rod-like features with increased diameter 30 to 50 nm were observed. It indicates that the degree of association is increased. For films generated from Nafion® dispersion in 50% water, the degree of association further increases and results an aggregated network like morphology. In other word, it makes a fibrillar-like structure, which might consist of several rod-like Nafion® aggregates. The diameter of aggregates or fibrils varies from 50 to several hundreds of nanometer. For the film generated from Nafion® dispersion in 20% water, the trend of aggregation or association with decreasing water content was disrupted. Instead, rod-like and extended-rod-like features with 15-25 nm diameter Nafion® bundle appeared on the substrate.

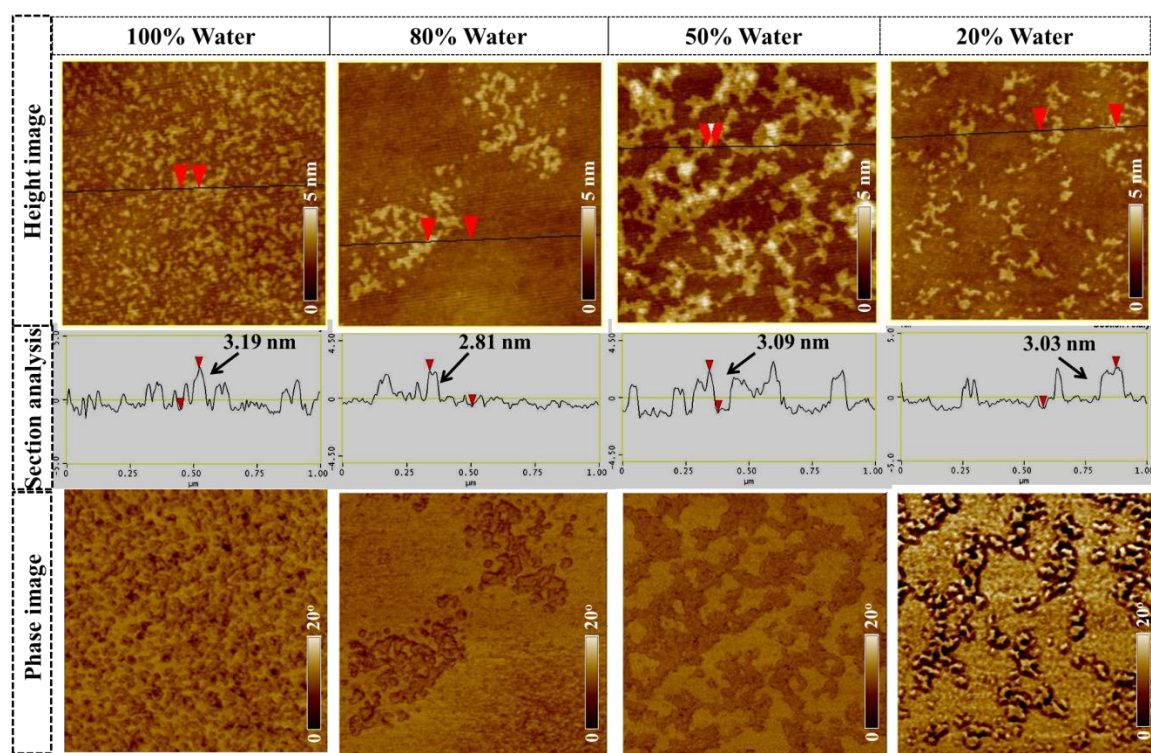


Figure 4.6: AFM height, section analysis and phase of films prepared from 0.1 wt% Nafion® dispersion in different water/IPA composition. Top row (height images), middle row (section analysis) and bottom row (corresponding phase images).

Middle row of the Figure 4.6 shows the corresponding section analysis of the height images (left to right: 100% water to 20% water). It is very interesting to note that the heights of the film features are restricted to a maximum of ~ 3 nm regardless of the composition of dispersion medium. This indicates that the nano-aggregates of Nafion® in the dispersion have at least one dimension of similar length scale, i.e. ~ 3 nm. During the self-assembly stage, both the intermolecular association or dissociation among Nafion® molecules and the interaction between substrate and Nafion® might be dominated by the dispersion media. However, it is inconclusive whether the apparent association or aggregation mainly happen in the dispersion media or during the self-assembly on the substrate. To investigate if any changes in the nanostructure of the Nafion® occur during the self-assembly process, attempt was made to characterize the particle size of Nafion® in 0.1 wt% dispersion of varying media composition and the findings are discussed in the later part of this section.

The bottom row of the Figure 4.6 represents the corresponding phase contrast image of height image (left to right: 100% water to 20% water). It is interesting as all phase images directly correlates to the height image. Phase image provides information more than the height differences where it depicts the surface properties. The origin of phase contrast will be discussed more details in the later part of this chapter. In this case, it is evident that phase image providing further proof of the height differences and distinguishes two distinct solid phases (Nafion® and silica). If the phase image of film prepared from 20% water (bottom row, right hand corner), is closely observed, a rod-like Nafion® phase further separated from the silica phase (continuous phase among the rod-like Nafion® phases) by a dark line. This dark line corresponds to the different properties which might be attributed to the hardness/softness or hydrophilicity/hydrophobicity. Most importantly, it distinguishes in-between the properties of the core of Nafion® bundle and substrate (SiO_2) surface portion.

However, when the water content in 0.1 wt% Nafion® dispersion (IPA dilutions) becomes negligible (water 0.4 wt%), it forms a continuous and homogenous films of Nafion® as observed in the Figure 4.7. The surface corrugation is lower than that of the film prepared from the same dispersion concentration but subjected to a washing step (washing with the same solvent) prior to blow drying in nitrogen. The thickness of the film was measured 4 nm [more details of thickness measurement have been described in the 4.3.3]. To investigate whether continuous films could be obtained at even lower concentration, Nafion® dispersion further diluted to 0.05 wt% (water 0.2 wt%). The corresponding self-assembled film was found to be discontinuous and a characteristic fibrillar Nafion® structure in highly aggregated phase was observed. Interestingly, the maximum height feature observed in AFM image was still ~3 nm. It can be argued that the 3-4 nm is one of the characteristic dimensions of the Nafion® nanoaggregate. It is also interesting to note that 3-4 nm is the characteristics length scale of Nafion® basic aggregated unit in hydro alcoholic solvent mixtures observed in the SAXS studies of the Nafion® dispersions [99-103].

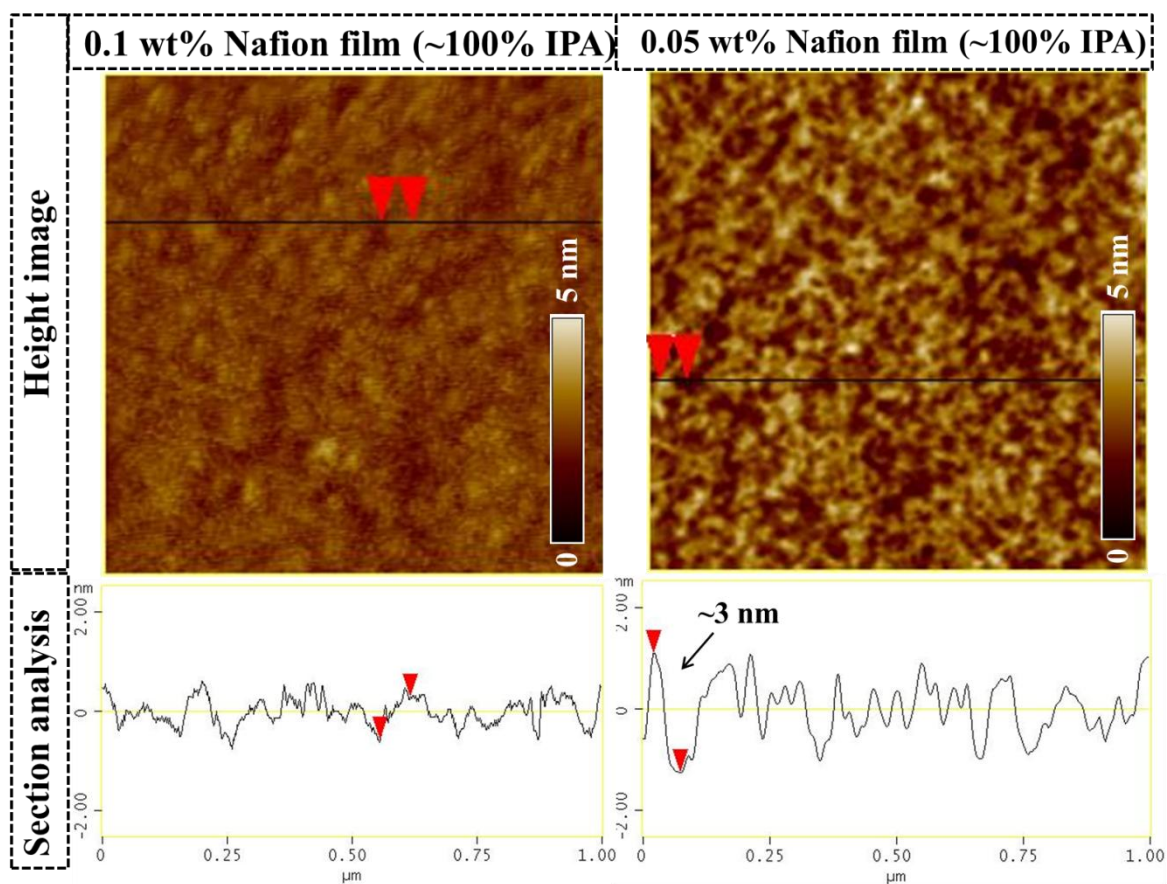


Figure 4.7: AFM height image and section analysis of Nafion® thin film prepared from 0.1 wt% dispersion (left) and 0.05 wt% dispersion (right) in IPA.

Particle size distribution in 0.1 wt% Nafion® dispersion in different IPA/Water composition: Attempt was made to probe this characteristic dimension via particle size distribution measurement using dynamic light scattering of 0.1 wt% Nafion® dispersion in various IPA/water mixtures. In addition, AFM imaging of spray deposited particle on the smooth substrates was carried out considering that the rapid evaporation of the solvent during deposition would kinetically freeze the state/structure of Nafion® in the dispersion.

Figure 4.8 shows a representative size distribution of Nafion® aggregates in dispersions of different media composition but same Nafion® content of 0.1 wt%. A broader range of

distribution was observed where most of the particle stayed between 100 to 300 nm diameter. For the dispersion in ~100% water, a narrow and homogeneous distribution was observed. For dispersion in 20/80 IPA/water mixture, homogeneous but comparatively wider range of particle size distribution was found. A much wider distribution pattern was obtained from dispersion in 50% and 20% water in between 100 to 1000 nm where a small fraction of the particles appeared in the size region <100 nm and > 1000 nm. For Nafion® dispersion in IPA media (0.4% water), Nafion® aggregated distributed in all three regions where a significant portion goes to higher particle size region (>1000 nm).

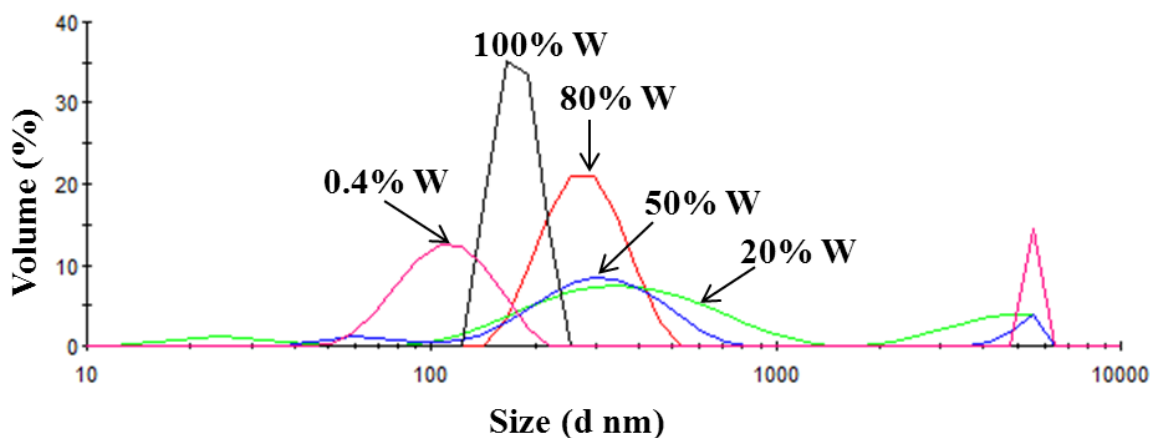


Figure 4.8: Representative size distribution of Nafion® in 0.1wt% dispersion in various Water/IPA composition termed as 100%, 80%, 50%, 20% and 0.4% water.

Figure 4.9 shows that volume percentage of Nafion® in terms of IPA/Water composition dividing into three different length scales – 0 to 100 nm, 100 to 1000 nm and more than 1000 nm. The three length scales correspond to the three aggregation states – molecular form, primary aggregation and secondary aggregation, respectively. The mean and the standard deviation have been calculated from the measurement of five samples. It was found that with decreasing water content the volume percentage of the primary aggregates decreased whereas and that of the

secondary aggregates increased. The volume percentage of the primary aggregates shows an increasing trend except for dispersion in 20 wt% water. Further discussion is presented later in this section in terms of the dispersion media properties.

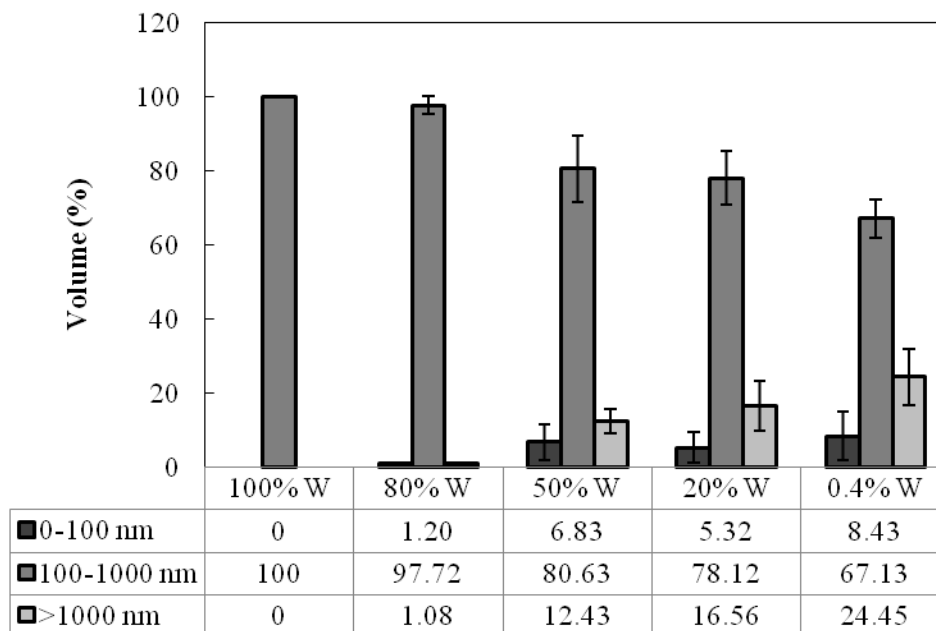


Figure 4.9: The volume fraction of Nafion® aggregates in 0.1wt% dispersion at three categories varying Water/IPA composition termed as 100%, 80%, 50%, 20% and 0.4% water.

Figure 4.10 shows the AFM image of spray deposited Nafion®. Small amount (1 to 2 mL) of dispersion was taken in an air gun spray and freshly cleaved mica substrate was allowed to pass through the particle flux during spraying. The sprayed sample was dried out in the open air for 4-5 h and AFM imaging was carried out. It was found that the particles were deposited as globular or spherical shape. The most homogeneous particle size with 10 to 20 nm diameter was observed in 100% water. With decreasing water content, particle size became inhomogeneous and particle diameter decreased. Wider particle size with the diameter 5 to 25 nm were observed

below the water content 50% or less which is consistent with the DLS results. Section analysis of each image provides the height distribution of the particles in terms of dispersion media composition. The highest and highly homogeneous height features have been observed in 100% water resulting ~2.5 nm. The height of the particle became inhomogeneous and decreased with decreasing water content. The inhomogeneous heights might be attributed from the dispersion state or due to restructuring/rearrangement of the particle after deposition. No large aggregation was observed in the spray technique whereas DLS results indicated the formation of secondary aggregation at low water content. It supports surface induced restructuring after deposition. The difference in particle size has been reported by Koestner *et al* [111] based on variation of deposition technique. They reported rod-like bundle structure of Nafion® due to slow adsorption whereas globular structure due to rapid sprays deposition. In both process, the reorganization and restructuring of Nafion® molecule both in dry and dispersion media have been discussed. Masuda *et al.* [113] also showed substrate inducted reorientation of adsorbed Nafion® molecule.

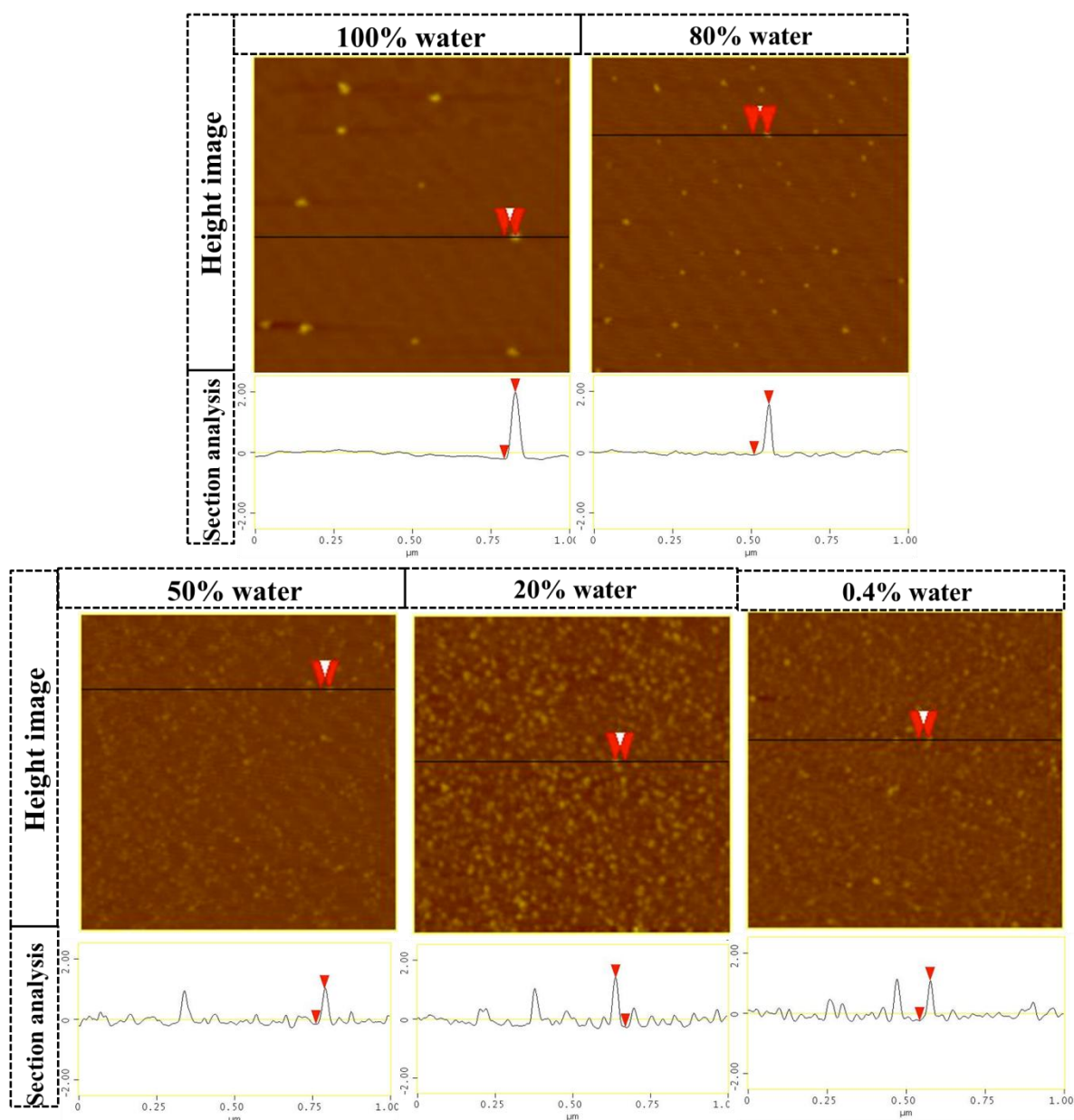


Figure 4.10: AFM image showing Nafion® particles deposited by spray drying of 0.1 wt% dispersion from various Water/IPA compositions.

Correlation between dispersion states to solid film morphology: Variation of particle size in different media composition can be explained by the solubility parameter (δ) and dielectric constant (ϵ) of the dispersion media. Solubility parameter is the determining indicator of the solubility – similar solubility parameter for both solvent and solute represent higher degree of

compatibility resulting in solvation, miscibility or swelling. On the other hand, dielectric constant corresponds to the polarizability of the solvent. Therefore, Nafion® in a dispersion media with high dielectric constant undergoes dissociation of ionic group resulting in a high surface charge density. Table 4.1 shows the calculated values of the solubility parameter and dielectric constants of IPA/Water mixtures according to the following formula [109].

$$\begin{aligned}
 \delta_m &= [E_{coh,m} / V_m]^{1/2} = \left[\sum X_i E_{coh,i} / \sum X_i V_i \right]^{1/2} \\
 \rho_m &= \sum X_i \rho_i = \sum X_i \epsilon_i^{1/2} M_i \\
 \epsilon_m &= \left[\rho_m / \sum X_i M_i \right]^2
 \end{aligned} \tag{4.2}$$

Where $E_{coh,m}$ is the cohesive energy of the mixture solvent, V_m is molar volume of the mixture solvent, X_i is the molar ratio of solvent i (the values for water and IPA are 1 and 4 respectively), $E_{coh,i}$ is the cohesive energy of solvent i, V_i is the molar volume of the solvent i (18 for water and 76.8 for IPA), ρ_i is the molar dielectric polarization of solvent i, ϵ_i is the dielectric constant of solvent i (78.4 for water and 19.9 for IPA), and M_i is the molecular weight of solvent i (18 for water and 60.1 for IPA). Among the various dispersion media mixtures employed in this work, pure water has the highest dielectric constant ($\epsilon=78.4$) and solubility parameter ($\delta=23.4$). With decreasing water content in IPA/water mixtures, both parameters decreased where IPA has lowest dielectric constant ($\epsilon=11.8$) and solubility parameter ($\delta=19.9$). Yeo *et al.* [53] investigated dual solubility parameter of Nafion® ionomer: $-\delta_1=17.3$ attributed to side chain and $\delta_2=9.7$ ascribed to the backbone.

Table 4.1: Solubility parameter (at 25 °C) and dielectric constant of different water/IPA composition.

| Iso-propyl alcohol: Water | Solubility Parameter | Dielectric constant |
|----------------------------------|-----------------------------|----------------------------|
| 0:100 | 23.40 | 78.40 |
| 20:80 | 21.08 | 47.00 |
| 50:50 | 17.60 | 29.96 |
| 80:20 | 14.12 | 22.72 |
| 100:0 | 11.80 | 19.90 |
| Nafion®-side chain | 17.30 ^a | |
| Nafion®-backbone | 9.70 ^a | |

^aReference [53]

As proposed based on SAXS, ESR and Cryo-TEM study [99-105,109], the cylinder core would comprise hydrophobic backbone and the sulfonic side chains would be extending outwards. The dielectric constant of the dispersion media promotes the dissociation of the sulfonic acid and thus a further association or aggregation is hindered by the electrostatic repulsion resulting in a uniform distribution of Nafion® bundles. This explanation is consistent with highly homogeneous Nafion® distribution obtained in DLS (Figure 4.8& Figure 4.9) and Nafion® particle size obtained in AFM (Figure 4.10) imaging technique. It also correlates well with the self-assembled film preparation from dispersion in 100% water (Figure 4.6).

With a decreasing dielectric constant of the dispersion media, the nano-cylinder surface gets less charged resulting in a higher possibility of side chains to aggregate and form bigger particles. It explains the increased particle size in DLS increased with decreasing water content correspond to the lower dielectric constant. However, bigger aggregated structural features have

not been observed in any of the AFM images. It is possible that the aggregates dissociates upon their interaction with the substrate. The restructuring and reorganization on a substrate surface are consistent with the observation by Koestner *et al.* [111] and Masuda *et al.* [113]. On the other hand, DLS experiments indicate that a significant fraction of the Nafion® in dispersion exists as mean particle size less than 100 nm with decreasing water content or moving to the IPA rich solvent system (Figure 4.8& Figure 4.9). One of the reasons might be the solubility parameters of solvent mixture gets closer to that of the Nafion® backbone. As a result, those solvent mixtures are highly compatible with Nafion® backbone. Therefore, the compactness of the cylinder might be decreased and undergone in small scale dissociation of the bundles. In IPA, the higher tendency of side chain aggregation (due to low dielectric constant of solvent) and the possible rearrangement of the backbone in the cylindrical core of Nafion® (due to comparable solubility parameter of solvent) might attribute to the continuous and homogenous thin film (Figure 4.7). However, the reasons of discontinuous films from water rich Nafion® dispersion remain unknown.

The solubility parameter of the 50/50 water/IPA dispersion media mixture ($\delta=17.6$) is compatible with that of the Nafion® side chain ($\delta=17.2$). Therefore, the solvent mixture may not have any influence on the backbone restructuring but promote side chain aggregation. This is consistent with the wider particle distribution observed in DLS measurements (Figure 4.8& Figure 4.9). In wider view, the highly associated behavior with the combination substrate induced restructuring might explain the fibrillar network type structure in self-assembled film (Figure 4.6).

4.3.3 Thickness of films self-assembled from Nafion® dispersion of varying concentration

In this section, the thickness of the self-assembled films resulting from Nafion® dispersions of varying composition has been characterized. For film preparation, first set of dispersion – Stock Nafion® dispersion dilution by IPA at various concentrations, was used. Three different techniques - AFM, XPS and ellipsometry – that probe the thickness over different extents of sample size were employed. AFM examined the thickness variation along a scratched length of a micron. The spot size for ellipsometry measurements were effectively an area covered by circle of a diameter of 50 microns. XPS measurements averaged the response from the film of an area of 2 mm².

4.3.3.1. Adsorbed film thickness and optical properties by VASE

Substrate selection and characterization: Silicon wafer covered with ~300 nm of SiO₂ (University wafer Item# 19271) was selected as a model substrate. Although the 2000 nm SiO₂ film samples were used initially for preparation of Nafion®-adsorbed films, we found that it was challenging to adequately fit the ellipsometry data to several variations of physical models discussed later. Because the thick SiO₂ layer generated too much background response, the response from the very thin Nafion® film is subdued in the ellipsometry spectrum. Therefore, all subsequent experiments were conducted with ~300 nm thick SiO₂ film samples, which also offered the advantage of modeling the SiO₂ film as a single-layer terminating with a smooth top surface.

The substrate SiO₂ film was characterized in terms of optical thickness and optical constants. Figure 4.11(a) shows the raw data obtained by Ellipsometry measurement at three

different angles. The thin SiO₂ film data could be fitted equally well with a two-layer model (Si/SiO₂ layer) where the top SiO₂ surface is considered to be uniform and a three-layer model (Si/SiO₂ layer/SiO₂-roughness-layer) with the top SiO₂ is considered to be rough. Interestingly, both models gave a thickness of SiO₂ layer of 305 nm comparable to supplier quoted value of 300 nm. The second model returned zero roughness. Moreover, the substrate was also fitted with two layer model (Si/SiO₂ layer) considering a extra fitting parameter ‘nonuniformity’ of the SiO₂ upper surface, that gave same thickness and optical constant but 1.17% nonuniformity of the surface with improved spectral fitting features. The refractive index of SiO₂ at wavelength λ_{5500} was found to be 1.46 and compares well with the literature values [155,156]

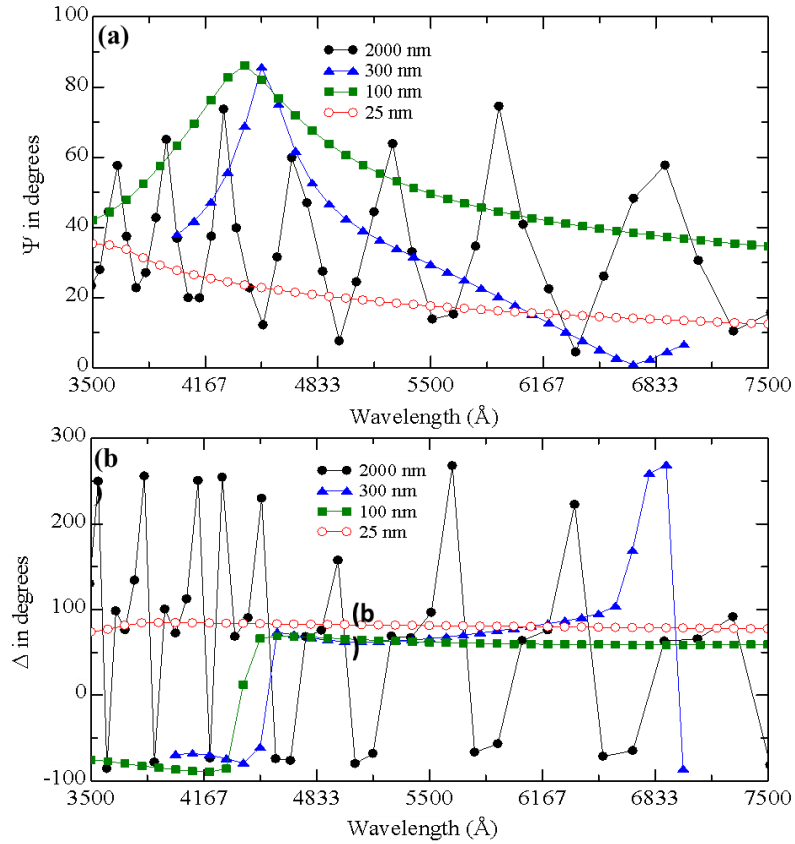


Figure 4.11: ψ (a) and Δ (b) spectra for the variation of blank SiO₂ thickness 25 nm to 2000 nm at incident angle 75°.

Approach to data fitting: Ellipsometry does not directly provide any film properties such as film thickness, optical parameters and roughness but it can generate wavelength dependent ψ and Δ spectrum. To extract the film properties, it is necessary to build representative structural models based on Fresnel equations considering fixed substrate information and relevant assumption of the experimental film. As the appropriate model building is concerned, there are several possibilities for describing the films in our study. Three models were considered - Model-1: a homogeneous film made of a material with effective property; this is usually termed as the Cauchy model, Model-2: a porous or not fully dense film that has full surface coverage, and Model-3: a film that has partial surface coverage. For Model-2, the porous Nafion® film is described by an effective medium approximation. For Model-3, the film can be considered to be dense but only to cover the surface partially. The AFM results do not support Model-3, so it has been discarded from further analyses and only consider the Cauchy Model (Model-1) and the Effective Medium Approximation (EMA) Model (Model-2). Since there are three distinct solid material phases for the sample – adsorbed Nafion®, SiO₂ film, and Si substrate – the structural model was composed of the three layers as shown in Figure 4.12.

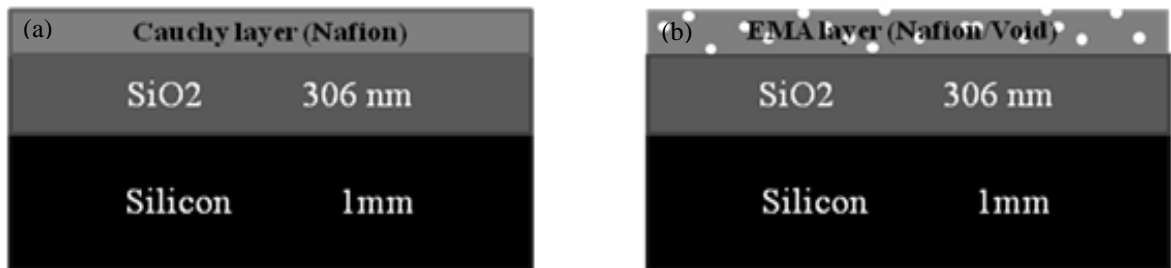


Figure 4.12: Three-layer model used for fitting Ellipsometry data, (a) Cauchy model and (b) EMA model.

Cauchy model fitting: The structural model for Cauchy fit comprises of Si/SiO₂/Nafion® as shown in Figure 4.12a. For each layer, there are two sets of parameters – the layer thickness

and optical constants – that affect the observed response. The thickness and optical constants for the SiO₂ and Si layers are already established.

Each layer's optical constants are described at each wavelength by a complex refractive index, $N=n-ik$ in which the real part, n refers to refractive index. The complex part, k refers to extinction coefficient, is the measure of how much light is absorbed in the materials and is related to the absorption coefficient α , where $k=(\lambda/4\pi) \alpha$. The Cauchy equation [157] can be expressed in the following equation where refractive index (n) is a function of wavelength (λ).

$$n(\lambda) = A + \frac{B}{\lambda^2} + \frac{C}{\lambda^4} \quad (4.3)$$

$$k(\lambda) = 0 \quad (4.4)$$

where, A , B , and C are the Cauchy parameters. For the SiO₂ and Si layers, the thickness and Cauchy parameters were confirmed by fitting the data for blank, clean SiO₂-terminated Si substrate. Thus, to fit the observed ellipsometry data for Nafion® film adsorbed on SiO₂/Si substrate, the thickness and Cauchy parameters of the Nafion® film are the fitting parameters. Further, there are two possibilities of describing the Nafion® film – uniform film and film with non-uniformity. We first fit the data assuming uniform film and extracted the film thickness and Cauchy coefficients (A , B and C). An improved fitting was observed when non-uniformity of film was considered.

Figure 4.13 shows the ψ and Δ spectra attributed from different films obtained from VASE at 65° incident angle. It is clearly seen that the position of peak is shifting with increasing corresponding Nafion® concentration. This shifting might be obtained due to any of the parameter including thickness, refractive index and non-uniformity changes. It also showed that

Cauchy model was perfectly fitted with experimental data. The results of the fit for all films are summarized in Table 4.2.

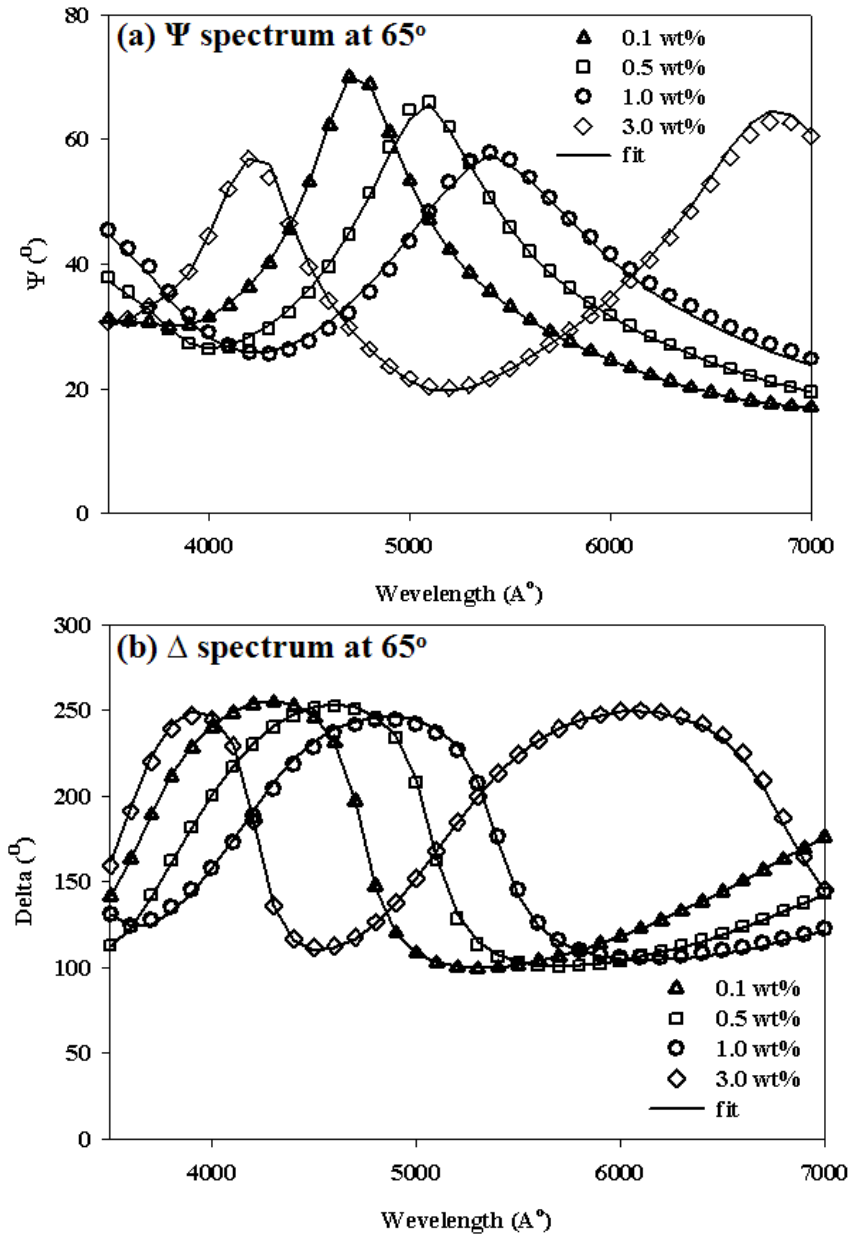


Figure 4.13: ψ and Δ spectra obtained from variable angle spectroscopic ellipsometry of 4 different films at 65° incident angle and corresponding fits with a Cauchy model.

It is noted that prior to the thickness confirmation, the different films have been generalized by the corresponding Nafion® dispersion concentration. For example, the self-assembled film obtained from 0.1 wt% Nafion® dispersion is termed as 0.1 wt% film. The most noteworthy observation from the data in Table 4.2 is that the Cauchy parameters for 0.1 and 0.25 wt% Nafion® films are significantly different than those of higher concentration films. The RI of Nafion® membrane/film has been reported as 1.36 (at 550 nm) in several studies [158,159], which compares well with the values for Nafion® films obtained from adsorption from solutions with concentrations of 0.5 wt% and higher. The low RI values for 0.1 wt% and 0.25 wt% films may be attributed to one of the two possibilities discussed. One possibility is that the 0.1 and 0.25 wt% films have inherently very different structure or molecular arrangement than that of high concentration films and bulk membrane. Another possibility is that the 0.1 and 0.25 wt% films have significant voidage and, as such, the effective optical property of the film as reflected in the Cauchy parameters is that of the porous Nafion® film. We have fitted the ellipsometry data by allowing for the porous nature of the film using the EMA model as discussed later.

Table 4.2: Summarized data for Nafion® film prepared from IPA diluted Nafion® dispersion.

| Nafion® Concentration | Nafion® Layer thickness (nm) | Refractive Index at 550 nm | Non-Uniformity (%) |
|----------------------------------|---|---------------------------------------|-------------------------------|
| 0.1 wt% | 4.0 | 1.19 | 3.9 |
| 0.25 wt% | 10.5 | 1.30 | 4.4 |
| 0.5 wt% | 31.5 | 1.37 | 9.8 |
| 1.0 wt% | 57.3 | 1.37 | 17.1 |
| 1.5 wt% | 74.7 | 1.37 | 9.8 |
| 2.0 wt% | 110.1 | 1.37 | 13.1 |
| 3.0 wt % | 160.1 | 1.37 | 8.8 |
| 5.0 wt% | 307.7 | 1.39 | 24.3 |

EMA model fitting: In the EMA model, again three layers – Si/SiO₂/Nafion® – are considered. Only the Nafion® layer is considered to be porous and its optical properties described by the effective media treatment. The constants of the EMA layer can be calculated by the following equation.

$$f_N \frac{\varepsilon_N - \varepsilon}{\varepsilon_N - 2\varepsilon} + f_V \frac{\varepsilon_V - \varepsilon}{\varepsilon_V - 2\varepsilon} = 0 \quad (4.5)$$

where, ε is the effective dielectric function for the mixed layer, ε_N and ε_V are the dielectric functions for Nafion® and void (air) respectively, f_N and f_V are the volume fractions of Nafion® and void, respectively. For the EMA model, the Cauchy coefficients of Nafion® (A=1.353,

B=0.0018 and C=0) reported for spin coated Nafion® film on glass substrate by Zudan *et al.* [158] was adopted. After assigning the Nafion® and void optical constants, two unknowns, voidage and film thickness of the Nafion® layer, of the EMA model remain and are obtained by fitting the model to the data. In addition, if the Nafion® film is considered to be non-uniform, another parameter – the degree of non-uniformity must be obtained from the fit of the data. The results of the model fit are presented in Table 4.3. The fit of the higher concentration films (1 wt% and higher) resulted in a negative voidage. This is due to the fact we have used the Cauchy coefficient reported by Zudan *et al* for Nafion® membrane, which results in an RI of 1.36 whereas the effective RI of the higher concentration films is greater than 1.36. For the 0.1 and 0.25 wt% Nafion® films, interestingly, the thickness and the effective RI of the mixed layer are similar as obtained by Cauchy model fitting (summarized in Table 4.2). Additionally, the voidage obtained from the EMA model fitting are 61.7 and 15.1 % for 0.1 and 0.25 wt% Nafion® films, respectively. Since both the Cauchy model and EMA model adequately fit the low concentration (0.1 and 0.25 wt%) films, the question still remains as to whether the difference between these films and those obtained from adsorption from higher concentration Nafion® dispersion are due to nano-structural differences of the films or due to the presence of voids? Results of the complementary AFM experiments may be useful in answering this question.

Table 4.3: Fitting results according to model in Figure 4.12(b).

| Nafion® conc. | Cauchy Coefficients for | | | Thickness | Void | RI | Nonuniformity |
|---------------|-------------------------|--------|---|-----------|------|--------|---------------|
| (wt%) | Nafion® [22] | | | (nm) | (%) | at 550 | (%) |
| | A | B | C | | | nm | |
| 0.1 | | | | 4.3±0.56 | 61.7 | 1.13 | 2.95 |
| 0.25 | 1.353 | 0.0018 | 0 | 10.5±0.21 | 15.1 | 1.30 | 4.41 |

4.3.3.2. Film thickness by AFM

AFM has been employed to determine the thin film thickness successfully using the film scratching method. Since the self-assembled films were thin, soft and prepared on a sufficiently hard silica substrate, it could be scratched easily all the way through the film thickness by a sharp blade without damaging the hard substrate surface. A line analysis of AFM height profile of the film across the scratched portion allows for an estimation of film thickness as shown in Figure 4.5 for the film deposited from 0.1 wt% Nafion®. Similar analyses were performed on films deposited from different Nafion® dispersions. Several AFM thickness measurements were performed on different regions of each sample to confirm the uniformity of the film thickness. The results of the measurements are reported in Table 4.4. Because the maximum vertical displacement was limited to 100 nm, the thicker films originating from the substrate immersion in 3 wt% and 5 wt% Nafion® dispersion could not be determined from this technique.

4.3.3.3. Film thickness by XPS

X-ray photoelectron spectroscopy was also used to determine the film thickness quantitatively and to identify any potential impurities qualitatively in the Nafion® film. Three films corresponding Nafion® concentrations 0.1, 0.25 and 3.0 wt% were examined. All films showed the correct composition and only in some samples a small peak for trapped nitrogen was observed. Representative XP spectra are presented in Figure 4.14 for a 0.25 wt% film at different angles. The inset shows the S_{2p} and Si_{2p} peak intensities normalized with respect to corresponding responses from 3 wt% (160 nm) film and bare substrate samples, respectively. The complete disappearance of Si_{2p} intensity from the 160 nm film can be noted.

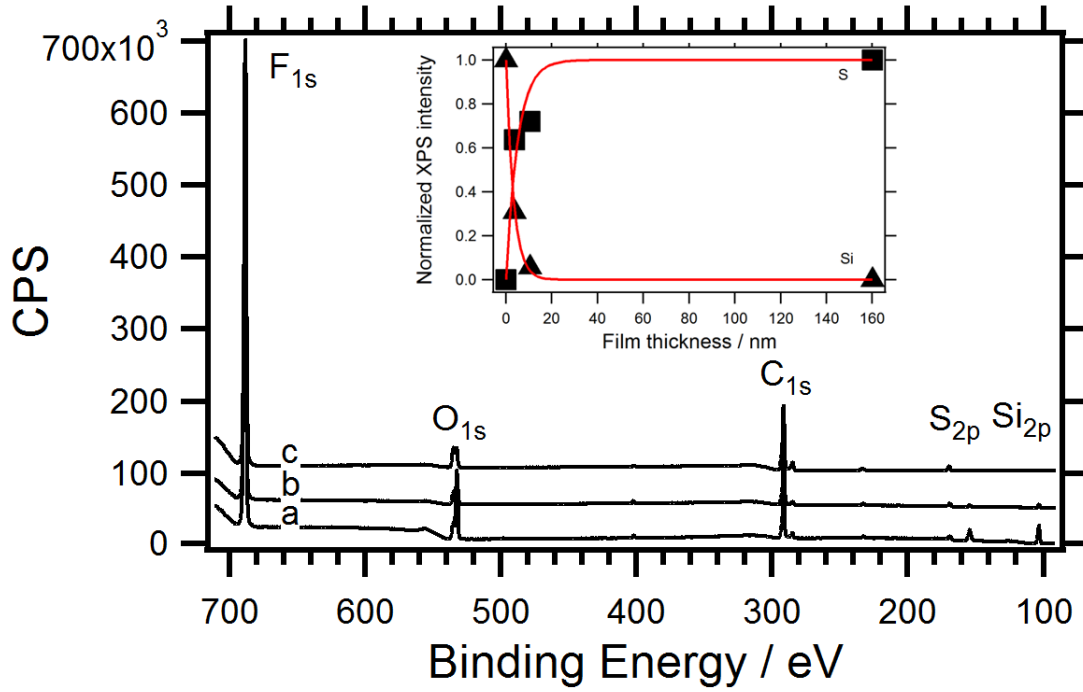


Figure 4.14: X-ray photoelectron spectra of the 10 nm Nafion® film as a function of electron take-off angle. a) 90°, b) 45°, and c) 10°. Spectra have been off-set for clarity. Insert shows the normalized XPS intensity for silicon (solid triangles) and sulfur (solid square) peaks at normal take-off angle as a function of film thickness.

First method:

$$\frac{I_{Si}}{I_{Si,bulk}} = \sin(\alpha) \cdot \exp\left(-\frac{d}{\lambda \sin(\alpha)}\right) \quad (3.4)$$

where, $I_{Si,bulk}$ is the photoelectron intensity produced by a clean silica substrate. At normal take-off angle ($\alpha=90^\circ$), this expression is similar to a Beer-Lambert absorption equation, where the electrons produced by the silica substrate are attenuated by the Nafion® film. Using this expression for the Si_{2p} intensities, the value of d/λ can be obtained (1.1758 and 2.8432 for the 0.1 and 0.25 wt% films, respectively). The film thickness can then be calculated directly by using $\lambda=3.7$ nm. The value of the electron mean free path varies with electron kinetic energy and the

composition and density of the medium through which it is traveling. The values chosen here were estimated by comparison with electrons of the same kinetic energy travelling through silica and several polymer films as quoted in the NIST database and calculated using the NIST standard reference database 71 software for possible densities for the film. The calculations result in film thicknesses of 4.3 and 10.5 nm for the 0.1 and 0.25 wt% films, respectively, in excellent agreement with the ellipsometry and AFM measurements (Table 4.4).

Second method:

$$\frac{I_S}{I_{Si}} = \frac{I_{S,thick}}{I_{Si,bulk}} \left(e^{\left(\frac{d}{\lambda \sin \alpha} \right)^{-1}} \right) \quad (3.5)$$

In this case, $I_{S,thick}$ is the intensity of sulfur in the bulk Nafion®, which was measured in the thick Nafion® films (3.0 wt%). The net result of this approach yields thicknesses of 4.1 and 9.6 nm for the 0.1 and 0.25 wt% films, respectively, within 10% of the simplest methodology (First method). Some variation was indeed expected as the model assumes a film of homogeneous thickness and homogeneous distribution of the monitored species. Indeed, only a 10% difference indicates these assumptions are reasonable. When the normalized XPS intensities obtained at 90° take off angle are plotted versus film thickness (insert of Figure 4.14), the profile is consistent with the expected exponential dependence. The profile is also consistent with the limit in probing depth of ~15 nm, equivalent to 4 times λ , for these films.

4.3.3.4. Comparison of thickness determination by AFM, XPS, and Ellipsometry

The thickness of self-assembled Nafion® films estimated using three different techniques is presented in Table 4.4. It is remarkable that three different techniques employing three different

measurement principles yield similar results. The XPS technique is limited to estimating film thicknesses less than 3-4 times the attenuation length of electrons from the substrate. The attenuation lengths typically range 2-4 nm ($\lambda=3.7$ nm for Si_{2p} electrons in this case), so films of thickness less than 16 nm only can be determined from XPS analysis. The surface roughness (discussed later) measurements from AFM indicate that the roughness is significantly lower than the lowest film thickness. This implies that no substrate area of any significant size remained uncovered and that the film completely covers the substrate. The roughness and surface feature size of Nafion® films also confirm that the non-uniformity of films at relevant length scales is small. Another important note is, regardless ellipsometry fitting models - Cauchy or EMA, the thickness was very similar however we could not get the evidence of voidage (as discussed in EMA model fitting results) at least in the length scale of AFM image (presented in Figure 4.16) and further exploration is beyond our scope. Therefore, we decided to rely on the Cauchy model fitting results. The characteristics film thickness from the second set of dispersion – Nafion® dispersion in water (more details discussion in the section 4.3.5) has also been included in the Table 4.4.

Table 4.4: Thicknesses of Nafion® films generated from different dispersions and concentrations.

| Nafion® dispersion concentration (wt%) | Film Thickness (nm) | | | |
|---|-------------------------|------|-----|-----------------------------|
| | IPA-diluted dispersions | | | Nafion®-in-water dispersion |
| | Ellipsometry | XPS | AFM | Ellipsometry |
| | | | | |
| 0.1 | 4.0 | 4.3 | 4 | |
| 0.25 | 10.5 | 10.5 | 11 | 11.6 |
| 0.5 | 31.5 | - | 32 | 27.5 |
| 1.0 | 57 | - | 55 | 57 |
| 1.5 | 75 | - | - | |
| 2.0 | 110 | - | - | |
| 3.0 | 160 | - | - | 173 |
| 5.0 | 308 | - | - | 313 |

4.3.4 Surface characterization

4.3.4.1. Surface wettability by water contact angle

To characterize the surface wettability, contact angle measurements with water were performed. The water contact angle of the blank substrate was determined to be 45°. The water contact angles for the films prepared from both IPA-diluted Nafion® and Nafion®-in-water dispersions and are presented in Figure 4.15. The images of sessile drops of water for 4 nm to 300 nm films prepared from IPA-diluted Nafion® dispersion are also shown in Figure 4.15.

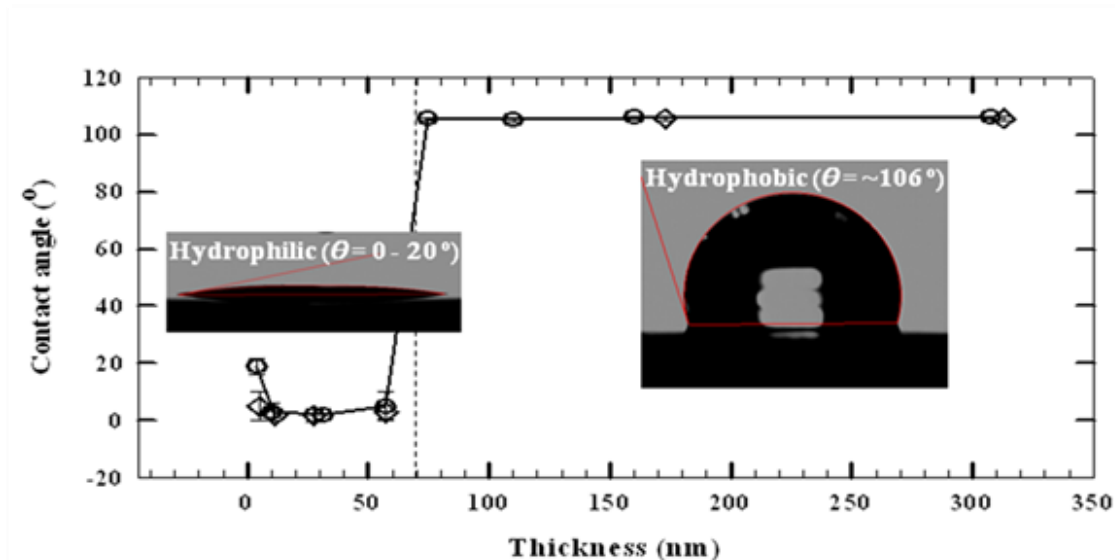


Figure 4.15: Water contact angle of Ultra-thin and thin Nafion® films varying film thickness. [Open Circles: Films from IPA-diluted dispersions; Open Diamond: films from Nafion® in water dispersions]

Two important observations can be made from the data in Figure 4.15. Firstly, all films except the thinnest (4 nm) exhibit either a very hydrophilic surface or a hydrophobic surface. Secondly, the films prepared from two different dispersions (in water and IPA-diluted) have nearly identical contact angles. Apparently, the latter observation supports the idea that Nafion® concentration in the dispersion rather than the nature of the dispersion media affects the film properties. For the thinnest film (4 nm), a very low contact angle of 22° can be noted. The 10, 30 and 55 nm films exhibited highly hydrophilic behavior wherein the water droplet immediately spread upon placement as resulting almost zero contact angle. Remarkably, for the films thicker than 55 nm, a sudden jump in contact angle to around 106°, exhibiting hydrophobic behavior of the film surface, was observed. The high contact angle of around 106° is comparable to the values reported for Nafion® membrane surfaces [47]. Furthermore, for the thicker films (>55 nm) the water droplet was stable as high contact angle did not break down small angle rather evaporates gradually by several hours. The contact angle for 4nm film requires some comments. The

measured contact angle of 22° is between that of the clean substrate (45°) and spreading behavior of the thicker films. A simplistic possibility is to think of the 4 nm film as partially covering the SiO_2 substrate resulting in a value that is intermediate of the contact angles of the two surfaces. On the other hand, AFM imaging of the substrate shows complete coverage of the substrate. It is not possible to ascertain the contribution of the substrate to the measured contact angle for the 4nm film. However, for the thicker films (10, 30 and 55 nm) the contact angle is spreading and not a non-zero value, which is strong evidence that the substrate does not contribute to the measurements.

The hydrophilic free surface of sub-55 nm films and hydrophobic free surface of thicker samples (> 55 nm films) is an indicator of changes in micro-domain structure. It is interesting to note that in a recent study, Eastman *et al.* [15] have also observed that the properties of Nafion® films of thickness less than 60 nm differ from those thicker than 60 nm. It would appear that 50-60 nm is an interesting length scale wherein perhaps the influence of substrate is still dominant resulting in a film with different free surface than the thicker films. The latter films have a free surface that is similar to those of bulk membranes.

Given that Nafion® is made of hydrophobic Teflon-like backbone and a hydrophilic sulfonic acid terminated side chain, it is natural to assign the hydrophilic behavior to the orientation of the hydrophilic sulfonic groups towards the air-film interface arising from an ordered structure in the thin films. In contrast, the Nafion® membrane surface is known to exhibit hydrophobic behavior attributable to the random structure of the membrane such that largely hydrophobic fluorocarbon backbones present itself to the air-film or air-membrane surface.

4.3.4.2. Surface morphology of films varying in thickness

The surface morphology of these films was examined by AFM to investigate whether the surface of the sub-55 nm and thicker (>55nm) films showed any differences. Here, the results for films generated from IPA-diluted dispersions only are presented. The AFM images of films generated from Nafion® dispersion in water are presented later part of this chapter. The height and corresponding phase contrast images obtained from AFM measurements are presented in Figure 4.16.

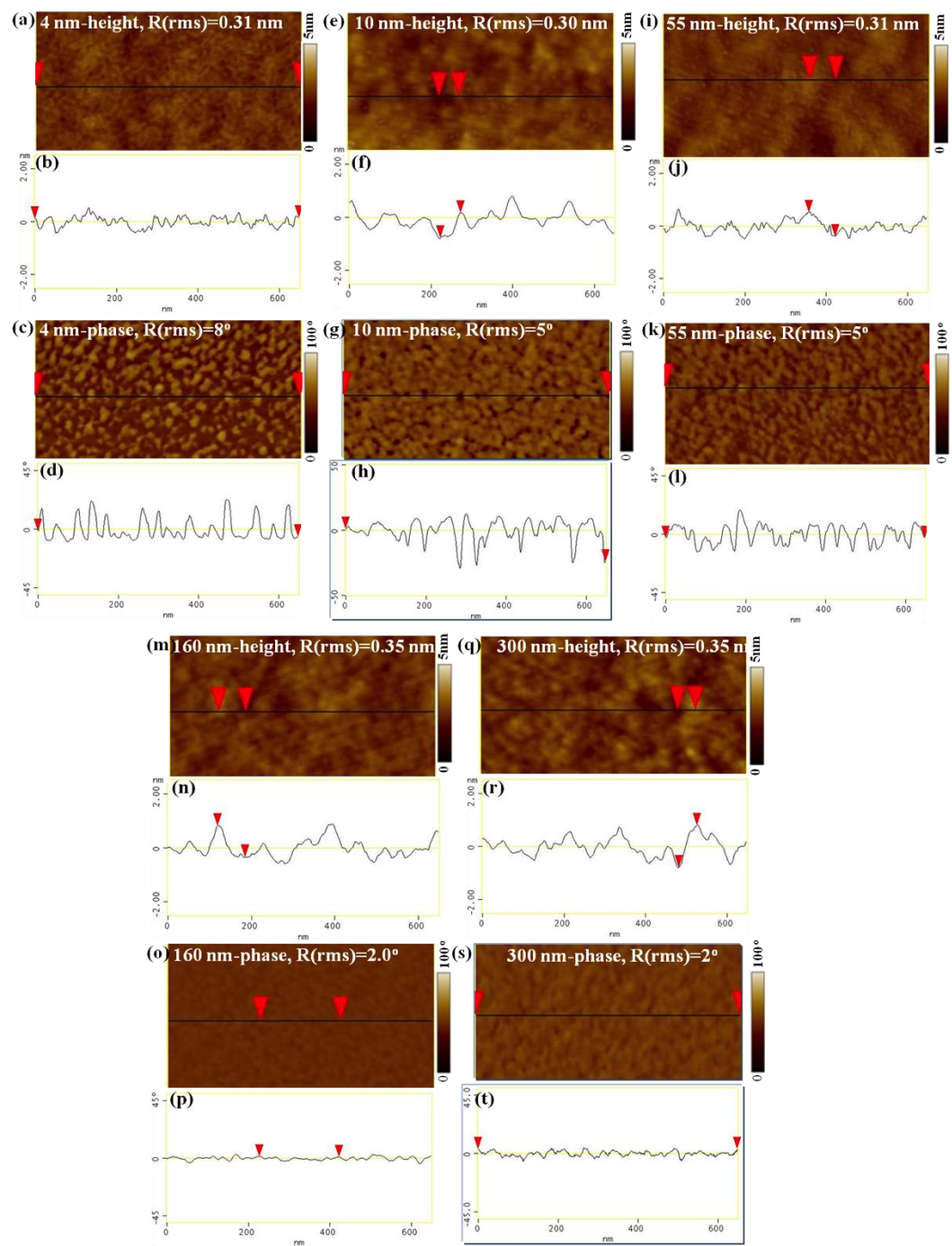


Figure 4.16: Height and corresponding phase images with section analysis of 4 nm film (a, b, c, d), 10 nm film (e, f, g, h), 55 nm film (I, j, k, l), 160 nm film (m, n, o, p), and 300 nm film (q, r, s, t). [Films prepared from IPA-diluted Nafion® dispersions].

Each of the phase and topographical image is accompanied by a line analysis to provide an insight into the distribution of the pertinent feature – phase shift angle or height. The root mean square (RMS) deviation of the pertinent feature is also indicated on the images. For the height/topography images, the RMS value represents the mean roughness as per the definition in Equation 4.1. For the phase contrast, an equivalent expression applies where the height is replaced with phase shift angle.

The topography images do not reveal any periodic or clear features. The root mean square surface roughness (R_{rms}) was found to increase only slightly from 0.31 nm for the 4 nm film to 0.35 nm for the 300 nm film. No significant differences in the surface roughness of thinner hydrophilic and thicker hydrophobic films exist. The examination of the phase images indicate connected fibre-like features for the ultra-thin films (<55 nm). The features in the phase images of thicker (160 nm and 300 nm) films are less clear, perhaps indicative of a more random orientation. Phase contrast can arise from in-homogeneity in physical (height), chemical (hydrophilicity/hydrophobicity), or mechanical (film modulus or hardness) properties of the film. The latter two arise from interaction between the tip and the film. Comparing the phase image and topographical images, it is evident that there is no obvious correlation between the two. As such, we attribute the features in the phase contrast images to arise from differences in the interaction (film modulus or hydrophilic/hydrophobic) of the AFM tip with different local chemical nature of the film.

To investigate whether some statistical parameters such as surface roughness could be correlated to the observed differences in the wettability, we analyzed the root mean square

deviation of phase shift angle. The use of phase contrast of Nafion® membrane as a metric of surface wettability has been reported by James *et al.*[145].

The trend was noted is that the RMS deviation of phase angle for hydrophilic films is greater than 5° whereas that for the hydrophobic films (160 nm and 300 nm) are only 2°. Incidentally the *mean* phase shift angles of all the films are all within 0.5 degrees of each other. However, the RMS deviations differ for the films indicating that the distribution of the phase shift angles differ. It appears that RMS deviation of phase shift angles may be an interesting measure for characterizing the differences in wettability of Nafion® films. However, further investigation is required to establish a clear correlation and is beyond the scope of the present study.

4.3.4.3 Compositional homogeneity of films by angle-resolved XPS

To explore whether the surface of thinner films were enriched with sulfonic groups and that of thicker films enriched with fluorocarbon backbones, we carried out angle-resolved XPS. For this purpose, representative peaks can be taken from the side chain and backbone, such that if layering is present in the films, these elements will show different angular distributions. We used the S_{2p} peak that originates from the Nafion® side chains and the F_{1s} peak, which originates predominantly from the backbone. Table 4.5 shows the integrated areas for these elements (corrected for transmission function and sensitivity factors). The C_{1s} peak is also shown as reference.

Table 4.5: Angle-Resolved XPS Data for 3 different films

| Film Thickness (nm) | Angle | Absolute intensities | | | $\frac{I_S}{I_F}$ | $\frac{G_S}{G_F}$ |
|------------------------|-------|----------------------|---------|---------|-------------------|-------------------|
| | | S | F | C | | |
| 4 nm | 90 | 433.2 | 19429.7 | 11166.1 | 0.0230 | 0.0192 |
| | 45 | 250.0 | 9221.9 | 5875.0 | 0.0271 | 0.0225 |
| | 10 | 94.4 | 3345.4 | 2591.6 | 0.0282 | 0.0214 |
| 10 nm | 90 | 490.4 | 15646.3 | 9624.6 | 0.0313 | 0.0246 |
| | 40 | 299.8 | 9479.1 | 6280.6 | 0.0316 | 0.0235 |
| | 10 | 179.8 | 6370.4 | 4251.4 | 0.0282 | 0.0201 |
| 160 nm | 90 | 680.4 | 20868.6 | 14338.9 | 0.0326 | 0.0247 |
| | 45 | 337.0 | 10332.4 | 7894.6 | 0.0326 | 0.0247 |
| | 10 | 101.6 | 3227.2 | 2649.7 | 0.0315 | 0.0238 |

The ratio of S to F concentrations appears to be constant for the thicker films, but an apparent increase in this ratio is observed for the ultrathin film as the take-off angle decreases. Such change could be associated with a structure in which there is an ordering of the Nafion® side chains in the top layer of the film (S rich). This interpretation is very tempting as it may account for the slightly more hydrophilic nature of the ultrathin film. However, a complete analysis of the ARXPS should consider the difference in the electron mean free path between the F_{1s} and S_{2p} electrons ($\lambda=2.8$ and $\lambda=3.7$ nm, respectively). The relationship is shown in Equation 4.6, where the stoichiometric ratio is represented by G_S/G_F .

$$\frac{I_S}{I_F} = \frac{G_S \lambda_S}{G_F \lambda_F} \left(\frac{1 - e^{-\left(\frac{d}{\lambda_S \sin \alpha}\right)}}{1 - e^{-\left(\frac{d}{\lambda_F \sin \alpha}\right)}} \right) \quad (4.6)$$

Upon correcting the data for the mean free path length of F_{1s} and S_{2p} electrons, according to Equation 4.6, we find that the actual stoichiometric ratio between the side chains and the backbone is constant for all the films. That is, within the error of the measurements, the heterogeneity within the films cannot be ascertained. Based on these results, we did not pursue AR-XPS investigation of films generated from water-based dispersions.

4.3.4.5. XDLVO surface energy calculations

Two distinct characteristics of thin films – hydrophilic up to 55 nm and hydrophobic above 55 nm are further illustrated by surface energy calculation. Surface energies were calculated by three liquid contact angle method as described in Chapter 3. The experiments were conducted on 4 nm and 160 nm Nafion® films. Additionally, measurements were carried out to calculate surface energy of Teflon, which serves as an internal reference. Contact angles measured using three different liquids of varying polarity are reported in Table 4.6. The surface energy components were calculated by matrix solution using Matlab for the 4 nm and 160 nm Nafion® films and the Teflon are also presented in Table 4.6. Repeat measurements on multiple samples (3 or more) of 4 nm and 160 nm films were made and exhibited the noted hydrophilic and hydrophobic behavior, respectively. Measurements made on 3-4 different locations on each of the 4 repeat samples yielded the average value reported in Table 4.6.

Table 4.6: Calculated surface energy of the adsorbed thin Nafion® films according to the XDLVO theory.

| Material | θ_w (°) | θ_d (°) | θ_e (°) | θ_f (°) | γ^{LW} (mJ/m ²) | γ^{\oplus} (mJ/m ²) | γ^{\ominus} (mJ/m ²) | γ^{Tot} (mJ/m ²) |
|----------------------------------|-------------------|-------------------|-------------------|-------------------|---------------------------------------|---|--|--|
| 4 nm film | 21.6±3.8 | 85.3±1.2 | 15.9±2.3 | - | 14.0 | 5.2 | 66.6 | 51.2 |
| 160 nm film | 106.1±0.6 | 86.3±0.6 | 97.8±0.7 | - | 14.1 | 0.5 | 5.8 | 17.5 |
| Teflon (in house) | 115.3 | 85.6 | - | 107.0 | 14.6 | 0.8 | 2.2 | 17.2 |
| Teflon (literature) ^a | | | | | 14.7 - 25.8 | 0.0 - 0.3 | 0.0 - 3.0 | 14.7 - 26.0 |
| Nafion® membrane ^b | | | | | 12.7 | 0.1 | 6.0 | 14.2 |
| Water ^c | | | | | 21.8 | 25.5 | 25.5 | 72.8 |
| Diiodomethane ^c | | | | | 50.8 | ≈ 0.01 | 0.0 | 50.8 |
| Ethylene glycol ^c | | | | | 29 | 3 | 30.1 | 48 |

θ_w , θ_d , θ_e and θ_f represent contact angle measurement using water, diiodomethane, ethylene glycol and formaldehyde respectively. ^aReference[161] ^bReference[134] ^cReference[150]

The intermediate thickness films were not assessed since, in the hydrophilic limit, the spreading water makes the small contact angle measurement inaccurate. The surface energy parameters for the liquids were obtained from literature [150]. Surface energies of Teflon or polytetra-fluoro-ethylene determined from measurements in our laboratory yield values within the range reported in literature. The surface energy components of the 160 nm film are comparable to that of the Teflon but slightly higher than those of Nafion® membrane surface energies reported by Kim *et al.* [134] On the other hand, the total surface energy of the 4 nm film is more than three time higher than that of the 160 nm film as well as the Nafion® membrane. Interestingly, a high value of the electron donating parameter (66.0 mJ/m²) for the 4 nm film indicates that the surface

is highly polar. This high polarity might be attributed due to presence of higher number of hydrophilic sulfonate groups at the surface. Furthermore, the van der Waal components of all films have a value comparable to the 14.6 mJ/m^2 value for Teflon. The total surface energy of 160 nm film is close to that of the Teflon surface (17.2 mJ/m^2) measured by the same method. This is expected since the Teflon-like backbone of Nafion® should dominate the van der Waal's interaction with the test liquid. The exact reason for the Teflon and 160 nm film possessing higher surface energy than literature reported Nafion® membrane is not clear. One possibility is the difference arising from the differences in the measurement conditions and the experimental setup. The results also support that the XDLVO type analyses offer useful insight into nature of interaction of Nafion® with other liquids and even other surfaces.

4.3.5 Influence of the solvent/dispersion media on self-assembled films

The films characterized in the previous section were prepared by self-assembly from first set of dispersion - IPA-diluted Nafion® dispersions of varying concentration. Upon dilution of stock solution by IPA, in addition to the change in Nafion® concentration, the dispersion composition also changed. The nature of dispersion media is known to have significant and non-significant effect on the nanostructure including the aggregation state of Nafion® in the dispersion. To delineate the concentration and dispersion media effects, a second set of films was prepared from Nafion® in water dispersions at same concentrations as that used for films from IPA-diluted dispersions. The thickness of films self-assembled from second set of dispersion - Nafion® dispersion in water, was determined by ellipsometry measurements. The data was fitted with Cauchy model. The fitting results are presented in the following Table 4.7.

Table 4.7: Summarized data for Nafion® film prepared from Nafion® -water dispersion.

| Nafion® | Film | Refractive | Non- | Contact | Roughness |
|----------------------|------------------|-------------------|-------------------|----------------|------------------|
| Concentration | thickness | Index | Uniformity | angle | (nm) |
| (wt%) | (nm) | At 550nm | (%) | (°) | |
| 0.25 wt% | 11.6 | 1.32 | 1.68 | <5 | 0.41 |
| 0.5 wt% | 27.5 | 1.36 | 4.90 | <5 | 0.40 |
| 1 wt% | 57.4 | 1.37 | 7.02 | <5 | 0.38 |
| 3 wt % | 172.9 | 1.37 | 14.24 | 105.7 | 0.43 |
| 5 wt% | 312.7 | 1.38 | 19.21 | 105.6 | 0.44 |

It can be noted that all films generated from Nafion® dispersion in water with concentrations ranging 0.25-5.0 wt% yield comparable thickness to those generated from IPA-diluted dispersions as presented in Table 4.4. One exception was the film self-assembled from the very dilute dispersion of 0.1 wt%. The morphology of the films obtained from 0.1 to 5 wt% dispersion in water was investigated by AFM measurement and presented in the next section. While the surface characterization is the main goal, films obtained from water dispersion of Nafion® show very similar distinct hydrophilic and hydrophobic surface characteristics in the 10 to 300 nm thickness range. It indicates that the different dispersion types have no significant effect on surface characteristics.

Characteristics of the film morphology obtained from Nafion® dispersion in water:

Figure 4.17 shows morphology and section analysis of 0.1 to 5 wt% film obtained from Nafion®-water dispersion. 0.1 wt% attributed discontinuous film. On the other hand 0.25 to 5 wt% accredited continuous film with negligible surface roughness. Roughness increases with increasing Nafion® concentration. Nonetheless, those surface corrugation is comparable with the

film obtained from IPA diluted Nafion® dispersion as discussed earlier. The feature height for 0.1 wt% film obtained more than 3 nm which is comparable to 4 nm continuous film thickness attributed from same concentration by different dispersion media. The corresponding section analysis of rest of the films showed 1 nm to 2 nm feature height which is insignificant compare to the film thickness 10 to 300 nm. It further proves the continuous nature of the films.

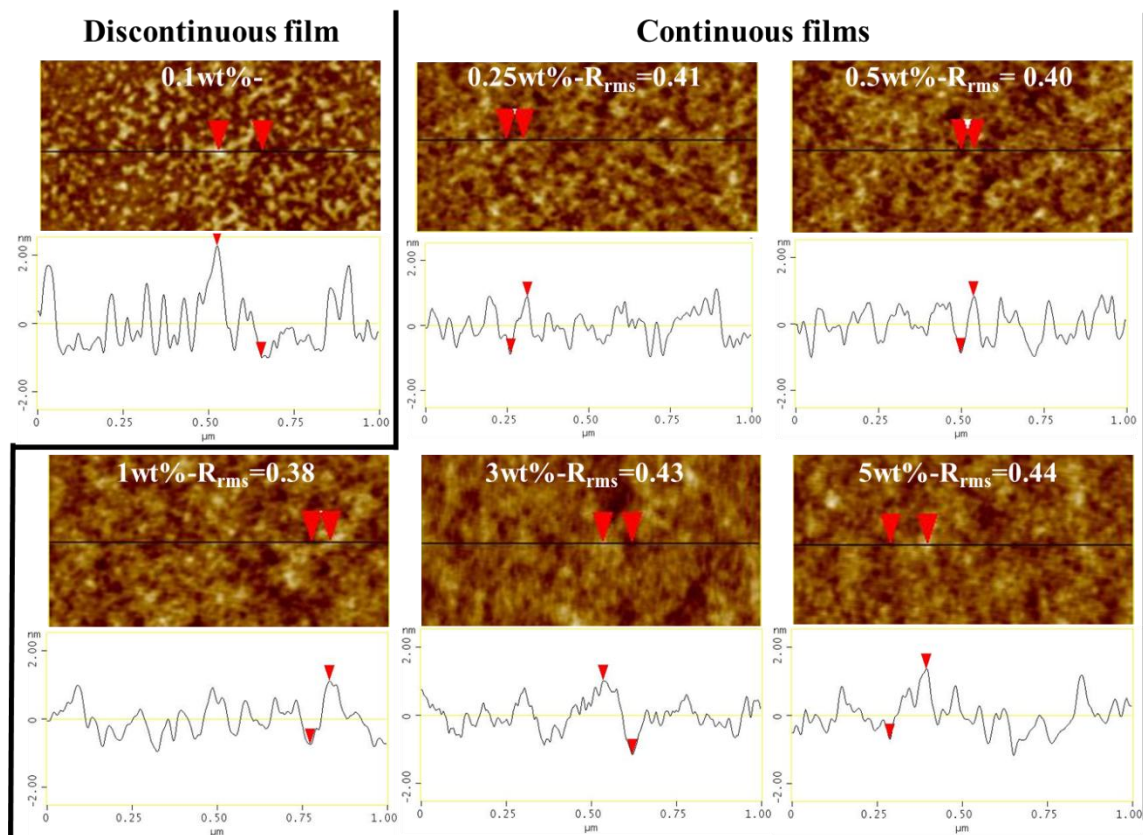


Figure 4.17: Morphologies and section analysis of self-assembled ultra-thin Nafion® film prepared from different Nafion® concentration in water.

Comparative ellipsometry raw data and refractive index: To investigate the similarity in the thickness and the nature of the films obtained from two types of dispersion, the raw

ellipsometry data and the refractive index were compared. Figure 4.18 shows the raw data of ψ spectra obtained from variable angle spectroscopic Ellipsometry of three different corresponding films at 75° incident angle. The pattern of spectrum was very similar; it gives the first impression of similar nature of the film. The slight deviation of data points might be attributed from difference in any of the parameters including thickness, refractive index, and non-uniformity.

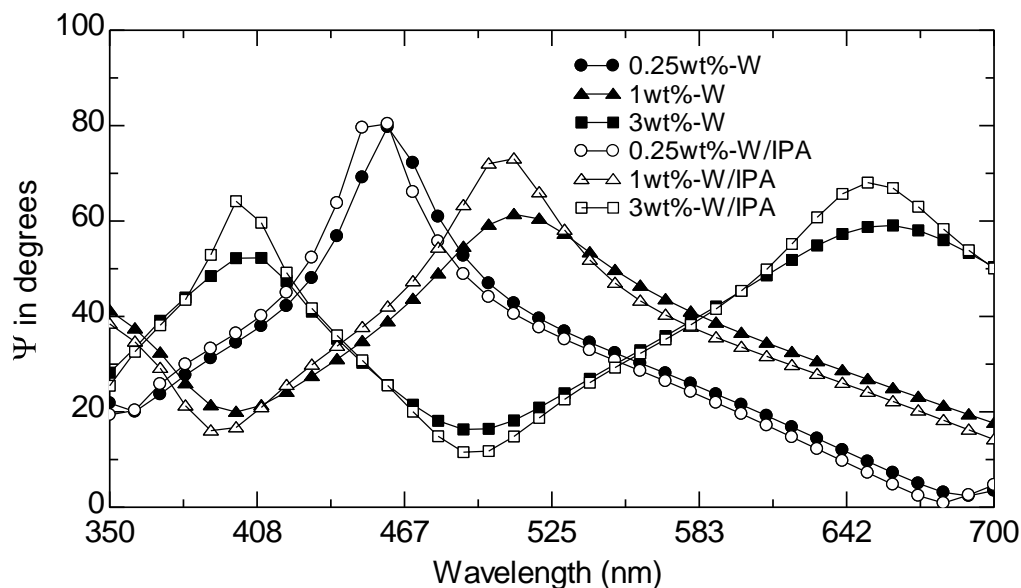


Figure 4.18: Comparative raw data of ψ spectra obtained from variable angle spectroscopic ellipsometry of three different corresponding films at 75° incident angle.

The refractive index (RI) was obtained from the Cauchy model fit to Ellipsometry data was similar with respect to thickness for the films prepared from the two different types of Nafion® dispersions. Figure 4.19 shows the comparative RI of two type of film in terms of thicknesses. It was found that 4 and 10 nm film has lower RI whereas RI was almost constant from the film thickness 30 to 300 nm generated from IPA dilution dispersion. The most significant and interesting part is that the comparable RI was obtained from both types of films.

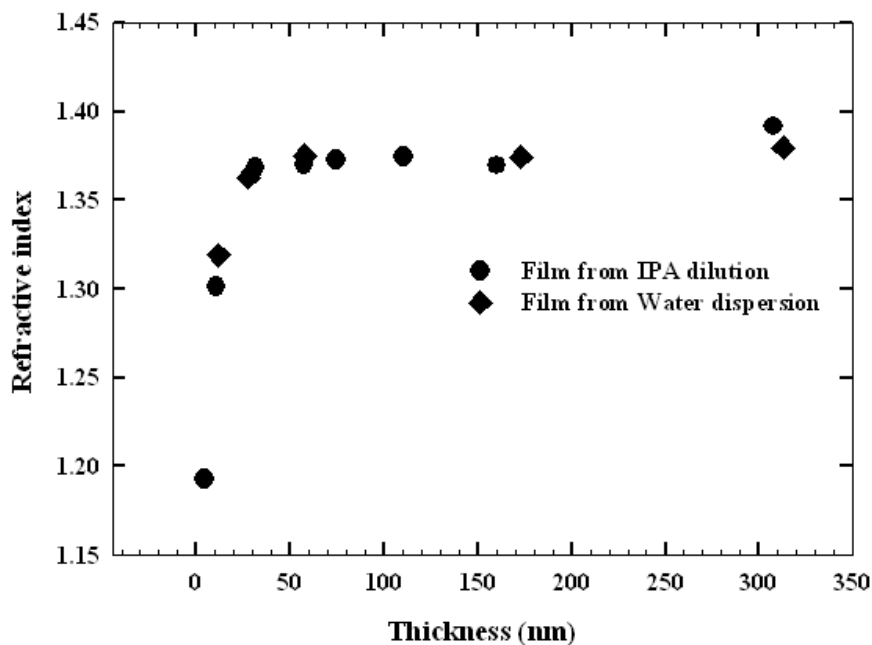


Figure 4.19: Refractive index of the films prepared from IPA diluted Nafion® dispersion and Nafion®-water dispersion in terms of thicknesses.

Size distribution of Nafion® in water dispersion: Dynamic Light Scattering (DLS) was adopted to probe the size distribution of Nafion® in water. The results are shown in the Figure 4.20. A narrow distribution was found for 0.1 wt% Nafion® dispersion with the maximum peak position ~150 nm. With increasing concentration, the distribution became broader where the peak diameter also shifted to the higher values resulting ~280 nm at 1 wt% Nafion® dispersion. When the concentration increased at 3 wt%, the peak further shifted to ~420 nm with much broader distribution where 30 volume percentages appeared with the particle diameter more than 1000 nm. .

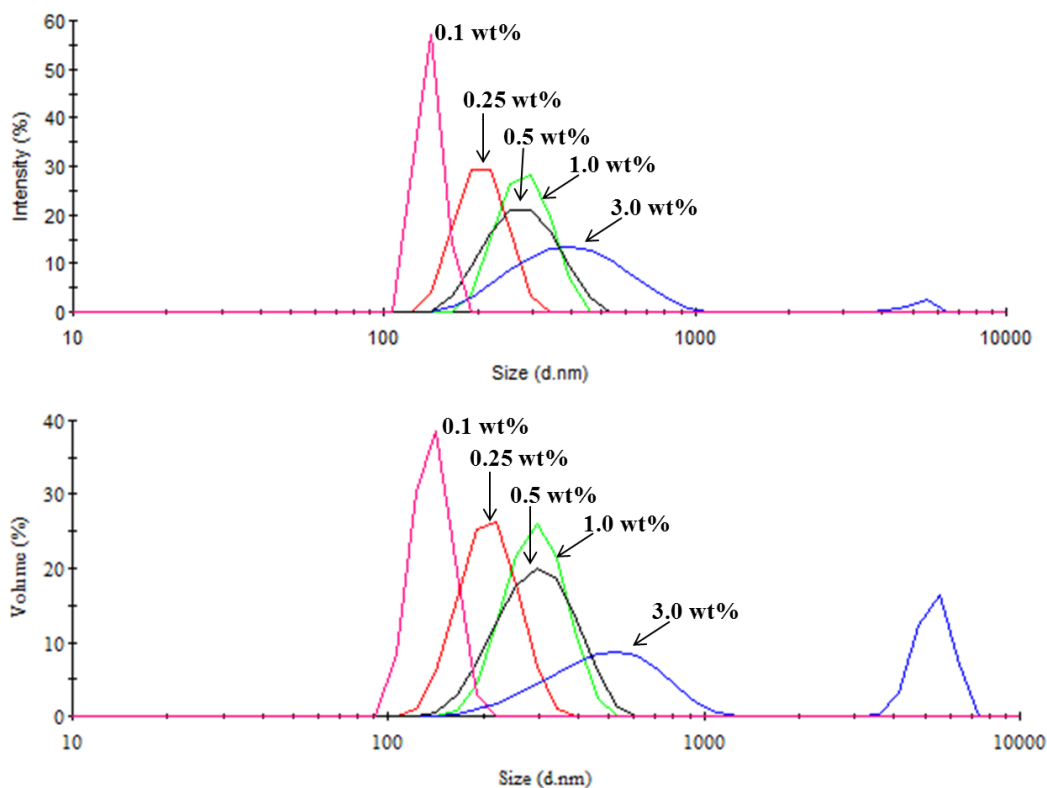


Figure 4.20: Size distribution of various Nafion® in water dispersions.

It indicates that the degree of association increases with an increasing concentration of Nafion® in dispersion. Thus, if the associated Nafion® adsorbs onto the substrate forming films with complete coverage, it can be expected that the thickness of the film would increase as the Nafion® concentration in the dispersion increases. This is consistent with the experimental finding of increased thickness of films generated from dispersions with increasing Nafion® concentration.

Combined thought on the effect of dispersion types on thin film morphology and properties: Similarity of properties/structure of films obtained from two different dispersions (water-based and IPA-enriched dispersions) is hinted from the similarity of spectral response in ellipsometry spectra. The similarity of thicknesses of the films prepared from similar

concentrations (0.25-5.0 wt%) is very interesting to note. Additionally, the surface wettability of both types of films exhibits similar contact angle values and follows the same trend with respect to film thickness. It is consistent with the idea that there are similarities in the surface structure and composition in between films prepared from two types of dispersion. In contrast, the dispersion medium compositions have influence on the size distribution and aggregation pattern in the 0.1wt% concentration level based on DLS measurement as discussed in Figure 4.8 & Figure 4.9. As a result, we have found discontinuous and continuous films for water dispersion and IPA diluted dispersion respectively. An interesting observation is the similar height feature in both discontinuous and continuous films. The height features of the films prepared from two different dispersion media but of same Nafion® concentration were also similar.

Nano-scale features of the Nafion® aggregates have been reported in literature and rod-like [99-103] or fringed rod-like [105-107] aggregates have been found for Nafion® dispersion in alcohol and water. Further agglomeration proceeds through the side chain interaction, which can be considered as a micro-scale feature. The dispersion media have greater influence on the determination of micro-scale feature than that of nano-scale features. Therefore, the reorientation and reorganization of Nafion® from micro scale to nano-scale in the film formation step is the dominating factor to determine the characteristics thickness and structure. It is inconclusive how the Nafion® organization is happening in dispersion media to thin films. However, based on similar thickness and surface properties, it can be concluded that dispersion type has insignificant impact as long as the concentrations are same. Further investigation might be useful to probe the nano-scale morphology. Most recently, based on the GISAXS and TEM study of self-assembled Nafion® thin film morphology, it has been inferred that the dispersion media (IPA vs water) have no significant impact on the self-assembly of the films for dispersions containing greater than 0.25 wt% Nafion® **165**].

4.3.6 Proposed nanostructure of self-assembled Nafion® films

We propose a thickness-dependent structure of the self-assembled films as depicted in Figure 4.21.

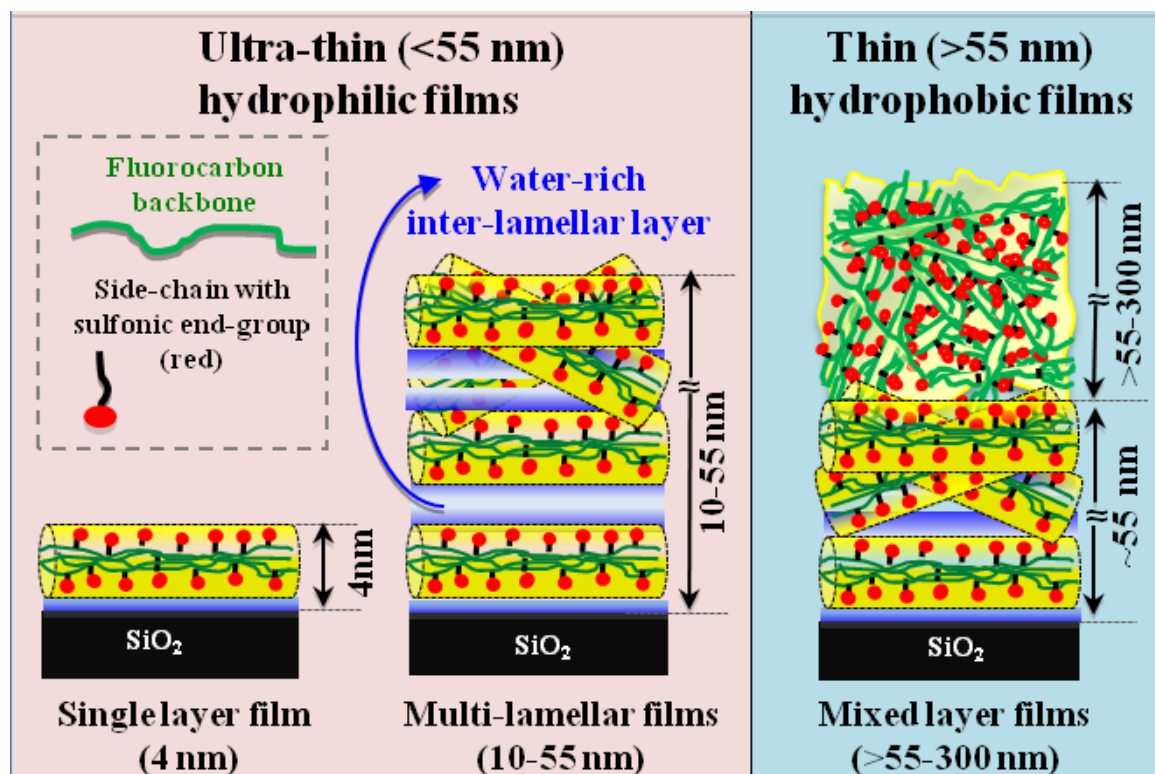


Figure 4.21: Thickness –dependent proposed nanostructure of ultra-thin and thin Nafion® films

Our thinnest film (4 nm) is the most interesting one not only because of the relevance of the length scale to the ionomer thickness observed in PEFC catalyst layer but because the thickness is remarkably close to the diameter of rod-like Nafion® aggregate observed in hydro-alcoholic solution by small angle scattering experiments [99-103]. The hydrophilic character of the free surface of these films, demonstrated by spreading of water droplet, is also consistent with the proposed structure of the Nafion® bundles/rods in hydro-alcoholic solutions with sulfonic

side chains protruding outwards. For the side of the film interfacing with the substrate, Nafion® likely interacts via hydrogen bonding with the thin hydration layer formed on the SiO₂ surface. We do not have a direct proof of whether the bundle-like structure remains intact or it opens up upon adsorption on SiO₂. However, given the coincidental thickness of the 4 nm film with the reported diameter of Nafion® bundles in hydro-alcoholic solutions/dispersions as well as the hydrophilic nature of the free surface, it is plausible that the 4 nm film is made largely of rods or bundles lying flat on the substrate. However, we have not been able to confirm this. Characterization of our films by GISAXS has not revealed any discernible features or the presence of ionomer domains. In Figure 4.21, a water-rich interfacial structure (between Nafion® and SiO₂) is depicted. This idea is derived from and consistent with the neutron reflectometry work by the NIST group [8] and that proposition by Hickner group [13].

For 10-55 nm films, a lamellar structure similar to that proposed by Dura *et al.* [8] seems to be plausible. The polymer-rich lamellas can either be made of rods or bundles have the sulfonic-group containing side-chains extending outwards or of less ordered structure. It can be argued that the free interface has significant sulfonic group density resulting in a hydrophilic film surface. The water in the inter-lamellar layers would have to come from tightly bound hydration shell that forms around the sulfonic group. The water would also be responsible for shielding the repulsive forces arising from the interaction of the sulfonic groups in the two lamellas. It is likely that the 30 and 55 nm have some bundles oriented at an intermediate angle between zero and 90 degrees.

For the 160 and 300 nm films, the hydrophobic free surface suggests that the surface structure of the films is similar to those of the membrane. Bass *et al.* [10] have proposed from their GISAXS study of 100 nm films formed on OTS-modified SiO₂ surface that a majority of the

Nafion® bundles near the free interface would have to orient vertically to the substrate consistent with a hydrophobic surface. The nature or structure of the film near the SiO₂-Nafion® interface may be multi-lamellar as has been noted by Dura *et al.* [8] from Neutron Reflectometry measurements, albeit on a spin-coated film.

4.4 Conclusions

In this study, we examined the surface characteristics of self-assembled films of Nafion®, on thermally grown on SiO₂ substrate, generated by immersion in Nafion® dispersion of different concentrations. In the film preparation approach, two parameters – immersion time and composition of dispersion medium (IPA/water), have been investigated on self-assembly phenomenon. It was found that it takes ~ 12 h to provide a continuous and homogeneous film. Dispersion medium composition has significant impact on the thinnest - 4 nm, film preparation where 0.1 wt% Nafion® dispersion in IPA/water mixture with negligible amount of water attributed a continuous film. Other than that, regardless dispersion continuous films were obtained.

The thickness of the resulting films were found to increase with increasing Nafion® dispersion concentrations, ranging from 4 nm for films generated from a 0.1 wt% solution to 300 nm for films generated from 5 wt% solutions. Consistent film thicknesses were obtained by three different techniques – XPS, AFM and Ellipsometry. The 4 nm film is one of *thinnest, continuous films* of Nafion® ever reported. The film thickness is of the same length scale as that reported for diameter of rod-like or fibrillar structure of Nafion® in polar solvent. One of the interesting findings of the study was thickness-dependent wettability of the films. The ultra-thin films (<55 nm) showed hydrophilic surface characteristics whereas the thicker films (>55 nm) showed

hydrophobic surface characteristics. The hypothesized sulfur-rich surface of thinner films was investigated with angle-resolved XPS and apparent enrichment in S/F ratio was noted. However, upon accounting for the angle effects and mean free path lengths of pertinent S and F electrons, the S/F ratio of all films was found to fall within the variance of the experimental measurements. Nonetheless, differences in surface features as noted in AFM-phase image and surface wettability between the ultra-thin (<55 nm) and thin (>55 nm) films indicate that ultra-thin films have structure and properties are distinct from the thicker films, which exhibit characteristics similar to that of free-standing membrane form of Nafion®.

Many factors are expected to influence the structure and properties of the films including the preparation methods (self-assembly, spin-coating, drop casting) and the surface chemistry of the substrate. It is expected that the substrate surface chemistry will play an important role in the organization of polymer molecules on the surface; as such the conclusions drawn here must be restricted to Nafion® films on SiO₂ substrate. Extrapolation of the findings to Platinum or Carbon substrates, pertinent to fuel cells, would be purely hypothetical at this stage given the differences in structure reported by Dura *et al.* [8] and Wood *et al.* [9].

Nonetheless, new findings on Nafion® thin films including the results from this study offer the cautionary note that the assumption of these films possessing similar properties as well-studied and characterized Nafion® membrane could result in serious errors. As with Nafion® membrane, a thorough understanding of all the influencing factors and a generalized law describing the interactions of Nafion® with substrates in different dispersion media will require extensive and multi-technique characterization of thin films of this interesting material.

Chapter 5

Protonic Conductivity of Ultra-Thin Nafion® Films

5.1 Introduction

Proton conductivity is a key functional property of the ionomer. As discussed in Chapter 1, the ionomer exists as an ultra-thin ionomer films in PEFC catalyst layer (CL). Considering Nafion® ionomer, the thickness of these films in the CL is comparable to ionic domain size (~4 nm) in the bulk Nafion® membrane. Very limited knowledge of proton conductivity in the ionomer films of thickness comparable to ionic domain size exists. Moreover, the conduction property of materials is highly regulated by its structural or morphological features. Recent studies have indicated that the nanostructure and morphologies of thin Nafion® film are different than that of Nafion® membrane [8-16]. One of the main reasons is the high interfacial area to volume ratio in Nafion® thin films such that the interfacial effect may dominate the film morphology and properties. Therefore, there are three vital questions – (i) is the proton transport property of thin supported films different than those of the free-standing membrane form? (ii) what are the factors responsible for the possible differences? (iii) is the proton transport mechanism in the thin films different than that of the membrane?

Activation energy of proton conduction can be considered as a parameter that can provide insight into differences in the mechanism for proton transport. Previous studies examining proton conduction of bulk Nafion® have reported activation energy ranging 10-14 kJ/mol for fully humidified membranes [69,167,168]. On the other hand, to the best of our knowledge, only Siroma *et al.* [14] have reported proton conductivity of thin Nafion® film. However, they prepared the films by spin coating rather than by self-assembly. Their work showed the Nafion®

conductivity to be film thickness dependent and the conduction is associated with higher activation energy.

In the previous chapter, the characteristics of self-assembled Nafion® thin films were described but with focused on surface morphologies and wettability only. Two distinct surface behaviors – hydrophilic surface for the films up to thickness 55 nm and hydrophobic surface for the films above 55 nm, were observed. A nanostructure of the film was proposed wherein the substrate induced organization of Nafion® in lamellar form extends to ~55 nanometers and beyond this thickness free reorganization of Nafion® occurs. It has also been indicated that there might have a thickness-dependent gradual orientation change of the Nafion® bundles. Transport characteristics of the self-assembled films might be a reflection of the morphological and structure features.

In this chapter, the investigation on the proton transport behavior of self-assembled Nafion® thin films varying in thickness from 4 nm to 300 nm is presented. Electrochemical Impedance Spectroscopy (EIS) was employed for impedance measurement of the Nafion® thin films on inter-digitated array (IDA) of gold (Au) electrode supported by SiO₂/Si wafer. An ideal equivalent circuit design and fitting of the experimental data to extract film resistance have been discussed. Film conductivity as a function of relative humidity and temperature was determined for films of various thicknesses and subjected to different post-fabrication treatment. A comparison of thin film conductivity and activation energy with those of its membrane counterpart is reported. Moreover, a correlation of the proton transport property to the film swelling property, water uptake and morphological features has also been investigated.

5.2 Experimental

5.2.1 Materials

Commercially available 5 wt% Nafion® dispersion was used as stock solution for thin film preparation. The self-assembled thin film preparation protocol was adopted same as described in the chapter 4. IPA diluted Nafion® dispersion was used for film preparation but SiO₂ supported interdigitated Au electrode and Pt electrode were used. The details of electrode, electrode cleaning, film preparation and film treatment have been discussed below.

5.2.2 The design and fabrication of Interdigitated array (IDA) of Au electrode

For impedance measurement, an IDA of Au electrode supported by SiO₂ (2000 nm)/Si wafer was used as substrate. IDA microelectrode consists of 110 teeth (each teeth is 0.8 cm in length and 10 μ m in width) with 100 μ m gap between two teeth as shown in Figure 5.1.

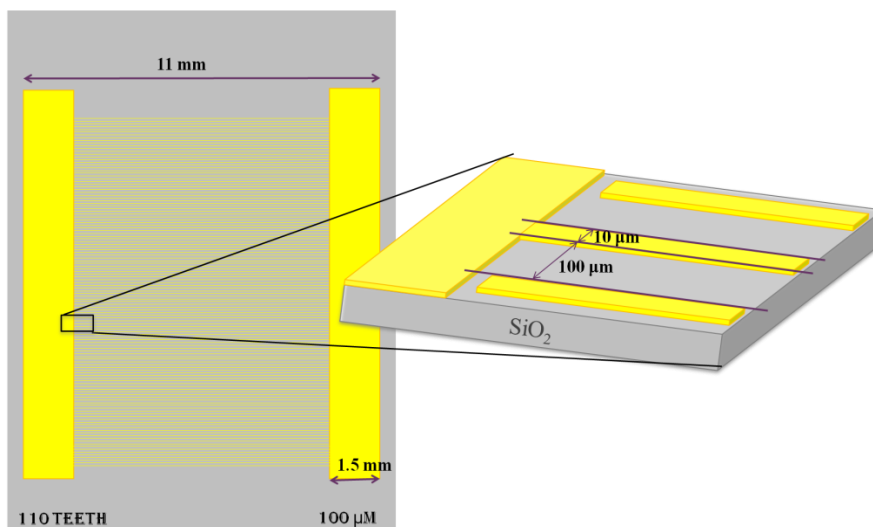


Figure 5.1: IDA of Au electrode supported by SiO₂ terminated wafer. Gray color represents SiO₂, golden color represents Au electrode. The electrodes were fabricated in the National Institute for Nanotechnology (NINT) lab, Alberta.

5.2.3 Preparation of self-assembled thin films on IDA

Electrode cleaning: The electrode was soaked into acetone for 30 min followed by sonicated for 2 min in each solvent (IPA, acetone and Millipore water). Finally, it was washed and repeated at least 3 times with a number of solvents including IPA, acetone and Millipore water. The electrode was dried by N₂ blow for 30 min and made ready for ultrathin film preparation on it. As the electrode consists of Au or Pt, therefore, it was not exposed in piranha solution. Highly oxidizing piranha solution can oxidize the metal electrode and detach from the SiO₂ surface rather cleaning the SiO₂ surface. However, impedance of blank electrode was measured before and after cleaning to ensure that the electrode was not damaged during the cleaning steps. The impedance measurement set up has been described later in the section 5.2.5.

Fabrication of Self-assembled thin films on IDA: Same protocol described in the chapter 4 was adopted for the preparation of self-assembled films on IDA. In this case, 5 wt% Nafion® dispersion was diluted at 0.1, 0.25, 0.5, 1.0, and 3.0 wt% by adding IPA. The diluted dispersion was equilibrated for 24 h at room temperature. Then the pre-cleaned electrodes were immersed into the diluted solutions. It was studied that 12 h is sufficient time to make a homogenous and continuous film on the SiO₂ substrate. Therefore, the substrates were taken out from the Nafion® dispersion after 12 h and dried in N₂ blow. Before impedance measurement, further film treatment protocol was adopted as described in the following subsection. The characteristic film thicknesses – 4 nm, 10 nm, 30 nm, 55 nm, 160 nm and 300 nm were adopted

for the 0.1, 0.25, 0.5, 1.0, 3.0 and 5wt% Nafion® dispersion, respectively as described in chapter 4. The thicknesses of those films on the electrodes were also confirmed by AFM scratching technique and XPS technique.

5.2.4 Treatment of self-assembled thin films

The IDA with Nafion® thin film was placed in an environmental chamber (Model 3911, Thermo Forma, USA) with relative humidity (RH) and temperature control for the further treatment before impedance measurement. The environmental chamber can control temperature 0 to 60 °C and RH ranging from almost 0 to 96%. To maintain RH below the ambient level – especially, close to zero RH, a dry air flow was connected to the chamber. As film water uptake and morphological changes have a great influence on the proton conductivity of the characteristics films, therefore, two treatments protocols (Protocol-1 and Protocol-2), were strictly maintained to get the films equilibrated at a certain temperature and relative humidity. The main point was to avoid any uncertainty of morphological changes at high temperature treatment. On the other hand, the films should be equilibrated at the highest measurement temperature to avoid any over/under estimation of impedance for temperature dependent measurement.

For both protocol-1 and protocol-2, the initial step was the same – the films were kept in the environmental chamber at ~25 °C and low (almost zero) relative humidity with continuous dry air flow for overnight (15 to 20 h). Protocol -1 was adopted for the impedance measurement at room temperature (25 °C), therefore, the impedance data was collected after the initial step further equilibrating at each RH, ranging from 20 to 95% RH. The equilibration monitoring protocol has been described in the impedance measurement subsection 5.2.5.

Protocol -2 was adopted for measurements at higher temperatures (30 to 60 °C). Hence, the as-prepared films were continued treatment with a step-by-step temperature increment up to the maximum measurement temperature, 60 °C and equilibrated at low RH condition. The equilibration was also monitored and confirmed by a single-frequency impedance measurement as described in the section 5.2.5. Once the equilibration was confirmed, the impedance data of the thin films were collected at 60 °C for RH varying from 20% to 96%. In each case, the equilibration was monitored and confirmed.

5.2.5 Impedance measurement of the self-assembled thin films

Impedance measurement set up: The measurements were accomplished by a two micro-probe setup connected to a Solartron 1260 frequency-response analyzer coupled to a Solartron 1296 dielectric interface. A humidity sensor (CMOSENS Tec., Switzerland) was placed in the close vicinity of the IDA sample to monitor the local equilibration for RH and temperature along with two other sensors in the different place of the chamber to monitor the overall equilibration of the chamber termed as external equilibration (Figure 5.2). Although the external RH and temperature equilibration were rapid and could be monitored by appropriate sensors, it does not guarantee the internal equilibration of film.

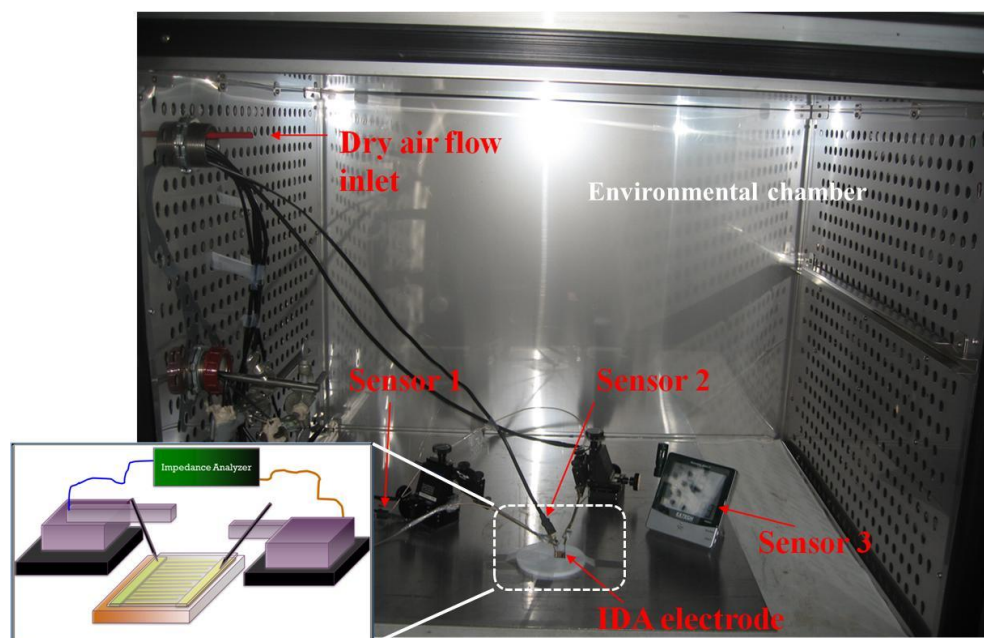


Figure 5.2: Impedance measurement setup inside the environmental chamber. Nafion® film on IDA of Au electrode has been connected by two probes to the impedance analyzer coupled with dielectric interface.

Equilibration monitoring protocol: The equilibration protocol is the combination of external and internal equilibration of thin film local environment. As discussed, the external equilibration established rapidly, which is monitored by the external sensors placed in the environmental chamber. In contrast, internal equilibration, which is essentially water absorption and polymer relaxation, is a slow process. The change in water content of the ionomer is associated with change in proton conduction because it is a water-mediated property. Therefore, a single-frequency impedance measurement was carried out to monitor the approach to ionomer film equilibration. It is known that film impedance at a constant frequency is RH dependent where constant impedance should be obtained at a fixed RH. In the approach, the film impedance was monitored with time at a single (constant) frequency and a fixed RH and temperature. When the impedance value became invariant with time, the film was deemed to be equilibrated at the set

RH and temperature. Both external and internal equilibrations were maintained for data collection.

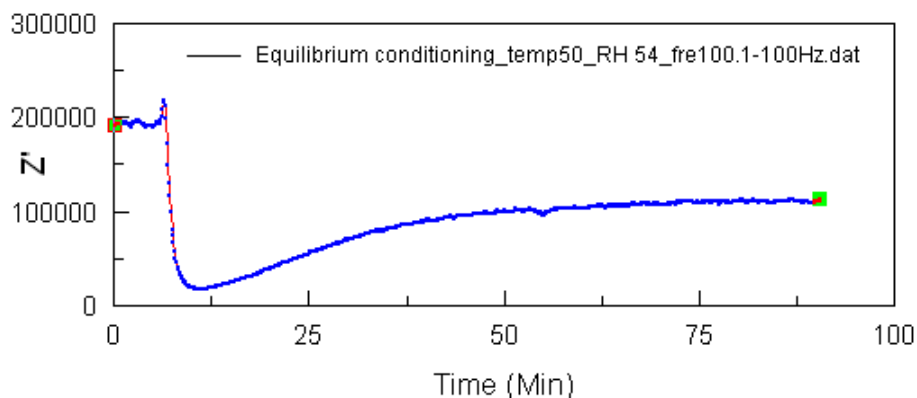


Figure 5.3: Impedance monitoring at a single frequency of 100 Hz for film subjected to RH change from 40 %to 50% at 50 °C.

Impedance data collection: Once the film was deemed to have been equilibrated, impedance data were collected by applying an alternating potential of amplitude 100 mV over a frequency ranging from 10 MHz to 0.01 Hz. At least three repeat measurements were recorded at the same measurement setup to verify reproducibility. Smart impedance measurement software (Solartron Analytical) was used for data collection. Z-view impedance software (Version 3.0a, Scribner Associates Inc.) was adopted for equivalent-circuit design, model fitting and data analyses as described in the following sections 5.3.2 and 5.3.3.

5.2.6 Water-uptake measurements

For swelling study, Nafion® thin film was prepared on SiO₂ terminated silicon wafer as same as the film used for thin film characterization in chapter 4. For QCM study, SiO₂ coated Au QCM crystal was used as substrate and the crystal was placed into the QCM holder with SiO₂

coating side exposed. The loaded QCM holder was immersed in the requisite Nafion® dispersion and dried according to the same protocol as adopted for film treatment in chapter 4. It is clearly stated that all of the films were prepared by the Author according to the developed protocol but water uptake measurements were carried out by Dr. Mike Hickner group at Penn State University. The following experimental procedure has been reproduced from our joint publication in macromolecules 165]. Film thicknesses were measured in situ under varying relative humidity (RH) using a J.A. Woollam RC2-XI dual rotating compensator multichannel spectroscopic ellipsometer. The change in the wave amplitude (Ψ) and phase shift (Δ) was measured over a spectral range of 240 to 1700 nm (0.75 - 5.15 eV). Once Ψ and Δ were characterized as a function of photon energy, a Lorentz oscillator-based homogenous single slab model with no roughness was used to derive the thickness and optical properties of the polymer films on optically characterized substrates. The change in thickness and complex refractive index were calculated for films exposed to 0, 25, 50, 75, and 90 % RH in an in-house constructed environmental cell held at ambient temperature. The cell was made with non-polarizing fused silica windows to maximize the amount of light transmitted. The % thickness change or % swelling (S) as a function of RH was calculated from the ellipsometric data by

$$S (\%) = 100 \% \cdot \frac{t_{RH} - t_0}{t_0} \quad (5.1)$$

where t_{RH} is the thickness at a given RH and t_0 is the thickness at 0 % RH.

Water uptake was measured using a QCM (Maxtek/Inficon, East Syracuse, NY) and Sauerbrey analysis. In QCM study, it is assumed that adhering material on the QCM crystal has the piezoelectric effect as same as that of the Quartz crystal. The entire QCM holder was enclosed in a poly(ethylene) in-house constructed humidity chamber maintained at ambient temperature.

The hydration number, λ_w (moles of water per mole of sulfonic acid group) was calculated from the mass uptake of the samples,

$$\lambda_w = \left(\frac{m_{RH} - m_0}{M_{H_2O}} \right) \cdot \left(\frac{1000}{m_0 \cdot IEC} \right) \quad (5.2)$$

where m_{RH} is the sample mass at a given RH, m_0 is the mass of the dry sample, M_{H_2O} is the molecular mass of water, and IEC is the ion-exchange capacity (0.909 mmol/g).

For humidification in both ellipsometry and QCM experiments, air at dewpoint was produced using a sparging system. The humidified wet air was mixed with a stream of dry air and the flow rates of the wet and dry streams were varied using electronic mass-flow controllers (Omega FMA5512, Omega Engineering, Inc., Stamford, CT) to achieve a specific relative humidity at ambient pressure. A RH probe (Omega HX15-W) was connected to the gas outlet from the ellipsometry or QCM in-house constructed humidity chambers for in-situ monitoring of the relative humidity of the sample environment.

5.2.7 Grazing-incidence small-angle X-ray scattering measurements

For GISAXS measurements, films were prepared on SiO₂ terminated silicon wafer (1 cm × 1 cm) as same as the film used for thin film characterization in Chapter 4. Though the sample was prepared by the author, the measurement was performed by Dr. Adam Weber group at Lawrence Berkeley National Laboratory. The experimental procedure has been reproduced from our joint publication [165]. Thin-film samples were placed into an in-house built environmental chamber with X-ray transparent Kapton[®] windows. The sample cell was equilibrated at 100% RH

at room temperature (20 °C) in less than 3 min, and GISAXS patterns were collected as a function of time for 25 min. All X-ray scattering experiments were performed in beamline 7.3.3 of the Advanced Light Source (ALS) at Lawrence Berkeley National Laboratory (LBNL). The X-ray energy used was 10 keV, with monochromator energy resolution E/dE of 100, and the patterns shown were acquired with a 2D Dectris Pilatus 1M CCD detector (172 μm x 172 μm pixel size). All the GISAXS patterns presented here were collected at an incidence angle of $\alpha_i=0.20^\circ$, well above the critical angle for Nafion® and just below that of Si in order to probe the entire film structure.

5.3 Results and discussions

5.3.1 Impedance responses

A typical impedance response for the self-assembled Nafion® thin film on IDA is shown in Figure 5.4. The real component of the impedance corresponds to the resistance and imaginary impedance is related to the capacitance. This plot is known as Nyquist plot. It can be noted that both real and imaginary resistance vary with AC frequency. Nyquist plot presents a correlation between real and imaginary impedance but the frequency-related information is not easy to glean. In Bode plots, both real and imaginary impedance are presented in terms of the frequency. Therefore, a complete impedance response can be obtained from both Nyquist plot and Bode plot.

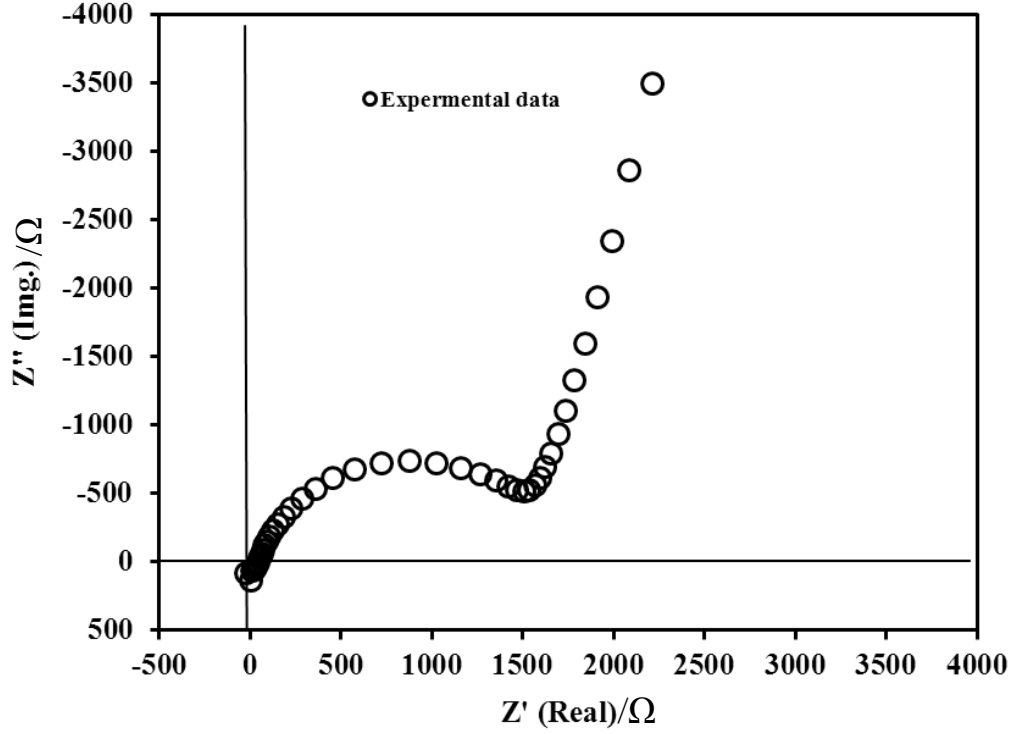


Figure 5.4: Typical impedance response of ultra-thin Nafion® film presented as a Nyquist plot.

The impedance response shown as a Nyquist plot is comprised of an inductive part, a suppressed semicircle at the high-frequency region and also a vertical-line like response in the low frequency region. Similar response has been reported elsewhere [78-80]. As indicated in the experimental part in section 3.2.5, generally, a semicircle type response typical of a parallel RC circuit is observed at higher frequency. At the same time, the vertical line represents capacitive behaviour only.

However, the main goal of the impedance measurements is to extract the resistance attributed by the Nafion® thin film. Eventually, the extracted resistance is employed for calculation of the proton conductivity considering the IDA electrode geometry. Unfortunately, the impedance response does not directly provide film resistance and capacitance unless it is fitted with an appropriate equivalent circuit. The equivalent circuit design based on understanding of

the system impedance contribution will be described in the section 5.3.2. Below, the impedance response in terms of relative humidity, temperature and film thickness have been presented to visualise and understand which part of the impedance plot can be attributed to film resistance.

Impedance responses at various RH: The impedance responses of 10 nm film varying RH at 60 °C have been presented in the Figure 5.5. The impedance was measured in the frequency range 10 MHz to 0.01 Hz. In each case, the typical impedance response was obtained. While the response pattern was same, the only observable change was the size of the semi-circle. It was found that the semicircle originated from the same place at high frequency but the diameter decreased with increasing RH.

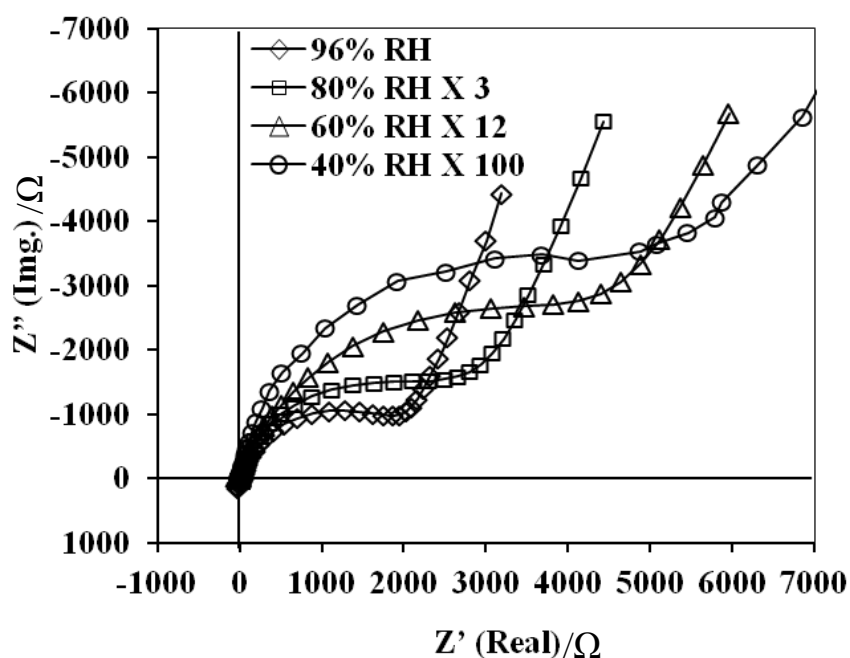


Figure 5.5: Nyquist impedance plots for 10 nm ultrathin Nafion® film at 60 °C and different RH. The data for 80, 60 and 40% RH have been reduced 3, 12 and 100 times respectively to fit into the scale.

It is known that the proton conductivity of Nafion® ionomer increases with increasing relative humidity. Therefore, the film resistance decreases with increasing RH. In this regard, it indicates that the semicircle is associated with the film resistance. Temperature-dependent impedance responses for further confirmation/evidence were also investigated.

Impedance responses for different temperatures: Impedance responses of 55 nm film at 80% RH and various temperatures from 30 to 60 °C have been presented in the Figure 5.6. Similar to RH-dependent impedance responses, major variation was observed in the semicircle diameter with a variation of temperature. It was found that the resulting semi-circle diameter decreased with increasing temperature from 30 °C to 60 °C. Since Nafion® film conductivity is dependent on temperature, an increase in temperature should result in a decrease in the film resistance. Considering that the semi-circle resistance is due to the film resistance, the observed decrease in semicircle diameter or resistance with increase in temperature is consistent with conductivity behavior of Nafion®.

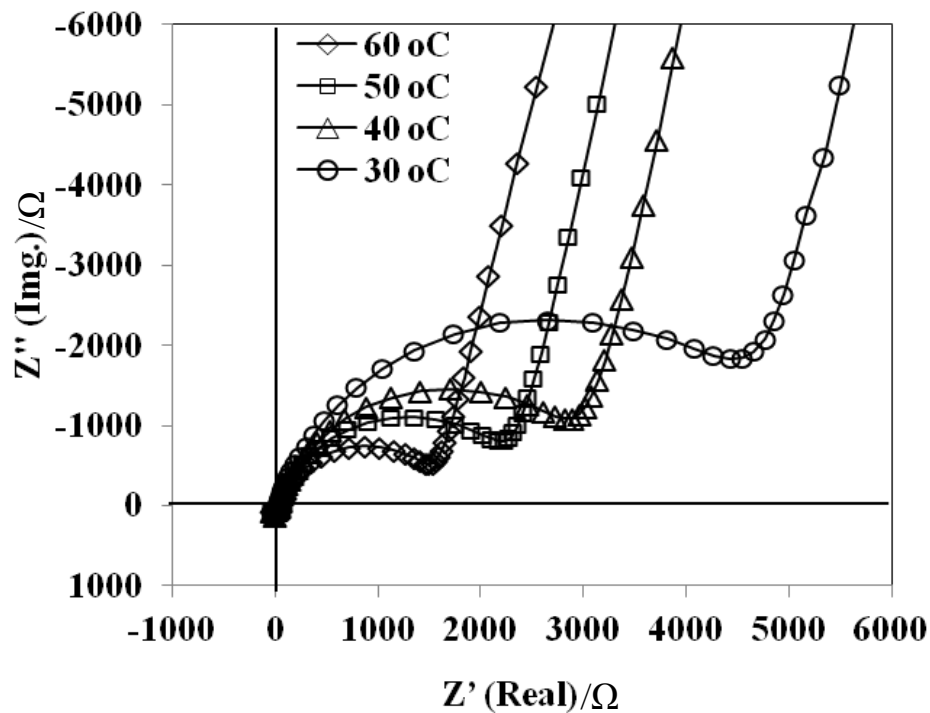


Figure 5.6: Nyquist impedance plot for 55 nm ultrathin Nafion® film at 80% RH and different temperature.

Impedance responses for thin films of various thicknesses: Impedance responses of the thin films with different thicknesses ranging from 4 nm to 300 nm at 60% RH and 60 °C have been presented in Figure 5.7. From the impedance responses, it can be noted that the semicircle diameter decreased with increasing thickness. Variation in the shape of the semicircle can also be noted. Interestingly, with decreasing thickness only partial semi-circle can be observed. Compare to the 55 nm and the 300 nm films, the impedance response of the 10 nm film appears distorted. An incomplete semicircle type response was observed for the 4 nm film. The reason of this distorted/incomplete semi-circle response has been discussed later in the section 5.3.3.

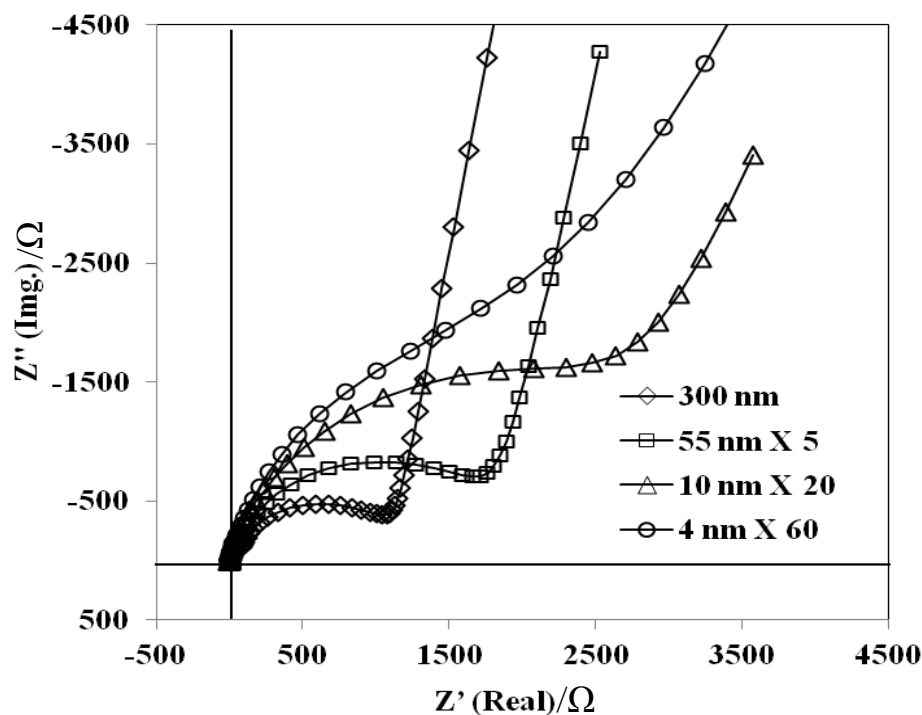


Figure 5.7: Nyquist impedance plots for ultrathin Nafion® film varying thicknesses at 60% RH and 60 °C. The data for 55, 10 and 4 nm film have been reduced 5, 20 and 60 times respectively to fit into the scale.

Impedance responses in different chemical atmosphere: Electrode reactions are expected to occur during ac impedance measurements since proton conduction in the film must be accompanied with the measured external electronic current. The key question is whether the high-frequency semicircle contains any significant contribution from the interfacial or charge transfer reaction, for example arising from oxygen reduction reaction. Impedance measurements in the absence of oxygen were carried out to investigate if electrode reactions contributed significantly to the high-frequency semi-circle response. In this case, a small closed chamber with gas inlet and outlet was used rather big environmental chamber. An oxygen sensor along with a RH sensor was placed inside the chamber and the electrode was connected to the impedance measurement set up.

A manual humidity controlling system – passing gas through the water, at room temperature was adopted for this measurement. First, air was bubbled through the water and allowed to pass into the chamber. The flow rate was maintained in such a way that 70% RH at room temperature (25 °C) was maintained. When the external and internal equilibration of the film was established as monitored by the single frequency impedance measurement protocol, impedance data was collected and termed as the impedance response at O₂ atmosphere. For the impedance measurement in N₂ atmosphere, air was replaced by N₂ gas and passed through the water for half an hour to degas the dissolved oxygen, then the N₂ gas flow through the small chamber. Again the flow was controlled to obtain 70% RH at room temperature. It was confirmed that N₂ has replaced all the O₂ in the chamber as monitored by the oxygen sensor. After equilibration, impedance data was collected – termed as the impedance response at N₂ atmosphere. Similarly, 5% H₂ with argon gas was used for generating 70% RH and oxygen free atmosphere and impedance data was collected – termed as the impedance response at H₂ atmosphere.

The comparative impedance responses for 55 nm film collected in O₂, N₂ and H₂ atmospheres have been presented in the Figure 5.8. Interestingly, almost identical semicircle responses were observed and the semicircle shape was unhindered even at highly inert N₂ atmosphere. It indicates that the impedance response is not generated due to an interfacial oxygen reduction reaction rather attributed due to the film resistance.

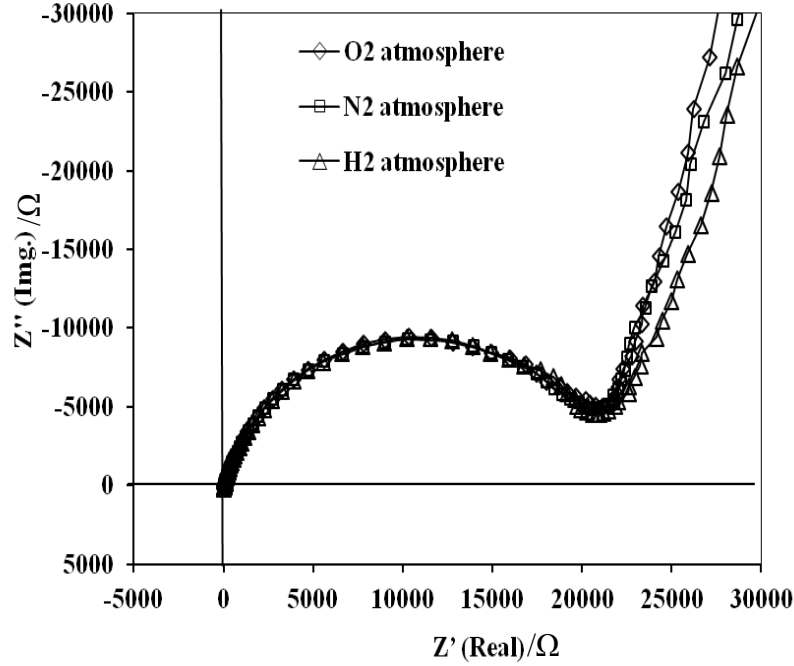


Figure 5.8: Nyquist impedance plots for 55 nm ultrathin Nafion® film at 25 °C and 70% RH varying local measurement atmosphere of the film.

5.3.2 Equivalent circuit design

To design an appropriate equivalent circuit, it is important to identify the key physical processes of the electrode/film system and represent it with a suitable electrical circuit element. An idealized circuit model has been proposed considering all the possible contributions from the thin film, the cell and the cell connectors in the Figure 5.9a. Each interface between thin film and electrode has been represented by a parallel combination of capacitance (C_{int-1}) - corresponds to the double layer capacitance, and an interfacial resistance (R_{int-1}). Primarily, it is assumed that Nafion® thin film has a film resistance (R_f) in parallel to a film capacitance (C_f). The cell contribution is the combination of the capacitance of electrode/SiO₂ interface (C_{int-2}) and a parallel connection of SiO₂ resistance (R_{SiO_2}) and SiO₂ capacitance (C_{SiO_2}). Beside the film and

cell resistance, there is a serial resistance (R_s) - originating partly from the contact between electrode and probe and partly from the wire resistance, and an inductance (not included in the equivalent circuit) – originating from the long wire connection.

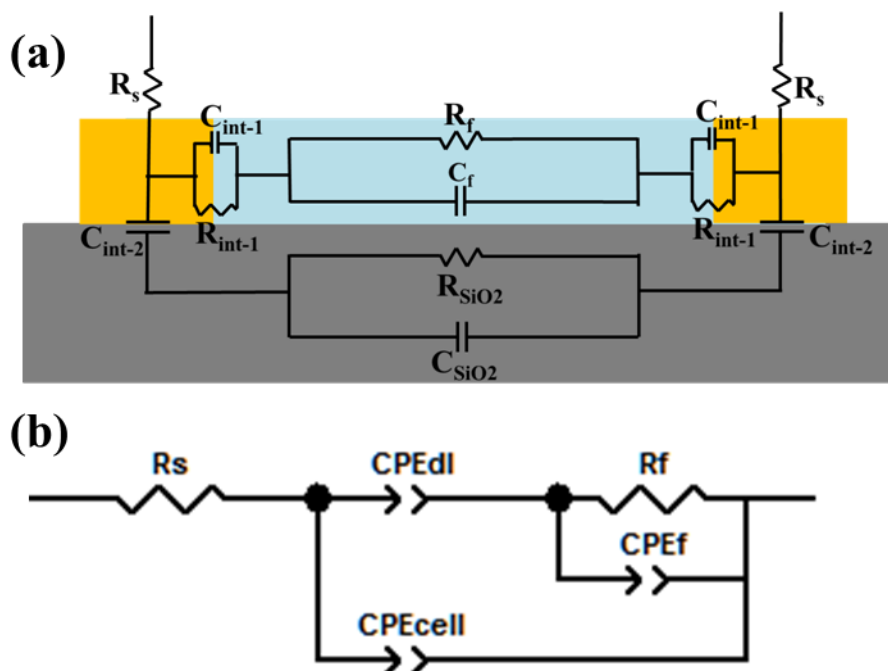


Figure 5.9: Equivalent circuit model – (a) possible impedance and capacitance components in the Nafion® thin film on SiO_2 supported IDA gold electrode. Gray color, yellow color and sky color represent SiO_2 , Au and Nafion® thin film respectively, (b) simplified equivalent circuit.

A simplification of the equivalent circuit with the adequate representation of the real system can be made. For the system under test, the electrode/film interfacial resistance can be omitted since negligible, if any, effect of interfacial reaction was observed at higher frequency. Since faradaic charge does not cross the interface, the interfacial response should be solely capacitive – defined as a double layer capacitance. On the other hand, the impedance measurement of blank electrode also shows that the response is highly capacitive at least in the

frequency range 10 MHz to 0.01Hz. A significantly high resistance of SiO₂ might be involved but did not appear in the frequency range of measurement. Therefore, R_{SiO₂} was omitted and combined the electrode/SiO₂ interfacial and SiO₂ capacitance as cell capacitance.

An ideal capacitor response would identify as a vertical line in the Nyquist plot – Z' (real) vs Z'' (Img.). Moreover, when the ideal capacitance is involved in the parallel combination with the resistance, a semicircle with definite radius is originated. However, from a close observation of the typical impedance response, it was found that the semicircle was suppressed and the lower frequency response deviates from the ideal (the vertical line) response. Generally, it has been recognized that the capacitance of solid electrolyte deviate from the ideal behavior due the inhomogeneity or surface roughness of the two parallel plates of the capacitor. It indicates that the capacitance involve in the semicircle and in the straight line are not pure capacitance rather it is better described by a constant phase element (CPE). CPE is a capacitor but represents the deviation by a power exponent (*n*) as below.

$$CPE = \frac{1}{(j\omega C)^n} \quad (5.3)$$

where, ω ($=2\pi f$) is the angular frequency and *n* is the exponent which value varies from 0 to 1. CPE depends on both ω and $0 < n < 1$ where CPE converts into pure capacitor when $n=1$. Based on the above observation and discussion the capacitance contribution of cell, film and double layer have been replaced in the simplified equivalent circuit as the constant phase elements – CPE_{cell}, CPE_f and CPE_{dl} respectively. However, the origin and existence of CPE_{cell}, and CPE_f in the the impedance response are still under debate. Soboleva *et al.* [78] and Yadav *et al.* [80] have indicated that Nafion® membrane has a capacitance in parallel to the resistance. The origin of capacitance has been described as the polarization of water inside the nanopore and the close

proximity of the sulfonate group. In contrast, Mikhailenko *et al.* [154] and Lee *et al.* [169] found that the capacitance associated with the semicircle of the typical response is due to the cell capacitance. In this study, part of the interest was to investigate the capacitance behavior of the thin films. Therefore, it is important to understand whether both capacitances are significantly contributing to the impedance response or one of the capacitance is dominating over another. In other word, whether there is an existence of both capacitances in the semicircle of the impedance response.

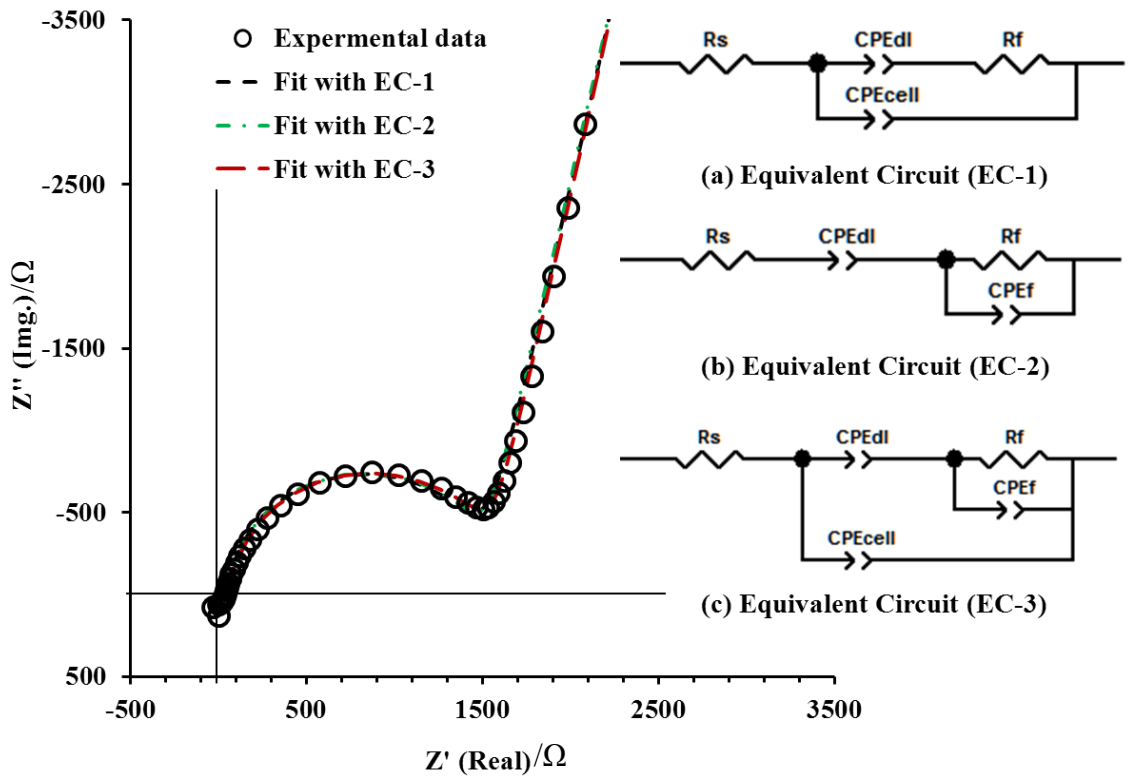


Figure 5.10: Typical impedance plot of ultra-thin Nafion® film and the fitting with three different equivalent circuits - (a) EC-1 (b) EC-2 and (c) EC-3 (inset)

To resolve the aforementioned issues, three equivalent circuits (ECs) were built up (i) EC-1, $[R-CPE_{cell}]$ (ii) EC-2, $[R-CPE_f]$ and (iii) EC-3, $[R-CPE_f-CPE_{cell}]$. The equivalent circuits

were fitted with the typical impedance response and the values of the components have been summarized in Table 5.1. Interestingly, it was found that all of the three ECs were fitted nicely and could not be distinguished among the fitting qualities. The fitting results of the EC-1 and EC-2 were comparable. Very similar CPE parameters were obtained though it was attributed due to cell and film contribution of the the EC-1 and the EC-2 respectively. In contrast, the film resistance by the EC-1 was 5% higher than that of the EC-2. When data was fitted with the EC-3, it was found that CPE_{cell} negligibly small whereas CPE_{film} and R_f are highly comparable to the EC-2. Apparently, it gave the impression that more simplified equivalent circuit EC-2 has a greater representation to the real system. However, more investigation is needed to claim the capacitance solely as the film capacitance. It is noted that regardless of ECs discussed above, the fitting parameters are comparable.

Table 5.1: Summarized equivalent circuit fitting parameters with three equivalent circuit considerations.

| Equivalent circuit (EC) | EC-1 (only CPE_{cell}) | EC-2 (only CPE_{film}) | EC-3 (both CPE_{film} and CPE_{cell}) |
|----------------------------|------------------------------|------------------------------|---|
| R_s | 57.76 | 57.10 | 60.17 |
| R_{film} | 1500 | 1410 | 1411 |
| CPE_{dl-T} | 2.58×10^{-07} | 2.60×10^{-07} | 2.54×10^{-07} |
| CPE_{dl-P} | 0.87 | 0.87 | 0.87 |
| CPE_{film-T} | - | 2.65×10^{-09} | 2.78×10^{-09} |
| CPE_{film-P} | - | 0.97 | 0.97 |
| CPE_{cell-T} | 2.43×10^{-09} | - | 6.3×10^{-19} |
| CPE_{cell-P} | 0.98 | - | 2.33 |

Model fitting results gave the understanding of the contribution of each equivalent circuit components to the impedance plot. However, it should be validated based on the experimental evidences. In the high-frequency region, impedance crosses the x-axis and goes to the positive values of imaginary impedance, which is due to the inductance. The x-intercept is due to the contact/series resistance R_s . The inductance and R_s contributions were confirmed by the impedance measurement of the shorted cell and found that the inductive and resistive response to be same as that obtained from the impedance from the cell with Nafion® thin film. The diameter of semicircle at high frequency region is the representation of the film resistance, which has been previously validated as only semicircle response changes with RH and temperature (section 5.3.1). The associated capacitance has been considered as the film capacitance – which will be further discussed in the later section 5.3.4 of this chapter. The straight line as low-frequency is solely capacitive which is attributed to the double layer capacitance. The appearance of the double layer capacitance in the low frequency has been discussed elsewhere [78-80,169].

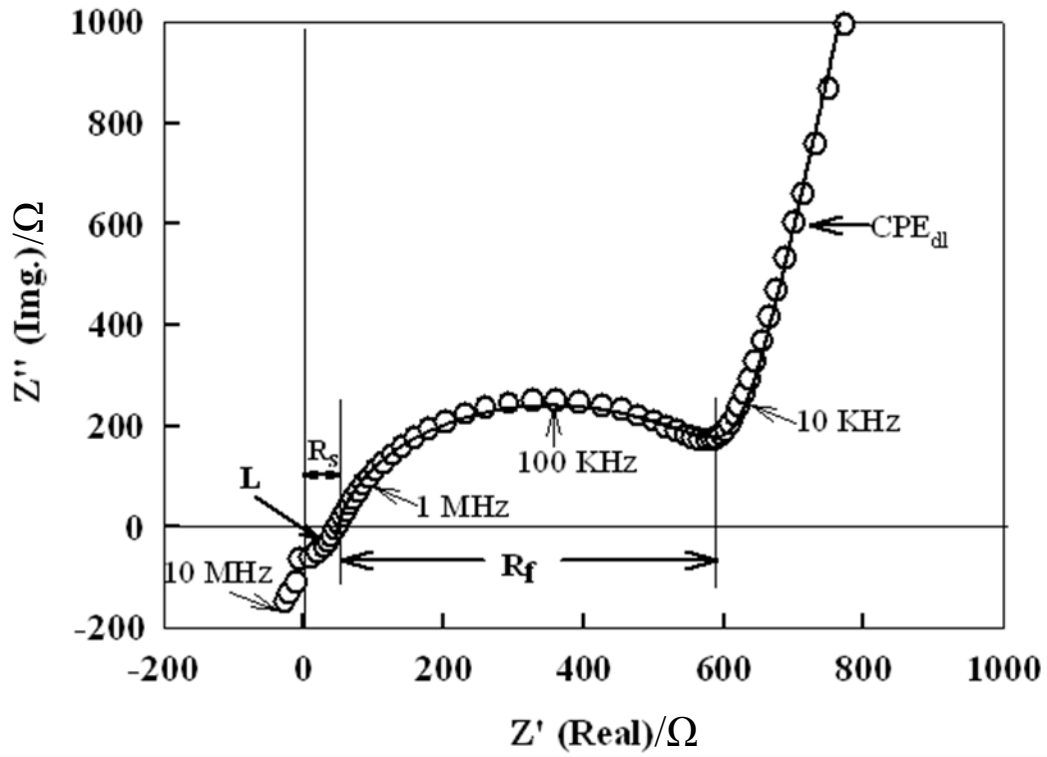


Figure 5.11: Nyquist plot for self-assembled Nafion® thin film at 60 °C and 96% RH. Experimental data (open circle) and fitted data with EC-2 (solid line)

The film conductivity (κ_f) was calculated from the fitted resistance (R_f) obtained from impedance measurements using equation 5.4, where, d is the space between the IDA electrodes (100 μm), t is the thickness of the film, l is the length of the teeth (0.8 cm) and N is the number of electrodes (110).

$$k_f = \frac{1}{R_f} \cdot \frac{d}{l(N-1)t} \quad (5.4)$$

5.3.3 Impedance response and data fitting

The shape of the typical semicircle impedance response can be varied with the thickness as described in the earlier section. In this section, the possible reasons of incomplete semicircle type of response based on impedance simulation are investigated. In this approach, EC-2 can be expressed as the following equation

$$Z(\omega) = R_s + \frac{1}{(i\omega C_{dl})^{n_{dl}}} + \left[\frac{1}{R_f} + (i\omega C_f)^{n_f} \right]^{-1} \quad (5.5)$$

where, $C_{dl}=CPE-T_{dl}$, $n_{dl}=CPE-P_{dl}$, $C_f=CPE-T_f$, $n_f=CPE-P_f$ have been used for the simplification. Considering the fitting parameters of the previous semicircle, the impedance plot as same as the experimental impedance plot was simulated by using Zview software. In the model fitting results for 55 nm film in Table 5.2, double layer capacitance, $CPE-T_{dl}$ is two orders of magnitude higher than film capacitance, $CPE-T_f$. It was assumed that the incomplete semicircle response might be due to the variation of the capacitance involved in the impedance plot. Therefore, varying $CPE-T_{dl}$ but keeping the other circuit elements constant, the impedance response was simulated. When the differences between $CPE-T_{dl}$ and $CPE-T_f$ became bigger by another one order of magnitude increasing $CPE-T_{dl}=2.6 \times 10^{-06}$, a more complete semicircle was obtained. With further increment of $CPE-T_{dl}=2.6 \times 10^{-04}$, a complete semicircle was formed. In contrast, when the difference between $CPE-T_{dl}$ and $CPE-T_f$ decreased in only one order of magnitude at $CPE-T_{dl}=2.6 \times 10^{-08}$, the semicircle became incomplete. The impedance response goes straight up without completing the semicircle. Remember, this type of response was observed for the 4 nm film. At $CPE-T_{dl}=2.6 \times 10^{-08}$, $CPE-T_{dl}$ and $CPE-T_f$ became almost similar where no semicircle can be noted rather a barely capacitive response was observed. It indicates that the shape of the impedance response can be determined by either of the capacitance values where at least two order of magnitude differences should be maintained to achieve apparently, a semicircle type response.

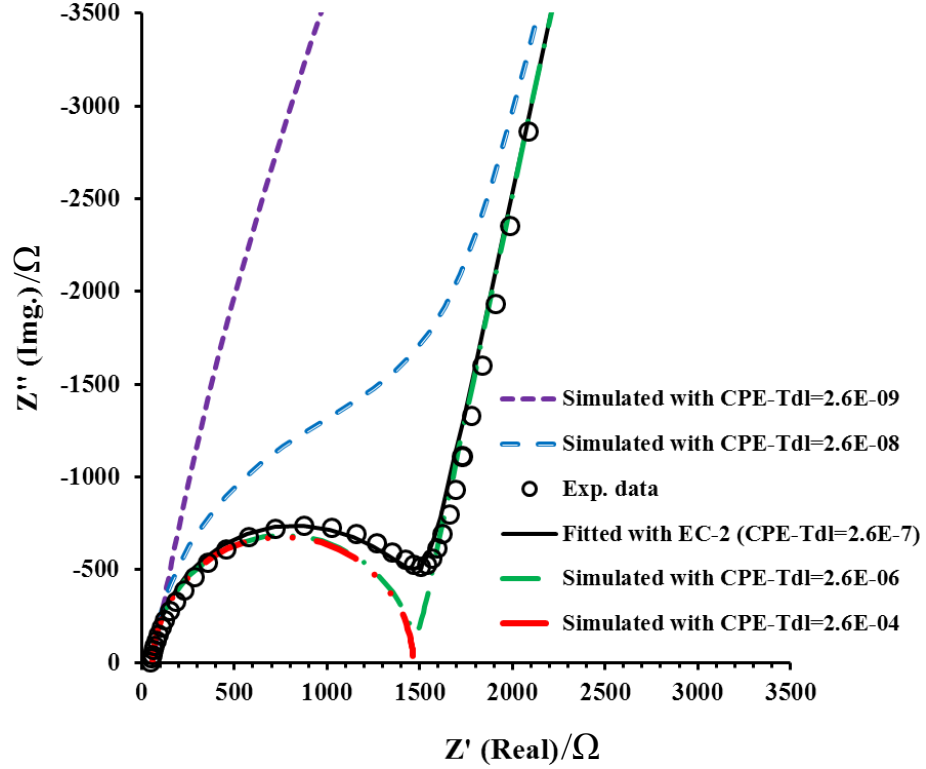


Figure 5.12: Nyquist plots – experimental data of 55 nm film (open circle), data fitting with EC-2 (solid black line) and simulated data according the EC equation 5.5.

To investigate more into the shape of the impedance response, data for the 4 nm film was fitted with EC-2 ($R\text{-}CPE_f$) as shown in Figure 5.13. It was found that the incomplete semicircle type response was attributed due to the less difference between CPE-T_{dl} and CPE-T_f as presented in Table 5.2. However, when the impedance was simulated with the same parameters except CPE-T_{dl} which was considered exactly two order of magnitude different than $\text{CPE-T}_f = 1.59 \times 10^{-09}$, the semicircle type response was obtained. Additionally, a complete semicircle response was obtained when a sufficiently high difference between capacitances was considered.

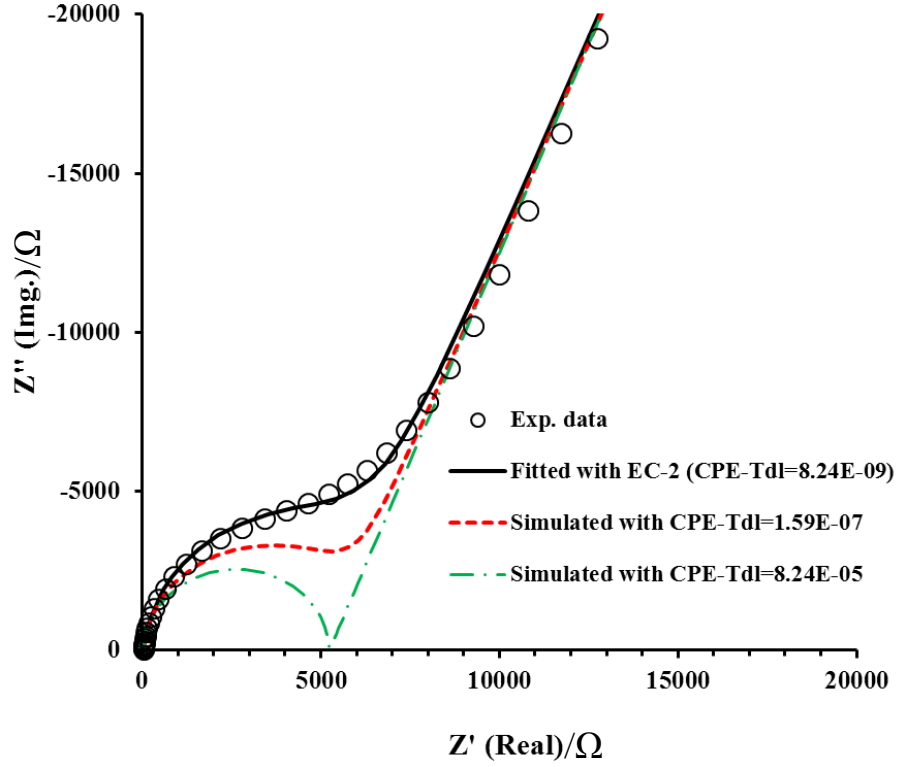


Figure 5.13: Nyquist plots – experimental data of the 4 nm film (open circle), data fitting with EC-2 (solid black line) and simulated data according the EC equation 5.5 (dotted red and green line).

Table 5.2: Summarized equivalent circuit fitting parameters with EC-2 for the 4 and 55 nm films.

| | 55 nm film (at 80% RH) | 4 nm film (at 96% RH) |
|--------------------|------------------------|------------------------|
| R_s | 57.1 | 57.4 |
| $C_{dl}=CPE_{dl}T$ | 2.60×10^{-07} | 8.24×10^{-08} |
| $n_{dl}=CPE_{dl}P$ | 0.87 | 0.77 |
| R_f | 1410 | 5196 |
| $C_f=CPE_fT$ | 2.65×10^{-09} | 1.59×10^{-09} |
| $n_f=CPE_fP$ | 0.98 | 0.99 |

5.3.4 Capacitance behavior of the Nafion® thin films

In this section, the capacitance extracted from EC-2 in terms of three parameters - relative humidity, temperature and film thickness, are discussed. The main goal is to find out whether the capacitance has a dependency on those three parameters and essentially, find a conclusion about the origin of the capacitance. The capacitance can be calculated by the following formula

$$C_f = Q_o (\omega_{\max})^{n-1} \quad (5.6)$$

where, $Q_o = CPE_f T$, ω_{\max} = the frequency at semicircle maximum, $n = CPE_f P$. The capacitances of all the films have been calculated on IDA electrode with 100 μm gap in the interdigitated electrodes. The calculated capacitances have been normalized by the thicknesses (F/nm) that have been presented in terms of relative humidity in the Figure 5.14.

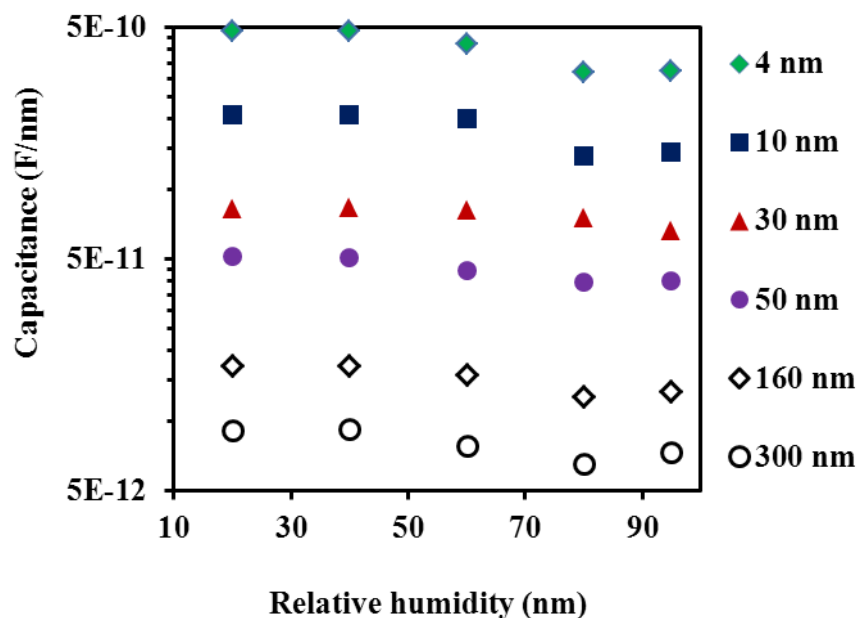


Figure 5.14: Capacitance of Nafion® thin films with different thicknesses as a function of relative humidity at 60 °C.

It was found that the capacitance decreased with increasing relative humidity for all of the thin films ranging 4-300 nm thicknesses. The decreasing capacitance with increasing RH is consistent with data reported for Nafion® 117 membrane [80]. The normalized capacitance also have been plotted in terms of thickness for different RH in the Figure 5.15. A exponential decay of capacitance (F/nm) was observed with increasing thickness. It indicates that the capacitances are highly thickness dependent.

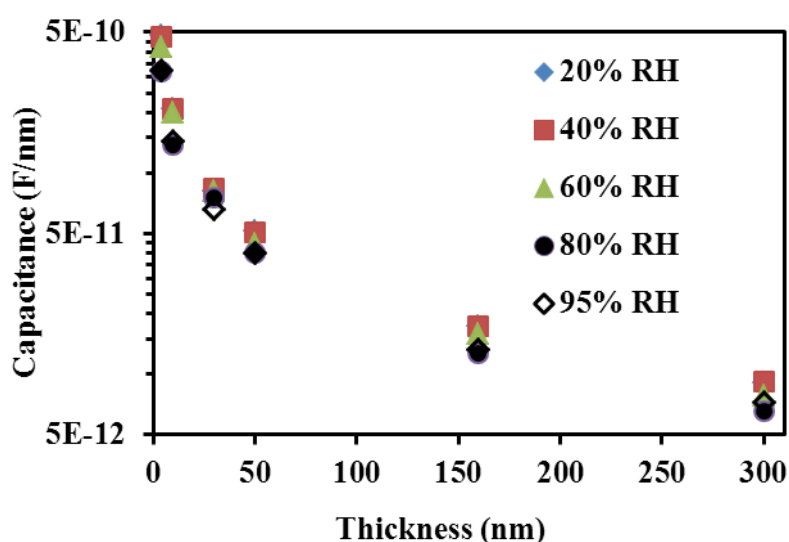


Figure 5.15: Capacitance of Nafion® thin films in terms of thickness at 20 to 96% RH and 60 °C.

Further, the capacitance was investigated in terms of thickness varying measurement temperature 30 to 60 °C as shown in Figure 5.16. It was found that the capacitance increased with increasing temperature. Moreover, similar exponential decay was observed for all the temperatures at both low and high relative humidity. The variation of capacitance with relative humidity and temperature support the film capacitance behaviour rather the substrate or cell capacitance. It is further supported by the increment of capacitance with increasing thickness.

Usually, the capacitance increases linearly with increasing thickness or the normalized capacitance remains constant for the same materials. However, the capacitance response was nonlinear with thickness. On the other hand, the normalized capacitance decayed exponentially rather constant, which are indicative to the thickness dependent morphological differences among the thin films.

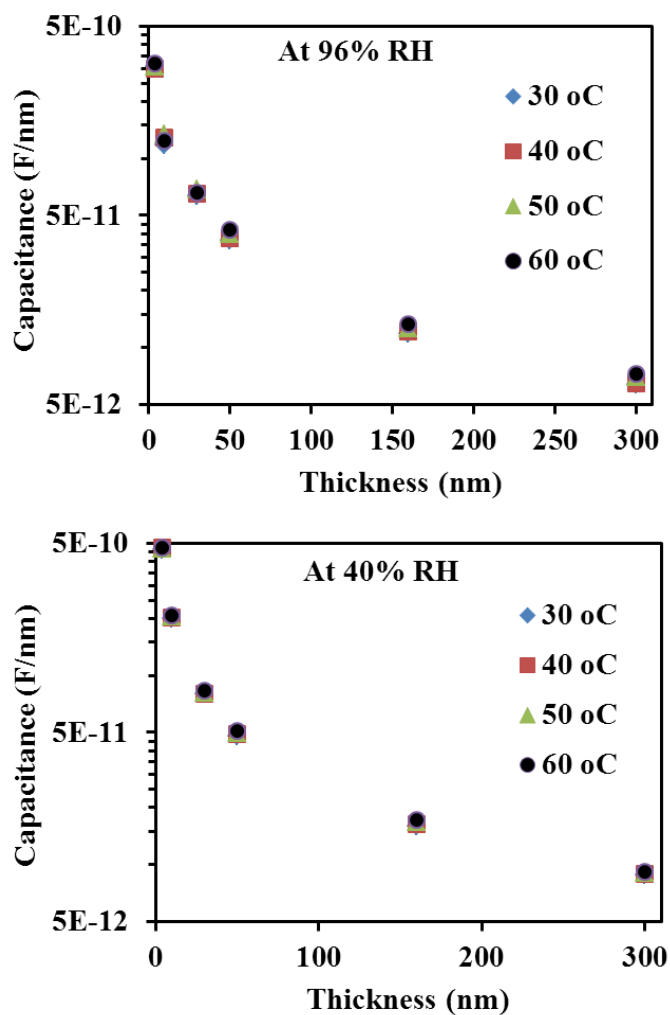


Figure 5.16: Normalized capacitance of the Nafion® thin films as a function of film thickness for various temperatures (30-60 °C) at 96% RH (Top) and 40% RH (Bottom).

5.3.5 Proton conductivity of the Nafion® thin films

In the experimental section of this chapter, two pre-treatment protocols of samples were described before the film conductivity measurement at two different temperatures (25 °C and 60 °C). In this section, we present the proton conductivity of the thin films in terms of two parameters – thin film thickness and relative humidity at two measurement temperatures. A comparison of the proton conductivities under two different treatment protocols is made to investigate whether the treatment protocol becomes a determining factor for the resulted proton conductivity of Nafion® thin films.

Proton conductivity at room temperature (25 °C): Proton conductivities of the Nafion® thin films with thickness ranging from 4 nm to 300 nm have been presented in terms of relative humidity at 25 °C in the Figure 5.17. The proton conductivities of Nafion® 117 [14] have also been plotted in the Figure 5.17 for the comparison between the thin film and the membrane conductivities. As expected, proton conductivity of the thin films increased with increasing relative humidity. Regardless of the thickness, the logarithm of the proton conductivity of the thin film could be expressed as a linear function of relative humidity over two different ranges of humidity. The slope in the 20-40% RH range was higher than that in the 40-95% RH range. The proton conductivity increased rapidly from dry condition to 40% RH but at a much slower rate at a higher RH. Similar behavior of proton conduction with RH has also been observed for the Nafion® membrane [69]. The water uptake in the thin Nafion® film measured by quartz crystal microbalance (QCM) is presented later in the section 5.3.10.

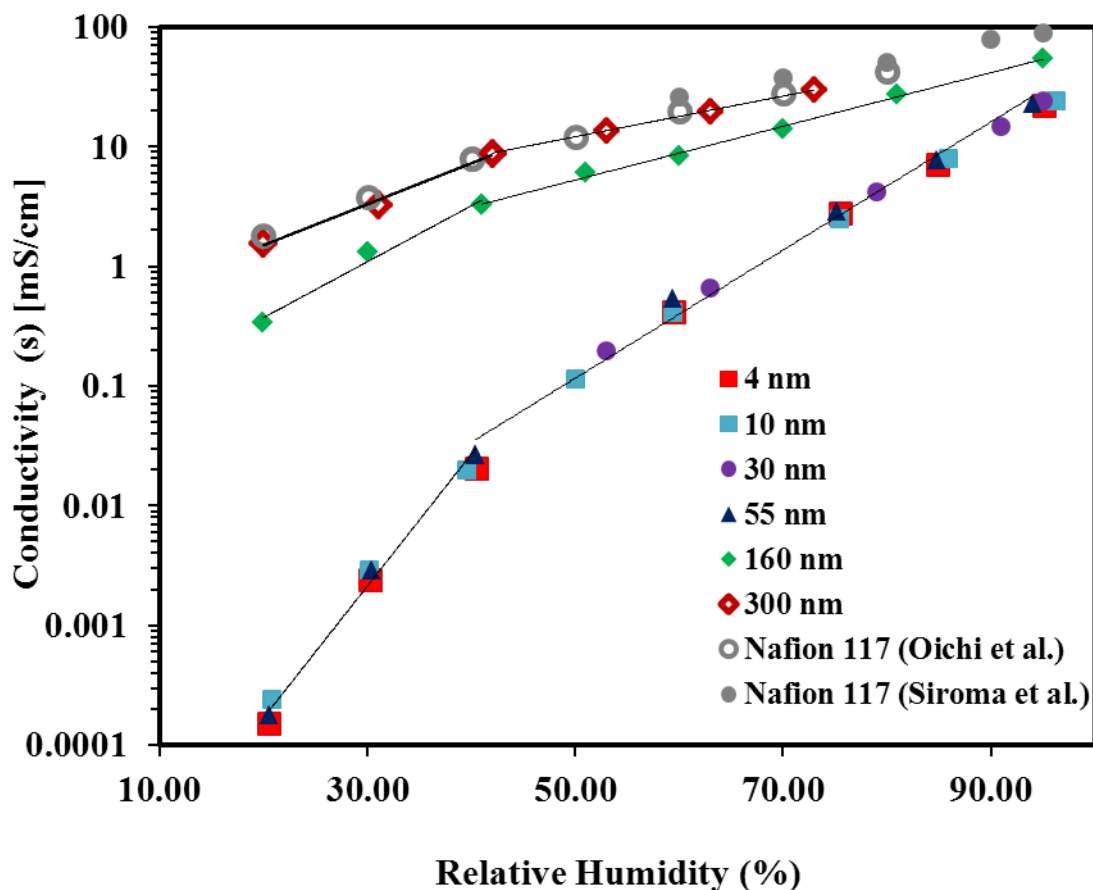


Figure 5.17: Proton conductivity of the Nafion® thin films varying thicknesses 4 to 300 nm at 25 °C as a function of RH

It is interesting to note that the proton conductivity of ultra-thin films (4 to 55 nm films), were very comparable to each other. In contrast, the conductivity of thicker films (160 nm and 300 nm films) varied with thickness whereas the 300 nm film had conductivity closer to that of Nafion® membrane [78-80]. Therefore, the proton conductivity of the ultrathin films is significantly lower than that of the thicker films as well as that of the Nafion® membrane. The differences in proton conductivity are more significant at lower RH.

To understand the RH and thickness effect, the proton conductivity data has been plotted as a function of thickness at low (40%) and high (95%) RH in Figure 5.18. At low RH, there was

a non-significant dependency of the proton conductivity on thickness up to 55 nm whereas it was about two orders of magnitude higher in thicker films. At high RH, similar independence of proton conductivity to thickness for films up to 55 nm was observed. However, the difference in proton conductivity of the ultrathin films and the thicker films reduced to about 2.5 times rather about 2 orders of magnitude as observed at low RH. In the earlier chapter (chapter 4), two distinct behavior for the thin film surface properties – films up to 55 nm thickness are hydrophilic whereas films with greater than 55 nm thickness are hydrophobic, were found. Interestingly, this bulk conduction property of the film directly correlates with the surface properties. However, more investigation is necessary to explain this particular interesting behavior.

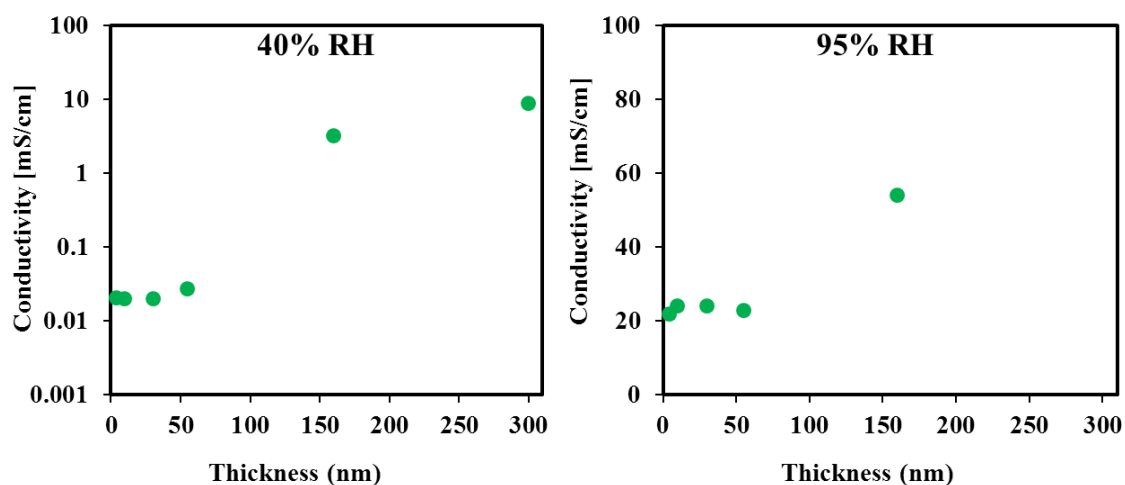


Figure 5.18: Proton conductivity of the Nafion® thin films as a function of film thickness at 25 °C.

Proton conductivity at higher temperature (60 °C): Proton conductivities of the Nafion® thin films of different thicknesses ranging from 4 to 300 nm as a function of relative humidity at 60 °C have been presented in the Figure 5.19. The equilibration of film at 60 °C was ensured according the pretreatment Protocol-2. Similar to data at 25 °C, the logarithm of conductivity shows linear behavior with respect to humidity with two different slopes over low

and high RH range. Unlike the low temperature data, the similarity in conductivity of lower thickness films becomes less obvious. Conductivity of all films maintained similar trend with RH and a thickness dependent conductivity was observed for the range of films (4-300nm). Similar behavior was reported by Siroma *et al.* [14]. This indicates that the film treatment has a significant role in proton conduction behavior. Overall, the high temperature (at 60 °C) proton conductivity was higher than the low temperature (at 25 °C) conductivity at high RH region, conversely, an inconsistency was noticed at low RH region.

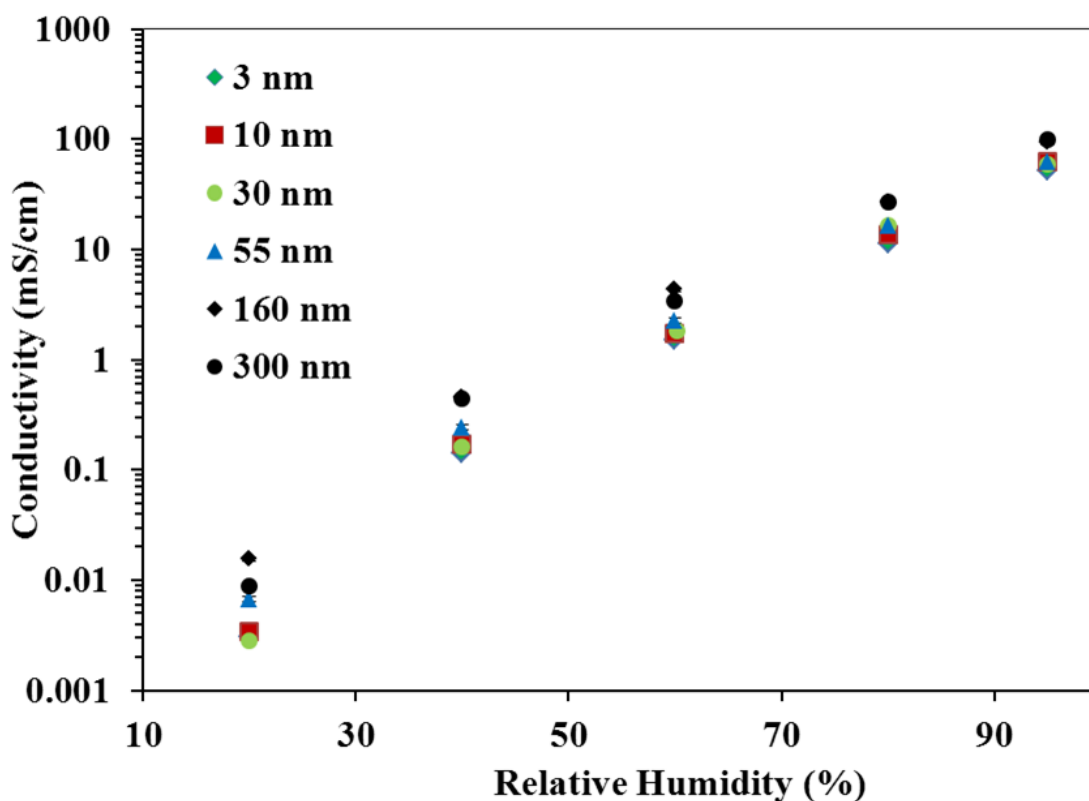


Figure 5.19: Proton conductivity of the Nafion® thin films with different film thickness in terms of relative humidity ranging 20 to 96% RH at 60 °C.

To investigate the thickness effect on the thin film proton conductivity at 60 °C, the proton conductivity data was plotted in terms of thickness at low (40%) and high (95%) RH in

Figure 5.20. At low RH, clear thickness-dependent proton conductivity was observed with increasing conductivity noted for increasing thickness. The conductivity difference between the lowest (4 nm) and the highest (300 nm) thickness film is two times at 60°C as opposed to two orders of magnitude for that at 25 °C. On the other hand, at 95% RH, similar thickness dependent conductivity was observed. The proton conductivity for the 300 nm film is ~100 mS/cm which is almost double that of the 4 nm film (~55 mS/cm). Unlike low temperature measurement, the proton conductivity variation between ultrathin and thicker films is not as significant. The difference in thickness-dependent conductivity at low and higher temperatures may be attributed due to two possible reasons – (i) film/substrate interfacial or un-equilibrated excess water (ii) internal structure changes upon heating to 60 °C. However, further insight may be gained by investigating the film conductivity at 25 °C without and with (before and after) 60 °C temperature treatment.

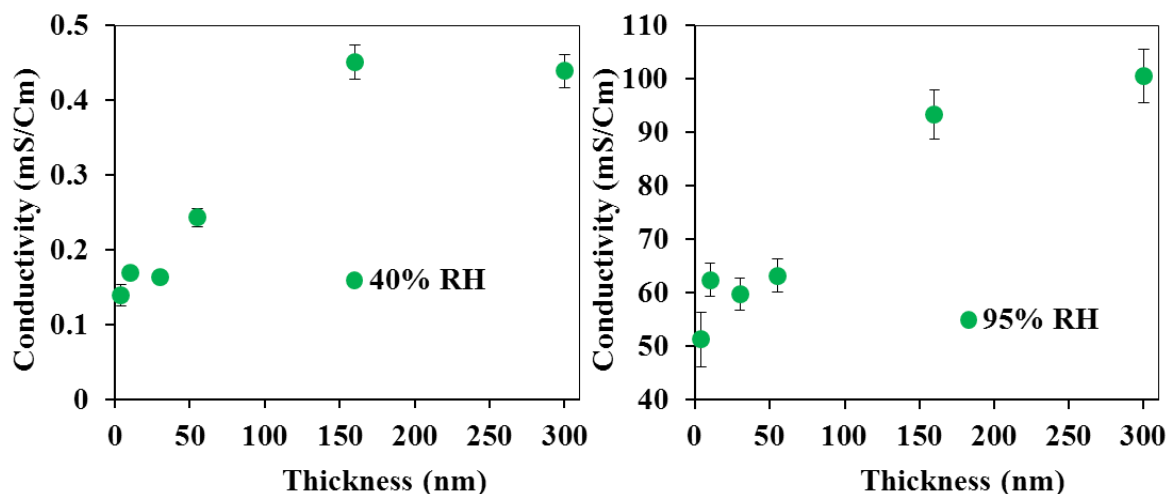


Figure 5.20: Proton conductivity in terms of film thickness at 60 °C for both low – 40 %, RH and high – 95 %, RH.

Film conductivity measured at room temperature (25 °C) without any high temperature treatment has been termed as un-treated film. On the other hand, film conductivity at the same

temperature after 60 °C treatment (after equilibration and impedance measurement at 60 °C) has been termed as treated film. The proton conductivity at 25 °C of both treated and un-treated films has been compared in the Figure 5.21. To deal with both interfacial or excess water and structural change issues, a prior understanding is required. In practice, the water is trapped and tightly bound in the film/substrate interface or confined in the ionic pore structure. An equilibration with the external atmosphere might be established without proper equilibration of those trapped or tightly bound water of the film especially at low RH and low temperature. In contrast, the water content of the films might not come back to the same level at the same low RH and temperature once complete removal of those trapped or tightly bound water at high temperature treatment. The difference in water content before and after heat treatment is defined as interfacial or non-equilibrated excess water. It is assumed that the interfacial water or non-equilibrated excess water in the film might contribute to the significant increment of the proton conductivity in the low RH measurement. At high RH, the change might be non-significant as the film reaches to the highest saturation point. In contrast, structural rearrangement might impact on the overall proportional change in proton conductivity regardless relative humidity. For the 10 nm film, it was observed that the proton conductivity of the treated film had an overall 5% reduction than that of the un-treated film. It indicates that a little structural rearrangement is outweighed than the interfacial or excess water effect. For the 160 nm film, the overall proton conductivity of treated film was lower than that of un-treated film where the difference became more significant with decreasing RH. The conductivity of treated film at 95% RH reduced ~30% than that of un-treated counterpart, however, reduced few order of magnitude at low RH. The observation suggests that before 60 °C treatment, there might have non-equilibrated excess water which attributed higher proton conductivity at low RH. At the same time, equilibration at 60 °C might be responsible for the structural rearrangement in such a way which impede water uptake. If the

hypothesis makes sense, there is lower rearrangement of the 10 nm film (in general, ultra-thin films) upon treatment and negligible non equilibrated water than that of the thicker, 160 nm film.

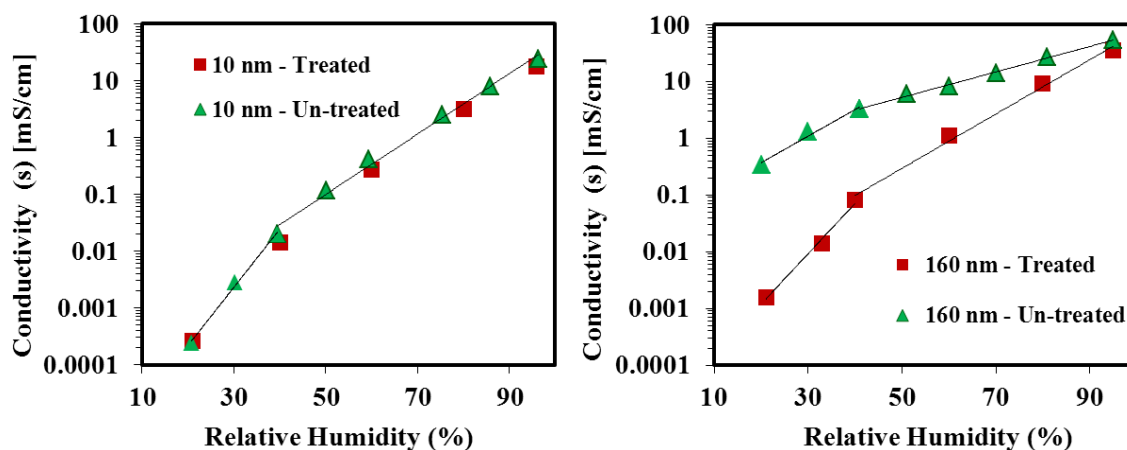


Figure 5.21: Comparative proton conductivity at 25 °C in between treated and un-treated films, for (a) the 10 nm film and (b) the 160 nm film.

It can be summarized that the proton conductivity of ultra-thin film is lower than that of membrane. The difference becomes more prominent with decreasing RH. A distinct behavior of proton conductivity –the films up to 55 nm have similar but lower than the membrane conductivity, and the thicker films tend to reach membrane like conductivity, at room temperature. The distinct features of bulk proton transport property highly correlate with the two distinct surface wettabilities as discussed in Chapter 4. In contrast, the films treated and measured the conductivity at 60 °C are highly thickness dependent where the conductivity increases with increasing thickness. High temperature treatment might be equally responsible for the removal of non-equilibrated water and structural rearrangement of the films. Therefore, the film pretreatment and equilibration history are very important to report film proton conductivity

5.3.6 Aging effect on the proton conductivity of Nafion® thin film.

To investigate the long-term aging effect, the 160 nm film was aged for several months at room temperature in a petri dish after initial measurement. The film was dried and sealed in the petri dish after each measurement at ambient condition (~40% RH and 25 °C). Therefore, the relative humidity and the temperature were grossly maintained close to the ambient conditions. The impedance was measured at 60 °C over a range of RH (20 to 95%) and over a 12 months period. The conductivity measurement soon after the film was prepared has been defined to that at zero month. The conductivity at 0, 8 and 12 months exhibited similar trend with RH but decreased with the aging time. At high RH of 95%, the conductivity loss was ~ 30% and ~60% after the 8 month and 12 month period of ageing, respectively (Figure 5.22). At low RH, the conductivity loss after first 8 month is significant but lesser over the next 4 month. The reason for loss in conductivity is not obvious and outside the scope of this work.

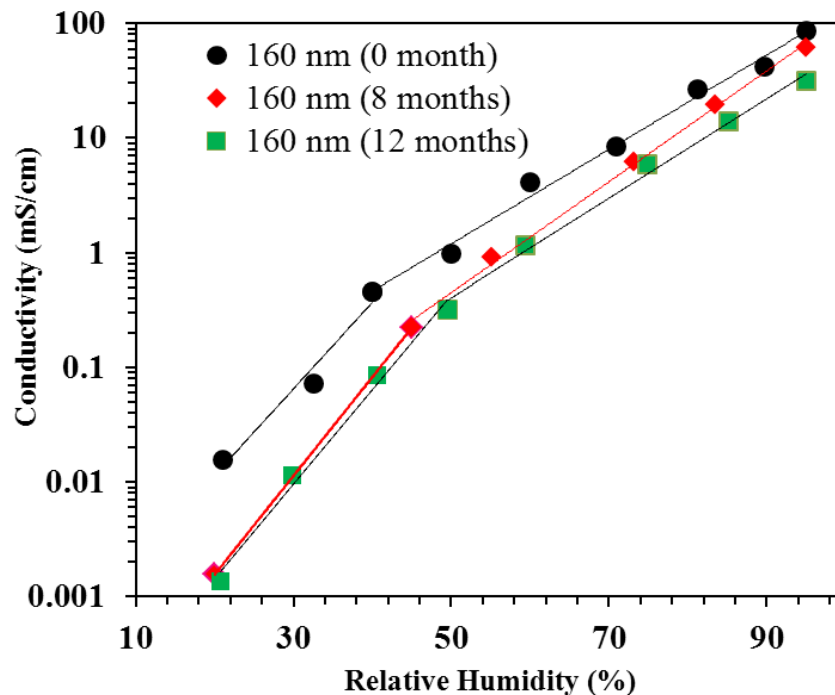


Figure 5.22: Proton conductivity of the 160 nm Nafion® thin film in terms of relative humidity at 60 °C symbolized as (●) 0 months, (◊) 8 months and (■) 12 months.

5.3.7 Effect of inter electrode gap on the proton conductivity of the thin films

So far, the proton conductivity of the Nafion® thin films was investigated adopting the Au IDA electrode with the inter-teeth distance 100 μm . At this point, a vital question needs to be answered, whether the proton conductivity of film varied if the inter-teeth distance of Au IDA is less or more than 100 μm . To answer the question, two more IDAs – (i) 30 μm gap and 110 teeth and (ii) 500 μm gap and 24 teeth were adopted for the investigation of 10 nm film conductivity. The film preparation and measurement protocol was as same as that for film prepared IDA electrodes with 100 μm gap. The proton conductivity of the 10 nm film on three different Au IDA electrodes at 60 °C and three different RH has been presented in the Figure 5.23. It was found that the proton conductivity of the 10 nm film on three IDAs was highly comparable and obtained

within 5 to 10% error. Therefore, the difference was acceptable as the results showed up in the sample-to-sample error range.

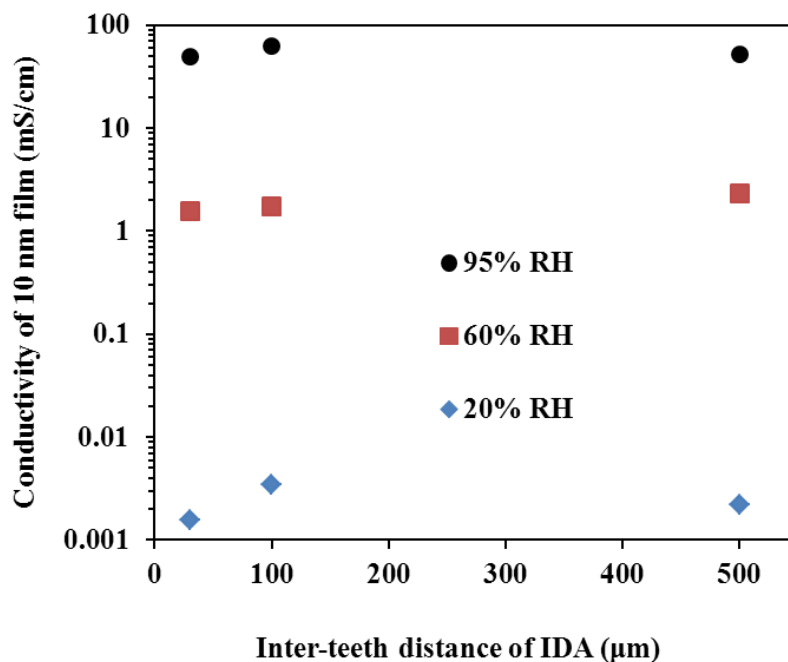


Figure 5.23: Proton conductivity of the 10 nm film in terms of inter-teeth distance of IDA electrode at 60 °C and three different RH conditions.

The capacitance for the 10 nm film was also investigated in terms of inter-teeth distance of IDA. The normalized capacitance has been plotted with inter-teeth distance in the Figure 5.24. It was found that the normalized capacitance increased with increasing the inter-teeth distances which fit into a straight line. The linear relationship supports the observed capacitance as film capacitance. However, it is difficult to rule out the cell capacitance contribution to the semicircle.

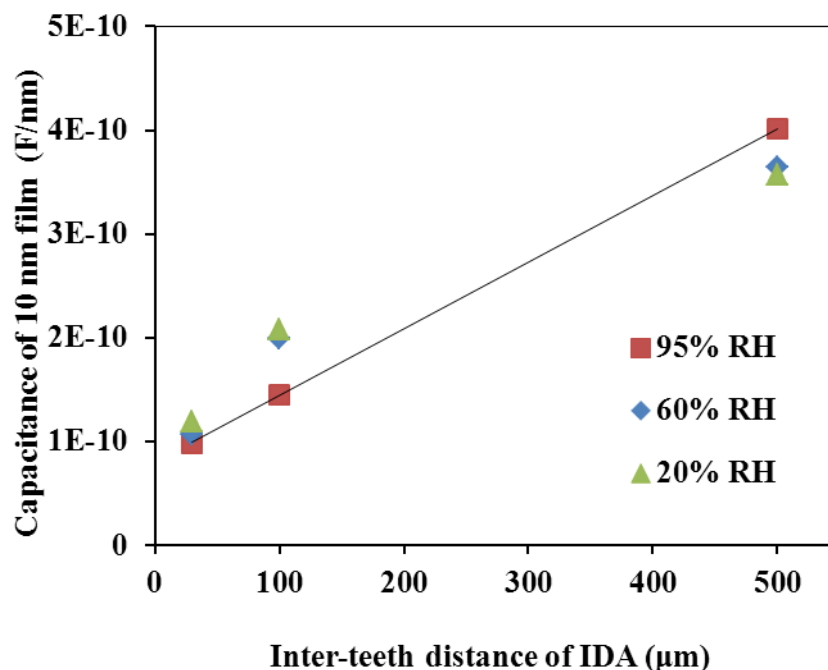


Figure 5.24: The normalized capacitance of the 10 nm film in terms of inter-teeth distance of IDA electrode at 60 °C and three different RH conditions.

5.3.8 Effect of electrode design and materials on the proton conductivity of the thin films

The impedance of the Nafion® thin films was investigated mostly based on IDA of Au electrode. However, there is another major question to be answered as a part of the confidence on the reported results. The question is whether the proton conductivity can be obtained reproducibly on IDA electrode with a different material and design. To answer the question, we adopted IDA of Pt electrode supported by same SiO₂ wafer. The description of electrode design and the comparative measurement results have been described below.

Interdigitated array of Pt electrode: Standard lithography procedures and electron beam evaporation were used to make platinum electrodes on a thermal oxide-coated silicon wafer as shown in Figure 5.25 below.

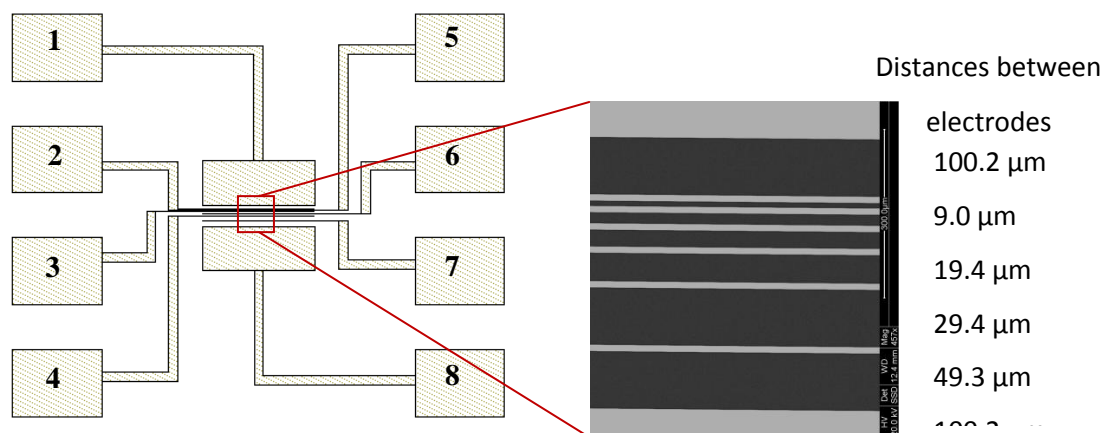


Figure 5.25: Image of Pt electrode design (left) and SEM image of center electrodes (right) and the corresponding distance between electrodes. Lighter color indicates platinum metal, darker color indicates silicon wafer in SEM image. [The electrode was designed and fabricated at the Penn State nanofabrication clean room facility by Stephanie Petrina from Dr. Mike Hickner group, Penn State University, USA].

- silicon oxide 93 nm thick (verified by spectroscopic ellipsometry)
- 4 contact pads on each side
- Probes extend from contact pads into the center
- Center probes $\sim 11 \mu\text{m}$ wide
- Spacings between electrodes vary from $10 \mu\text{m}$ – $100 \mu\text{m}$ (image on right)

The film preparation and the impedance measurement methods were same as the film on Au electrode. For Pt electrode, the probe connection was made in the pads 4 and 7 to maintain the

same gap between electrodes as adopted for Au electrode (100 μm). The comparative film conductivity of the 55 nm film on both Pt and Au electrodes has been presented in terms of RH in Figure 5.26. The proton connectivity of the film on Pt electrode varied 5 to 10% at high RH region where it was over estimated in the low RH region compare to the film on Au electrode. However, the film conductivity on Pt electrode was considered as same as the Au electrode as the difference fall into the sample-to-sample variation range. Therefore, it can be concluded that the variation in electrode design and electrode materials has no significant impact on the measurement results. Moreover, the proton conductivities and capacitances of the same film were measured varying inter electrode gap as shown in the Table 5.3. The proton conductivity was consistent as fall into the sample to sample variation range, As expected, the normalized capacitance increased with increasing inter electrode gap which is consistent with the film capacitance behavior.

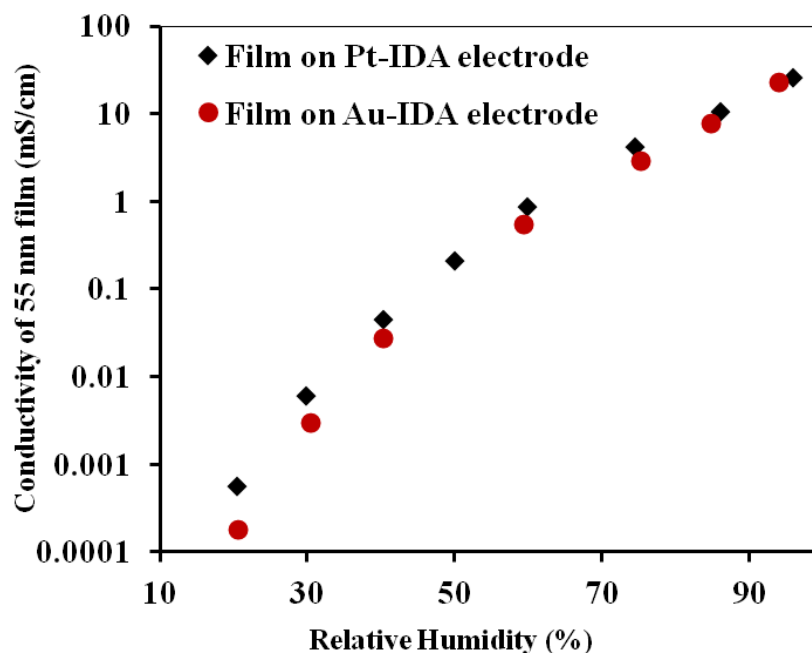


Figure 5.26: Proton conductivity of the 55 nm film measured on Pt and Au IDA electrode system at 25 °C in terms of relative humidity

Table 5.3: The conductivity and capacitance of the 55 nm film on Pt electrode at 95% RH and 25 °C in terms of inter electrode gap distance.

| Film thickness | Inter electrode gap | Conductivity | Capacitance |
|----------------|---------------------|--------------|------------------------|
| (nm) | (μm) | (mS/cm) | (F/nm) |
| 55 | 30 | 27.63 | 1.51×10^{-11} |
| | 50 | 23.52 | 1.54×10^{-11} |
| | 100 | 25.96 | 1.75×10^{-11} |

5.3.9 Activation energy of the proton conduction in Nafion® thin films.

Temperature dependent proton conductivity of the Nafion® thin films was investigated over a range of relative humidity. The main goal for collecting this set of data is to generate an Arrhenius plot and extract the activation energy. In this section, we discuss about the activation energy of proton conduction associated in Nafion® thin films. How activation energy varies in terms of two parameters – (i) relative humidity and (ii) thickness, is a part of the investigation. Another particular interest is to investigate whether the activation energy of the Nafion® thin films are different than that of its membrane counterpart.

The impedance of the Nafion® thin films (4-300 nm) was measured over a range of temperature from 30 to 60 °C and a range of relative humidity from 20 to 95%. Prior to the measurement, the protocol -2 of the film treatment was followed, i.e. the equilibration of the film first at 60 °C. Moreover, the impedance measurement at 20% RH at various temperatures in backward and forward directions (from 60 °C to 30 °C and then to 60 °C) were carried out. The reproducibility of the impedance response within ~2% measurement error at 20% RH and the

same temperature in both directions ensured the quality of data. Then all the impedance data was collected at a fixed RH at different temperatures ranging from 60 °C to 30 °C in the backward direction to avoid any non-equilibrated extra water influence or the effect of structural rearrangement in the conductivity. The temperature dependent proton connectivity at different RH was calculated for 4 to 300 nm films.

Arrhenius plots of conductivity (logarithm of conductivity vs 1/T) for the 10 and 160 nm films at different RH are shown in Figure 5.27. As can be noted, each plot was fitted by Arrhenius equation (as shown below) with excellent linearity. The slope of these plots yields the activation energy of the proton conductivity.

$$\text{Arrhenius equation: } \ln \sigma = \ln \sigma^o - \frac{E_a}{R} \cdot \frac{1}{T} \quad (5.7)$$

$$\text{Activation energy: } E_a = \text{Slope} \times R \quad (5.8)$$

where E_a is the activation energy, σ is the proton conductivity and R is the universal gas constant.

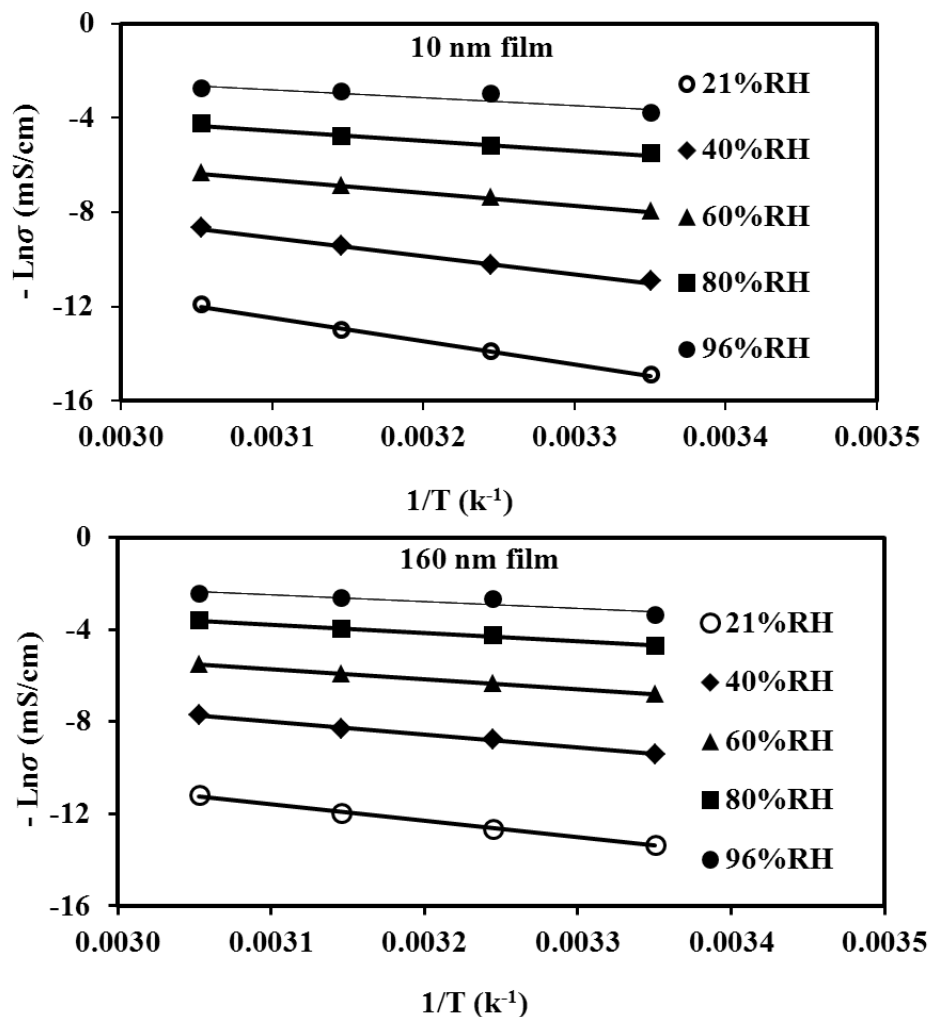


Figure 5.27: Arrhenius plots for conductivity of the 10 nm and the 160 nm Nafion® thin films.

The resulting activation energy for the proton conductivity of the thin films (4-300 nm) has been shown in terms of RH in the Figure 5.28. The activation energy associated with the proton conduction in the bulk membrane also has been included in the Figure 5.28 for comparison. It was found that the activation energy decreases exponentially with increasing relative humidity irrespective of the thickness of the thin Nafion® films. Similar to the proton conductivity at 60 °C, the thickness-dependent activation energies can be noted. The thickness

dependency of activation energy at high RH seems to be non-significant whereas it is prominent at low RH. Regardless of the thickness and the relative humidity, the activation energy of the thin films exceeds the activation energy of Nafion® 112 membrane that does not vary much with RH up to 20%. The thickness dependent behavior in the activation energy among thin films as well as membrane has been discussed dividing into two categories - at low and high relative humidity below.

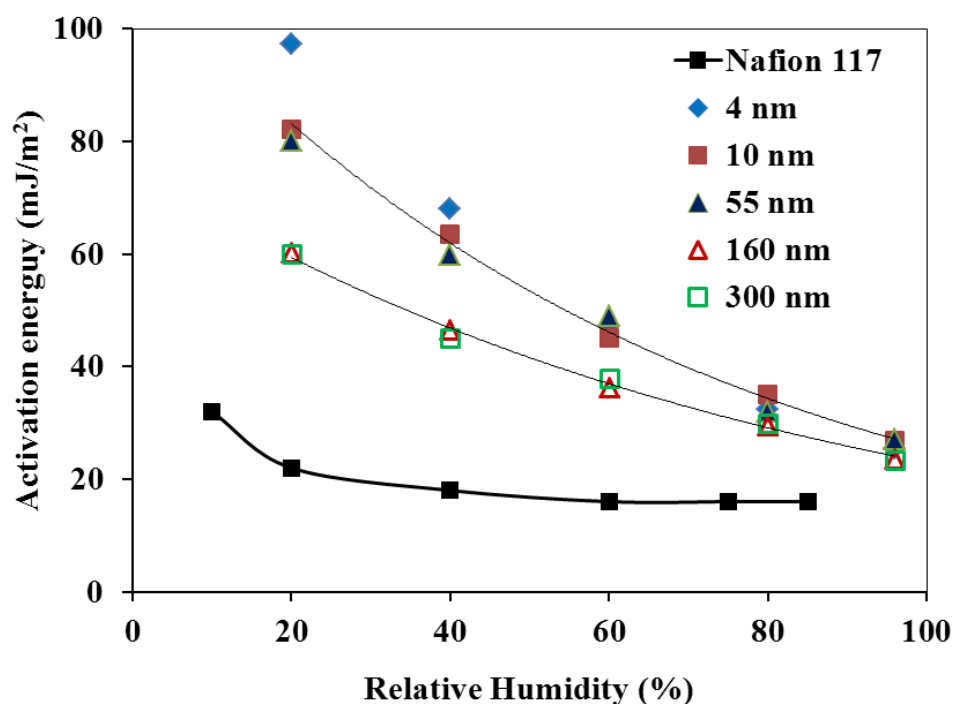


Figure 5.28: Activation energy of the proton conductivity varying film thickness in terms of relative humidity ranging 20 to 96% RH.

The activation energy of the thin Nafion® films at low (40%) and high (95%) RH has been plotted in terms of film thickness in Figure 5.29. The dot line indicates the activation energy of the bulk membrane at the respective RH. At low RH, the activation energy of the ultra-thin films (4 to 55 nm) was ~30 - 35% higher than that of the thicker films (160 and 300 nm). In contrast, the activation energy difference at high RH became less significant where 10 to 15%

higher activation energy was observed in the ultra-thin films than that of the thicker films. The activation energy of Nafion® 117 equilibrated with liquid water was reported varying from 9 to 14 kJ/mol [69,167,168] while those for Nafion® 120 [167] and Nafion® 112 [14] was reported to be close to 15. The three different bulk Nafion® membrane (Nafion®-112, 117, and 120) differing in thickness exhibit similar activation energy indicating similar intrinsic properties of the bulk membrane including molecular orientation and rearrangement behavior. In comparison to membrane, the activation energy of the thin films is 2 to 3 times higher at 40% RH and further increased with decreasing RH. The high activation energy corresponds to the high associated energy of the proton mobility, is responsible for the lower proton conductivity at low RH. On the other hand, the activation energy of the thin films is closer to the membrane at 96% RH.

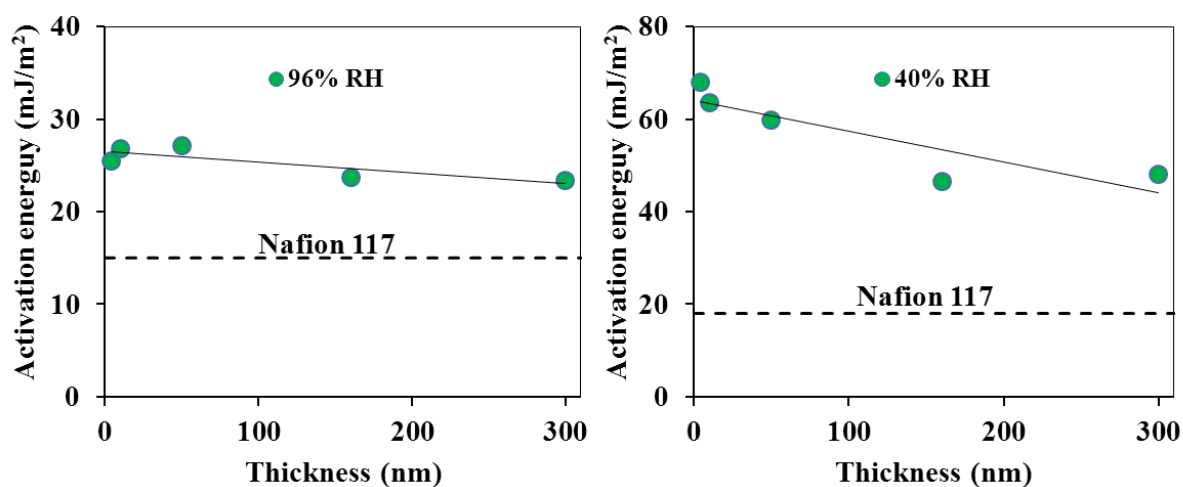


Figure 5.29: Activation energy of the proton conductivity in terms of Nafion® thin film thickness at both high (96%) and low (40 %) RH.

However, the differences in the activation energy may be attributed to the differences in the internal structural features of Nafion® thin films. In another word, the differences might be possible due to the different arrangement of the proton conduction pathway. As discussed in the literature, the proton conduction in Nafion® membrane occurs through 4-6 nm diameter of the

nano-channels. It is not clear whether such nano-channels exists in the ultra-thin Nafion® films, especially, in the 4 and 10 nm films, and it is plausible that the proton conduction may be impeded. As discussed in the chapter 4, the substrate may influence the orientation of the molecule to form a lamellar arrangement in these thin films. Thickness dependent activation energy indicates the gradual change of structure of the film, perhaps from a lamellar structure of the 4 and 10 nm films to the membrane-like structure of the 300 nm film.

5.3.10 Water uptake and swelling behavior of Nafion® thin films

To elucidate the nature of the ionic-transport suppression of Nafion® thin films, the water uptake was assessed both by measuring the thickness swelling and the mass uptake at various humidity levels. The swelling measurement was conducted using ellipsometry and water uptake measurement using Quartz Crystal Microbalance (QCM). These measurements were carried out at Mike Hickner's group at Penn State University, USA.

Figure 5.30 presents both the changes in thickness and hydration number (λ_w) as a function of RH and initial (dry) film thickness. It was found that swelling increases with decreasing film thickness. Further, it was also found that water uptake in the 4 nm and 10 nm abnormally higher – more than 3 times, than that of the thicker films as well as membrane. However, the high swelling percentage in the thinnest films is also consistent with the high water uptake. The resulted water uptake in the self-assembled Nafion® film on SiO₂ is in opposite trend as reported on the drop casted thin film on Au substrate. It was reported [12] that the water uptake decreased with decreasing thickness of the Nafion® thin films on Au. In contrast, it is also reported that the thinner film on SiO₂ has higher uptake than that of the thicker film on the same substrate [13]. The observed anomaly behavior of the thinnest film indicates that there might

have morphological differences due to high interfacial wetting properties. With decreasing the film thickness, the interfacial area to Nafion® volume ratio increases dramatically. Therefore, the interfacial effect dominates the morphology and properties of the film. A common characteristic of polymer film is the highly confined structure with decreasing thickness [3-6]. The confined polymer belongs to high restoration force, which might dictate the higher percentage of swelling of the thinnest film in presence of water. Nevertheless, the observed proton conductivity does not correlate with the water uptake behavior in the thin films. Usually, higher water uptake attributes higher proton conductivity. The opposite trend indicates, the morphological variation of the thin film upon confinement corresponds to the limited conduction path or inhomogeneous distribution of water might be responsible for the transport limitation.

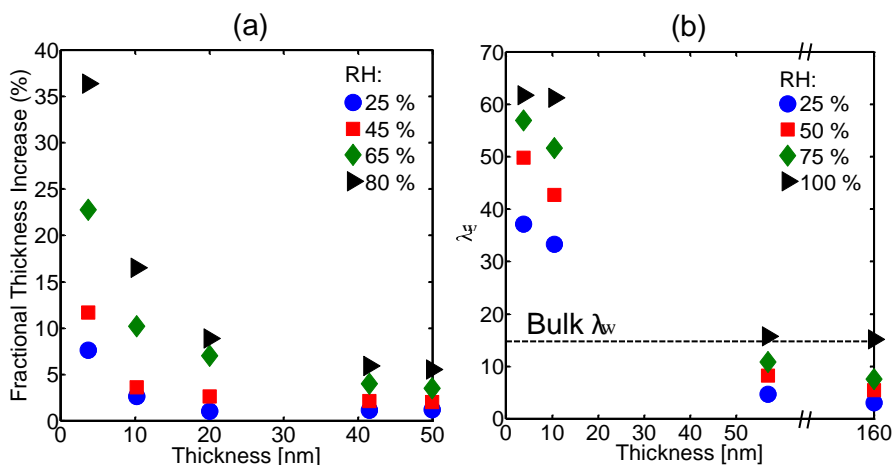


Figure 5.30: Thickness changes upon water uptake (left) and λ_w values (moles of H_2O /mol of sulfonic acid group) (right) show that thinner films uptake significantly more water than thicker and even saturated-vapor-equilibrated bulk Nafion® 117 (dotted line) at all humidity levels. [The measurements were performed by Stephanie Patrino from Dr. Mike Hickner group, Penn State University, but the films were prepared in Queen's laboratory by Author].

5.3.11 Internal structure of the Nafion® thin films by GISAXS

To understand how the morphology of confined Nafion® films affects the proton transport, Grazing incidence small angle x-ray scattering (GISAXS) patterns were obtained for films of different thicknesses after equilibration in a vapor-saturated environment. The self-assembled thin films on SiO₂ as same as the sample for film characterization (described in chapter 4) were prepared in our laboratory but the measurements were performed at Lawrence Berkeley National Laboratory, Berkeley, USA by Dr. Adam Weber group. The details protocol of GISAXS measurement has been described in our joint publication [165].

The characteristic ionomer peak (intensity peak 1 to 2 nm⁻¹) is absent in thinner films (4 and 10 nm), it starts appearing in the 55 nm film whereas a pronounced peak is observed in the 160 nm film. First of all, it indicates that there is a morphological difference in between ultrathin films - 4 to 55 nm and thicker film – 160 nm. Second, the morphological change or nano-orientation of the films change gradually with increasing thickness and move toward Nafion® membrane like structure. This observation is consistent with the proposed model in the chapter 4 of this thesis. No ionomer peak is also consistent with the proposed lamellar structure in the ultra-thin films. The line profiles at the specular position clearly show the difference in scattering for these four films. They also indicate that for films of 55 nm in thickness the domain size (d-spacing = 5.7 nm) is larger than for the thicker 160 nm films (d-spacing = 4.5 nm), which is consistent with a higher degree of water uptake as described earlier section 5.3.10.

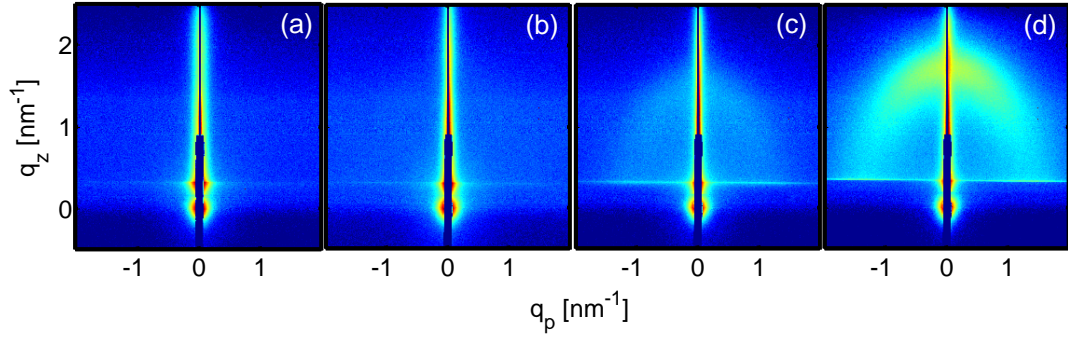


Figure 5.31: 2D GISAXS patterns from Nafion® films of (a) 4, (b) 10, (c) 50 and (d) 160 nm in thickness equilibrated at 100% RH. The patterns presented only show scattering arising from periodic ionic domains for films of 50 and 160 nm in thickness. Thinner films do not show any appreciable scattering, suggesting a loss in correlations between ionic domains in the polymer. (q_p refers to the in-plane scattering vector, and q_z corresponds to the out-of-plane scattering vector) [The measurements were performed at Lawrence Berkeley National Laboratory by Weber group, but the films were prepared by the author].

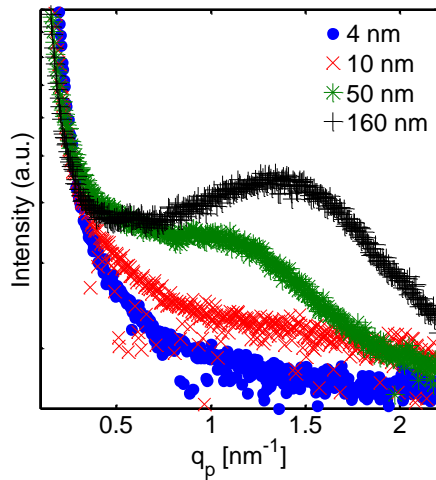


Figure 5.32: Line cuts from the GISAXS patterns for q_p at the specular position only show an intensity decay for 4 and 10 nm films and no indication of order in the films, while 50 and 160 nm films present a typical ionomer peak resulting from correlations between conducting domains. [The measurements were performed at Lawrence Berkeley National Laboratory by Weber group, but the films were prepared by the author].

However, it is inconclusive as to what causes the higher degree of water in the ultrathin films but does not contribute to the proton conduction process. However, the morphological or the structural differences in the thinner films are evident. Further investigation is needed to investigate where the large amount of water is exists in the thinnest film. A synchrotron based Neutron Reflectometry study of the films may give the answer based on the depth density profile analysis but is out of the scope of this study.

5.4 Conclusions

The impedance measurement protocol of the Nafion® thin films has been developed on the IDA of Au electrode system. The details of the impedance response, equivalent circuit design, data fitting and analyses have been investigated for the first time. The proton conductivity and the capacitance of the Nafion® thin film has been discussed in terms of treatment condition, relative humidity, temperature, thickness and IDA geometry. It was found that the proton conductivity of the Nafion® thin films is lower than that of the membrane. Apparently, film thickness and treatment protocols/thermal history are the two influencing parameters on the proton conductivity of the Nafion® thin films. At room temperature (25 °C) measurement (Protocol-1), the proton conductivity of the Nafion® thin films up to 55 nm was thickness independent whereas that of the thicker films was thickness dependent and approaches that of the membrane. The two distinct behaviors of the proton conductivity are highly consistent with the distinct surface wettability of the thin film as discussed in Chapter 4. In contrast, at high temperature (60 °C) measurement (protocol-2), the conductivity of the entire thin films is thickness dependent where that was decreased with decreasing thickness. Similar thickness dependent activation energy was observed but conversely, the activation energy was increased with decreasing thickness. Both thickness dependent proton conductivity and activation energy are consistent with the only other set of thin

Nafion® film conductivity data in the literature by Siroma *et al.* [14]. However, high water content and high swelling rate are inconsistent with the lower proton conductivity in the thinner films. It indicates that the anomaly behavior might be attributed by the morphological differences, which are evident by GISAXS study.

Chapter 6

Effect of Thermal Annealing and Liquid Water Exposure on Surface and Bulk Characteristics of Ultrathin Nafion® Films

6.1 Introduction

This chapter deals with the thermal annealing of thin Nafion® films and subsequent exposure to liquid water treatment on the morphology and properties of Nafion® thin films. Thermal annealing on the Nafion® thin films is of particular interest for polymer electrolyte fuel cell (PEFC) application because the membrane electrode assembly (MEA) comprising the CLs and the membrane is subjected to a hot pressing step by heating to a temperature ranging 125-195 °C under elevated pressure [33-35]. On the other hand, the subsequent exposure of annealed films to liquid water was carried out to simulate the local water generation and prolonged water exposure of thin film in the fuel cell operation condition.

As introduced earlier, Nafion® has hydrophobic, tetrafluoroethylene-like backbone and a hydrophilic sulfonate-group containing side chain, is being used as a thin film in the CLs of PEFC [1]. The polar side chain of Nafion® has a tendency to self-aggregate resulting in a hydrophilic ionic domain that is segregated from the non-polar backbone, which tends to be semi-crystalline hydrophobic matrix. As a result of wetting interaction with the substrate, Nafion® thin films are expected to alter the structural and morphological features from those of the membrane form of Nafion® [8-10,13,164] and also affect its properties including water uptake [12,13], swelling [165] and proton conductivity [14].

In general, substrate induced confinement effect in thin polymer films is a well understood factor which leads to change the chain dynamics [3, 4], physical properties (5) and morphologies [6]. Long range Van der Waals interaction with the substrate is another factor which can further change the polymer chain conformation and orientation up to a thickness of 100 nm [170]. Glass transition temperature (T_g) of thin film is one of the properties that can change due to the confinement effect. It has been found that T_g of thin film can either increase (e.g., poly styrene) [6,171,172], or decrease (e.g., PMMA) [173,174] or remain constant [175,176] upon confinement depending on the polymer and the substrate type and the interaction between the two. On the other hand, thin films are prone to rupture and dewetting when treated above the glass transition temperature [177,178]. Therefore, dewetting is another influential parameter, which changes the thin film morphology and properties. Dewetting can be controlled by thickness, thermal stability and wetting interaction [179,180]. Changing the wetting interaction through the modification of the substrate or the polymer is one of the common strategies to improve the dewetting property of polymer. For example, polystyrene (PS) thin film dewets below the thickness of 40 nm, but introduction of sulfonate group to PS turn into poly styrene sulfonate (PSS) ionomer prevent dewetting due to high degree of association or self-aggregation [177]. Ideally, thin film morphology during annealing, tends to achieve thermodynamically stability with minimizing the surface energy. As an example, the ultra-thin film of methylcellulose exhibited thickness dependent hydrophobic switching nature upon annealing above its T_g [181]. Under the same treatment condition, the component with the lower surface energy, such as fluorine, is expected to preferentially segregate to the air interface, decreasing the energy of the overall system for fluoro-polymers.

Similar to non-functionalized polymers, the nano-structure/properties for Nafion® thin films on a substrate is dominated by the confinement of polymer [11,15,162]. Expectedly, films

of lower thickness have structure and property more strongly influenced by the substrate. Unlike non-functionalized di-block copolymers, Nafion® thin films at least in submicron thickness scale is highly stable upon heat treatment. As evidence, no dewetting of 200 to 400 nm Nafion® thin films on SiO₂ substrate was observed even after prolonged annealing at above 200 °C [120]. On the other hand, the thin films of Nafion® behave as similar as that of other functionalized copolymers. For example, poly(4-ammonium styrenesulfonic acid) thin films show 5 orders of magnitude decrease in the diffusion coefficient for water when the thickness goes down to 3 nm [7]. It has been hypothesized that the decrease in the diffusivity is attributed to the coupling of the water mobility within the polymer film to the local chain motion due to highly confined structure [182]. Similar diffusion coefficient loss is also evident in Nafion® thin film with decreasing thickness [15]. However, there is a lack of understanding about confined structural feature/reorganization/properties, associated wetting interaction/dewetting behavior of the Nafion® thin film thickness pertinent to PEFC CLs when the film is heat treatment above T_g.

The proton conductivity of Nafion® thin films is the most desired property. So far, it has been suggested that the proton conductivity of the Nafion® thin films might be suppressed due to thermal annealing. As evidence, crystalline domain was observed in 100 nm Nafion® film upon annealing at 200 °C. It was proposed that the crystallinity, characterized by scattering peak of SAXS at $q=0.55 \text{ nm}^{-1}$, may restrict water uptake and as such water-mediated proton transport property [11]. In a separate study [12], it was shown that the kinetics of water uptake of 33-500 nm thick Nafion® films was significantly retarded upon thermal annealing and attributed it to formation of a hydrophobic skin. However, there is no direct experimental evidence of reduction in the proton conductivity of Nafion® thin films upon annealing exists in the literature.

In the previous chapters, thickness-dependent characteristics of self-assembled ultrathin Nafion® films have been reported where the films of nominal thickness below 55 nm show different surface and bulk characteristics than thicker films. These films were prepared by self-assembly and were not subjected to any thermal annealing step. Here, the effect of thermal annealing on surface and bulk properties of self-assembled ultrathin Nafion® films is reported. Contact angle measurement, Atomic Force Microscopic (AFM) and X-ray Photoelectron Spectroscopy (XPS) techniques have been employed for surface characterization. Electrochemical Impedance Spectroscopy (EIS) have been adopted to investigate proton conductivity, a key bulk property. An interesting aspect of the study was to examine the effect of exposure of the thermally annealed films to liquid water for extended periods of time to mimic the local environment in a liquid-water flooded CL.

6.2 Experimental

Preparation of self-assembled Nafion® thin films on SiO₂-terminated silicon wafer and IDA have been described in Chapters 4 and 5, respectively. According to the protocol, a series of thin films of thickness ranging from 4 nm to 300 nm were prepared for the study of thermal annealing. The self-assembled films were annealed at elevated temperature to investigate the changes in the film morphology and the proton conductivity. The annealing protocol has been described below.

6.2.1 Thermal annealing protocol of the Nafion® thin films

The Nafion® thin films were classified into two categories based on heat treatment - unannealed and annealed films. For the unannealed films, the self-assembled Nafion® films on

the substrate are subjected to two drying steps, (i) 30 min drying at N₂ blow right after film preparation (ii) dry at vacuum (-760 mm Hg) oven at 40 °C for 17 to 20 h. For annealed films, an additional thermal treatment step is carried out where the unannealed films are heat treated at a specified temperature (exceeding 100 °C) under vacuum for 1 h. The oven is thermally equilibrated at the annealing temperature for at least 3 h before placing the sample inside. The oven temperature was maintained within ± 0.5 °C of the set point temperature during annealing.

6.2.2 Characterization of Nafion® thin films

Contact angle measurement: Water contact angles were measured for both the unannealed and annealed films by a goniometer (VCA Optima, AST Products INC.). The contact angle analyzer equipped with a video camera and software (winvca32) for image grabbing and analysis. A sessile drop of about 0.75 μ L water was placed on the top of the surface of the film using a micro syringe. The image was captured within 5 sec of the water drop placement on the surface. Several images were also taken every 30 sec interval for at least 3 min to check the stability of the droplet. It was observed that the contact angle of sessile drop decreased with time. This could happen due either to adsorption of water by the polymer or to water evaporation. The reported values are the ones obtained within the first approximately 5 seconds after placing the drop on the surface.

AFM measurement: The surface morphology of the films before and after annealing was determined by AFM imaging using Nanoscope IIIa (Di Digital Instrument). Measurements were performed with silicon tip (Tip radius < 10 nm) mounted on the cantilevers in tapping mode at ambient laboratory condition. Further image analyses and roughness calculations were performed using software. For thickness measurement, the thin film was scratched with sharp needle gently

without damaging the substrate. The thickness was obtained from the cross-sectional height analysis of the scratched thin film.

XPS measurement: X-ray photoelectron spectra were obtained on a Kratos AXIS UltraDLD 39-3061 instrument using a monochromated Al source (1486.6 eV). All the spectra were obtained with constant pass energy of 80 and an energy step of 200 meV. The pressure of the vacuum system was maintained at $\sim 2 \times 10^{-10}$ torr. Samples were introduced into the vacuum system immediately before measurement, minimizing the time in vacuum (atmosphere to measurement ~ 40 mins). To prevent excessive charging, a charge neutralizer was used. The binding energy scale was further calibrated by setting the F_{1s} peak to 690.0 eV. This results in a Si_{2p} peak at 103.2 eV when present, well within the range for SiO_2 and silicon-supported SiO_2 films [143-145]. The carbon peak is not used directly because the multiple contributions of the Nafion® film produce slight shifts in this peak. Calibration of the instrumental behavior (intensity dependence of the collection solid angle) during angle-resolved measurements was performed using a freshly sputtered copper sample. Elemental quantification of the Nafion® films and the underlying silica was determined using the Si_{2p} , S_{2p} , C_{1s} , O_{1s} and F_{1s} peaks with a Shirley background subtraction in the CasaXPS software [146].

EIS measurement: For impedance measurement, an interdigitated array (IDA) of Au electrode supported by SiO_2 (2000 nm)/Si wafer was used as substrate. The IDA microelectrode consists of 110 teeth (each teeth is 0.8 cm in length and 10 nm in width) with a 100 μm gap between two teeth. For impedance measurement, the IDA with Nafion® film was placed in an environmental chamber (Model 3911, Thermo Forma, USA) with relative humidity (RH) and temperature control. The measurements were accomplished by a two micro-probe setup connected with a Solartron 1260 frequency-response analyzer coupled to a Solartron 1296

dielectric interface. The detailed measurement protocol and fitting analysis have been described in the Section 5.2.5 of Chapter 5.

6.3 Results and discussions

6.3.1 Characterization of surface properties of the annealed thin films

6.3.1.1 Surface wettability by water contact angle measurement

Water contact angles of Nafion® thin films of different thicknesses after being treated at different annealing temperatures have been shown in the Figure 6.1. There are two distinct classifications of unannealed ultrathin Nafion® films (dried at 40 °C) based on surface wettability. Films thickness <55 nm are hydrophilic whereas >55 nm are hydrophobic as described in the chapter 4. In this section, we investigate the temperature annealing effect on surface wettability.


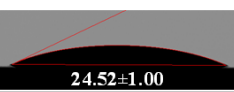


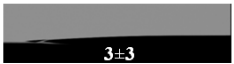






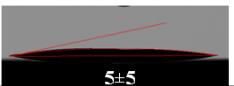

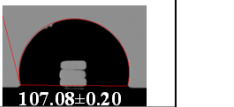







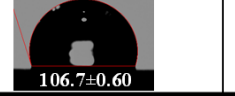

| Film Thickness (nm) | Film Treatment Temperature | | | |
|---------------------|---|--|--|---|
| | 40 °C ^a | 110 °C (bulk T _g) | 146 °C | 160 °C |
| 4 |  18.86±2.54 |  24.52±1.00 |  58.17±4.33 |  106.5±0.10 |
| 10 |  3±3 |  26.95±2.24 |  107.17±0.30 |  107±0.80 |
| 30 |  2±2 | *  105.9±0.82 |  107.25±0.30 | |
| 55 |  5±5 |  105.2±0.41 |  107.08±0.20 | |
| 75 |  105.5±0.54 |  105.5±0.82 |  107.1±0.50 | |
| 110 |  105.2±0.72 |  105.8±0.52 |  107.4±0.60 | |
| 160 |  106.1±0.50 |  106.7±0.60 |  108.07±0.45 | |

Figure 6.1: Images of water sessile drop on films of various thicknesses and annealed/thermally treated at 40, 110, 146 and 160 °C.

To investigate the effect of thermal treatment on the un-annealed films, one of the selected temperatures was the glass transition temperature (T_g) of bulk Nafion®, i.e. 110 °C. It is well-known that if a polymer is treated or annealed at T_g, it achieves chain or segmental mobility and goes through the rubbery state. Over time, molecules rearrange itself into a thermodynamically favorable state minimizing its surface energy. Upon thermal treatment at 110 °C, the free surface of the 4 and 10 nm films remained hydrophilic exhibiting water contact

angles of 25° and 27°, respectively. In contrast, the water contact angle for the 30 and 55 nm films changed from almost zero to ~105° after thermal treatment at 110 °C. Contact angle of films with thickness greater than 55 nm remained unchanged exhibiting hydrophobic surface. Interesting observations on contact angle change with time also have been made as discussed in the later part of this section.

Next, a thermal treatment temperature of 146 °C, which is above the T_g of bulk Nafion® was adopted to see the change in surface property. Another particular reason to select this temperature as it is within the temperature range for hot pressing in fuel cell MEA fabrication step. It is noted that film annealing was always conducted on dried films at 40 °C. Similar to the treatment at 110 °C, the 4 nm film still showed hydrophilic surface but with a higher contact angle of ~60° upon treatment at 146 °C. Unlike 110 °C treatment, the 10 nm film switched from super hydrophilic to hydrophobic exhibiting a contact angle of 107°. For the rest of films, the contact angle increased only slightly up to a contact angle of 107° which is similar to 110 °C treatment.

Finally, an even higher thermal treatment temperature of 160 °C was employed to investigate the surface switchability of thinnest – 4 nm film. Interestingly, it was found that the 4 nm film surface converts from hydrophilic to hydrophobic exhibiting a contact angle of ~106° in such a high temperature treatment. Rest of the film surface switched to the same hydrophobic as same as 146 °C treatment. It is noticeable that regardless of annealing temperature and film thickness, ~ 108° is the highest contact angle was observed. Another important note is the high temperature treatment corresponds to high energy, required to the surface switchability with decreasing film thickness.

Thermal treatment/annealing effect offers interesting insight into the behavior of the polymer films regarding the polymer mobility and confirms the confinement effect of polymers in the ultra-thin Nafion® films. Initially, sulfonate group rich surface might be responsible for the super hydrophilicity for films with thickness of up to 55 nm. During the annealing process, the polar component of Nafion® on the free surface may turn towards the bulk exposing the non-polar part resulting in a hydrophobic surface. This reorientation process depends on the film thickness and the radius of gyration (R_g) of polymer molecules. For Nafion®, R_g is related to the radius of the cylindrical bundle, R , in the solution, as defined by Aldebert *et al.* (1988) [99], $R^2 = 2R_g^2$. Based on the SAXS or SANS data, the radius of cylindrical Nafion® bundle in low surface energy solvent has been reported in the literature [99-103] to range 2.0-2.5 nm resulting in a R_g of 1.4-1.8 nm. When the polymer film was annealed at the Tg of bulk Nafion® (109 °C), it was found that the film thickness $<10R_g$ was still hydrophilic. Thus, the 10 nm film has hydrophilic free surface. Film thickness $>10R_g$, convert into highly hydrophobic. Interestingly, the 30 nm film showed high contact angle but the angle collapse to a lower value within 30 sec of droplet placement on the surface as shown in Figure 6.2. In contrast, film thickness greater than 30 nm showed high stability of water droplet until complete evaporation of water occurred. Overall, it can be concluded that the 10 nm film goes through a minor surface rearrangement due to treatment at 110 °C. In the same treatment condition, the 30 nm film showed pseudo-hydrophobicity – seems hydrophobic at the initial stage, but readily get back to the hydrophilic stage in presence of water due to insufficient reorientation. The 55 nm film surface undergoes complete reorientation which causes the water droplet stable over the drying period.

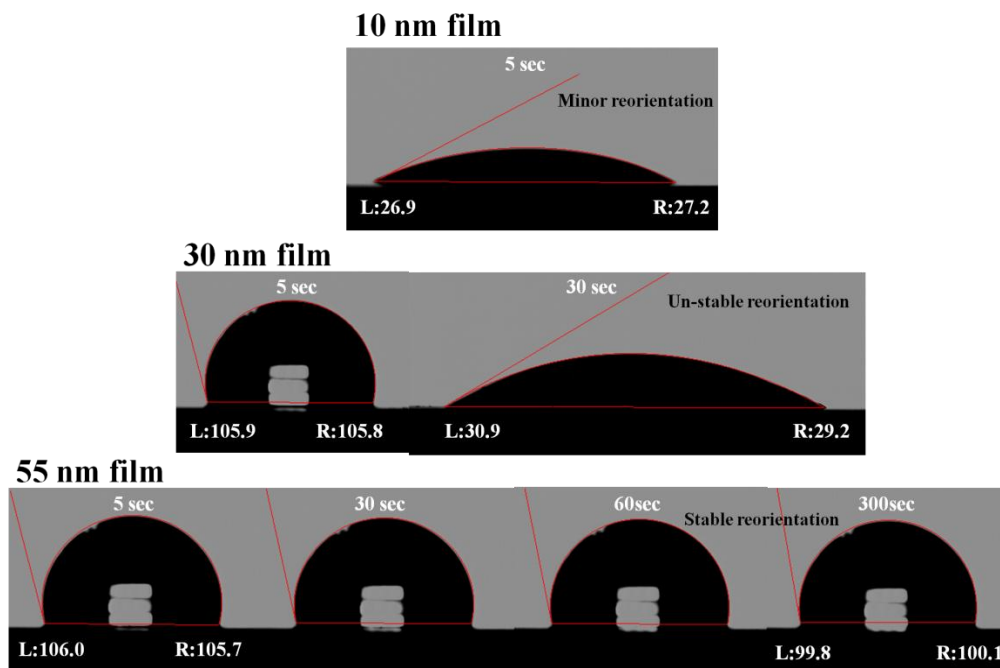


Figure 6.2: Water contact angles on the 10, 30 and 55 nm ultra-thin Nafion® films with time when the films were treated at 110 °C.

Upon thermal treatment at 146 °C, the thinnest film still exhibited hydrophilic surface indicating that the molecular mobility is strongly dominated by interfacial effect, which restricts the polymer mobility even temperatures at significantly above the bulk Nafion® T_g. It is noted that with increasing film thickness, the interfacial area to polymer volume ratio increases. Upon thermal treatment at 160 °C, it was found that even the 4 nm film became hydrophobic and did not switch back or contact angle did not break down to the small contact angle over the several hours monitoring period rather gradually evaporated. This phenomenon may be explained by restricted segmental movement of polymer molecules as confined to the substrate surface. Thus, the T_g of the ultra-thin films on SiO₂ substrates and of thickness $<10R_g$ can be argued to be significantly higher than bulk Nafion® T_g, which also indicates a favorable interaction between the substrate and the polymer molecules. The change in wettability of the surface indicates a

reorientation of polymer bundle. Thickness dependent Tg of the ultra-thin and thin Nafion® films can be measured by Ellipsometry or IR technique but that is out of scope of this study.

The whole process can be explained in terms of three effects. 1) Confinement effect: when polymer film thickness decreases to less than a polymer chain coil size or agglomerated basic unit which is comparable to some multiples of R_g , polymer chain cannot stay on the support retaining its original coil or agglomerated base structure where deformation occurs. As a result, polymer molecules/bundles become less mobile in a thin film. 2) Hard layer formation: polymer chains tend to form ordered structure exhibiting layered structure near the substrate/polymer interface and this is related to the radius of gyration of the polymer. Due to interfacial hard layer and confinement effect, polymers achieve less mobility at and near the interface. 3) Interfacial effect: irrespective of the thickness of the film, the ordered/organized polymer hard layer or confined polymer layer thickness become constant, this is termed as interfacial effect [181]. Therefore, polymer molecules up to a certain thickness in thin films become restricted in mobility due to its confinement and interfacial effect.

6.3.1.2. Estimation of hydrophilic fraction of the thin film surface

In the above section, it was found that film surface switches from hydrophilic to hydrophobic at elevated temperature treatment. The change of surface heterogeneity might correspond to the surface switchability. The surface can be quantified in terms of the degree of heterogeneity using the Cassie-Baxter equation [128].

$$f_1 = \frac{\gamma_{aw} \cos \theta - (\gamma_{2a} - \gamma_{2w})}{(\gamma_{1a} - \gamma_{1w}) - (\gamma_{2a} - \gamma_{2w})} \quad (3.8)$$

where, γ 's are the interfacial energy between different phases and subscripts "1", "2", "a", and "w" designate phase 1, phase 2, air (vapor), and water, respectively. For Nafion® thin films, surface may be composed of two different phases, the sulfonic group rich region that is hydrophilic (phase 1) and Teflon-like backbone region that is hydrophobic (phase 2). The interfacial energies of the hydrophilic region are considered to be similar to that of water and those of the hydrophobic region similar to that of Teflon. Considering the associated interfacial energies (Table 6.1), the fraction of hydrophilic surface was quantified and summarized in the Table 6.2.

Table 6.1: Interfacial energy parameters

| | Parameter | Surface energy (mJ/m ²) |
|--------------------|---------------|-------------------------------------|
| Water to air | γ_{aw} | 73 ^a |
| Phase (1) to air | γ_{1a} | 73 ^a |
| Phase (1) to water | γ_{1w} | 0 |
| Phase (2) to air | γ_{2a} | 17.2 |
| Phase (2) to water | γ_{2w} | 46 ^b |

^aReference [186], ^bReference [185].

Un-annealed film thickness up to 55 nm have more than 95% of the surface that is hydrophilic, which is as similar to the hydrophilic surface of Nafion® membrane equilibrated in water [128]. In contrast, the hydrophilic fraction of the annealed thin films significantly went down to ~6 to 8% which is consistent with the dry Nafion® membrane (hydrophilic fraction ~5%). It is noted that the surface tension of hydrophilic part of the film to the water has been considered zero, which is not obvious, therefore, the calculated hydrophilic fraction is only an estimate of the real surface composition.

Table 6.2: Calculated hydrophilic fraction (%) of both un-annealed and annealed films

| Thin Nafion® film thickness | Un-annealed film | Annealed film |
|-------------------------------|----------------------------------|----------------------------------|
| | f_1 = hydrophilic fraction (%) | f_1 = hydrophilic fraction (%) |
| 4 | 94.8 | 7.7 |
| 10 | 99.7 | 6.8 |
| 30 | 99.7 | 6.8 |
| 55 | 98.9 | 7.0 |
| 75 | 8.9 | 6.9 |
| 110 | 9.2 | 6.6 |
| 160 | 8.1 | 5.8 |
| 300 | 8.3 | 6.5 |
| Nafion® membrane ^a | 95 (in water) | |
| | 5 (dry polymer) | |

^a[128]**6.3.1.3. Surface energy of Annealed films by three liquid method**

In this section, surface energies of the annealed films by three liquid contact angle measurements with the combination of extended DLVO theory are calculated. The calculated surface energy parameters of the annealed films are summarized in Table 6.3. Except the 4 nm film, the Nafion® films subjected to 146 °C for 1 h were used for the experiment. For the 4 nm film, data was obtained for the sample subjected to 160 °C treatment for 1 h. It was found that the

surface energy components yielded comparable values regardless of the film thickness. For the 4 nm film, the electron donating parameter (γ^{\ominus}) drops from 66 mJ/m² to 0.7 mJ/m² upon annealing. It indicates that sulfonic groups correspond to the electron donating parameters disappeared from the surface and have been replaced by non-polar energy components. Total surface energy of the annealed films is also sufficiently lower than that of the un-annealed 4 nm film but comparable with Teflon surface energy – 17.2 mJ/m².

Table 6.3: Surface energy parameters of unannealed and annealed ultra-thin Nafion® films

| Material | γ^{LW} (mJ/m ²) | γ^{\oplus} (mJ/m ²) | γ^{\ominus} (mJ/m ²) | γ^{Tot} (mJ/m ²) |
|---------------------------------|---------------------------------------|---|--|--|
| 4 nm (Un-annealed) ^b | 14.0 | 5.2 | 66.6 | 51.2 |
| 4 nm film ^c | 17.8 | 0.2 | 0.7 | 18.6 |
| 10 nm film ^d | 17.8 | 0.3 | 0.4 | 18.4 |
| 55 nm film ^d | 17.5 | 1.0 | 0.1 | 18.0 |
| 160 nm film ^d | 17.5 | 1.7 | 0.0 | 18.1 |

^bChapter 4, ^cAnnealed at 160 °C, ^dAnnealed at 146 °C

6.3.1.4. Surface morphology by AFM

In this section, surface morphologies of the annealed films are investigated by the AFM height image and phase contrast. In the previous chapter 4, a good correlation between the surface wettability and the AFM phase contrast was reported for the unannealed films. Similar investigation is carried out for the annealed films.

AFM height and phase image of the 4 nm film after different treatment conditions have been shown in the Figure 6.3. The images have been presented in the dimension of 1000 nm X 1000 nm with 5 nm and 50° scale for height and phase image, respectively. The 4 nm unannealed film was found to be continuous and homogenous as observed in the Figure 6.3. The corresponding phase contrast can be interpreted in terms of the chemical properties of the surface. The origin of the phase contrast may be the surface hydrophilicity and hydrophobicity as described in the previous chapter 4. When the 4 nm thick un-annealed and continuous film was annealed at 146 °C for 1 h, biscontinuous morphology was observed (Figure 6.3d). In other word, a phase segregated network, built of aggregated bundles with 30 to 50 nm diameters, was found. The cross-sectional analysis of the corresponding height image in Figure 6.3e showed the feature height of about ~2.5 nm. It indicates that the film become rough and nonhomogeneous. The biscontinuous and phase segregated morphology are also evident in the phase contrast image of Figure 6.3f. Unlike the 4 nm unannealed film, a correlation between height and phase contrast images can be noted. However, when the 4 nm unannealed film was annealed at 160 °C, morphology with random pores/holes rather than phase segregated pattern was observed in Figure 6.3g. The corresponding sectional analysis shows that the depths of the holes are around ~3 nm. It indicates that the pore depth might go all the way down to the substrate surface. In the corresponding phase image, a negligible phase contrast without any particular feature was observed. It is noted that the biscontinuous morphology or hole formation in the surface may be due to dewetting effect. More discussion and interpretation based on the observation have been included after describing the rest of the film morphologies later of this section.

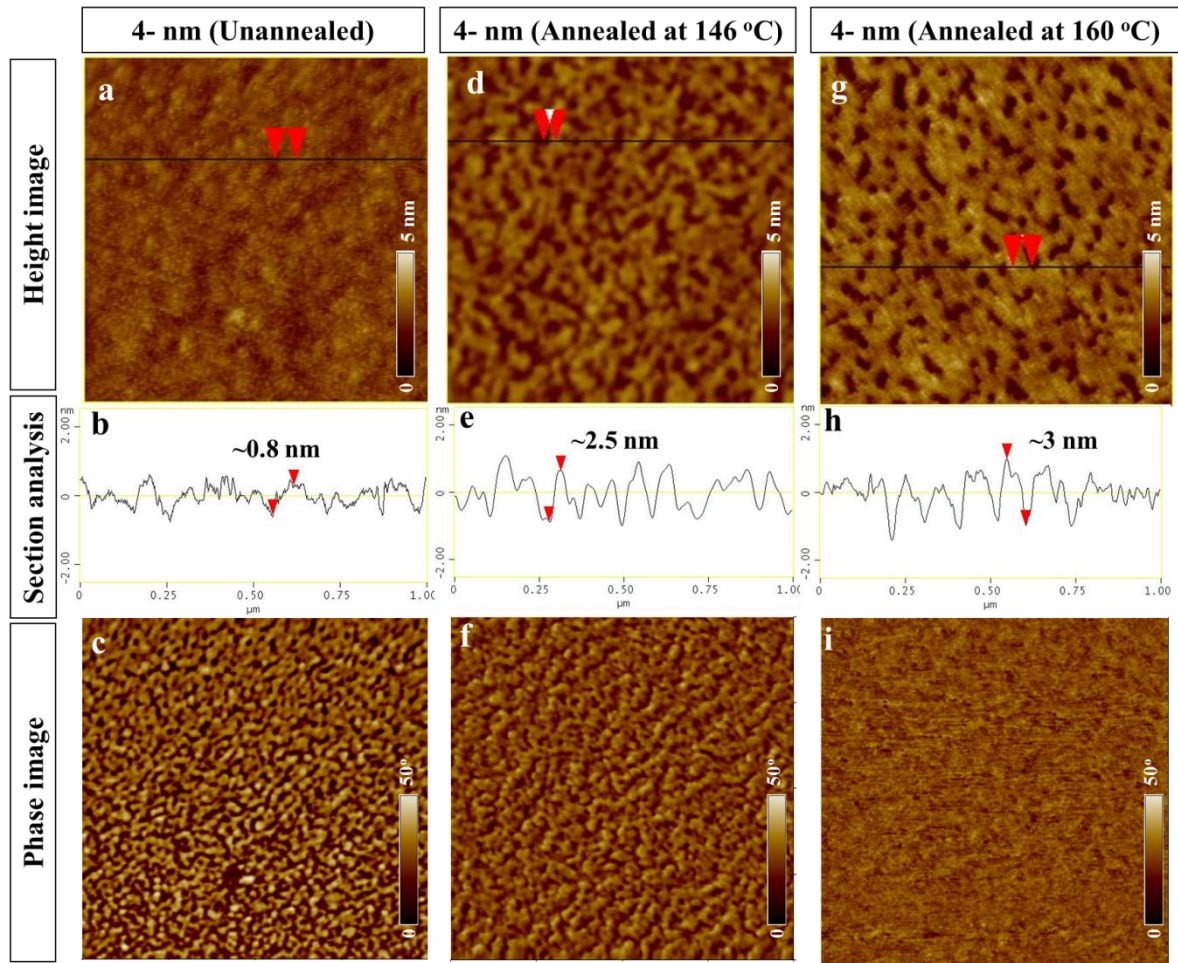


Figure 6.3: AFM height and phase image (1000 nm X 1000 nm) of 4 nm film; (a) height (b) section analysis (c) phase at 40 °C treatment; (d) height (e) section analysis (f) phase at 146 °C treatment; (g) height (h) section analysis (i) phase at 160 °C treatment

The morphology, section analysis and phase contrast of the unannealed and the annealed surface of 10 nm film have been shown in Figure 6.4. Unlike the 4 nm film, the morphology of the 10 nm film was continuous upon annealing. Although it appears to be smoother, no significant differences are observed in section analysis (Figure 6.4b and Figure 6.4e). On the other hand, phase contrast image showed a difference in between unannealed and annealed film. The surface features seem to have disappeared due to annealing. It indicates that there is a change in surface properties.

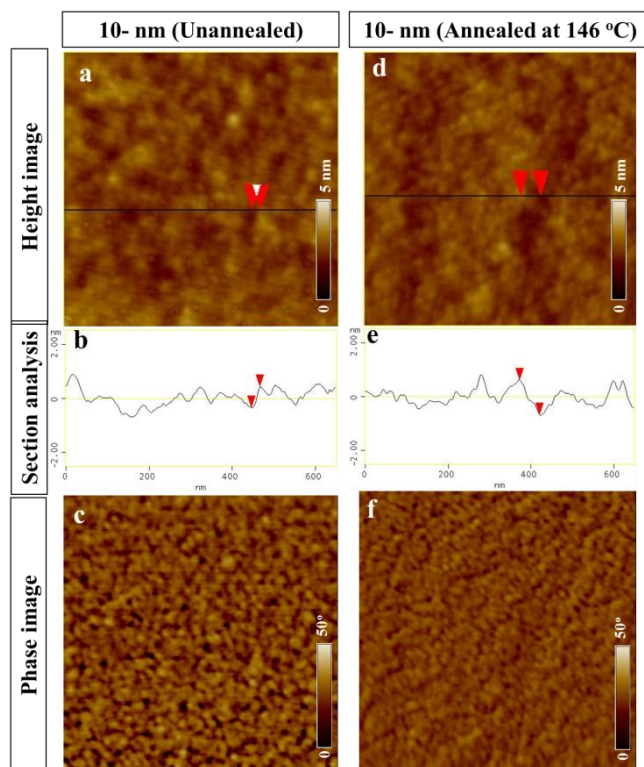


Figure 6.4: AFM height and phase image (650 nm X 650 nm) of the 10 nm film; (a) height (b) section analysis (c) phase at 40 °C treatment; (d) height (e) section analysis (f) phase at 146 °C treatment.

For 55 nm film, it was found that surface morphology of annealed film is smoother compared to the unannealed film as shown in Figure 6.5a and Figure 6.5d. The corresponding section analysis of height image showed that the feature height reduced upon annealing. It indicates surface rearrangement due to annealing and might attribute to lower surface roughness. The thickness dependent surface roughness of the Nafion® thin films has been discussed in the later part of this section. Figure 6.5c and Figure 6.5f represent a comparative phase image of the 55 nm unannealed and annealed films, respectively on a 50° scale. Similar to the 10 nm film, the 55 nm film surface upon annealing cannot be distinguished in terms of phase contrast which indicates the changes in surface properties.

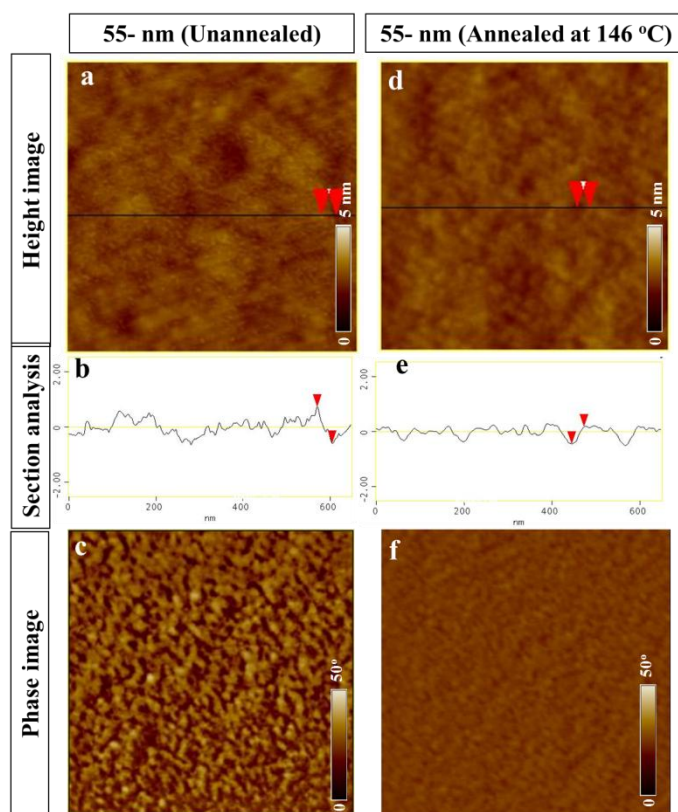


Figure 6.5: AFM height and phase image (650 nm X 650 nm) of 55 nm film; (a) height (b) section analysis (c) phase at 40 °C treatment; (d) height (e) section analysis (f) phase at 146 °C treatment.

For much thicker film – 300 nm, a significant change in morphology of the annealed film compare to the unannealed counterpart was observed in Figure 6.6. The surface corrugation of the annealed film seemed to be reduced, which is clearly evident in the section analysis. The feature height in the annealed film reduced two to three times than that of the unannealed film as shown in Figure 6.6b and Figure 6.6e. Unlike the 10 and 55 nm films, there is no change in phase contrast image between the unannealed and annealed 300 nm films. Although not much change in the surface properties was noted, a significant surface rearrangement in surface morphologies due to annealing may be observed.

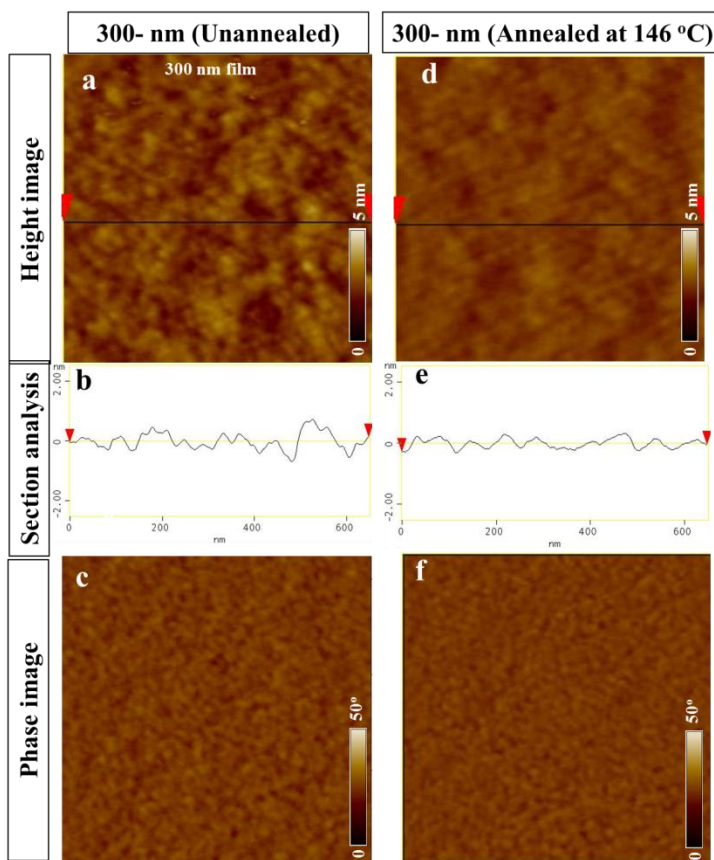


Figure 6.6: AFM height and phase image (650 nm X 650 nm) of 300 nm film; (a) height (b) section analysis (c) phase at 40 °C treatment; (d) height (e) section analysis (f) phase at 146 °C treatment.

The comparative surface roughness of the unannealed and annealed films in terms of thickness has been presented in Figure 6.7. The surface roughness ranged from 0.31 to 0.35 nm for the 4 to 300 nm unannealed films respectively. Upon annealing, the film thickness 30 to 300 nm became smoother resulting surface roughness ~ 0.2 nm. The roughness remained almost constant for the 10 nm film. In contrast, a higher surface roughness was observed for the 4 nm film due to annealing. The high surface corrugation was attributed due to biscontinuous or phase segregated morphology as observed in the surface morphology (discussed earlier).

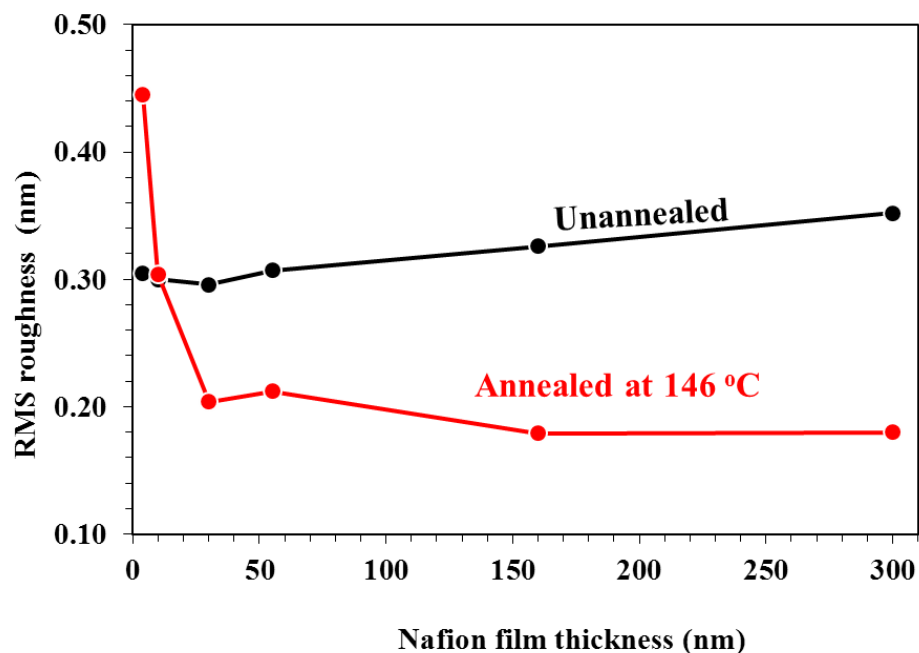


Figure 6.7: Thickness dependent surface roughness of thin Nafion® films (a) unannealed (b) annealed at 146 °C.

The comparative roughness in phase contrast between the unannealed and annealed films is presented in Figure 6.8. It was found that the high phase roughness of the unannealed films – thickness up to 55 nm, reduced more than two times. Comparatively, lower reduction of phase roughness was observed for 160 and 300 nm films. The change in phase contrast and corresponding roughness indicates to the different surface properties as discussed in the later part.

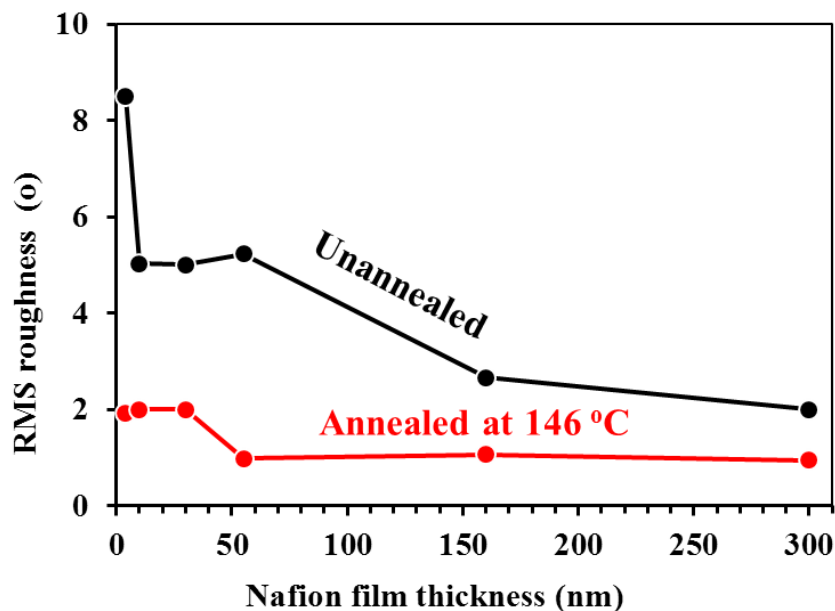


Figure 6.8: Thickness dependent surface roughness in phase of thin Nafion® films (a) unannealed (b) annealed at 146 °C.

Surface rearrangement of the ultrathin Nafion® films is evident from the morphology differences in the height image and reduction of the corrugation in the section analysis. With increasing thickness, higher rearrangement of surface results lower surface roughness. In contrast, two distinct features have been observed in the phase images of the unannealed films which correspond to the surface hydrophilicity/hydrophobicity. Recently, Ohira *et al.* [187] correlated the lighter and darker color of thin film phase image with surface hydrophilicity and hydrophobicity, respectively. The disappearance of the distinct features in the phase contrast may also indicate that the surface is dominated by either the hydrophobic or the hydrophilic component of Nafion®. The significant phase change upon annealing for films of thickness up to 55 nm is consistent with the switching of surface wetting properties. In the thicker films, a greater extent of surface rearrangement might happen but the phase change is not apparent as it was already in the stable state with favorable surface properties, which is consistent with no change in

free surface wettability. Similar to the finding in the present work, thickness-dependent wettability switching was observed for methylcellulose upon annealing [181].

However, the 4 nm film showed a different characteristic compared to other thin films in the present study. The biscontinuous morphology and hole formation in the 4 nm thin film is consistent with the common thin film behavior of other polymers which have been identified due to dewetting effect [177-180]. It is interesting to note that Nafion® thin films of thickness of 10 nm and greater do not dewet but it does when the thickness becomes sufficiently low as noted for the 4 nm thin film. Thickness-dependent dewetting behavior is also reported in literature where dewetting suppressed for the fictionalized polymer because of its higher degree of association [177]. The finding is also consistent with Hill *et al.* [120] who reported no dewetting was observed for 200 nm Nafion® thin film even after several days of annealing.

6.3.1.5. Elemental and surface analysis by XPS

A concern with annealing of Nafion® film is the possibility of damage or chemical modification of the film as indicated in a number of literature [94-98]. XPS is a useful technique to identify the compositional variation and differences in the local atmosphere of the element due to damage or chemical modification or physical changes. XPS measurements were performed on the Nafion® thin films before and after annealing. For each film, the spectra were obtained to contain all the relevant regions (F_{1s} , C_{1s} , O_{1s} , S_{2p} , and Si_{2p}). These peaks were integrated to quantify the composition of the films. The ratio of sulfur to fluorine (S/F) intensities has been previously used in chapter 4 to identify the branches vs backbone exposure and in particular the degradation of the films by decomposition of the branches at the ether oxygen. In this work, the S/F ratio remained within error for all the films before and after annealing. This result indicates

that the films do not degrade significantly upon annealing and any observed changes in conductivity or surface behaviour must result from conformational changes within the film.

For the thinnest films (4 nm), XP spectra show that upon annealing there is a slight increase in the Si_{2p} peak (Figure 6.9). An increase in the intensity of the underlying silica support would traditionally suggest a thinning of the film. However, an alternative explanation consistent with the AFM data is the clustering of the film into thicker regions that result in the additional exposure of the underlying silica support. The dewetting behaviour shown in Figure 6.3 would be consistent with a slight increase in the Si_{2p} intensity.

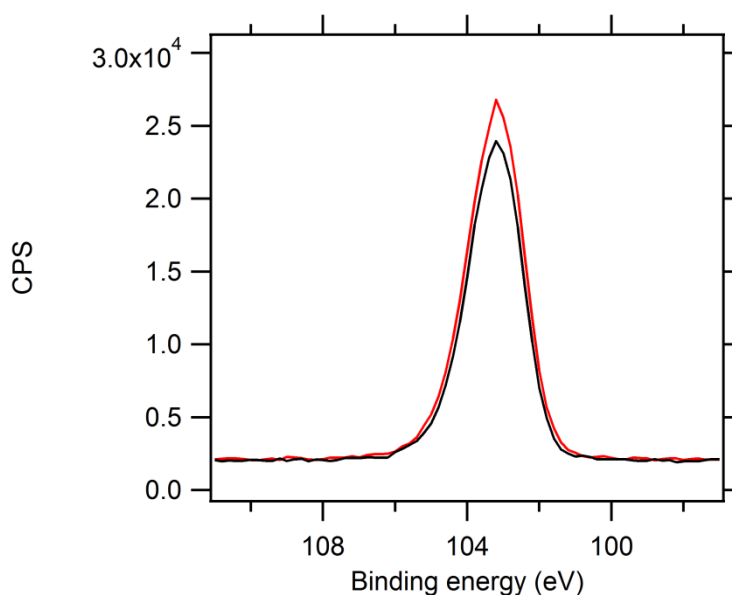


Figure 6.9: Silicon signal increase as the 4 nm film is annealed. Si_{2p} peak region, normal incidence. Black line before annealing, red line after annealing.

For both thinner and thicker films, changes upon annealing seem to be related to conformational changes and crosslinking of the chains. The most significant change as observed by XPS occurs in the carbon region (Figure 6.10), whereupon annealing a growth in the peak at

286.5 eV is observed. The binding energy of the carbon peak can be correlated to the number of electronegative atoms bound to each carbon [189]. The peak at 291.8 eV has been previously identified as carbon bound to multiple fluorine atoms, while the peak at 286.5 eV corresponds to carbon bound to at least one oxygen or fluorine atom. The growth of the peak at 286.5 eV may arise from cross linking of fully fluorine coordinated carbons as it appears to be the case on the thicker films, or from ether type bonding between chains of more hydrocarbon type carbons which are always present in the sample (peak at 284.8 eV). Although no change in the oxygen or sulfur signal could be resolved, either mechanism of the growth of the 286.5 eV carbon peak indicates a morphological change in the film.

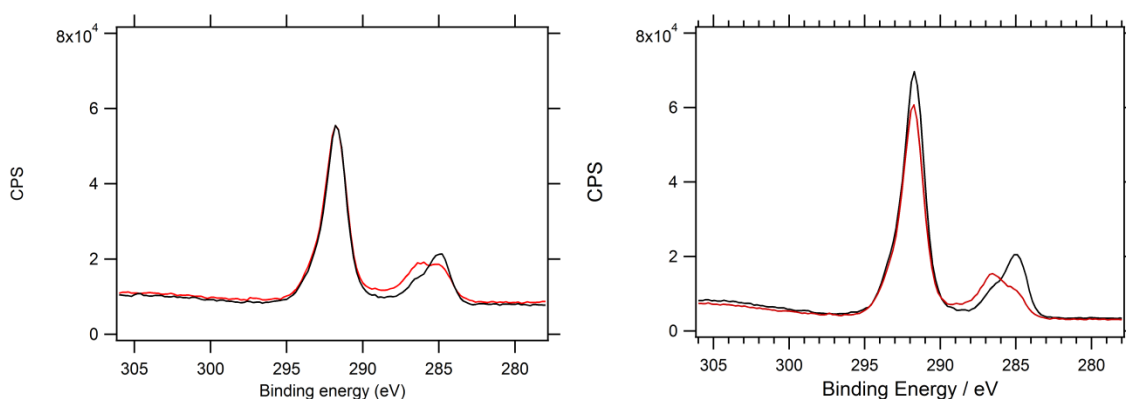


Figure 6.10. XPS carbon region. a) C_{1s} region for the 4 nm film; b) C_{1s} region for the 30 nm film. Black line before annealing, red line after annealing.

6.3.2 Characterization of bulk proton conductivity of annealed thin films

In this section, the proton conductivity of the thin Nafion® films upon annealing has been investigated by electrochemical impedance spectroscopy (EIS). A comparison of proton conductivity associated activation energy between the un-annealed and annealed films is made. All the films were prepared on IDA of Au electrode supported by SiO_2 . Films without any heat

treatment are termed as unannealed films and those treated at 146 °C for 1 h are termed as annealed films.

6.3.2.1. Impedance response of annealed Nafion® thin films

The comparative impedance response of the 10 nm unannealed and annealed films have been shown in the Figure 6.11. In Nyquist plot, a semicircle response was observed in both cases where the semicircle diameter increased to a greater extent due to annealing. It indicates that the annealed film is associated with high film resistance corresponding to lower proton conductivity. Nyquist plot does not show the frequency associated with the impedance whereas Bode plot does. Bode plots represents real (Z') and imaginary (Z'') part of impedance as a function of frequency. In low frequency region, a clear separation of impedance response has been observed.

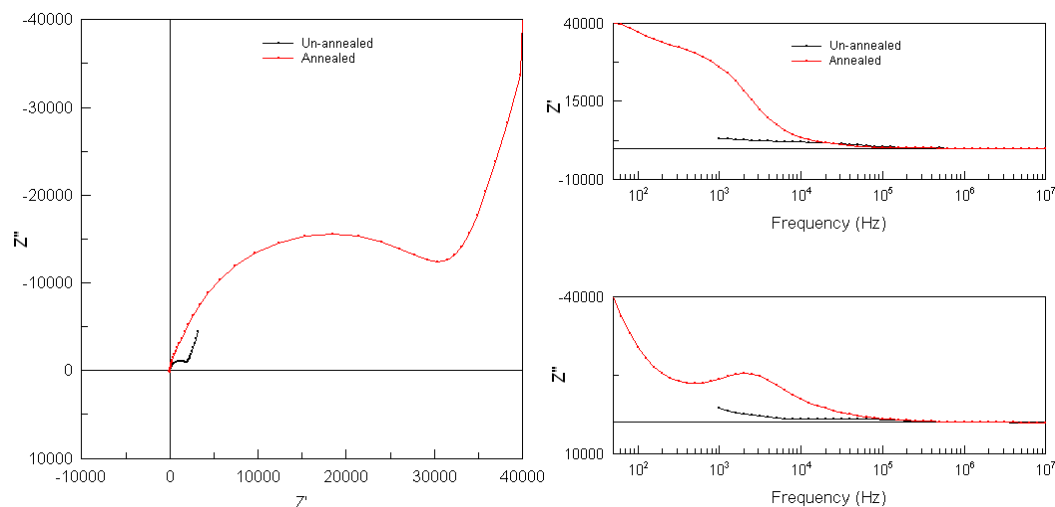


Figure 6.11: Impedance response of the 10 nm films – unannealed (black line) and annealed (red line). Nyquist plot (left hand side) and Bode plot (right hand side)

A comparative impedance response of the 55 nm films between unannealed and annealed films is shown in Figure 6.12. Similar to the 10 nm film, the annealed 55 nm film showed a larger semicircle diameter than that of the unannealed counterpart. Bode plots showed the impedance characteristics in terms of frequency where the associated high impedance upon annealing is also evident. The important observation is the higher film resistance as the characteristics semicircle diameter increased significantly because of annealing.

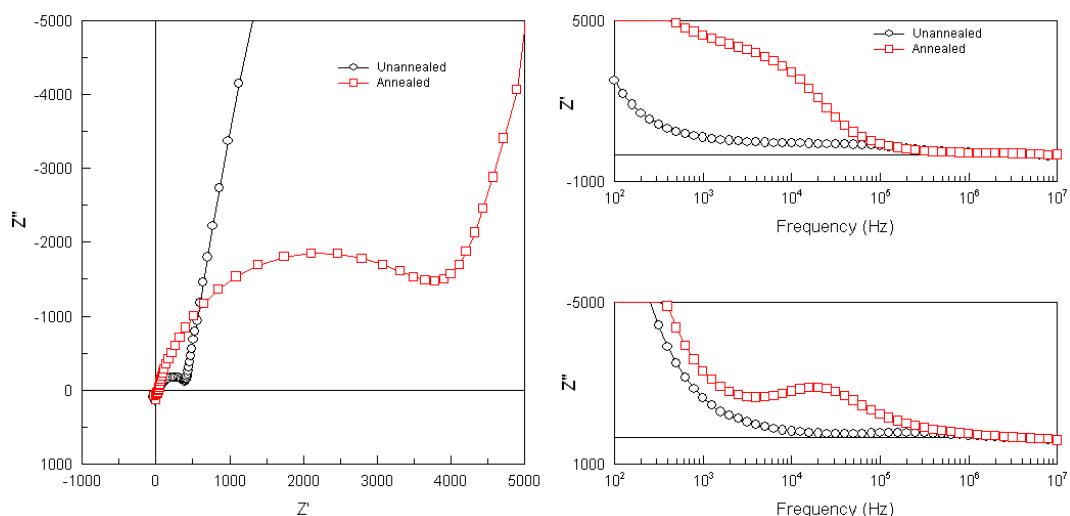


Figure 6.12: Impedance response of the 55 nm films – unannealed (black line) and annealed (red line). Nyquist plot (left hand side) and Bode plot (right hand side).

6.3.2.2. Proton conductivity of the annealed Nafion® thin films with thickness

The impedance spectrum was fitted with equivalent circuit as discussed in the Chapter 5. The extracted film resistance was used to calculate the proton conductivity. In this subsection, how the conductivity of annealed films varies with its thickness is discussed.

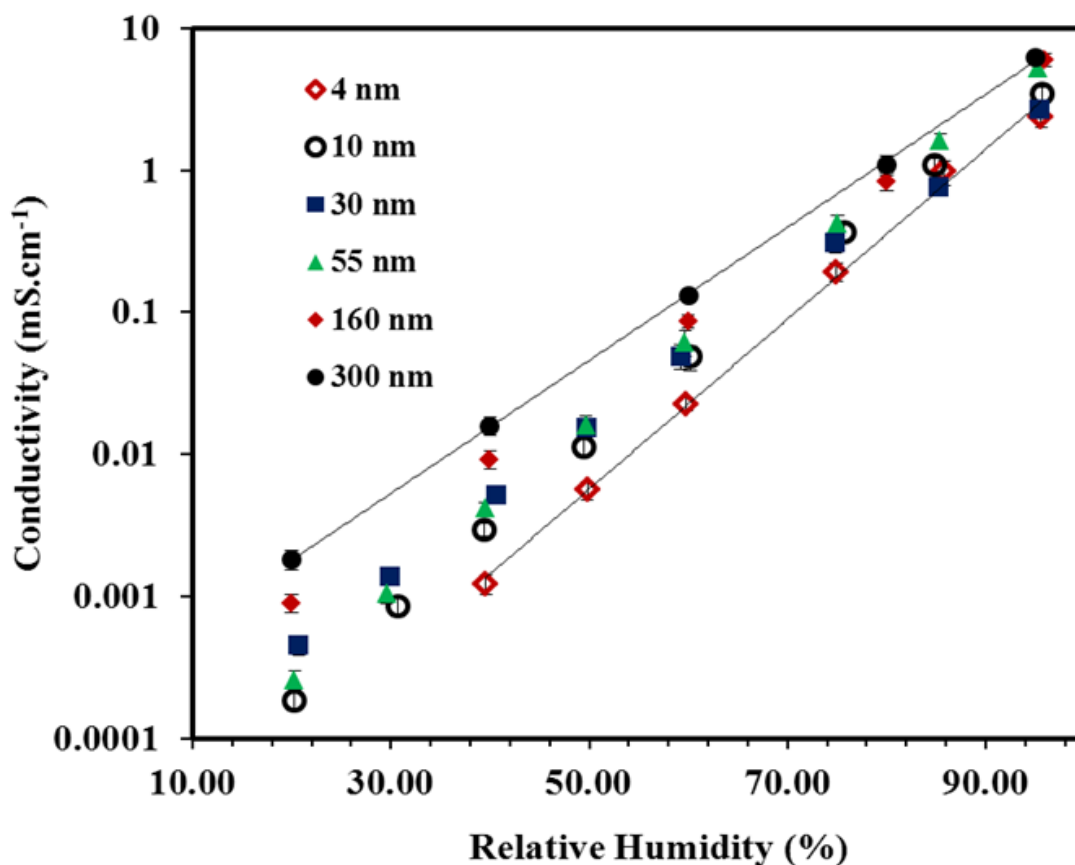


Figure 6.13: Proton conductivity of annealed Nafion® thin films with different thicknesses in terms of relative humidity at 60 °C.

Proton conductivity of 4-300 nm thin films upon annealing at 146 °C has been presented as a function of relative humidity in Figure 6.13. For the Nafion® thin films, the conductivity increased exponentially with increasing relative humidity 20% to 96%. Ultimately, a thickness-dependent conductivity was observed where the conductivity mostly increased with increasing thickness. High thickness dependency of the proton conductivity was observed at low relative humidity. It diminishes with increasing relative humidity and becomes the lowest at 95% RH. At 40% RH, the conductivity increased more than one order of magnitude as the film thickness increased from 4 nm to 300 nm whereas the difference is around 1/3rd of an order of magnitude at

95% RH. Below 40% RH, the impedance response for the 4 nm film was such that the proton conductivity could not be determined.

6.3.2.3. Proton conductivity – un-annealed vs annealed thin films

There is a significant difference in impedance responses between unannealed and annealed films as discussed in the earlier of this section. In this subsection, the proton conductivity of Nafion® thin films – 4 nm to 300 nm, at a specific RH and temperature has been compared.

The proton conductivity of the unannealed and annealed films is compared in the Figure 6.14. As indicated from the impedance response, the conductivity was reduced significantly due to annealing. In each film, at least three different films were measured after annealing and found the conductivity within 5 to 15% error. At 96 % RH, the proton conductivity increased with increasing film thickness in both unannealed and annealed form of the films. The most significant part is the reduction of the proton conductivity of the annealed films in an order of magnitude than the unannealed counterparts regardless of thickness. At 40% RH, the annealed film conductivity further reduced in two orders of magnitude than that of the un-annealed films. It can be summarized that regardless thickness of films, the proton conductivity suppresses more than one order of magnitude which corresponds to the 90 to 98% conduction loss. The exact reason of lower proton conductivity is not fully investigated. It has been confirmed that this is not due to the molecular damage as confirmed in the section 6.3.1.4. Moreover, the suppressed proton conductivity is due to the insufficient equilibration in water vapor has been ruled out by the discussed in the subsection 6.3.4.1.

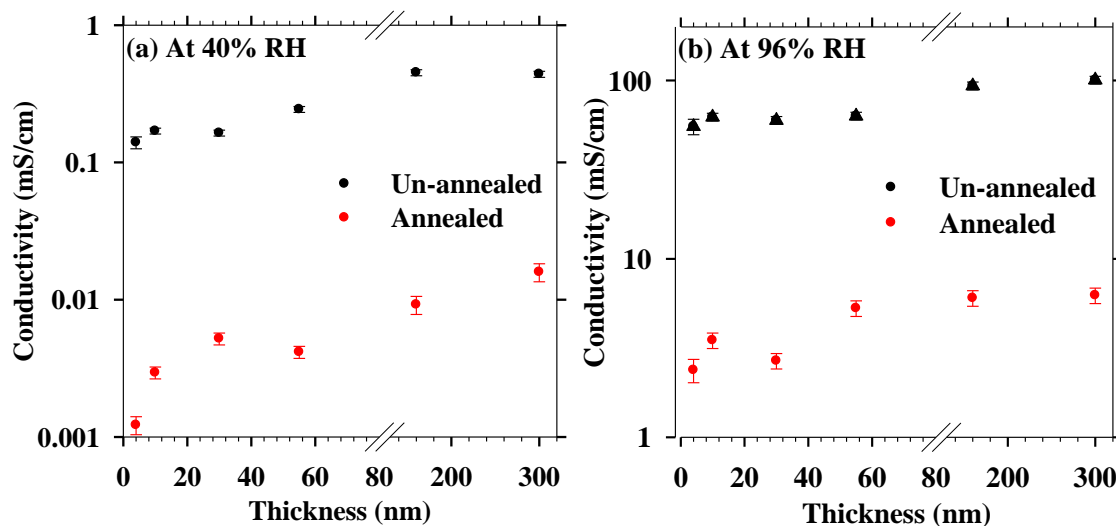


Figure 6.14: Proton conductivity at 60 °C of both unannealed and annealed Nafion® thin films as a function of film thickness (a) at 40% RH, (b) 96% RH.

6.3.3 Effect of Treatment Temperature on Surface and bulk properties of Nafion® thin film

In this section, both surface property (wettability) and bulk property (proton conductivity) of the 10 nm film was investigated in terms of thermal treatment temperature. The 10 nm film was of particular interest because of its pertinence to the Nafion® in PEFC catalyst layer. In each case, the unannealed film was taken and heated at a specific temperature for 1 h in vacuum oven. The contact angles of the 10 nm film in terms of treatment temperature have been plotted in Figure 6.15.

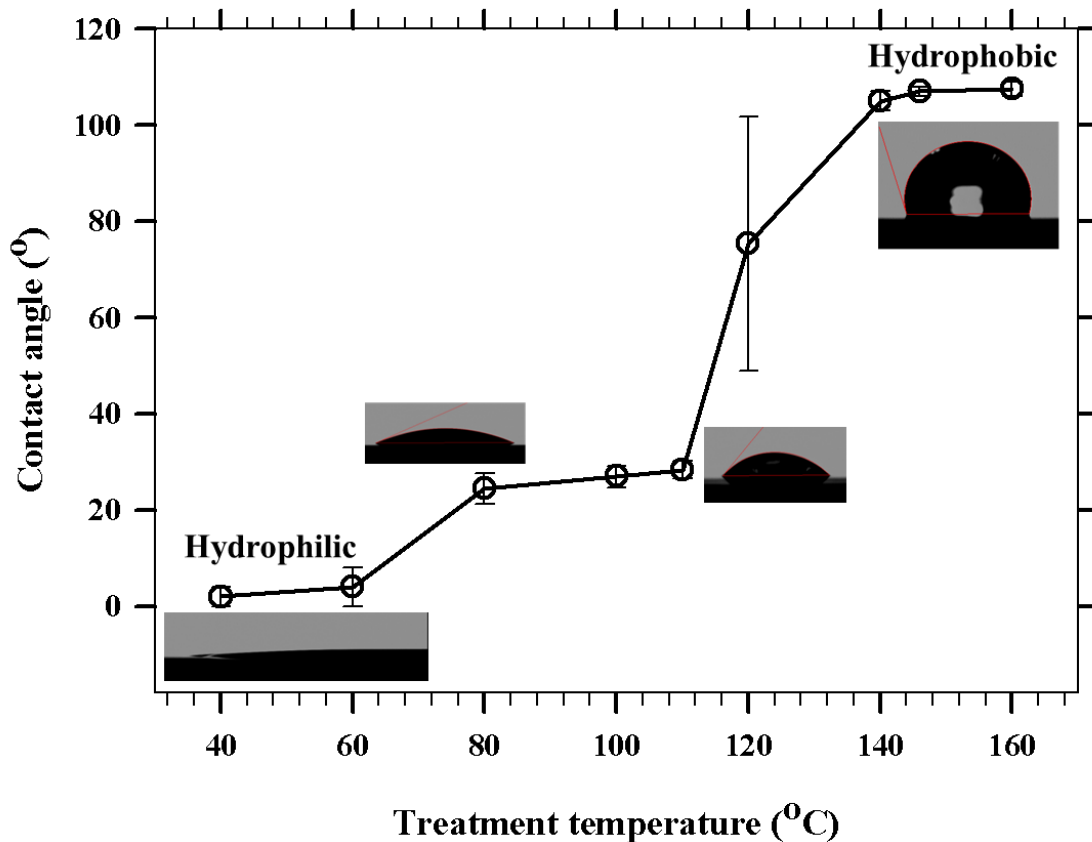


Figure 6.15: Surface wettability of heat-treated (annealed) ultra-thin (10 nm) Nafion® film. (Solid lines are only guides for eye). Error bar represents standard deviation of results obtained from four different points of each of triplicate samples.

It can be noted that the free surface wettability switches from super hydrophilic for the unannealed film to hydrophobic for the film annealed at 160 °C as discussed previously. Here, the film treatment at different temperature shows whether the surface wettability switching process occurs gradually or at a specific temperature. For the unannealed 10 nm film (dry at 40 °C), the contact angle showed an almost spreading behavior. The same spreading behavior was observed even after further treatment at 60 °C. While the films heat treated at 80, 100 and 110 °C showed small but significant change in contact angle ranging 25-27°. Incidentally, the 110 °C is slightly

higher than the bulk Nafion® T_g (109 °C) of Nafion®. Upon heat treating the film at 120 °C, i.e. above the bulk Nafion® T_g, a large variability in the surface wettability of the samples was observed. Some samples exhibited hydrophilic surface while some others showed hydrophobic surface. Furthermore, in some cases, higher contact angle appeared initially but quickly changed into a lower contact angle within a few seconds. It is noted that the lowest contact angle upon film treatment at 120 °C was higher than the contact angle observed for films treated at 110 °C. Interestingly, upon increasing the treatment temperature by another 20 °C, i.e. heat treatment at 140 °C, the film turned into a completely stable hydrophobic surface with a contact angle of 105±2.1° that did not collapse into lower angle even after several minutes. The contact angle reached a peak value of 107° after a heat treatment at 146 °C and remained constant with heat treatment at higher temperatures of up to 160 °C.

This is not entirely surprising, because for some thin polymer films due to favorable interaction with the substrate, the film T_g is observed to be higher than that of the bulk polymer [188]. It must be noted that the treatment time was kept constant in all our experiments, the treatment time effect was not examined. It is possible that the molecules may be mobile at 110 °C but not possess sufficiently high mobility to attain a relaxed state in the relatively short time. Nafion® is made of two distinct components – a hydrophobic Teflon-like backbone and a side chain terminating with hydrophilic, sulfonate-group-containing moiety. The small but measurable change in wettability for samples heated at 80-110 °C compared to untreated film may be explained considering the mobility of the side chain, which are significantly more mobile than the bulk backbone. The extremely hydrophilic surface of the unannealed films can be attributed to large number of sulfonic groups extending outwards of the free surface. These mobile chains may fold down or hide away from the free surface upon thermal treatment at sufficiently high temperature. Since, the surface of films heat treated at 80-110 °C is still hydrophilic, a large

number of hydrophilic side chains must still be present on the free surface. Finally, it is noticeable that contact angle did not change further upon heat treatment at temperatures higher than 146 °C, which indicates that the maximum surface reorganization occurs at ~146 °C.

In the previous section, it was found that when the film treated at 146 °C, the conductivity reduced significantly. It was conjectured whether the heat treatment temperature was significantly higher than that experienced by ionomer during the hot-pressing stage of MEA preparation and whether the ionomer structure could be damaged in some manner. To examine the effect of heat treatment, the films were heated at 110 °C and 160 °C and measured proton conductivity of those films at 60 °C has been presented in Figure 6.16. Recalling that the 110 °C heat-treated film showed only small change in surface wettability, it was hypothesized that only a small reorganization must have taken place and, accordingly, the proton conductivity of this film should not exhibit a high reduction. However, as shown in Figure 6.16, even the 110 °C heat-treated film exhibited significantly depressed proton conductivity. On the other hand, the proton conductivity of 160 °C annealed film were essentially the same as that of the 146 °C annealed film.

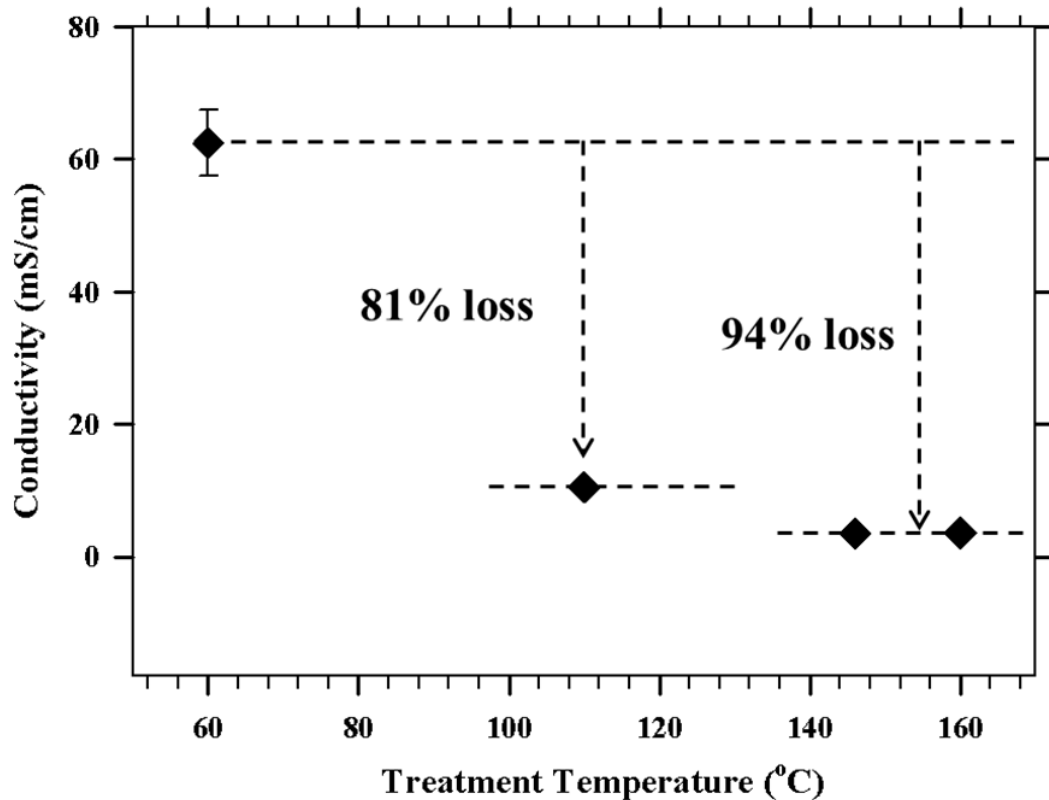


Figure 6.16: Proton conductivity of treated ultra-thin Nafion® film with different film treatment temperature at 95 % RH and 60 °C.

Based on the aforementioned discussions, a general conclusion can be drawn that the thermal treatment temperature affects both the bulk (conductivity) and surface (wettability) properties simultaneously and in a similar manner. Recalling that the 110 °C (correspond to bulk T_g) heat-treated film showed only small change in surface wettability, the partial reduction in the bulk transport properties at the same film treatment condition is highly consistent with the simultaneous changes. On the other hand, the films that were thermally treated at 146 °C and 160 °C exhibit similar bulk and surface properties indicating complete surface and bulk reorganization to have occurred upon annealing at 146 °C. It is worth noting that this is the first finding where it

has been shown that an elevated temperature treatment of Nafion® ultra-thin films has a significant impact on both surface wettability and its bulk proton conductivity.

The highly reduced conductivity of annealed thin films is confounding considering that an almost membrane-like-conductivity values have been reported for ionomers in CLs [183,184]. As discussed earlier, fabrication of MEA often requires a hot pressing step wherein the catalyst-coated membrane (CCM) is pressed against porous carbon backing at 120-195 °C to minimize contact resistance and enhance durability. Also, MEA prepared by decal transfer technique involves high temperature (usually 130 to 210 °C) transferring process [36,37]. Thus, if the ionomer in the CL were to exhibit property changes similar to that observed in the present study, then for MEAs subjected to a hot-pressing step were expected a significantly poor electrochemical performance that is limited by proton-transport in the CL. Experimental evidence suggests that instead of a loss in performance, an enhancement of that is observed for MEAs subjected to hot pressing indicating that heat treatment or annealing does not have adverse effect on CL ionomer conductivity.

6.3.4 Effect of external environments on the annealed Nafion® thin films.

In the previous Section 6.3.3, it was observed that the surface and bulk rearrangement of ultra-thin films occur simultaneously during heat treatment resulting in a hydrophobic surface and depressed proton conductivity, respectively. Several questions arise from these observations. First, whether the surface and bulk properties changes/regenerates at long exposure to ~100% RH? Second, what happens if the film is treated/exposed with liquid water for certain hours? In fuel cell, both liquid water and water vapor environment are experienced by the ionomer thin

film. Therefore, prolonged vapor and water exposure effect on the thin films is discussed in this section to answer the questions.

6.3.4.1. Water vapor exposure effect

Water vapor exposure effect on the surface wettability of Nafion® thin films: Water contact angle of vapor exposed films was measured to check the surface switchability. A comparison of water contact angles between the annealed films and sequential vapor exposed films has been presented in terms of thickness in the Figure 6.17. In this process, the annealed films (annealed at 146 °C) were hydrated with 100% relative humidity at room temperature for a week. Then contact angle was measured after similar treatment done for the unannealed film (dry at 40 °C in vacuum oven for 15 h). It was found that 10 to 300 nm films have very similar wettability as observed in the annealed films. The only exception was 4 nm film where the lower contact angle was observed after prolong vapor exposure. It indicates that the surface molecules are organized in such a way during annealing which cannot be altered or got back the surface properties similar to unannealed state even after prolonged high relative humidity exposure. As previously found that, the 4 nm film had an incomplete orientation at 146 °C, upon annealing it may go into little reorganization resulting lower contact angle.

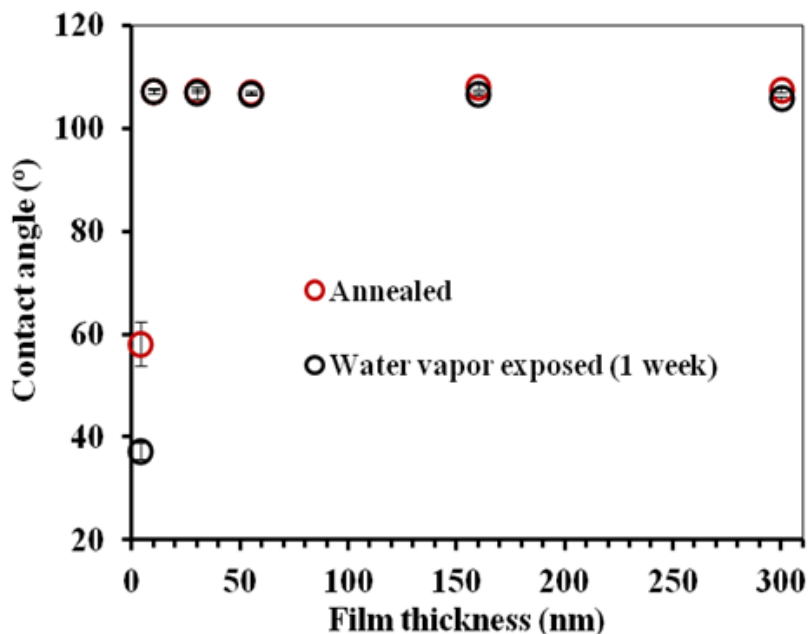


Figure 6.17: Water contact angle of Nafion thin films - Annealed (red open circle) and water vapor exposed for a week (black open circle), at ambient measurement condition.

Water vapor exposure effect on the proton conductivity of Nafion® thin films:

Impedance measurement of annealed thin films was conducted by exposing the films to high relative humidity (96% RH) for long period. This experiment was aimed at investigating whether the observed depression in conductivity was caused by insufficient equilibration and if long exposures to high RH would regenerate the conductivity.

In particular, impedance data was monitored on 10 nm film at a fixed 100 Hz frequency during prolonged exposure at relative humidity 96% and 30 °C over an 18 h period. The real impedance at 100 Hz in terms of time has been presented in Figure 6.18. At each 6 h of equilibration at such high RH, impedance data was collected in the full range of frequency (10 MHz to 1 Hz) as shown in Figure 6.18b. First of all, the impedance was almost constant with little fluctuation over the time. Second, the impedance spectra after each 6 h equilibration were

super imposed each other. Therefore, it indicates that prolong exposure of the annealed film to high RH does not change film resistance and corresponding proton conductivity as long as it is completely equilibrated. It also noted that this phenomenon was also observed irrespective of the film thickness. Long time vapor exposure at high temperature up to 60 °C also did not help to regenerate the proton conductivity.

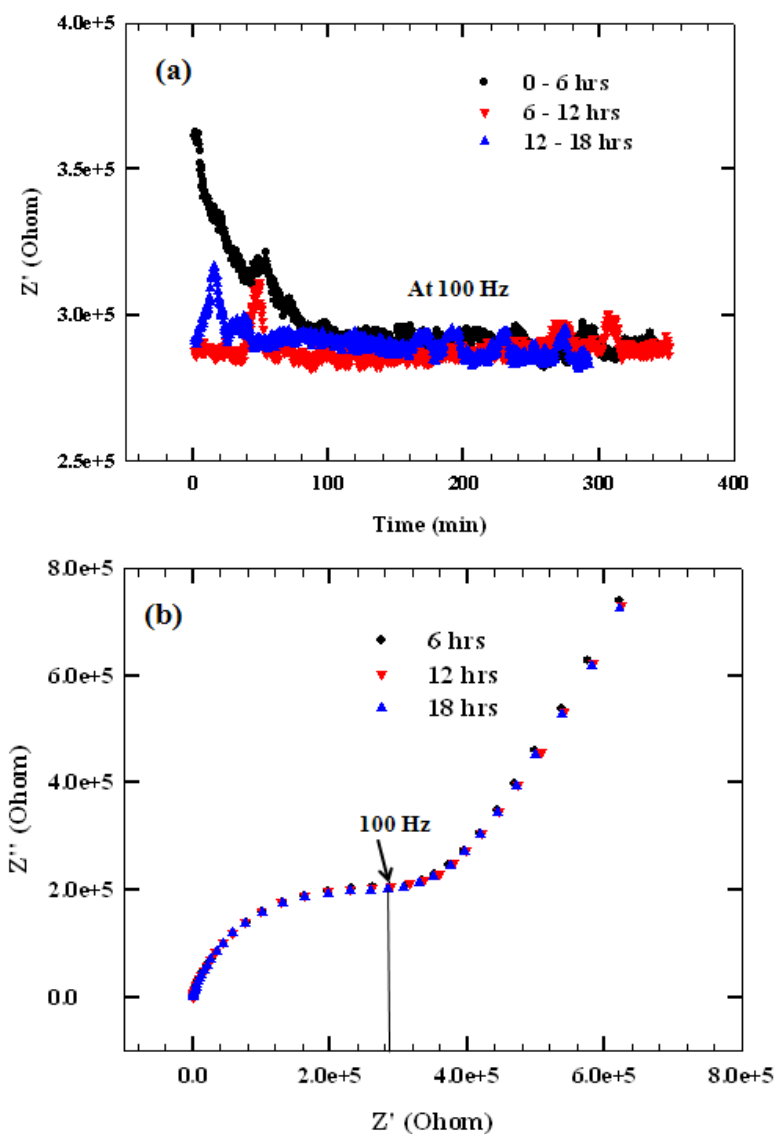


Figure 6.18: Impedance response of 10 nm Nafion® film exposed to 95% RH at 30 oC over 18 hours (a) fixed frequency (100 Hz) impedance monitored over 360 mins (6 h) periods of

0-6h, 6-12h, 12-18 h. (b) impedance spectroscopy data (10 Mhz-1 Hz) after 6, 12 and 18 h exposure.

In summary, the surface of annealed film behaves similarly to that of membrane. In membrane, the presence of a hydrophobic surface layer is well discussed which show hydrophobic characteristics even after exposure at 97% RH [69]. This hydrophobic surface layer is also identified as a possible cause of lower uptake in membrane in vapor atmosphere than that liquid water environment. In contrast, the lower water uptake might cause due to high crystallinity of the Nafion® thin film upon annealing [11]. Therefore, the hydrophobic surface layer and lower water uptake might be responsible for depressed proton conductivity where water vapor cannot break the rigidity of the layer.

6.3.5.2. Liquid water exposure effect

In this section, the effect of external liquid water treatment rather water vapor, on the surface wettability and proton conductivity of the thin films varying thickness is discussed. Experiments were carried out wherein the films were exposed to liquid water. The film was fully covered with Millipore water and kept in a closed environment where the water evaporation was negligible during the exposure period – 24 h or more. Then the water was dried out on the sample to ensure, no Nafion® is washing out with the exposed water.

Liquid water exposure effect on the surface wettability of Nafion® thin films: The liquid water equilibrated film was dried again by N₂ gas blow and subjected to same treatment step as that for “unannealed” film (drying in the vacuum oven for overnight at 40 °C). Next, the

water contact angle was measured at ambient condition. The contact angle was monitored and recorded initially within 5 sec and after each 30 sec. The results are presented in Figure 6.19.

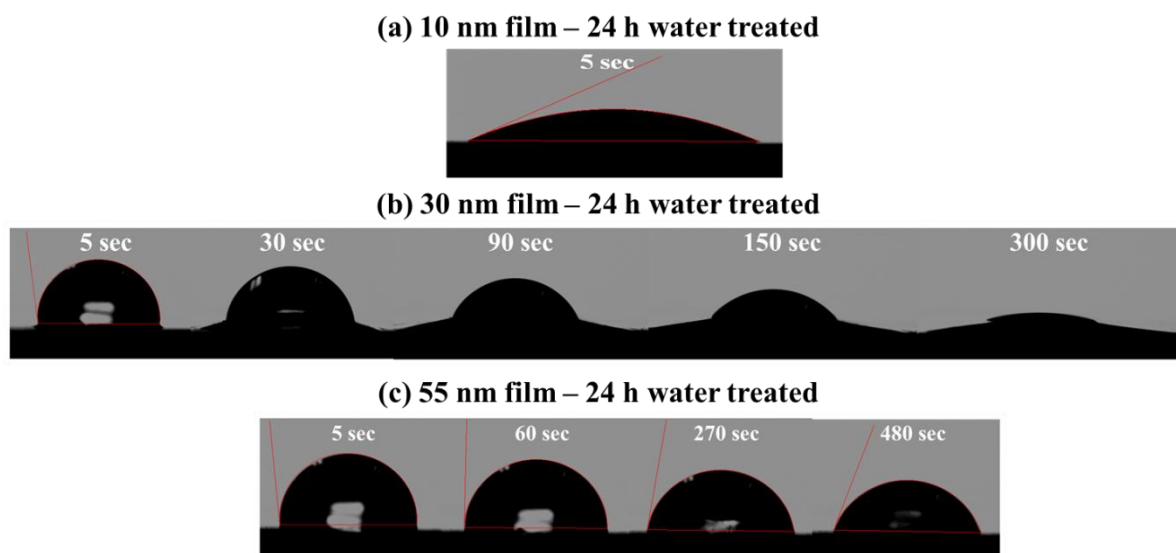


Figure 6.19: Water contact angle and time effect on liquid water treated films with the thicknesses (a) 10 nm (b) 30 nm and (c) 55 nm.

It was found that the free surface of the 10 nm annealed film turns hydrophilic after water exposure for 24 h similar to that of the unannealed films. In contrast, the 30 and 55 nm films showed hydrophobicity resulting in contact angle of $\sim 100^\circ$, which is slightly lower than that of annealed films ($\sim 107^\circ$). Interestingly, the water drop on the 30 nm film started spreading on the film within first few seconds and complete spread by 300 sec, though some water might get evaporated besides spreading. It might happen due to incomplete reorientation. However, the 55 nm film showed stable hydrophobicity as there was no sign of spreading of water droplet with increasing time. As shown in the Figure 6.19, even after 480 sec, the diameter of water droplet did not change but size of the droplet got smaller due to water evaporation. The droplet was

disappeared with further increasing time rather spreading or breaking down to smaller contact angle.

The main point is that the thin Nafion® films reorganize and tend to return to its unannealed state in the presence of liquid water. It is assumed that the hydrophilic sulfonate group hides in the bulk in the dry environment and get back to the surface in the water atmosphere due to high affinity for water. However, the polymer dynamics are highly regulated by the thin film thickness. A similar but opposite phenomenon observed for heat treatment and water treatment of thin films. In both cases, 30 nm is the characteristics thickness where incomplete reorientation happens. During annealing, there was a slower mobility of polymers with decreasing thickness of the film. In contrast, there was a faster mobility of polymers with decreasing thickness upon water treatment. The first issue was explained by the confinement effect in the earlier section 6.3.1. The latter issue may be due to the high restoring force of the confined polymer wherein the polymers in the thinner films relax faster in the presence of water where the role of substrate is vital. However, the free surface for the 10 nm film goes back to hydrophobic again due to annealing for the second time at the same annealing condition. The repeated switchability has been summarized in the Figure 6.20.

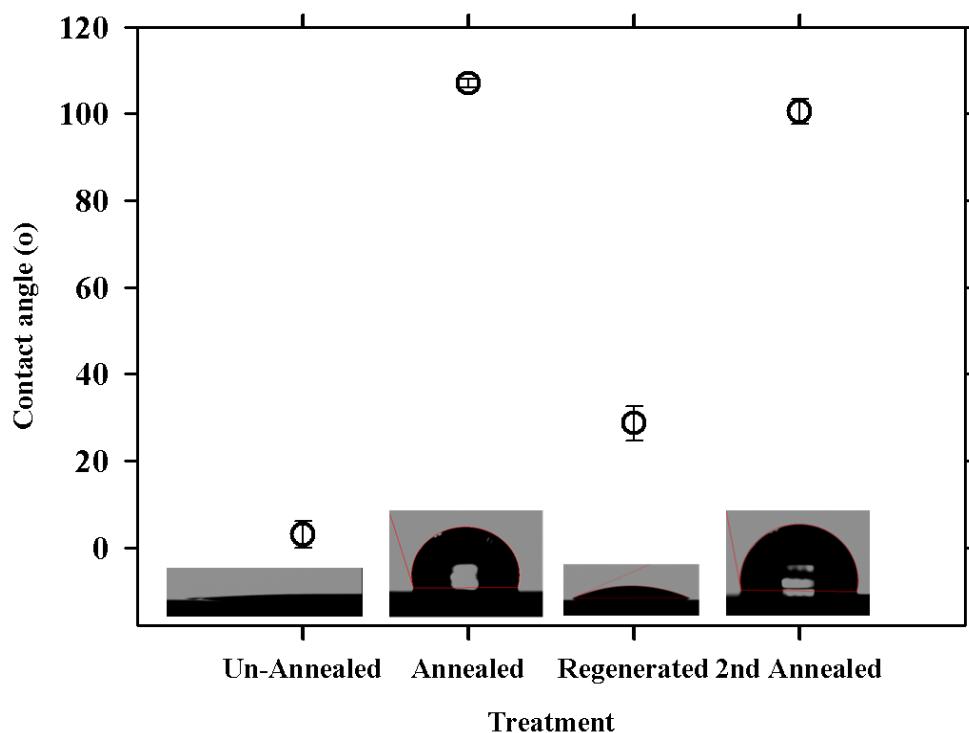


Figure 6.20: Switchability of surface wettability of the 10 nm ultra-thin film subjected to thermal annealing (annealed film) and liquid water exposure (regenerated film).

Liquid water exposure effect on the proton conductivity of Nafion® thin films: To investigate the liquid water exposure effect on the proton conductivity of the annealed thin films, at first, the 55 nm annealed film was treated by water for 24 h. It was followed by impedance measurement and then exposed to liquid water for even extended hours. The impedance response at 60 °C and 95% RH of the unannealed, annealed, and the water-exposed annealed films are presented in Figure 6.21. For the film exposed to liquid water for 24 h, the high-frequency semi-circle attributed to film resistance is higher than that of the un-annealed film but appears to be lower than that of annealed film as shown in the Figure 6.21. This finding highly correlates with the surface wettability, which indicates that 24 h water exposure is not sufficient to reorganize

polymer to get back to the original wettability and proton conductivity at least in this thickness scale. The measurement was repeated with the same 24 h water treatment on the same film followed by impedance measurement in the same protocol. Very similar impedance response to the first water treated film was given which straightened to our hypothesis – 24 h is not good enough to achieve complete reorganization in this thickness scale. The same film was further exposed to 96 h (4 days) and collected the impedance response. Interestingly, it was found that the diameter of the semicircle was almost overlapped with the response of the un-annealed film.

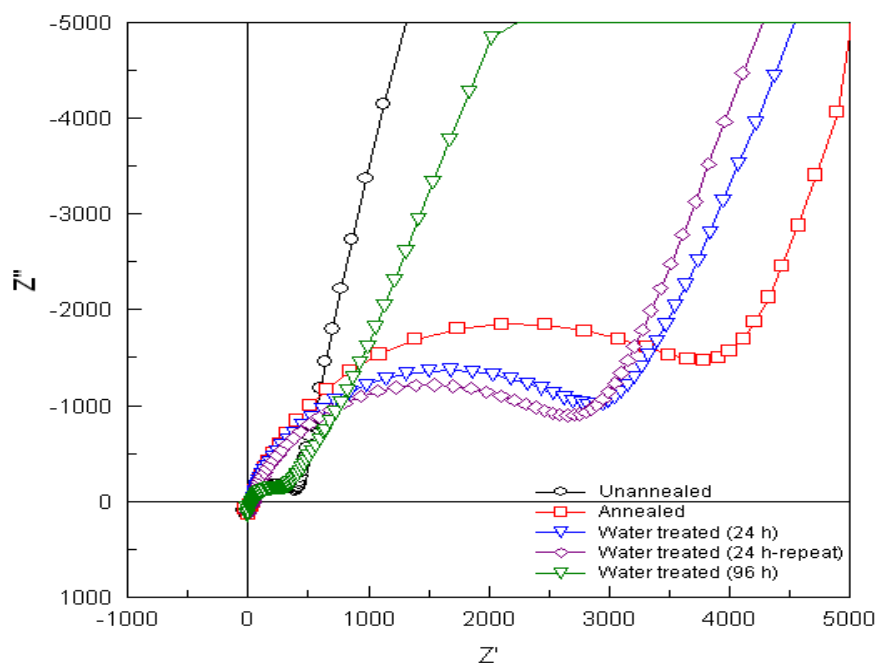


Figure 6.21: Impedance response of 55 nm films – unannealed (black open circle), annealed (red open square), 24 h water treated (blue open triangle), 24 h-repeat water treated (purple open diamond) and 96 h water treated (green open triangle).

The proton conductivity of the 55 nm at 60 °C and different RH has been plotted in terms of treatment condition in the Figure 6.22. The truncated terms - Un-ann, Ann-1st, WT (24 h) and WT (96 h) have been used for the film treatment conditions - Un-annealed, 1st Annealed, 24 h

Water treated and 96 h Water treated respectively. It was found that proton conductivity of 24 h water treated film was very similar to the annealed films in the RH range 20 to 96%. In contrast, the conductivity of 96 h water treated film went back to unannealed film after 96 h water treatment at high RH where it did not recover completely at low RH. It is noted that the 55 nm film takes longer water exposure time to be regenerated.

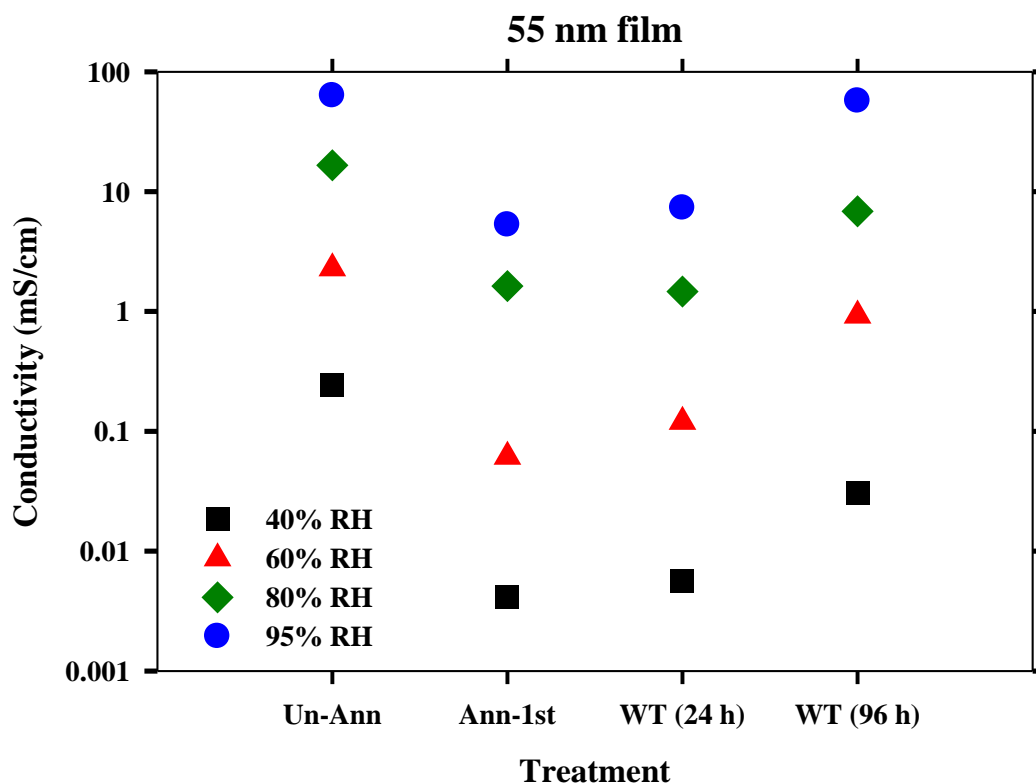


Figure 6.22: Conductivity vs relative humidity of the 55 nm films at 60 °C and different treatment condition – unannealed (black open circle), annealed (red open square), 24 h water treated (blue closed triangle) and 96 h water treated (green closed diamond).

To investigate the thickness effect, impedance response of water treated 10 nm film was compared between the un-annealed and annealed films in the Figure 6.23. The impedance measurement was conducted at 60 °C and 95% RH in all cases. It was found that the semicircle

diameter of the water treated film was smaller than that of the un-annealed film. It indicates that the film conductivity regenerated and even achieved higher proton conductivity over the original film. The water treated film was annealed again according to the annealing protocol termed as 2nd annealed film. Interestingly, it was found that the semicircle diameter did not go back to the annealed state again but staying in between unannealed and water treated film response.

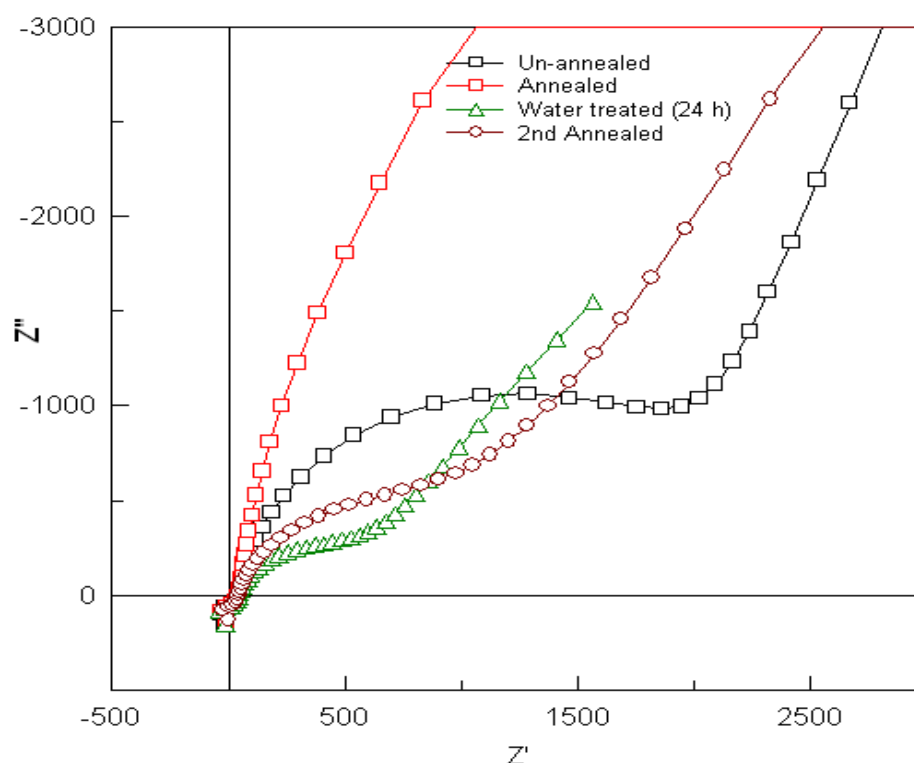


Figure 6.23: Impedance response of 10 nm films – unannealed (black open circle), annealed (red open square), 24 h water treated (green open triangle).

Unlike the 55 nm films, 24 h water treatment was sufficient to regenerate the protonic conductivity for 10 nm annealed film. As shown in the Figure 6.24, the 24 h water treated film (regenerated film) exceeded the proton conductivity than that of the unannealed 10 nm. Similar to the switchability of surface wetting properties upon water treatment, there is a thickness effect on

the regeneration of proton conductivity. Higher water exposure time is required for film with higher thickness.

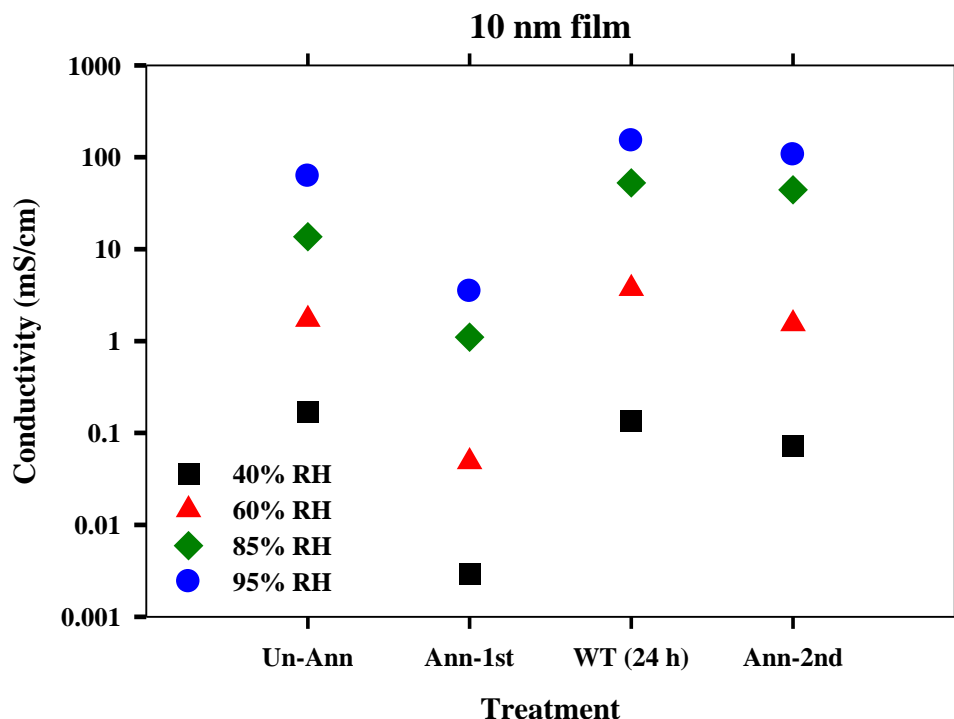


Figure 6.24: Proton conductivity for 10 nm Nafion® film subjected to the various treatments.

It can be summarized that the surface and bulk reorganization of Nafion® molecule occur simultaneously in the presence of water. The phenomenon is thickness dependent. This phenomenon is highly correlated to the annealing effect in terms of thickness dependency but opposite in terms of molecular mobility. During annealing, Nafion® is highly confined and show restriction in mobility with decreasing thickness. In contrast, the high restoring force of Nafion® molecule is responsible to higher in mobility in presence of water with decreasing thickness. However, the time scales of those change and associated energy have not been investigated. On a separate note, the 2nd time annealing of the 10 nm film showed comparable proton conductivity to the unannealed counterpart rather go back to depressed proton conductivity as much as annealed

film as shown in Figure 6.24. Some hypothesis and deductions can be made from these observations. Expectedly, annealing induces relaxation/reorganization of the polymer molecules. The relaxation comprises of mobility of both the longer-chain backbone as well as the much shorter side-chains (~1 nm). Given the size and structure of the backbone and the side chain, it can be argued that the side chain mobility is faster than that of the backbone. The 1st-time annealing results in a major reorganization of the molecules (side chain) on the surface and in the bulk. Kongkanand [12] found that the rate of water uptake for annealed Nafion® films was greatly reduced compared to the unannealed films. They accredited this to the formation of a hydrophobic skin at the free surface of the annealed film. Thus, it would be tempting to attribute the lower conductivity of annealed films to lower water uptake because of its hydrophobic skin. However, since the 2nd-time annealed film, which also exhibits a hydrophobic surface, shows high conductivity rules out that the hydrophobic skin is primarily responsible for low conductivity. Therefore, a possible explanation of low proton conductivity of 1st time annealed may be the formation of static crystalline domain due to high temperature annealing which may impede water uptake and could be reason of significant reduction of proton conductivity. Without microstructural information, any further hypothesis regarding annealing and regeneration due to liquid water contact will be highly speculative. A more understanding about surface induced polymer dynamics is necessary to explain those interesting findings.

6.3.5 Activation energy for ionic conduction

Measurement of the proton conductivity at different temperature at constant RH allowed the determination of activation energy for proton conduction. The activation energy can provide some insight on the similarities or differences in the mechanism for proton conduction amongst the unannealed, annealed and water treated films.

Figure 6.25 shows Arrhenius plots of the annealed and water treated films. Proton conductivity was measured in the range of temperature 30 to 60 °C at each RH (40 to 96% RH). It was observed that the proton conductivity data was nicely fitted with the Arrhenius equation. Activation energy was calculated from the slope of the Arrhenius plots.

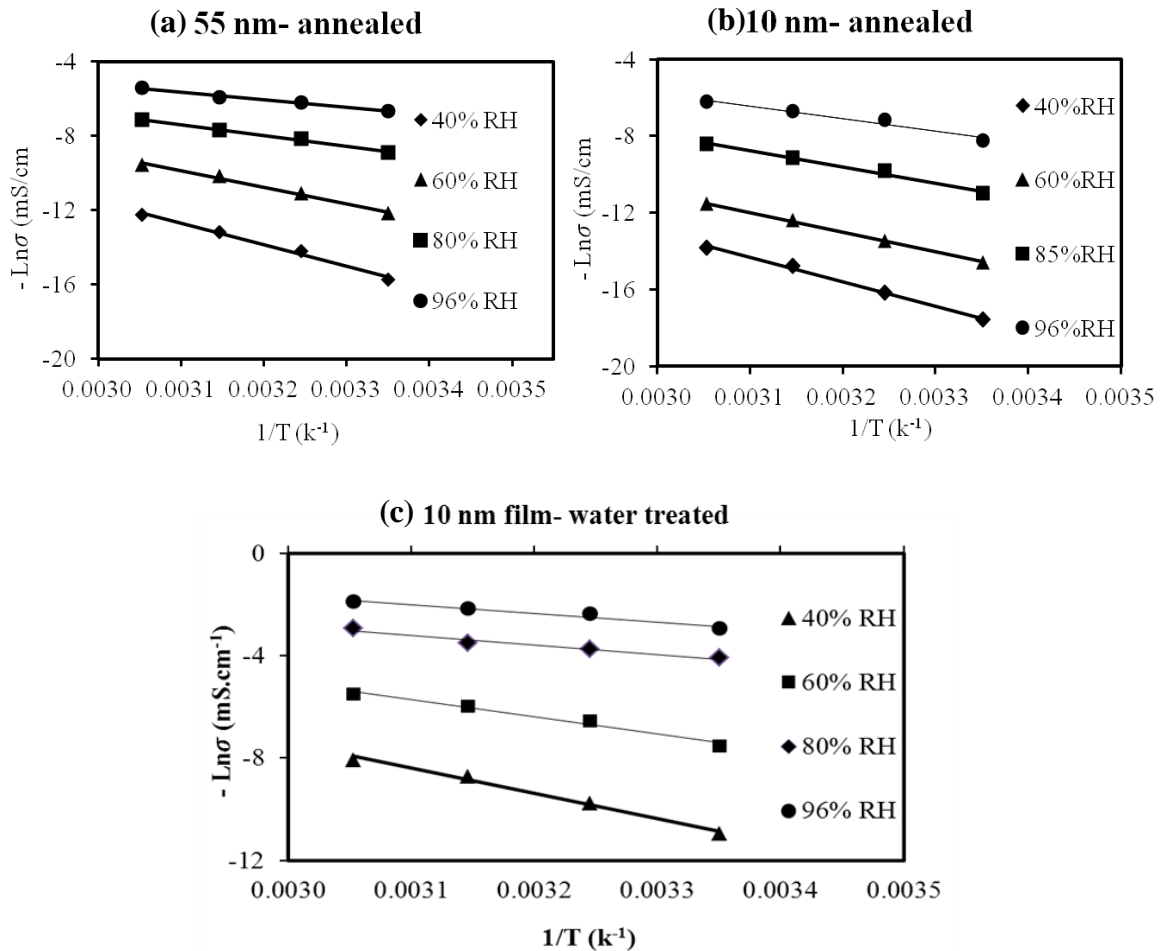


Figure 6.25: Arrhenius plots of annealed and water treated films – (a) 55 nm (annealed), (b) 10 nm (annealed) and (c) 10 nm (water treated).

A comparison between activation energies of the un-annealed and annealed 55 nm films have been shown in Figure 6.26. It was found that the activation energy significantly increased upon annealing where the difference became higher with decreasing RH. It indicates that the proton conductivity in annealed films is further restricted by the high associated energy in proton mobility. The finding is consistent with the low proton conductivity in annealed film. To examine the thickness effect, the activation energy of much thinner film was also investigated.

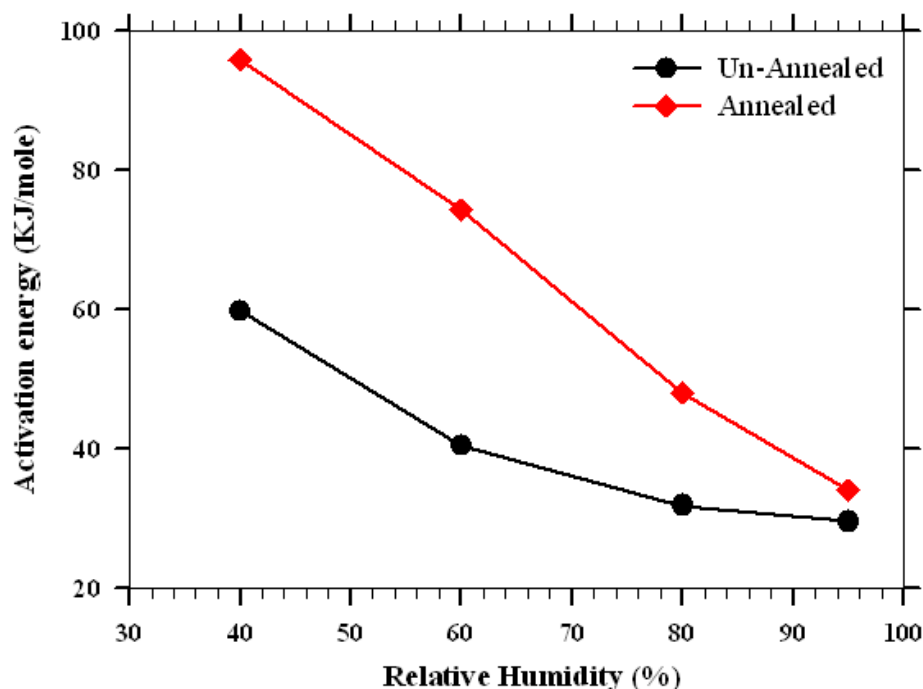


Figure 6.26: Activation energy of 55 nm film as a function of RH for untreated (●), and annealed (■).

The activation energy of the 10 nm films at three different treatment conditions have been plotted in Figure 6.27. Similar to the 55 nm film, activation energy of the 10 nm film significantly increased upon annealing. Unlike the 55 nm film, the activation energy of annealed film was nearly two times compared to that of the unannealed films. This higher activation energy may be a result of less proton mobility due to less water uptake or some other intrinsic properties

changes. At 95 % RH, the activation energy of the regenerated film (24 h water treated film) is almost the same as that observed for the unannealed film but the proton conductivity is higher in the regenerated film than that of the unannealed film. On the other hand, the proton conductivity for the regenerated and unannealed films at 40 % RH is comparable whereas significant differences in the activation energy can be noted. Therefore, it is difficult to make a direct correlation in between the activation energy and the proton conductivity.

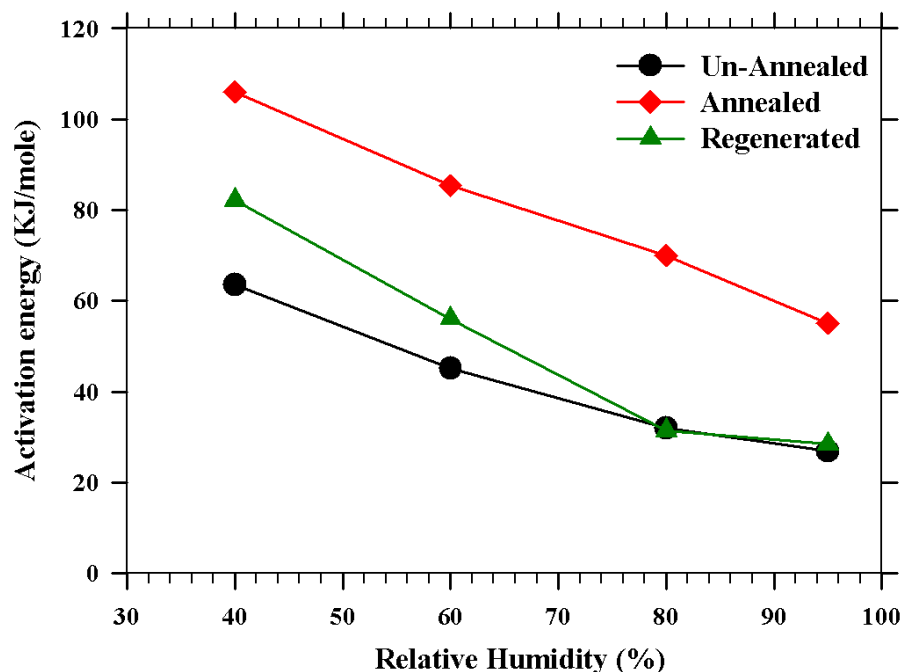


Figure 6.27: Activation energy of the 10 nm film as a function of RH for untreated (●), annealed (■) and water treated (▲) films.

6.4 Conclusions

Thermal annealing has a great impact on the morphology and properties of the thin Nafion® films. The change in morphology and properties are highly thickness dependent. A number of unknowns have been unveiled for the first time in the following.

1. Surface wettability of Nafion® films switches from hydrophilic to hydrophobic upon annealing. The switchability is restricted with decreasing thickness and required more energy, which might be due to interfacial wetting interaction and confinement.
2. Nafion® thin films do not dewet unless the film thickness goes to the thinnest, 4 nm thickness. High aggregation behavior of persulfonated Nafion® polymer might be the reason of not to dewet, contrary to some other block copolymer.
3. Proton conductivity of the Nafion® thin films upon annealing goes down in many folds irrespective of thickness. Once annealed, the proton conductivity is decreased with decreasing thickness. The possible explanation might be static crystalline domain formation due to annealing which impede water uptake [11].
4. A simultaneous hydrophobic switching of the film surface and the suppression of proton conductivity happen in terms of treatment temperature. It indicates that surface and bulk rearrangements of the Nafion® thin films are a simultaneous process.
5. Prolonged exposure of water vapor cannot regenerate the surface and bulk properties of Nafion® thin films once the surface switched to hydrophobic or the proton conductivity suppressed upon annealing.
6. In contrast, exposure to liquid water regenerates both surface and bulk properties. The water treated regeneration process also thickness dependent. In presence of water, the switchability of properties enhanced with decreasing thickness. The possible reason might be high restoration force of substrate/film interfacial Nafion® molecules upon confinement. Water treatment effect is highly correlated to the annealing effect in terms of thickness dependency but opposite in terms of molecular mobility.

Chapter 7

Substrate Effect on Ultrathin Nafion® Films

7.1 Introduction

In conventional PEFC fuel cell, Pt catalyst and carbon support are used in the catalyst layers (CLs). Recently, a number of non-Pt catalyst and non-carbon supports are being considered to enhance the performance and durability [190]. Nevertheless, ionomer (Nafion®) exists as a thin film on the catalyst and support in the CLs. The extent of interaction between ionomer and substrates (catalyst and support) determine the stability of catalyst as well as CLs. On the other hand, the nature of substrates has an influence on the thin film nano-structure that further determines the transport properties in the CLs. So far, the investigation has been restricted on spin-coated films up to thickness 50 to 100 nm on a limited number of substrates [8-13]. In those studies, substrate induced variation in morphology and nano-orientation of Nafion® ionomer are evident. For example, Bass *et al.* [10] reported parallel and perpendicular orientation of Nafion® bundle on SiO₂ and OTS substrate respectively. Wood *et al.* [9] found that restructuring in Nafion® ionomer thin film happen during switching the substrate wettability - hydrophilic to hydrophobic. However, the nature of characteristics thin film (self-assembled) in the length scale (thickness 4 to 10 nm) of the PEFC CLs is completely unknown. In order to introduce a larger scope in high efficient catalyst and material selection and development, an understanding of the ionomer/substrate interaction and substrate influences on the morphology and properties of the ionomer film is required.

In the previous chapters, the characteristics of the Nafion® thin films on SiO₂ have been investigated. The effect of dispersion medium compositions on interfacial interaction and film morphology was examined. Moreover, the surface wettability and bulk proton conductivity have also been investigated in terms of film thickness, thermal treatment and liquid water exposure. In this chapter, the knowledge is extended on some other substrates including Carbon, Platinum (Pt), Gold (Au) and modified silicon wafer like Octadecyltrichlorosilane (OTS)/SiO₂. The main goal of this chapter is to investigate the substrate effect on the morphology and properties of the Nafion® thin films. More specifically, the effects of a number of influencing parameters including composition of dispersion medium, wetting property of the substrates (hydrophilicity/hydrophobicity), Nafion® concentration, and heat treatment, are investigated in determining the morphology, wettability and water uptake of the Nafion® thin film.

7.2 Experimental

7.2.1 Materials

Commercially available 5 wt% Nafion® (20% water and 75% alcohol mixture) was used as the stock Nafion® dispersion. Previously, Chapter 4 to Chapter 6, the experiments were limited to the use of thermally grown SiO₂ (300 nm)/Si wafer as substrate. In this chapter, a number of substrates including silicon with native SiO₂, C, Pt, Au and OTS modified silica are introduced. For C, Pt and Au, a thin physical layer of the respective materials has been deposited on the silicon wafer. In contrast, a chemically modified OTS layer has been introduced on silicon wafer. Carbon and Au substrate were fabricated in the nanofabrication lab of Penn state University, the procedure has been described elsewhere [192]. Pt substrate was obtained from

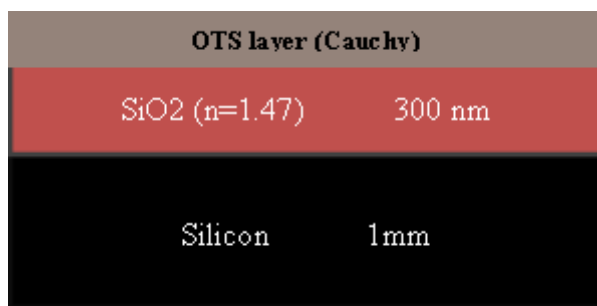
NINT, Alberta. OTS modified silicon wafer was prepared, optimized and characterized in house. The modification process has been described below.

SiO₂ Surface modification by silanization: SiO₂ terminated Si substrate was cleaned by HCl;MeOH (50:50) mixture followed by 18 M H₂SO₄. Before and after of each steps, the substrate was washed by ethanol, acetone and Millipore water. After cleaning, the substrate was dried by dry air blow and kept under uv light at O₃ atmosphere for overnight. As a result, the SiO₂ substrate was maximized with surface hydroxyl group. The resulted zero degree contact angle of water was considered as a proof of hydroxyl group formation and maximization. Next, the pre-cleaned silicon wafers were dipped into 1mM octadecyltrichlorosilane (OTS) in anhydrous toluene for 0.5 h to 3 h. The reaction was conducted in a dry box at N₂ atmosphere and room temperature. The modified substrate was washed by toluene several times and dried by air blow. The modified substrates were also sonicated for 2 min in toluene for removing any possible adhering layer and washed again by chloroform and then dried in vacuum at 40 °C. Several reactions were carried out for optimizing the reaction parameters to determine the extent of the modification. The reaction condition and parameters have been summarized in Table 7.1.

Table 7.1: Reaction condition of OTS modified silica substrate preparation

| <i>Reaction parameters</i> | |
|----------------------------|--------------------------------|
| Reactants | Octadecyltrichlorosilane (OTS) |
| Temperature | Room temperature (~25 °C) |
| Solvent | Toluene |
| Reactant concentration | 1 mM |
| Reaction atmosphere | N ₂ atmosphere |
| Reaction time | 0.5 h to 3 h |

Ellipsometry thickness measurement of OTS layer: Ellipsometry of different OTS modified wafers was measured at three different angles in the wavelength 200 to 800 nm. The spectra were fitted with a 3-layer Cauchy model shown in Figure 7.1. The fitting results have been summarized in the Table 7.2.



Cauchy model

Figure 7.1: Cauchy model for ellipsometry data fitting to extract OTS layer thickness.

Table 7.2: The summarized parameters of OTS layer on SiO₂ with the variation of reaction time.

| Reaction time | Cauchy Coefficients | | | Thickness (nm) | RI at 550 nm | Non-uniformity (%) | MSE |
|------------------------|---------------------|---------|---|-------------------|-----------------|-----------------------|------|
| | A | B | C | | | | |
| 0 h(SiO ₂) | | | | 300.38±0.13 | 1.47 | 1.01 | 2.25 |
| 0.5 h | 1.396 | 0.03816 | 0 | 3.33±0.08 | 1.41 | 1.68 | 2.27 |
| 1.0 h | 1.41 | 0.00434 | 0 | 3.03±0.06 | 1.42 | 1.08 | 1.74 |
| 1.5 h | 1.412 | 0.00924 | 0 | 3.92±0.07 | 1.44 | 1.42 | 1.82 |
| 2.0 h | 1.429 | 0.00421 | 0 | 3.65±0.05 | 1.44 | 1.06 | 1.28 |
| 2.5 h | 1.417 | 0.00642 | 0 | 3.42±0.05 | 1.43 | 0.97 | 1.27 |
| 3.0 h | 1.400 | 0.00742 | 0 | 3.23±0.06 | 1.42 | 1.06 | 1.48 |

The quality of fit was excellent as can be justified by the low MSE values. Time dependent thickness and RI of OTS layer have been further plotted in the Figure 7.2. It was found that OTS thickness varied little bit with reaction time. Interestingly, thickness and refractive index of OTS layer increased up to 1.5 h reaction time and then started decreasing. At this reaction time, thickness scale is also comparable to the theoretical molecular length of OTS. Therefore, it can be argued that OTS monolayer formation occurred at 1.5 h reaction time. A water contact angle of $\sim 106^\circ$ was obtained for OTS modified SiO_2 that is significantly higher than that of blank SiO_2 ($\sim 45^\circ$). The water contact angle is consistent with the literature reports for OTS modified wafer [191].

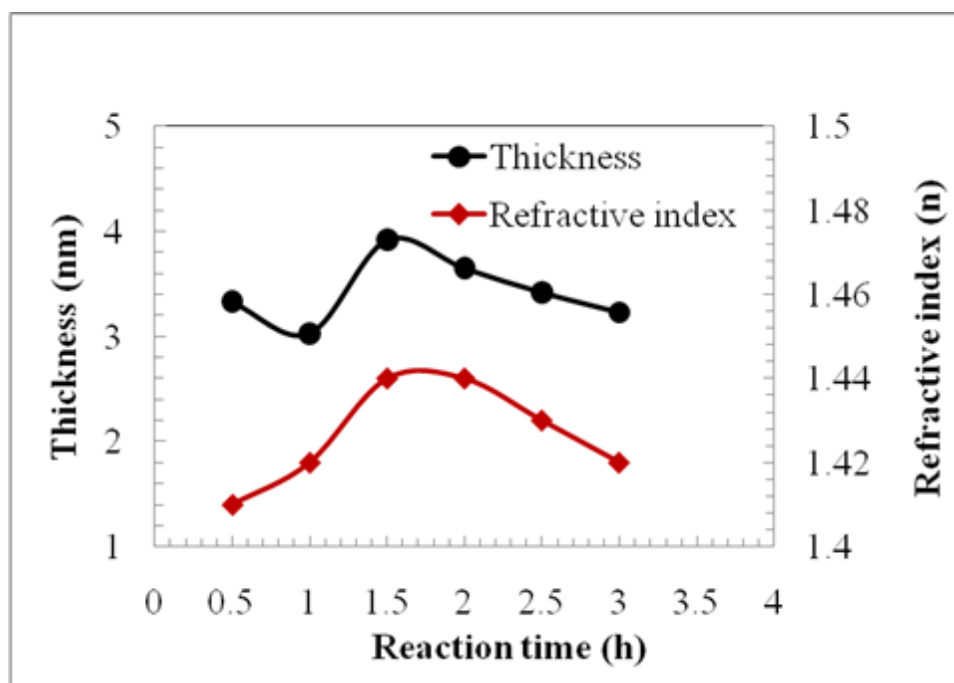


Figure 7.2: Variation of OTS layer thickness (black circle) and refractive index (red diamond) with reaction time.

7.2.2 Substrate cleaning

The substrates – Au and Pt, were soaked into acetone for 30 min, followed by sonication for 2 min in each of the following solvents: IPA, acetone and water. Finally, those were washed at least 3 times with IPA, acetone and Millipore water. The electrodes were dried by N₂ blow for 30 min and made ready for ultrathin film preparation on it. On the other hand, the substrate with carbon layer were gently washed by IPA and dried by N₂ blow before film preparation. For silicon wafer with native oxide, the same cleaning protocol as that employed for thermally grown SiO₂ was adopted (described earlier in the Section 4.2.1 of Chapter 4).

7.2.3 Film preparation and treatment

For self-assembled film preparation, same protocol as that employed for film preparation on SiO₂/Si wafer and described in the Section 4.2.1 was adopted. The 5 wt% Nafion® dispersion was diluted at 0.1, 0.25, 0.5, 1.0, and 3.0 wt% by adding IPA. Moreover, to investigate the effect of dispersion medium composition, a number of 0.1 wt% Nafion® dispersion with varying dispersion medium composition - IPA:Water; 0:100, 20:80, 50:50, and 80:20, were also prepared using 5wt% Nafion® dispersion in water. Next, the pre-cleaned electrodes were immersed in the diluted solution. It was found that 12 h is sufficient time to make a homogenous and continuous film on the SiO₂ substrate as described in the Section 4.3.1 of Chapter 4. Therefore, the substrate was taken out from the Nafion® dispersion after 12 h and dried in N₂ blow. Prior to film characterization, Nafion® thin film were further treated and classified into un-annealed (dry at 40 °C) and annealed (at 146 °C). The treatment protocols have been described in the Section 6.2.1 of Chapter 6.

7.2.4 Film characterization

The characterization of the film has been mainly restricted to the examination of surface morphology and wettability by AFM and water contact angle measurement, respectively. A key bulk characteristic, namely proton conductivity, of the thin film especially on C, Au and Pt could not be investigated. This is because of the inability to measure film resistance due to the highly conductive nature of the substrates. Nonetheless, another bulk property, the water uptake of the thin films was investigated by QCM (experimental protocol has been described in the Section 5.2.6 of Chapter 5).

AFM measurement: Surface morphology, roughness and film thickness of the Nafion® thin films were examined by AFM as per the same protocol described earlier in the section 4.2.2 of Chapter 4.

Contact angle measurement: The contact angle measurement procedure has been described earlier in the Chapter 4 and Chapter 6 for both unannealed and annealed thin films, respectively. The same protocols were adopted, however, it is noted that the reported contact angle in this chapter was recorded within 5 sec of the drop placement. For surface energy measurement three liquid contact angle techniques was adopted and surface energy was calculated according the XDLVO theory as described in the Section 3.2.4 of Chapter 3.

7.3 Results and Discussions

7.3.1 Dispersion medium effect on Nafion®/carbon interaction

The effect of dispersion media on the formation of self-assembled Nafion® thin film on the carbon substrate was investigated. 0.1 wt% Nafion® dispersion in various IPA:Water mixtures; 0:100, 20:80, 50:50, 80:20 and 100:0 termed as 100%, 80%, 50%, 20% and 0.4% water, respectively. The film morphology was investigated by AFM and has been presented in the Figure 7.3 below.

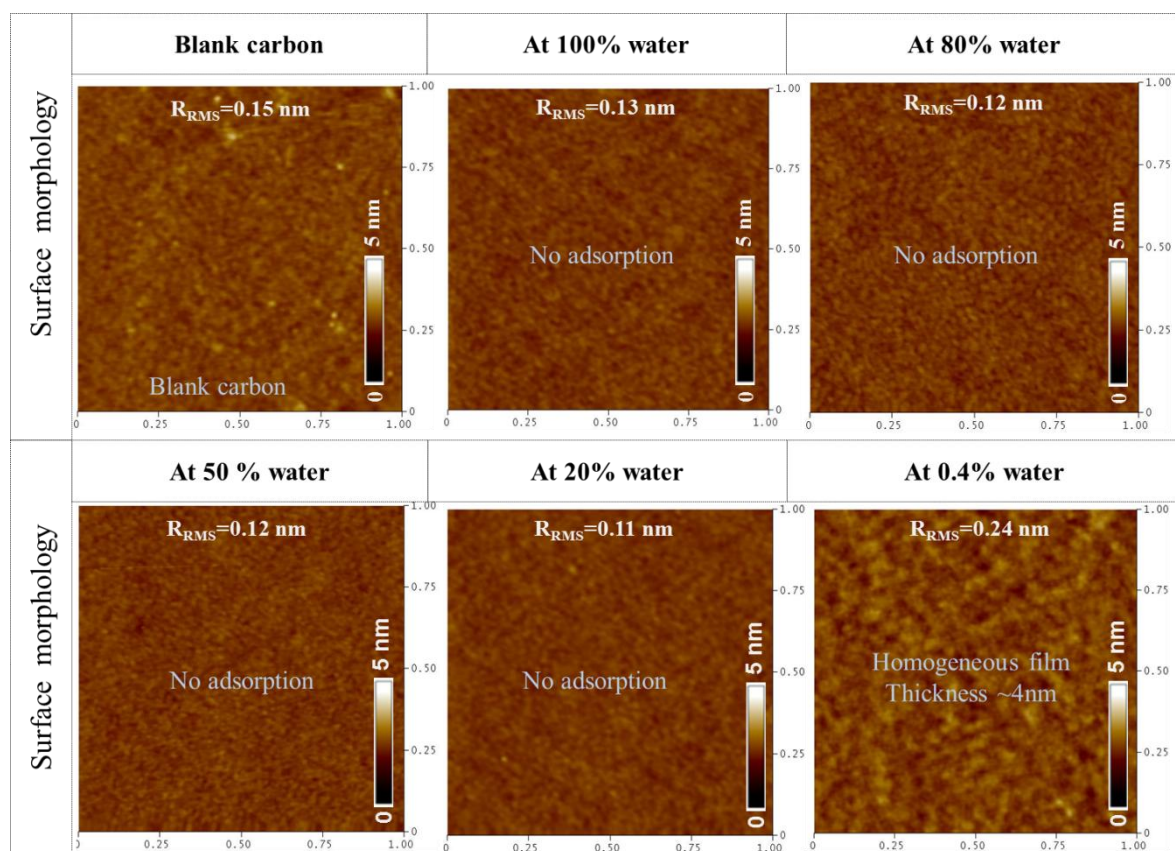


Figure 7.3: AFM height images (1 μ m X 1 μ m) of the self-assembled films on carbon substrate obtained from 0.1wt% Nafion® dispersion in different dispersion medium compositions.

AFM image and surface roughness of blank carbon show that the surface was smooth with negligible roughness. After the film preparation steps, several images of the thin films were

measured and presented in terms of the water content of the dispersions (100% to 0.4%). The morphology and roughness of the films generated from 100% to 20% water dispersions were as same as the blank substrate. This is indicative of no Nafion® adsorption on the carbon substrate from these dispersions. Attempt was made to scratch out the film by sharp needle and image the scratch by AFM following a method similar to film thickness measurement by AFM. Absence of line profile in the section analysis further confirms that there was no adsorption or self-assembly of Nafion® occurred. In contrast, the corresponding film of Nafion® dispersion in 0.4 wt% water showed the morphology and roughness that was significantly different from that of the blank substrate. The morphology and section analysis (not shown in the figure) were consistent with the continuous and homogeneous film surface. It is useful to mention that a scattered deposition of Nafion® ionomer bundles with almost constant height were observed for Nafion® dispersion in 100 to 20% water on SiO₂ as described in Section 4.3.2 of Chapter 4. The lack of adsorption/self-assembly of Nafion® on C substrate from the same dispersion medium composition indicates that there is a vital role of substrate in that process. Therefore, the interaction behavior between Nafion® ionomer and substrate is aimed to investigate in terms of substrate nature (hydrophilicity/hydrophobicity) and substrate wetting property (surface energy of the substrates). One of the particular interests is to make a correlation between the substrate surface energy and film morphology.

7.3.2 Substrate surface characterization

Three-liquid contact-angle method was employed for substrate surface energy measurements. In addition to water, contact angle measurements with another polar liquid (formamide) and an apolar liquid (diiodomethane) were carried out. The contact angles have been presented in terms of substrates in the Figure 7.4.

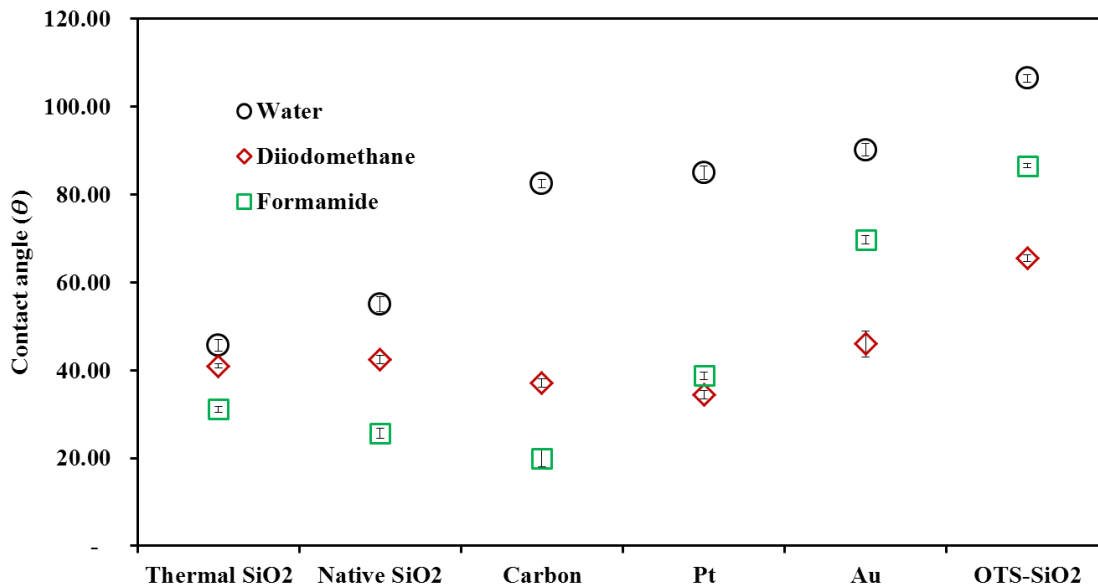


Figure 7.4: Contact angles of water, diiodomethane and formamide for different substrates.

Water contact angles represent the corresponding hydrophilicity ($\theta < 90^\circ$) and hydrophobicity ($\theta > 90^\circ$) of the substrates. Based on the water contact angles, the substrates have been classified into three broad categories i) hydrophilic – thermal SiO₂ and Native SiO₂, ii) intermediate – carbon and iii) hydrophobic – Pt, Au and OTS/SiO₂. OTS-SiO₂ has the highest hydrophobicity among the substrates. Other two liquid contact angles also varied with substrate as presented in the Figure 7.4.

The surface energy components of different substrates were calculated using XDLVO theory (discussed in section 3.2.4 of Chapter 3) and have been summarized in the Table 7.3. The total surface energy (γ^{total}) of the substrates follows the following trend: thermal SiO₂~native SiO₂ > Carbon ~Pt > Au > OTS/SiO₂. On the other hand, the substrates can also be distinguished into two distinct categories based on acid base component of surface energy (γ^{AB}), where SiO₂ belongs

to high energy and the rest of the substrates have comparatively low surface energy. In the next section, substrate induced film morphology is investigated in terms of substrate surface energy.

Table 7.3: The calculated surface energies of different substrates

| Films (nm) | γ^{LW} | γ^{+} | γ^{-} | γ^{AB} | γ^{total} |
|--------------------------|---------------|--------------|--------------|---------------|------------------|
| Thermal SiO ₂ | 38.15 | 1.24 | 29.38 | 12.07 | 50.2 |
| Native SiO ₂ | 37.68 | 2.94 | 15.62 | 13.56 | 51.2 |
| Carbon | 41.01 | 3.87 | 0.08 | 1.10 | 42.1 |
| Pt | 42.29 | 2.99 | 0.01 | 0.38 | 42.7 |
| Au | 36.16 | 0.04 | 3.36 | 0.73 | 36.9 |
| OTS-SiO ₂ | 25.29 | 0.09 | 0.67 | 0.49 | 25.8 |

7.3.3 Substrate effect on the morphology of the Nafion® thin films

The morphologies of Nafion® thin film on four different substrates including SiO₂, carbon, Au and OTS/SiO₂, obtained from 0.1 wt% Nafion® dispersion in 0.4% water, have been presented in the Figure 7.5. As discussed in the previous section, the surface energy of substrates followed the order SiO₂>Carbon>Au>OTS/SiO₂. It was found that the film morphologies changed with the substrate surface energy. A continuous film was obtained on SiO₂, C and Au substrate but the aggregation pattern or the morphology became different. With decreasing surface energy of the substrate, higher aggregation of Nafion® was observed in the AFM image. In contrast, when the surface energy of substrate went down to ~25 mJ/m² for OTS, no Nafion® was adsorbed on the OTS as confirmed by AFM morphology, roughness and film thickness measurement approach.

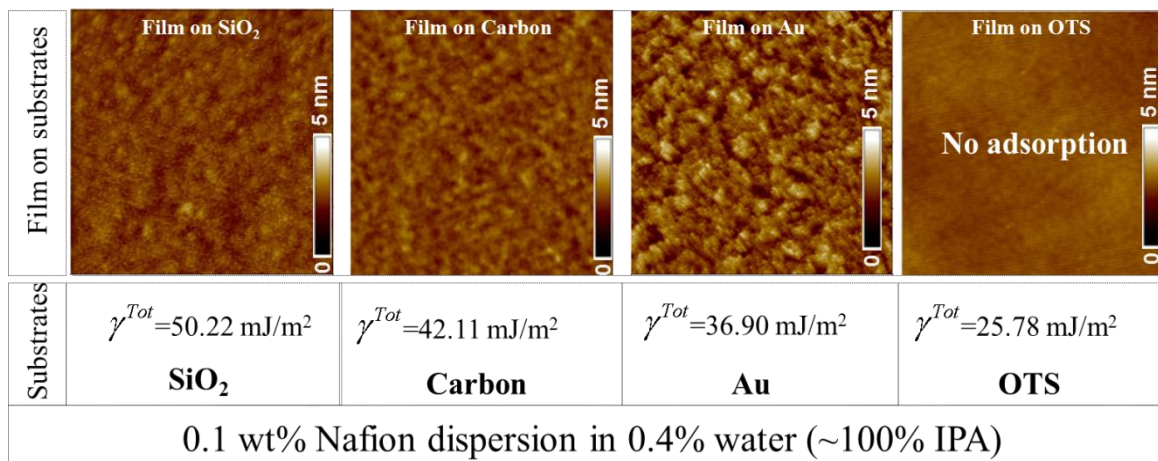


Figure 7.5: AFM height images (1 μm X 1 μm) of the self-assembled thin films from 0.1wt% Nafion® dispersion in 0.4 % water. The film morphologies have been presented in terms of substrate surface energies.

At this point, the effect of dispersion medium composition on the film morphology has been presented in the Figure 7.6. With increasing water content in the Nafion® dispersion, partial coverage of Nafion® film was observed on SiO₂ substrate. In contrast, no adsorption of Nafion® was observed on the carbon, Au and OTS substrates. Similar effect was observed with the further increment of water composition in the dispersion, i.e., for dispersion in 20 to 100% water. This phenomenon is consistent with the categorized behavior of the acid base component of substrate surface energies.

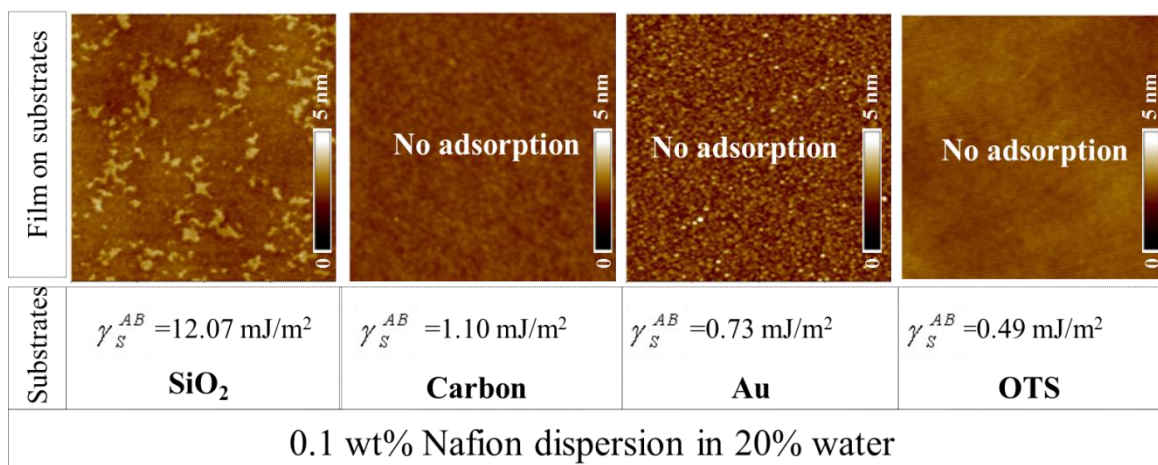


Figure 7.6: AFM height images (1 μm X 1 μm) of the self-assembled films from 0.1wt% Nafion® dispersion in 20 % water. The film morphologies have been presented in terms of acid base component of substrate surface energies.

It can be summarized that the percentage of water in the dispersion plays a significant role on Nafion®-substrate interaction. Continuous thin films are produced from the Nafion® dispersion in sufficiently low water content (e.g., 0.4 wt% water). At this condition, the film morphologies significantly vary with substrate surface energies. Irrespective of the dispersion compositions, Nafion® does not adsorb on the substrate with the surface energy as low as $\sim 25 \text{ mJ/m}^2$. In the next section, the free surface wettability of the films was investigated with respect to the substrate nature (hydrophilicity/hydrophobicity).

7.3.4 Substrate effect on thin film wettability

Water contact angles on the Nafion® thin films supported by three substrates – SiO₂ (hydrophilic), Carbon (Intermediate) and Au (hydrophobic), have been presented in Figure 7.7. Again, the films were obtained from 0.1 wt% Nafion® dispersion in 0.4 wt% water. Therefore, the corresponding film thickness varied from 4 to 6 nm on different substrates measured by

ellipsometry and AFM techniques. Interestingly, two completely opposite wettability of the Nafion® films were observed based on the substrate type. Hydrophilic – SiO₂, substrate exhibited hydrophilic free surface of the film whereas intermediate and hydrophobic substrates generated hydrophobic free surface of that. The nature of interaction is not fully understood but it is clear that the substrate surface energy and wetting interaction have a great influence on the orientation of the molecule in the resulted Nafion® thin films.

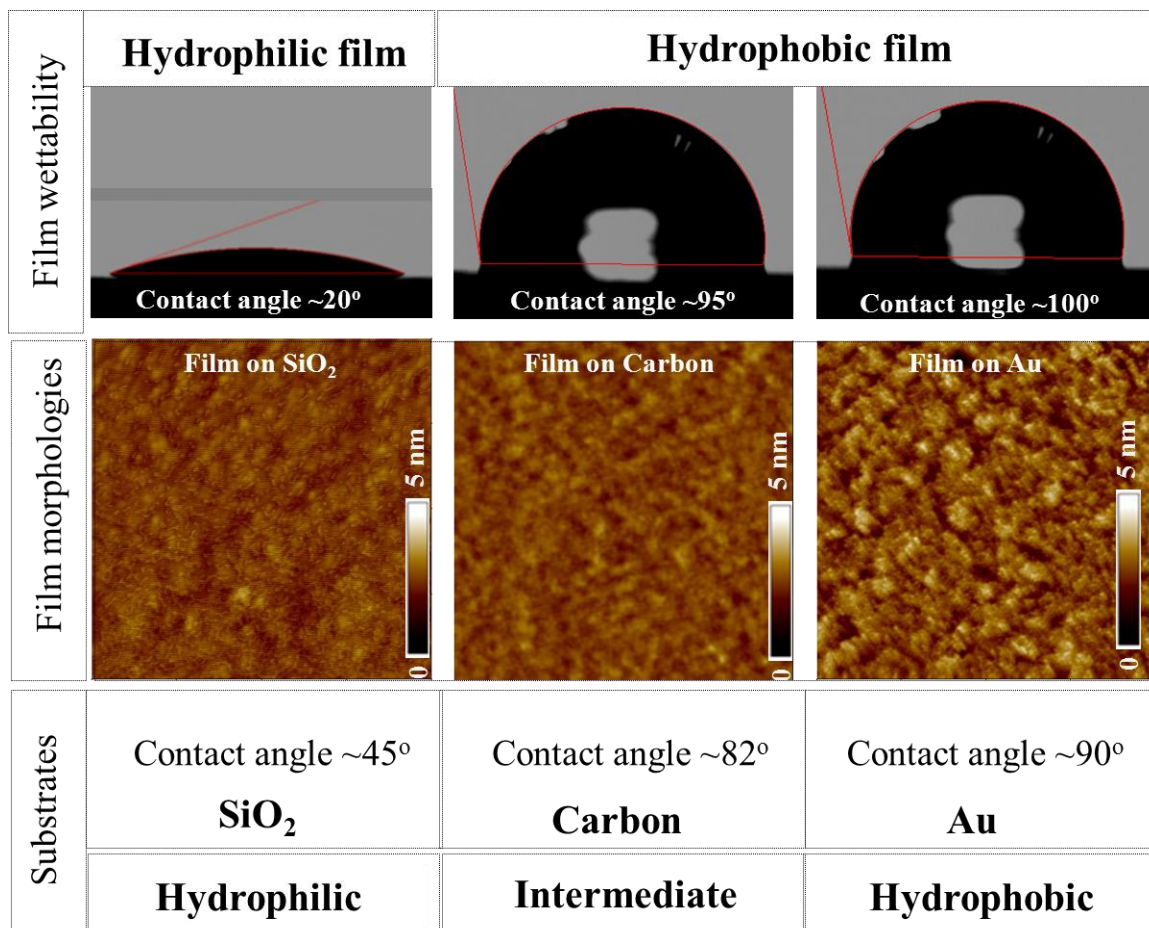


Figure 7.7: Water contact angles on and surface AFM images of Nafion® thin films (4 to 6 nm) on substrates of different wettabilities - SiO₂ (left), Carbon (middle) and Au (right).

Effect of annealing: The morphology, section analysis and water contact angle of the annealed Nafion® thin films (4 to 6 nm) on hydrophilic, intermediate and hydrophobic substrates have been presented in Figure 7.8. As discussed in Chapter 6, only the thinnest film (4 nm thick) on hydrophilic SiO₂ dewetted upon annealing. Interestingly, similar thickness on both intermediate and hydrophobic substrate dewetted after annealing as well. Section analysis of the corresponding films indicated the depth of the holes. The height of the hole depth on Au substrate was measured ~4.2 nm from the section analysis, which is consistent for the film thickness – 6 nm, on Au substrate. Therefore, it can be generalized that Nafion® thin film dewet when the thickness goes down to 4 to 6 nm irrespective of the substrates. However, the thin film became hydrophobic for all of three substrates where a dramatic switching from hydrophilic to hydrophobic surface upon annealing was observed for the thin film on SiO₂.

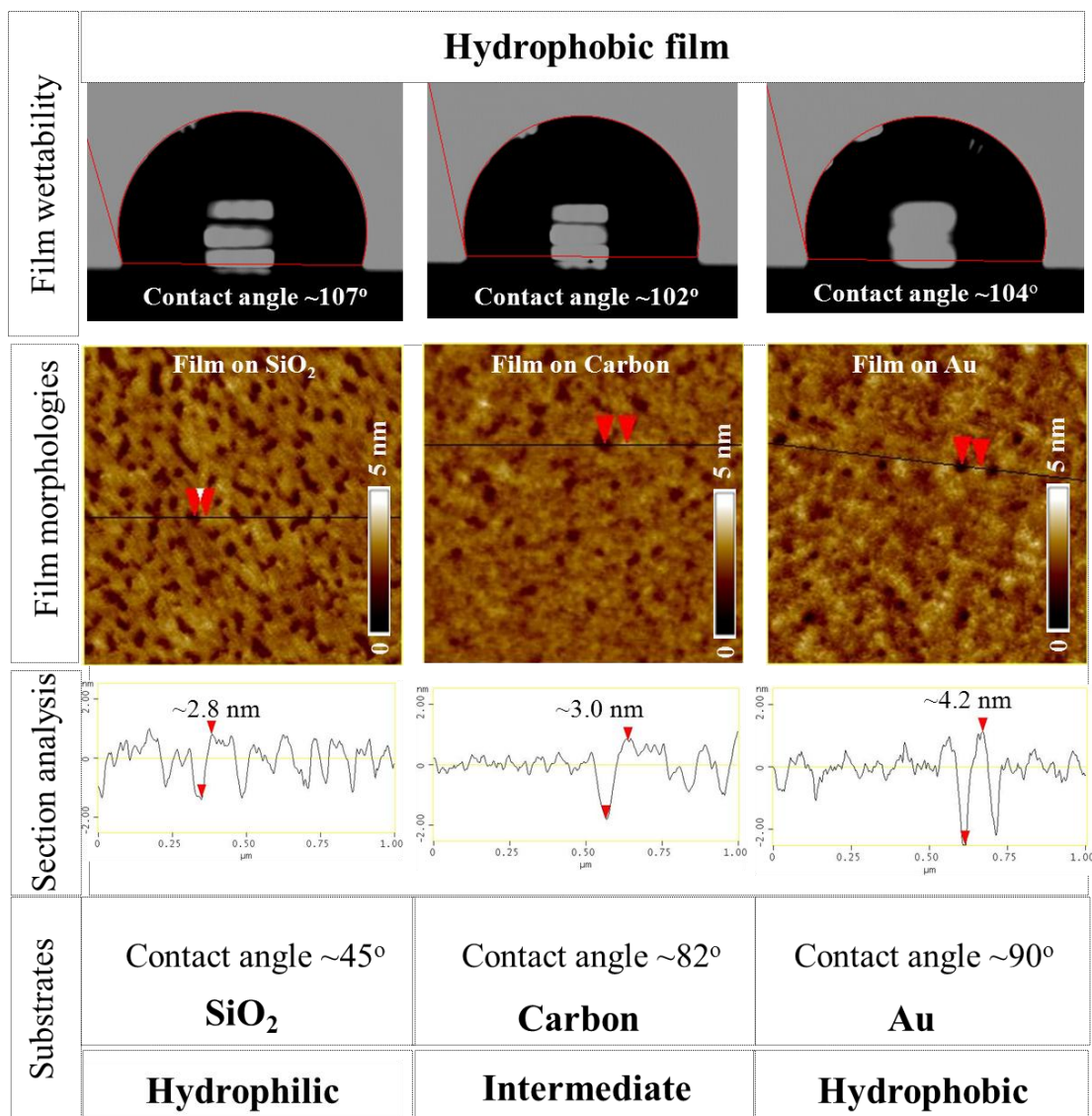


Figure 7.8: The morphologies, section analysis and contact angles of annealed Nafion® thin films (4 to 6 nm) at different substrate wettabilities – Film on SiO_2 (left), film on Carbon (middle) and film on Au (right).

7.3.5 Thickness dependent morphology of films on Carbon and Au substrates

In the above sections, only the thinnest film on different substrates was investigated. The goal of this section is to study how the film characteristics (thickness, morphology) vary with the

dispersion concentrations of Nafion®. Results for the films on two different substrates – carbon and gold, are presented.

Films on carbon substrate: The morphology and roughness of both un-annealed and annealed (at 146 °C) film were investigated by AFM as shown in Figure 7.9. The thickness of unannealed films was measured by ellipsometry and the AFM scratching technique. It was found that the morphology was changed with increasing of the corresponding Nafion® concentration in the dispersion. Higher concentration resulted higher state of aggregation as described in Chapter 4, which corresponds higher film thickness and associated higher roughness. Upon annealing, the roughness of 25 nm and 150 nm film decreased while that of the 4 nm increased. On the other hand, the roughness of the 10 nm film remained unchanged.

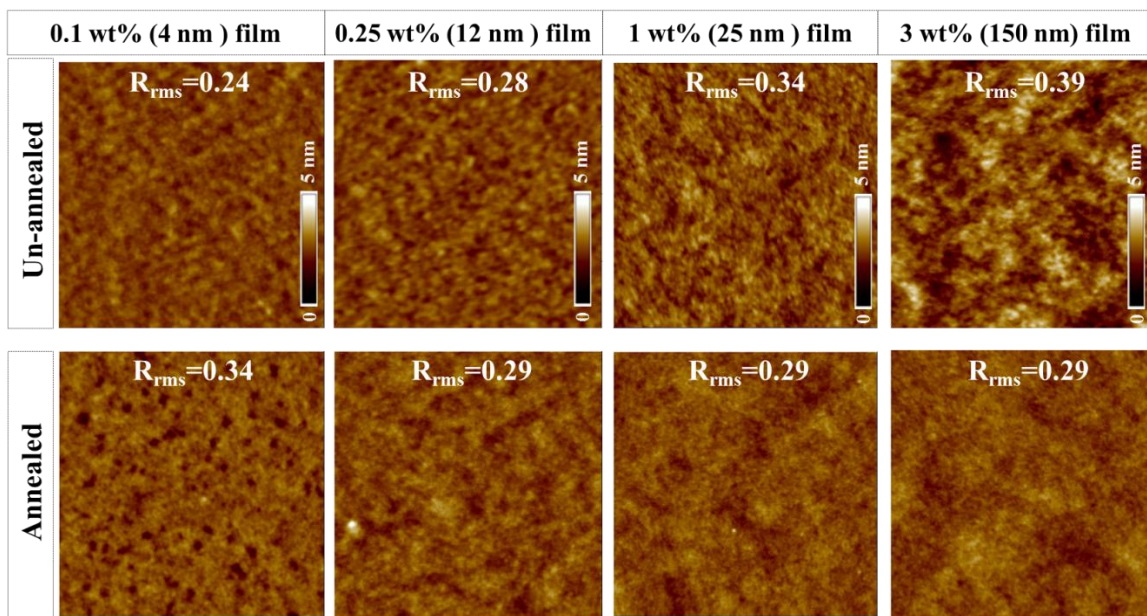


Figure 7.9: AFM height images (1 μm X 1 μm) and roughness of the self-assembled films on Carbon. Both un-annealed and annealed film morphologies have been presented with increasing thickness (left to right).

Films on Au substrate: Film morphology and roughness of the Nafion® thin films on Au substrate were characterized by AFM as shown in Figure 7.10. In the un-annealed films, there was a morphological difference with increasing concentration and corresponding thickness. Annealing had similar effect on surface roughness as that for the films on carbon. This indicates that annealing results in a rearrangement/reorientation of the polymer in such a way, the film become flatter irrespective of the substrates. The only exception is the thinnest film in each case where de-wetting makes the film surface rougher.

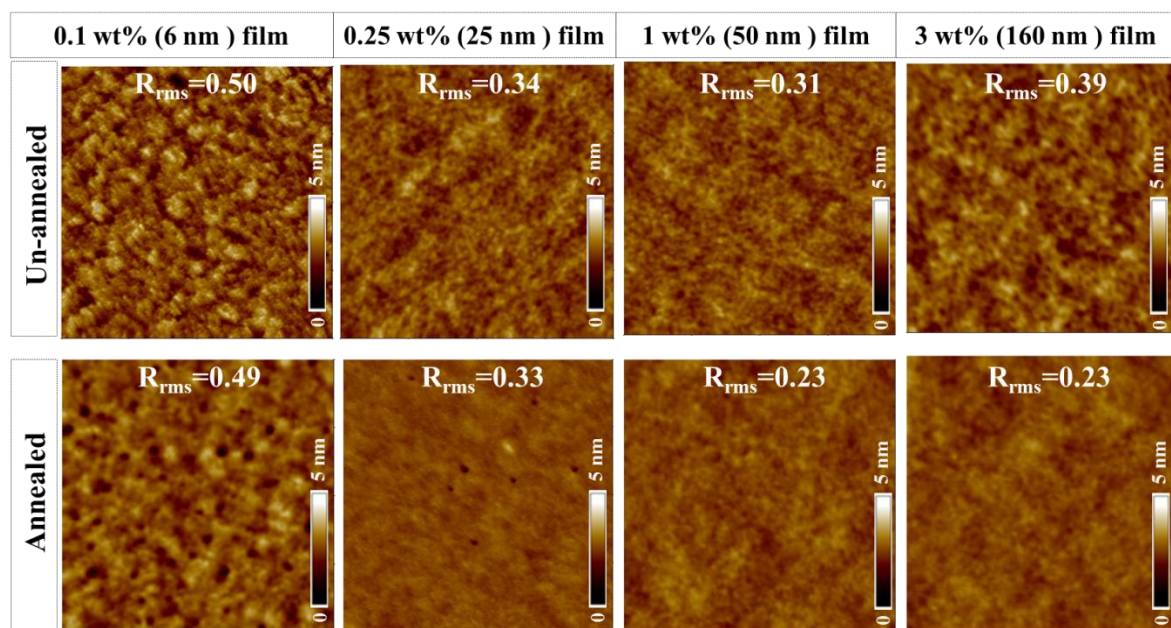


Figure 7.10: AFM height images (1 μ m X 1 μ m) and roughness of the self-assembled films on Au. Both un-annealed and annealed film morphologies have been presented with increasing thickness (left to right).

Summary: It can be summarized that de-wetting of 4-6 nm film occurs upon annealing irrespective of the substrate type but the films of higher thickness are stable. Sufficient rearrangement occurred for the films of thickness greater than 10 nm and surface became

smoother upon annealing. Similar observations were made for the films on Pt substrate (not presented here). Interestingly, no adsorption or self-assembly of Nafion® occurred on hydrophobic OTS/SiO₂ substrate irrespective of dispersion concentration 0.1 wt% to 5wt%, confirmed by the ellipsometry and AFM measurement. It indicates that poor interaction of Nafion® might happen with strong hydrophobic OTS substrate even in the presence of negligible amount of water in dispersion. However, the next question would be what about the wettability of the Nafion® thin films on different substrates with thickness and thermal treatment.

7.3.6 Thickness-dependent surface wettability

Water contact angles were measured for the films on different substrates (Carbon, Pt and Au) obtained from 0.1 to 3 wt% Nafion® dispersion that have been summarized in the Figure 7.11. The contact angles of the unannealed films increased with increasing film thickness but varied between 95° and 104°. Upon annealing, the contact angles increased slightly to values between 103° and 107°. Similar to the unannealed films, the contact angles increased with increasing thickness for the annealed films. The main observation is the differences in film surface wettability between unannealed films on non-SiO₂ substrate (i.e., C, Pt and Au) and those on SiO₂ substrate. It may be recalled (section 4.3.4 of Chapter 4) that two distinct characteristics of surface wettability were noted for films on SiO₂ substrate - hydrophilic surface for sub-55 nm films and hydrophobic surface for films greater than 55 nm. Conversely, the thin films on Carbon, Au and Pt were hydrophobic irrespective of the thickness. Similarly, all of the films exhibited hydrophobic free surface upon annealing regardless of the substrate and thickness.

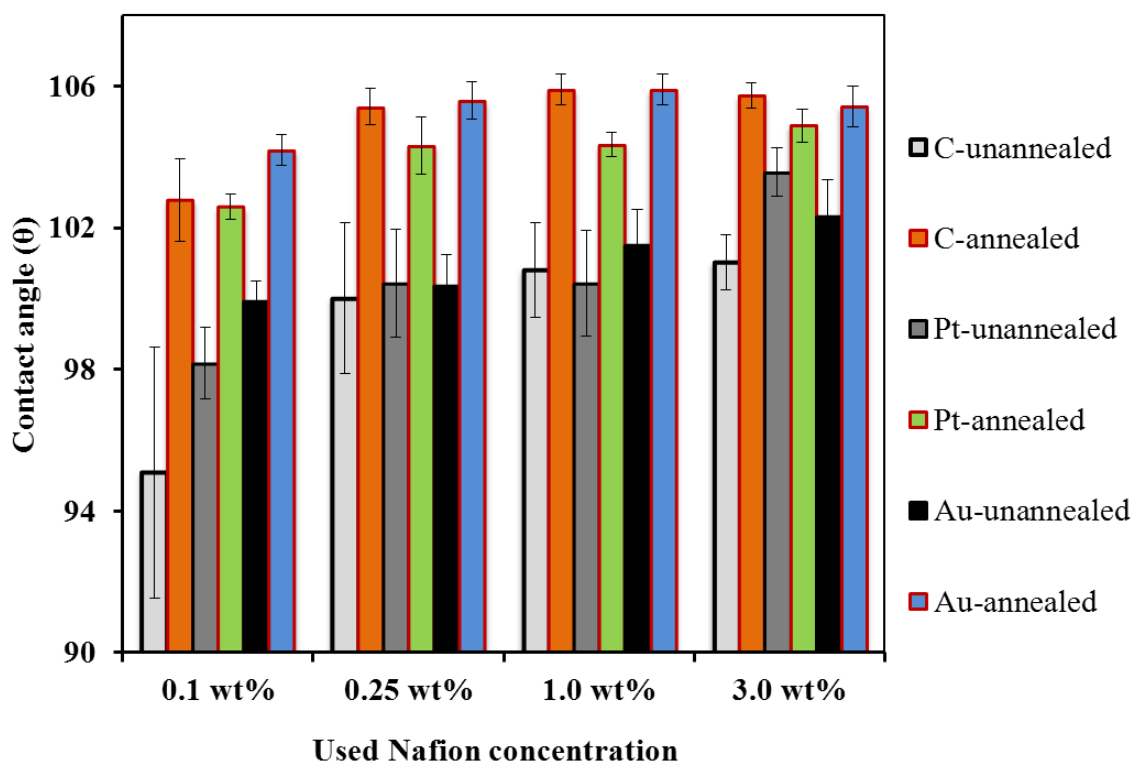


Figure 7.11: Contact angles of both un-annealed and annealed Nafion® thin films on carbon, Au and Pt with the variation of Nafion® concentration correspond to the thickness.

7.3.7 Substrate influence on water uptake

Water uptake of the Nafion® thin films on Au substrate was measured by QCM. The main goal of this study is to understand whether the hydrophobic substrate has any influence on water uptake compare to hydrophilic substrate. The moles of water per mole of sulfonic acid group as terms as λ_w for different film thickness has been plotted in terms of relative humidity in the Figure 7.12. It was found that λ_w decreased with decreasing film thickness in the range of relative humidity 25 to 100%. The results are consistent with the GM findings [12] where they found lower uptake with decreasing thickness from 500 nm to 33 nm. In this study, the only exception is the thinnest (6 nm film), the λ_w values increased rather going further down with

decreasing thickness. In this regard, it can be recalled that the exceptionally high λ_w values for the 4 and 10 nm films on hydrophilic SiO₂ substrate were also observed (Section 5.3.10 of Chapter 5). However, the λ_w values for the 160 nm thin film on hydrophilic SiO₂ substrate are also presented in the Figure 7.12. The same film thickness on hydrophobic Au substrate showed lowered water content. The finding is consistent with Abuin *et al.* [16] who reported that water content depends on substrate nature where decreased with substrate hydrophobicity. Two factors may be responsible for the apparent difference in the water content. First, the interfacial effect i.e., the hydrophobic substrate tends to repel water which might diminish the total water content in the thin film. Second, the differences in the film morphology or existing ionic domain size in the thin film on different substrate may influence on the water uptake of the respective films. For the thinnest film, the high interfacial area to volume ratio and significant differences in morphology compared to the thicker films may lead to the anomaly behavior of the films.

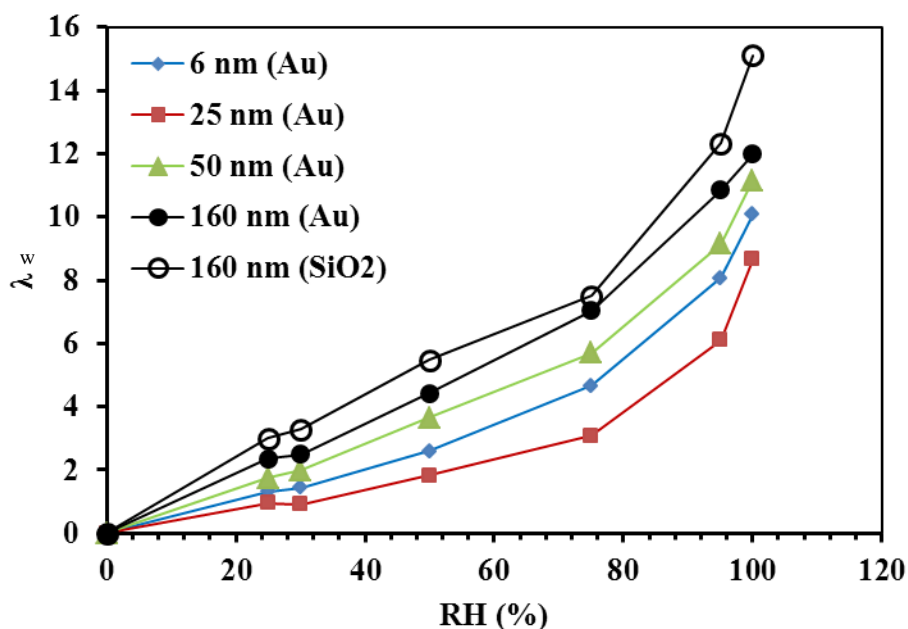


Figure 7.12: Water uptake of self-assembled Nafion® thin film on Au in terms of relative humidity. The measurement was conducted in Penn State University but the films were prepared by the author at Queen's.

7.4 Conclusions

In this chapter, the effect of substrate nature on the self-assembly of Nafion® has been investigated. The influence of Nafion® dispersion media was also explored. A number of blank substrates were characterized in terms of surface wettability and surface energy. The film characteristics have been interpreted in terms of substrate surface properties. The main conclusions have been summarized below.

1. The compositions (IPA/Water) of Nafion® dispersion medium play a significant role on ionomer-substrate interaction. A continuous and homogenous film on the substrates (SiO₂, Carbon and Au) was obtained only for the Nafion® dispersion with low water content. Even from the same Nafion® dispersion, no interaction between substrate and ionomer (resulted no ionomer film) was observed when the surface energy of the substrate goes down to 25 mJ/m².
2. At higher water content in the Nafion® dispersion, the lack of adsorption or self-assembly of ionomer was observed on hydrophobic substrates like Carbon and Au, conversely, ionomer adsorption on SiO₂ with incomplete coverage was noted. This is consistent with the differences in acid-base component of surface energy where SiO₂ has significantly higher value than that of carbon and Au.
3. The morphology or aggregation pattern of the ionomer in the thin films varied with decreasing surface energy of the substrates. Thus, higher aggregation in film morphology was observed for substrates with lower surface energy.
4. The thinnest un-annealed film (4-6 nm) exhibited hydrophilic free surface on hydrophilic SiO₂ substrate. In contrast, the similar film exhibited hydrophobic free surface on intermediate (Carbon) and highly hydrophobic (Au) substrates. The annealed films are hydrophobic irrespective of the substrates.

5. De-wetting of 4–6 nm Nafion® thin films was noted upon annealing irrespective of the substrate, but not for thicker films.
6. The water uptake in Au supported Nafion® thin films decreased with decreasing film thickness; the only exception is the thinnest 6 nm films. However, the overall water uptake is significantly reduced in the film supported by hydrophobic substrate (Au) in comparison to the hydrophilic substrate (SiO₂).

Chapter 8

X-ray Beam Damage of Ultra-Thin Nafion® Films

Preface

This Chapter is presented in a manuscript form. In fact, it is the final version of the manuscript that was submitted and has been published in the Journal of the Electrochemical Society 193]. The work was motivated by discussion in the literature that x-rays can have a damaging effect on Nafion® ionomer. Since x-ray based techniques such as XPS, GISAXS, energy dispersive x-ray (EDX) and x-ray diffraction (XRD) are increasingly being employed for characterization of thin polymer films and fuel cell components, it was of interest to investigate the effect of x-rays on ultra-thin Nafion® films. A simple experiment was designed wherein 10 nm thin films were deposited on IDA used for ionic conductivity determination. Three samples were prepared at the same time and the ionic conductivity of the films was determined. The samples were then subjected to x-ray in XPS system. Three different power settings were applied for three different samples. The changes in the photoelectron response of key elements were monitored as a function of time. The sample was withdrawn after 45 min of exposure. The ionic conductivity of the x-ray exposed samples were then determined. Loss in sulfur and fluorine was observed during x-ray exposure. Also, a significant loss in ionic conductivity occurred after x-ray exposure.

8.1 Introduction

X-ray based techniques have been increasingly applied for both *ex-situ* and *in-situ* characterization of device components and constituent materials of Polymer Electrolyte Fuel Cells (PEFCs) [194]. In particular, in the last decade, state-of-the-art x-ray based techniques including x-ray radiography [195,196], x-ray topographic microscopy (XTM) [197,198], and Synchrotron x-ray imaging [199] with x-ray power 10 to 30 keV have been used due to their high spatial resolution. These techniques are employed to determine the porous microstructure of electrodes. Soft x-rays have been employed to investigate liquid water distribution in the cell components for PEFCs under operation. Moreover, x-ray photoelectron spectroscopy (XPS) [200-202], energy dispersive x-ray (EDX) [200] and x-ray diffraction (XRD) [202] with 20 to 40 keV x-ray has been used to investigate elemental distribution and degradation of ionomer in the catalyst layer. The underlying assumption in all these measurements is that the conclusions obtained are applicable to the functional polymer electrolyte. Surprisingly, little concern have been raised over the potential adverse effect of x-rays on component structure and, therefore, on the properties and performance of fuel cell components upon exposure. In particular, if the damage is sufficient to alter the proton conducting properties of the electrolyte, then the structure (or similar property) measured is not applicable to the working component.

One of the first studies wherein the influence of x-ray exposure on PEFC performance was reported only recently in 2010 by Schneider *et al.* [203] They reported that the open circuit voltage decayed under synchrotron radiation (SR) but recovered on switching off. On the other hand, the cell performance showed significant unrecoverable degradation. It was hypothesized that the cell performance decay may be associated with reduced proton conductivity and wettability changes due to damages to the polymer electrolyte membrane (PEM) and Teflon-

treated carbon paper, respectively. It would appear that the polymeric components of the PEFC are more susceptible to the damages due to radiation. Thus, it can be expected that the ion-conducting polymer (ionomer) in the catalyst layer (CL) [1] may also be affected by x-ray radiations. The most commonly employed ionomer in PEFCs is Nafion[®], a copolymer of tetrafluoroethylene and perfluoro[2-(fluorosulfonylethoxy) vinyl] ether monomers. When employed as a PEM, the thickness of Nafion[®] is typically 50 microns or greater. On the other hand, in the CL, the typical thickness of the Nafion[®] film, covering the Pt/C catalyst aggregate, is in the 3-10 nm range. Recently, grazing incidence small angle x-ray scattering (GISAXS) technique has been employed by Bass *et al.* [10] and Modestino *et al.* [11] to study the nano-structure of Nafion[®] thin films, albeit these films were much thicker than 10 nm. Although these measurements are adding new insight to the ionomer structure/property, the damage caused during the measurements has not yet been quantified.

In fact, very few studies have been performed to explore Nafion[®] damage upon by x-ray exposure. Chen *et al.* [8] reported that X-ray radiation does not cause any damage of the chemical structure of a Nafion[®] membrane even after 2 hours of exposure with a 350 W source (1486.8 eV). On the other hand, Schulze *et al.* [204] found that prolonged exposure (20 h at 300 W) of a Nafion[®] membrane to x-rays causes permanent damage to both backbone and side chains of Nafion[®]. A similar observation has been reported by Militello *et al.* [205] after 15 h exposure. Both groups mention that the side chain degradation is faster than that of the backbone. Recently, Roth *et al.* [206] conducted an intensive study on SR effects on fuel cell materials by XTM. They have shown that the performance decay happens due to fast ionomer degradation resulting in the disintegration of the CL.

In summary, it can be stated that there is an emergence of evidence that x-ray exposure can result in the degradation of the ionomer. For PEFCs, ionomer degradation in the catalyst layer may result in a much stronger impact on the functional property, viz. the proton conductivity. To understand the radiation damage of Nafion[®], the influencing factors and their effects must be quantified. For example, what is the impact of the two obvious parameters: x-ray power and exposure time on the degree of polymer degradation? What is the nature of degradation? That is, which part of the Nafion[®] molecule is more susceptible to damage? Further, is there a correlation between structural damage and the pertinent functional properties of Nafion[®], i.e. its ability to conduct protons? And, finally, does the extent of X-ray damage on ultra-thin films differ from that on bulk membranes?

To resolve some of the aforementioned issues, in this study, we have employed ultra-thin Nafion[®] films (10 nm) self-assembled on a SiO₂ surface of an inter-digitated electrode as a model for the ionomer in the PEFC CL. The influence of x-ray exposure on the ionomer films is studied using the x-ray source in a XPS instrument. The changes in the elemental composition during x-ray exposure are monitored as function of time during the XPS measurements. The effect of x-ray source power is investigated by measurements on three different samples exposed to three different x-ray powers. The time effect on degradation was gathered by monitoring the XPS response over a period of 45 min X-ray exposure. The proton conductivity of the ultra-thin ionomer films was measured before and after the 45-min X-ray exposure. A large drop in sulfur response was observed and a corresponding dramatic loss in conductivity was measured. This is the first study wherein the side chain damage has been correlated by direct ionomer conductivity measurements.

8.2 Experimental

8.2.1 Materials and sample preparation

Thermally grown SiO₂ (thickness ~2000 nm), on Si wafer, supporting a comb-shape interdigitated array (IDA, 110 gold teeth of 0.8 cm length and 100 μm apart) of gold electrodes was used as the substrate. Nafion[®] films were generated by self-assembly using a stock solution of Nafion[®] (Du Pont, EW 1100, 5 wt%) in a water-alcohol mixture (75/20 w/w alcohol to water) obtained from Ion Power (USA). This stock solution was diluted to desired concentrations of 0.25 wt% by addition of isopropyl alcohol (IPA) (Sigma Aldrich). The sample preparation method has been previously described [164,163]. Briefly, the diluted solutions were sonicated for 5 min and equilibrated for at least 24 h. IDAs were immersed into the diluted Nafion[®] solutions for 12 h to prepare self-assembled Nafion[®] thin films and subsequently dried by N₂ flowing immediately after. The characteristic film thickness were measured by three different techniques, namely Ellipsometry, Atomic Force Microscope (AFM) and XPS [163,162].

8.2.2 Electrochemical Impedance Spectroscopy

For conductivity determination, impedance spectroscopy measurements were accomplished by a two micro-probe setup connected with a Solartron 1260 frequency-response analyzer coupled to a Solartron 1296 dielectric interface. Impedance was measured before and after X-ray exposure to the samples following the protocol described in our early publications [164,163]. Briefly, the IDA with Nafion[®] films was placed in an environmental chamber (Model 3911, Thermo Forma, USA) with relative humidity (RH) and temperature control. All measurements were carried out at 60 °C, comparable to fuel cell operating conditions. A humidity sensor (CMOSENS Tec., Switzerland) was placed in the close vicinity of the IDA sample to

monitor the local equilibration for RH and temperature. Single-frequency impedance measurements were carried out to monitor the approach to ionomer equilibration. When the impedance value no longer varied, the film was deemed to be equilibrated at the set RH and temperature. At equilibrium condition, impedance data were collected by applying an alternating potential of amplitude 100 mV over a frequency ranging from 10 MHz to 0.01 Hz. Smart impedance measurement software (Solartron Analytical) was used for data collection and Z-view impedance software (Version 3.0a, Scribner Associates Inc.) was adopted for equivalent-circuit design, model fitting and data analysis. The film conductivity (κ_f) was calculated from the fitted resistance (R_f) obtained from impedance measurements using equation 1, where, d is the space between the IDA electrodes (100 μm), t is the thickness of the film, l is the length of the teeth (0.8 cm) and N is the number of electrodes (110).

$$k_f = \frac{1}{R_f} \cdot \frac{d}{l(N-1)t} \quad (5.4)$$

8.2.3 X-ray Photoelectron Spectroscopy

XPS measurements were performed in an ultra-high vacuum (UHV) chamber with base pressure of $\sim 3 \times 10^{-10}$ torr. Samples were introduced into the vacuum system such that vacuum equilibration time was kept constant at around 4 hrs. Samples of Nafion[®] thin films (nominally 10 nm thick) grown on gold interdigitated electrodes grown on silica (2000 nm film on silicon wafers) were exposed to an X-ray gun as XPS measurements were taken simultaneously. XP spectra for all relevant regions were taken in the following sequence: survey, sulfur, oxygen, fluorine, silicon and carbon. The sequence lasted 15 min such that consecutive spectra for the same region were obtained every 15 min although the sample was continuously irradiated. Separate samples were used for irradiation with 100, 200 and 300 W with an Al source (1486.6

eV). X-ray irradiation was performed at 45° and all XPS response was collected at a constant 90° take off angle. The different X-ray powers were obtained by setting the voltage and emission current in the X-ray source (10.0 kV/10.0mA, 13.58 kV/14.8 mA, and 14.26 kV/20.7 mA). The three powers were in the linear response region of the photoemission current for XPS measurements (20 nA/100 W). The X-ray dosage on the Nafion[®] film has been estimated using mass attenuation values for Teflon [207] and an approximate density of the film. Total dosage for 100, 200 and 300 W irradiation after 45 min was 1.7×10^5 , 3.4×10^5 and 5.1×10^5 MGy, respectively. The XPS spectra were fitted using CasaXPS software [146]. Peak quantification is typically considered to have an error as high as $\pm 10\%$ of the atomic percentage. The changes arising from film degradation were quantified within 5% error.

Binding energies are reported uncorrected for potential charging effects. No correction was needed as the Si_{2s} peak appears at 154.7 ± 0.1 eV, in good agreement with the expected literature value for SiO₂ films grown on a Si wafer (154.6 eV) [145,208]. The remaining peaks appear at approximately 689 eV, 533 eV, 291 eV and 169 eV, for the F_{1s}, O_{1s}, C_{1s} and S_{2p} peaks, respectively, as expected by comparison with Teflon, thiomethylsulfonate and polytetrafluoroethylene (PTFE) data [209-211]. The specific peaks resulting from fitting of each element envelop is discussed below.

8.3 Results and Discussion

8.3.1 Film degradation

X-ray photoelectron spectroscopy is routinely used to explore elemental composition, film thickness and layering on polymer samples. In such experiments, a compromise must be

reached between the highest possible power of the X-ray source, which enhances resolution and intensity of the data, and the potential damage to the sample produced by the radiation or by the photo-produced electrons.

The elemental composition of the Nafion[®] films obtained by XPS is shown in Table 8.1, together with the expected composition. Three samples were prepared for this study and each subject to a different X-ray power for elemental composition measurement by XPS. The samples denoted as Sample-1, Sample-2 and Sample-3 were measured by 300, 200 and 100 W X-ray power, respectively. Atomic% of each sample was calculated from the first survey scan of each sample. The reported data shows that the composition of the films is consistent between the different measurements (within the error of the measurement) and comparable to the expected composition.

Table 8.1: Atomic % of different elements of Nafion[®] in the Ultra-thin films.

| Sample no. (X-ray Power) | Sulfur | Oxygen | Carbon | Fluorine |
|--|--------|--------|--------|----------|
| Sample-1 (300 W) | 1.9 | 7.5 | 39.5 | 51.0 |
| Sample-2 (200 W) | 1.6 | 7.8 | 39.1 | 51.6 |
| Sample-3 (100 W) | 2.2 | 8.0 | 36.0 | 53.7 |
| Nafion [®] ^a (EW=1100) | 1.5 | 7.6 | 30.8 | 60.0 |

^aCalculated

One of the first effects of X-ray irradiation that can be noted is the thinning of the Nafion[®] film. This is evident from the increase in the Si peak arising from the underlying silica support. Figure 8.1 shows the Si_{2s} integrated peak intensity increase for all three X-ray powers used. The thickness change was calculated by adopting the equation $\Delta d = \lambda \cdot \Delta(\ln I)$ based on Beer–

Lambert law. Where, d is the thickness, I is the Si_{2s} intensity and λ is the attenuation length. After 45 minutes, irradiation with either 300 or 200 W X-rays results in $\sim 27\%$ reduction in the film thickness that is, from its nominal 10 nm to 7.3 nm. Irradiation with 100 W results in a less pronounced thinning, although the errors in these measurements are much higher due to the low intensity of the peak.

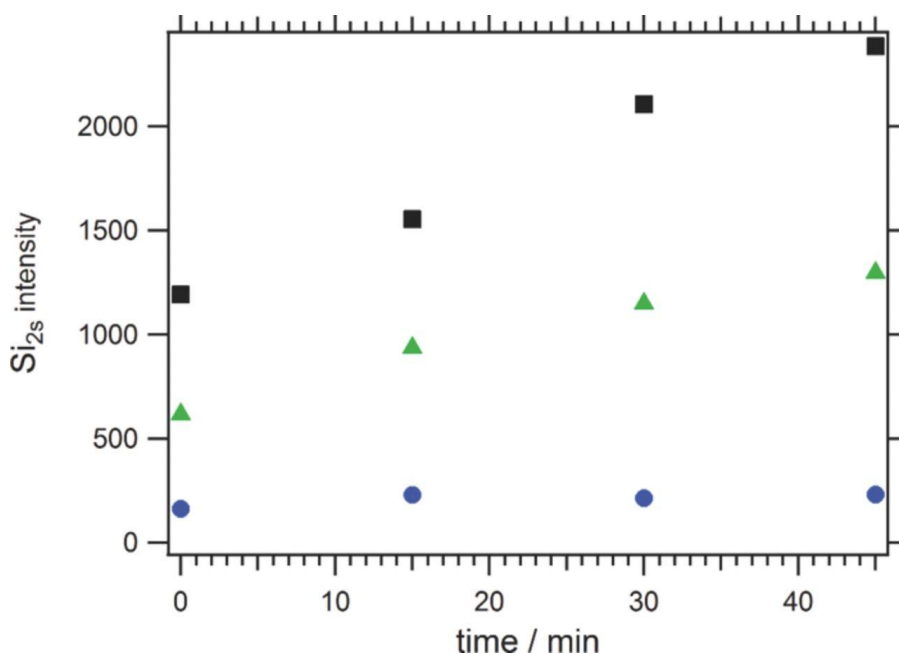


Figure 8.1: Film thinning observed by the increase in Si_{2s} intensity as a function of irradiation time. X-ray source power: (■) 300W, (▲) 200W, and (●) 100W.

Film thinning could be due to a chemical degradation of the Nafion[®] molecules or to a structural rearrangement of the film. To assess these possibilities, we must individually determine the variations in all the Nafion[®] components.

The degree of degradation was expected to be more significant at higher X-ray powers. It is therefore convenient to start our discussion with the observed changes in XPS signal as a

function of exposure at 300 W X-ray radiation. Figure 8.2a shows the S_{2p} region as a function of different exposure time. The spectra clearly show a decrease in the sulfur signal indicating that a change is occurring in the Nafion[®] film.

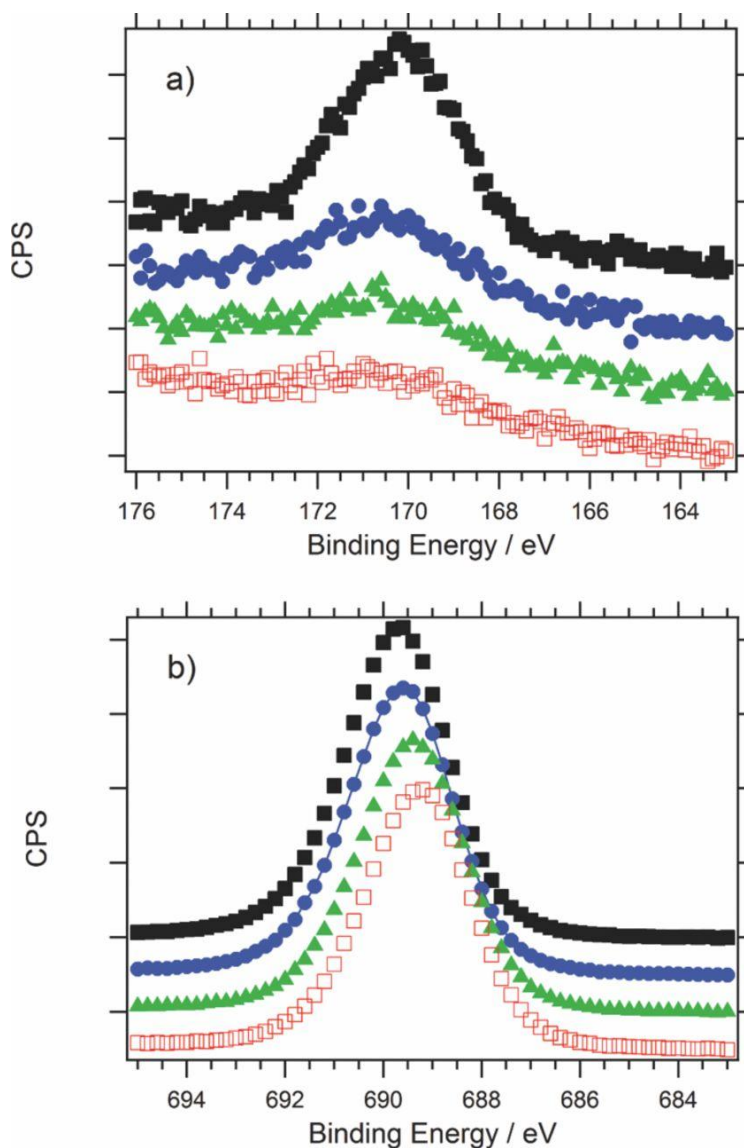


Figure 8.2: Film degradation under 300 W X-ray source. S_{2p} region at times 0 (■), 15 (●), 30 (▲) and 45 (□) minutes exposure. a) S_{2p} peak; b) F_{1s} peak. Traces have been offset for clarity.

The sulfur signal arises only from the branches (side chains) of the Nafion[®] polymer. To assess if the damage to the film is homogeneous, we observed the fluorine signal, which primarily arises from the backbone of the polymer (Figure 8.2b). The number average ratio of fluorine in the backbone to side chain for 1100 EW Nafion[®] is 2.7. A comparative quantification of the changes observed in these signals (Figure 8.3) provides an indication of where the damage is more significant. The decrease in sulfur intensity seen in Figure 8.2 can be quantified by obtaining a fitted peak area for each spectrum. Figure 8.2 (black squares) show that a 78% decrease in intensity is observed after 45 minutes under 300 W X-rays. In contrast, the fluorine intensity decreases by only 8% after 45 minutes under the same irradiation.

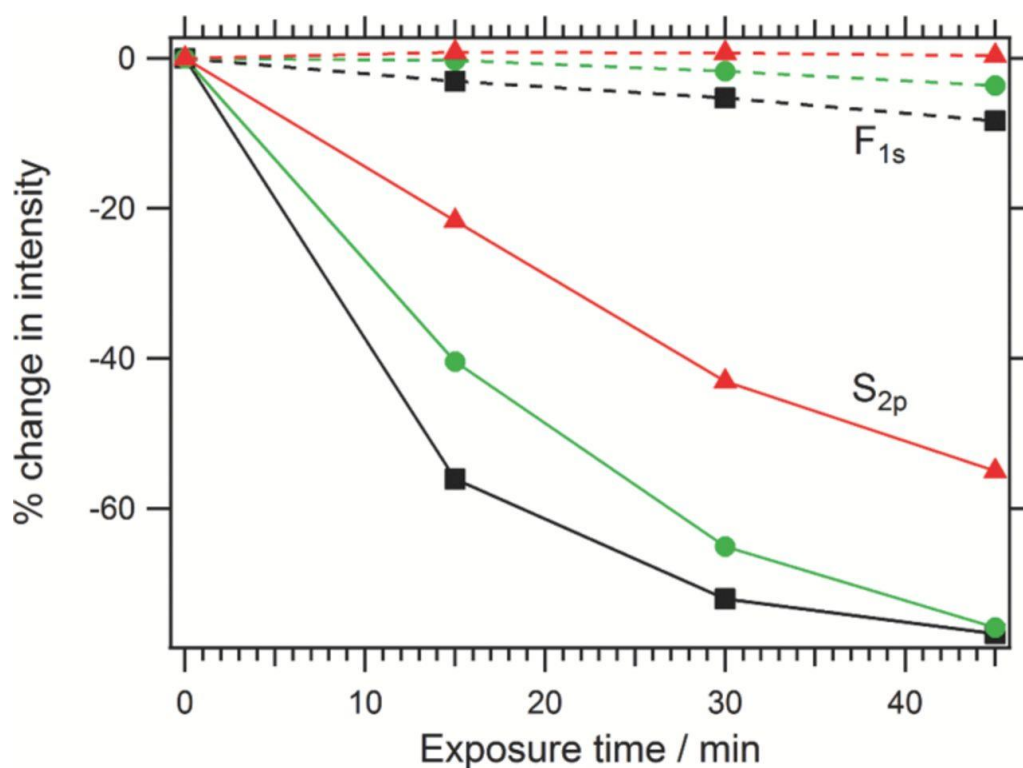


Figure 8.3: Change in intensity of the XPS signal as a function of exposure time. Solid lines indicate sulfur and dashed lines indicate fluorine intensities for exposure at 300 W (■), 200 W (●), and 100 W (▲).

The Nafion[®] thin film used for these experiments (EW=1100, Figure 8.4) is fluorine rich on the backbone. However, as can be seen from Figure 8.3, the observed degradation for sulfur is more pronounced and more rapid than for fluorine suggesting that the primary pathway for degradation is the loss of sulfonic groups from the side chains.

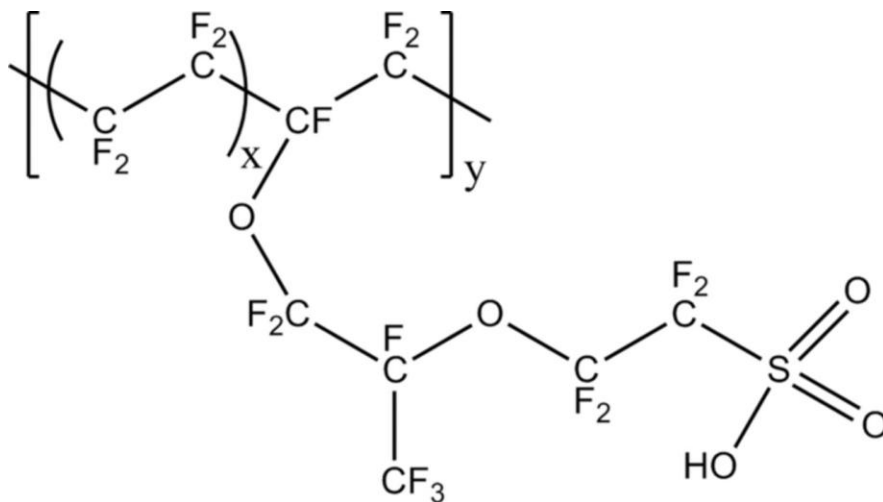


Figure 8.4: Nafion[®] molecule (EW=1100; x=6, y=1) molecule. Sulfur and oxygen are present only on the side chain. Fluorine ratio is 27:10 (backbone:side chain).

To elaborate on the decomposition of Nafion[®], we monitored the changes in the oxygen signal upon irradiation. The oxygen 1s region is characterized by two well-defined peaks (Figure 8.5). A high binding energy peak arising from oxygen bound to sulfur (sulfonic groups) is seen at 535.8 eV. This peak can be seen to decrease significantly upon irradiation supporting the idea that the sulfonic groups are ejected from the sample. The low energy peak, at 533.1 eV, corresponds to the overlap between the oxygen signal arising from the ether groups in Nafion[®] and the one arising from the underlying silica support. The fate of the ether oxygen as well as quantification of each oxygen component is made difficult by the thinning of the film (discussed above), which increases the contribution of oxygen from silica. The contribution of the silica peak can also be inferred by the sharpening of the O_{1s} peak at 533.1 eV.

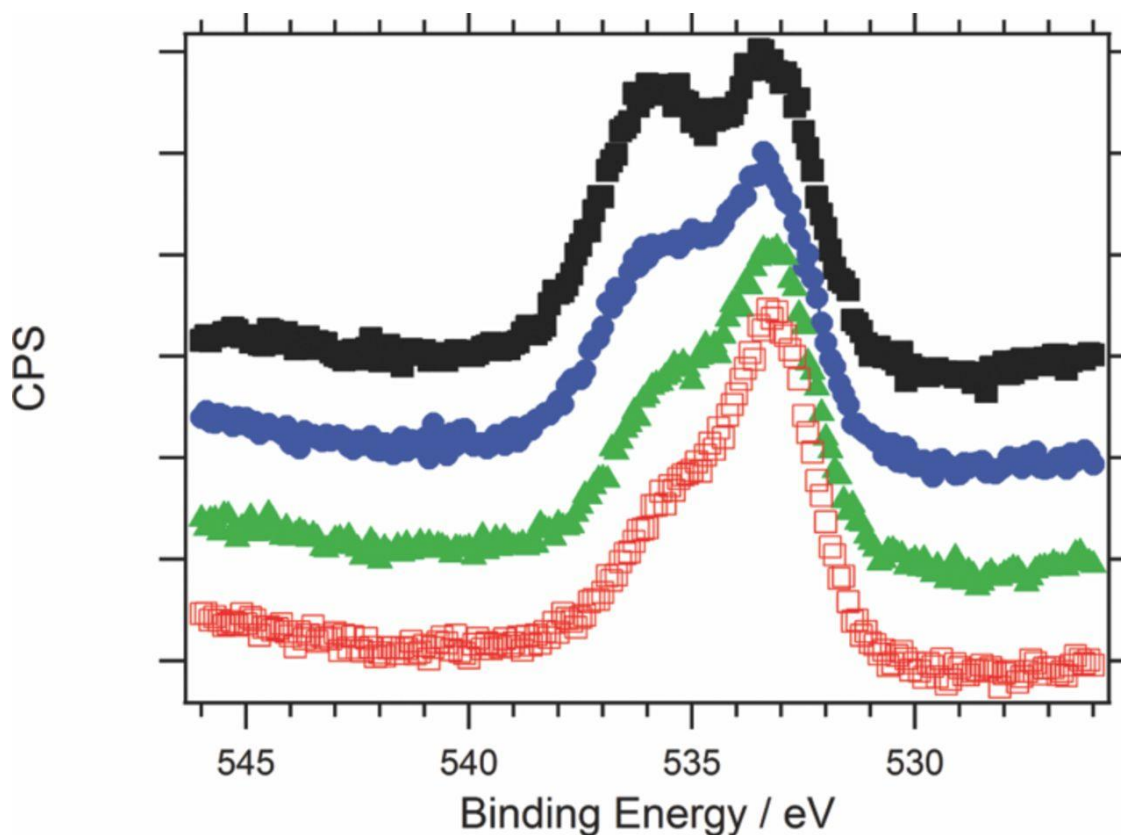


Figure 8.5: Oxygen degradation under 300 W X-ray source. O_{1s} region at times 0 (■), 15 (●), 30 (▲) and 45 (□) minutes exposure. Traces have been offset for clarity.

Accompanying the disappearance of sulfonic groups, the degradation of Nafion[®] can result in changes in the carbon moieties present. Figure 8.6 shows the carbon 1s region at different exposure times. Using Benson group nomenclature we can identify five distinct carbon components in a molecule of Nafion[®], namely C-(C)₂(F)₂, C-(C)₂(F)(O), C-(C)(F)₂(O), C-(C)(F)₃, and C-(C)(F)₂(S). However, resolving five components is beyond the resolution of the instrument. The large number of carbon environments does produce peak broadening, which makes fitting of multiple components necessary to obtain a reasonable account of the carbon intensity. As can be seen for the 45 minute trace, four peaks of reasonable Full Width at Half Maximum (FWHM) (~2-3 eV) are needed to appropriately fit the C_{1s} region. As has been assessed for similar polymers, the binding energy of each component can be correlated with the number of “more

electronegative” atoms bound to the carbon. The components can be grouped to be loosely assigned to: a) carbon bound to fluorine atoms at high binding energy, subsequently labeled as C_F , which dominate the spectrum of Nafion[®] before irradiation; and b) carbon in a more carbon-like environment (binding energy below 290 eV), labeled as C_C . It is tempting to assign the lowest binding energy carbon (~ 286.6 eV) as adventitious carbon, however one must keep in mind that even upon degradation of the Nafion[®] film this carbon component likely contains carbon bound to at least one oxygen or one fluorine atom, and that the remaining carbon will be immersed in a highly electronegative environment.

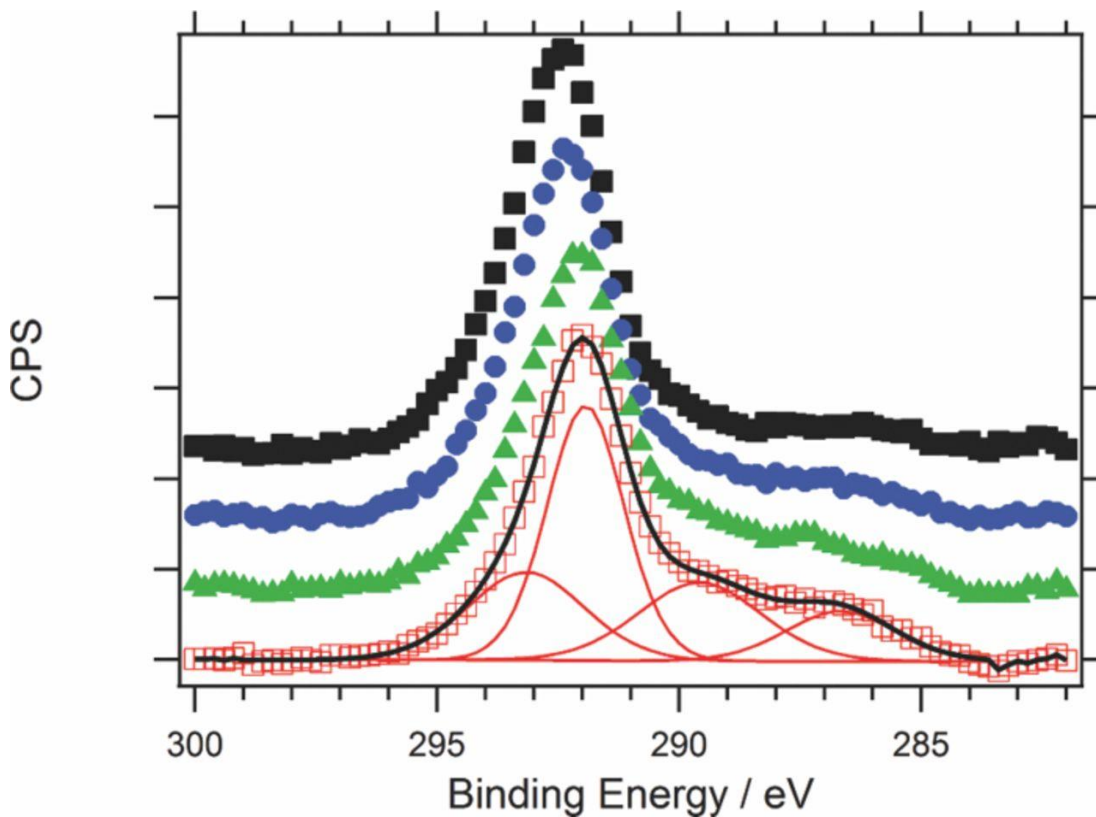


Figure 8.6: Change in C_{1s} signal under 300 W X-ray source. Spectra at times 0 (■), 15 (●), 30 (▲) and 45 (□) minutes exposure. Traces have been offset for clarity. Four fitted components and the resulting envelope are shown as solid lines for the 45 minute exposure spectrum.

Before irradiation, the Nafion[®] spectrum in the carbon region is dominated by the C_F component. In fact, this is the only component expected for pure Nafion[®] and any low binding energy peaks are assigned to fluorine deficient carbon and other impurities (hydrocarbons, CO, etc). Upon irradiation, the peak intensity of the C_F component decreased and its maximum shifted toward lower binding energy (lower average fluorine content). Simultaneously, the C_C components increased indicating a chemical degradation whereby the polymer loses fluorine and carbon-carbon bonds are formed.

8.3.2 Degradation extent and mechanism

The degradation mechanism may depend on photon energy as well as on total X-ray power. In particular, energy absorption becomes more favorable at lower photon energies [207]. The photon energy chosen for these experiments (1486.6 eV) is a typical laboratory source for any XPS experiments and it is therefore relevant for comparison with existing literature.

To consider the dependence of the observed degradation on X-ray power, it is useful to focus on the first 15 minutes of exposure. Figure 8.7 shows the decrease in elemental signal for each component upon irradiation with 300, 200 and 100 W. The figure shows a decrease in sulfur intensity accompanied by a decrease in sulfonic oxygen clearly pointing to the removal of sulfonic groups. In addition, a small decrease in fluorine and carbon bound to fluorine is observed due to the removal of some fluorine from the structure but more importantly, the large increase in low binding energy carbon (C_C) indicates that although only a small amount of fluorine may be lost from the film, a substantial amount of cross linking and carbonization occurs. It is interesting to note that the total carbon intensity remains largely unchanged, that is no significant amount of

carbon is lost from the film. Changes in ether oxygen are less conclusive, as a small decrease in intensity is compensated by an increase in intensity arising from the underlying silica support during the thinning process.

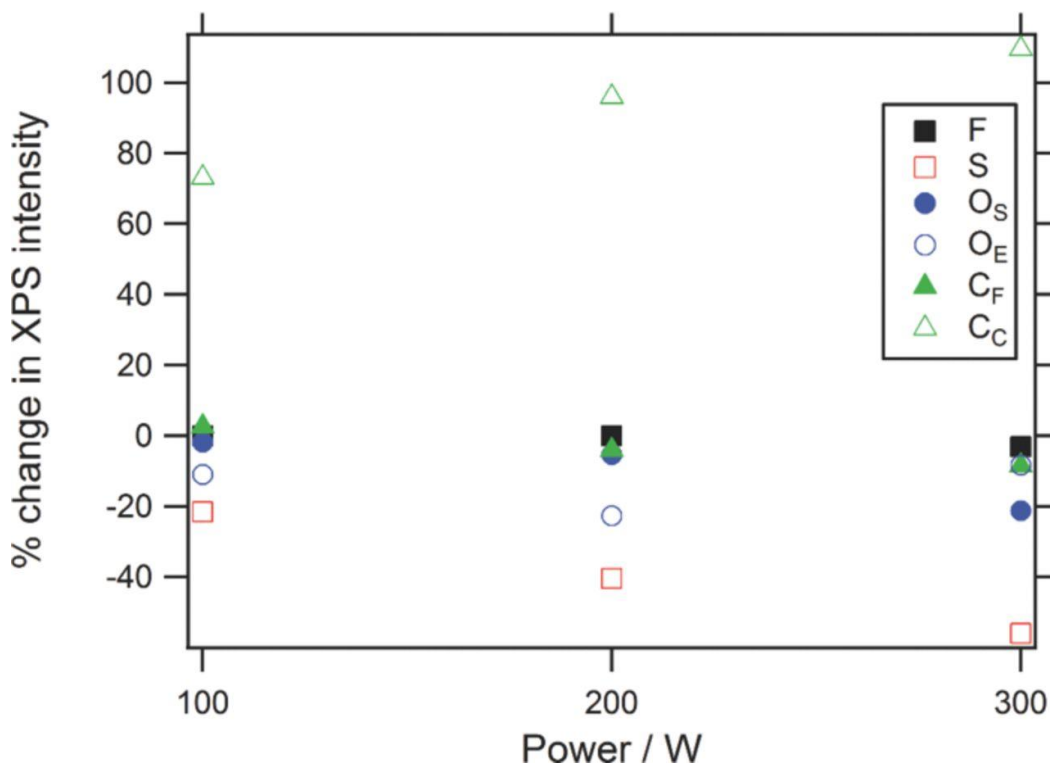


Figure 8.7: Changes in XPS intensity for the components of Nafion® upon irradiation during 15 minutes.

Upon further irradiation, the carbon and oxygen components of the XPS continue to change qualitatively in the same manner, but quantization becomes more troublesome as contributions from the underlying silica support and from the UHV environment start to play a role. Therefore, to understand the mechanism of degradation of the Nafion® film, we must focus on the sulfur and fluorine components; the ratio of sulfur to fluorine loss provides insight. The sulfur intensity arises only from the Nafion® side chains. Therefore, if we consider the cleavage of the complete side chain in each case we can estimate the change that would be observed in the

fluorine response. In a homogeneous structure of Nafion[®] EW 1100, for every sulfur atom in the side chain, we have 10 side chain fluorine atoms (F_{side}) and 27 backbone fluorine atoms (F_{back}) atoms. A fractional loss, Z , in sulfur response due to complete cleavage of side chain would correspond to the following loss in Fluorine response (equation 8.1):

$$\text{Loss in F response} = Z \cdot F_{\text{side}} / (F_{\text{side}} + F_{\text{back}}) = 10Z/37 \quad (8.1)$$

Thus, a 75% loss in sulfur intensity ($Z=0.75$) as produced by irradiation of Nafion[®] for 45 minutes under 300W (see Figure 8.3) would correspond to 20% change in fluorine response. The fact that we observe only 8% loss in F response would indicate that the likelihood of complete side chain cleavage is low. If the cleavage occurred at the -C-O-C- bond within the side chain, then for every loss of sulfur, only 4 fluorine atoms would be lost. In such a case, the loss in F response turns out to be $4Z/37$. For, a 75% sulfur loss, we expect a 8.1 % loss in fluorine intensity, remarkably consistent with the observed value. Although the agreement is less remarkable for the other irradiation powers, it is clear that the loss of fluorine is too low to correspond to side chain cleavage. A small contribution may also be expected from loss of fluorine from the backbone, but the kinetics for that process have been estimated to be much slower [205].

8.3.3 Proton conductivity of 10 nm thin film before and after X-ray exposure

Figure 8.8 shows impedance response of Ultra-thin Nafion[®] film at 94% RH and 60 °C. Three samples (10 nm ultra-thin Nafion[®] film on SiO₂ supported gold IDA) were subjected to the AC impedance measurement by impedance analyzer coupled with a Dielectric interface according to our standard protocol [164,163]. The typical impedance response including a high

frequency semi-circle followed by a low frequency straight line was obtained. The semi-circle diameter is associated with film resistance while the straight line represents double layer capacitance as described earlier [164]. Remarkably, all three samples gave identical semi-circles in the impedance response. This indicates that the film preparation process is highly reproducible. We also investigated the measurement reproducibility by collecting at least three impedance responses at the same temperature and RH. It was found that measurement was also highly reproducible with 2% error. After the initial impedance measurements, Sample-1, Sample-2 and Sample-3 were exposed to the X-ray beam with power 300, 200 and 100 W, respectively, for 45 min during XPS measurements. Adopting the same set up and same protocol, impedance measurement of X-ray exposed ultra-thin Nafion[®] films was conducted. The three films gave characteristic impedance response where larger semi-circle diameters were obtained indicating higher resistance involved in the film.

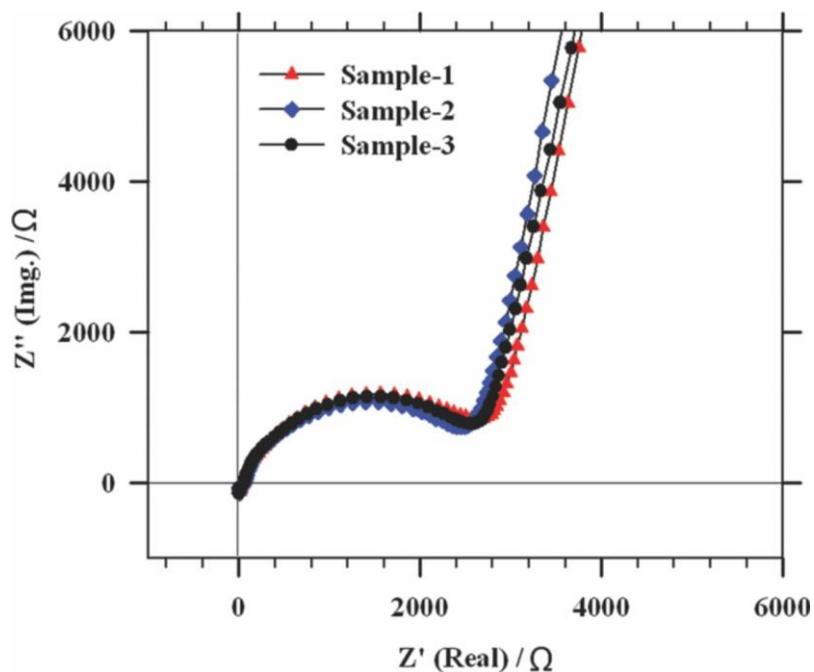


Figure 8.8: Impedance plots of three samples (10 nm ultra-thin Nafion[®] films) before X-ray exposure at 94% RH and 60 °C.

Figure 8.9 represents proton conductivity of both X-ray unexposed and exposed ultra-thin Nafion[®] films at both 60% and 94% RH. It was found that proton conductivity was significantly lower due to X-ray irradiation. The extent of proton conductivity decrease was dependent on the X-ray power. The highest suppression of proton conductivity (99%) was observed in the film exposed to highest X-ray power (300W). While 97% and 95% decrease in proton conductivity were found due to X-ray irradiation with power of 200 and 100 W respectively.

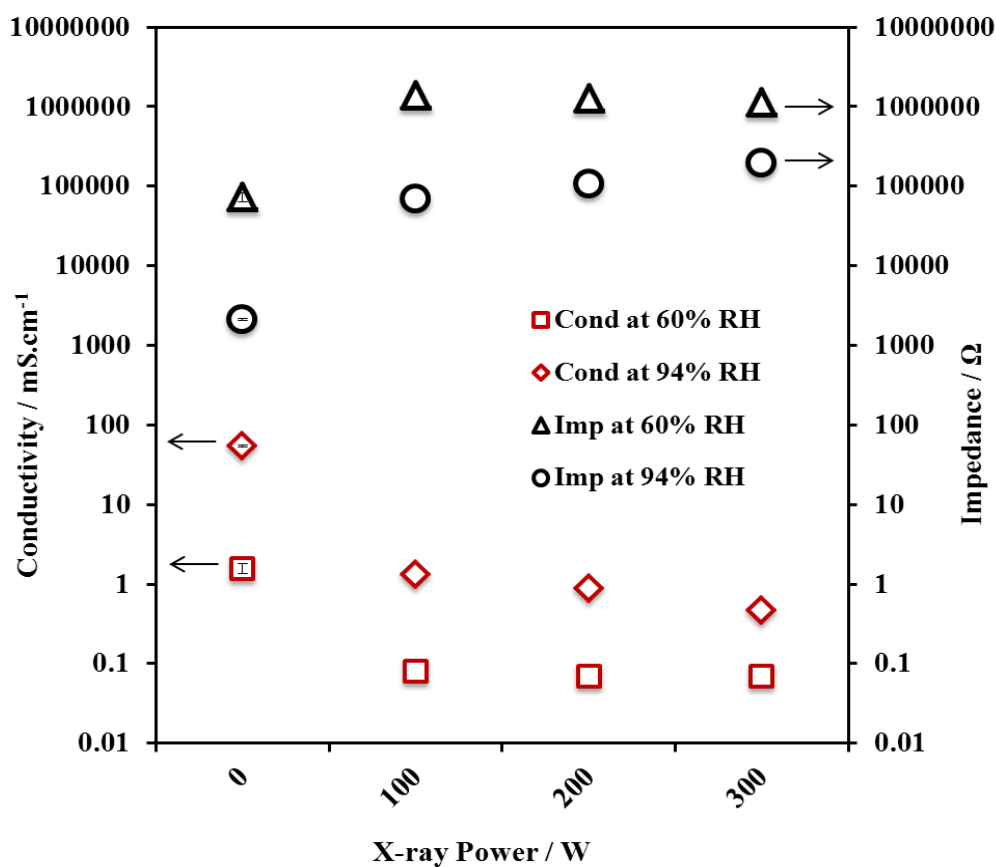


Figure 8.9: Proton conductivity of 10 nm films before (termed as 0 W) and after X-ray exposure (Sample-1, Sample-2 and Sample-3 were exposed to 300, 200 and 100 W X-ray power, respectively) for 45 mins (impedance measurement conducted at both 60 % & 94% RH and 60 °C).

Proton conductivity in Nafion[®] has been typically assigned to the network of sulfonic groups in its side chains. A disruption of the SO₃⁻ network by complete or partial removal, or by chemical modification of the sulfonic groups will result in a decrease in proton conductivity. We can, therefore, correlate the observed decrease in proton conductivity with the decrease in intensity of the sulfur signal in XPS. For the highest exposure, 300 W for 45 mins, a decrease in intensity of 78% results in a 99% reduction of the conductivity. It would indicate that the remaining sulfur present may be in the form of isolated sulfonic groups or in the form of chemically distinct sulfur species resulting from the decomposition of Nafion[®]. Schulze *et al.* [204] reported that during X-ray exposure to the Nafion[®] membrane, some sulfonic acid groups might be completely dissociated from the membrane surface and at the same time other sulfonic acid groups might be converted into sulfite species which have no capability to take part in the proton transport process. Therefore, the higher extent of proton conductivity loss directly indicates that X-ray, regardless of power, damage ultra-thin film proton conductivity significantly by dissociation and chemical modification of sulfonate moieties of Nafion[®]. Ultra-thin films (10 nm) are highly vulnerable to X-ray exposure because the radiation can penetrate the whole film thickness whereas only a few nm at the surface of a thick membrane (25 μ m to 170 μ m) might be damaged, which might not have significant impact on the membrane performance.

8.4 Conclusions

It has been shown that ultra-thin Nafion[®] films are particularly sensitive to damage by X-ray radiation. Supported Nafion[®] films of 10 nm thickness exposed to Al K α radiation (1486.6 eV photons) with an X-ray source of 300, 200 and 100 W for up to 45 minutes were found to have lost 78, 74 and 54%, respectively of their sulfur content. Removal of the sulfonic groups was accompanied by a slight loss of fluorine, likely due to cleavage of the ether group within the side

chains of Nafion[®]. The net result is a dramatic loss of the proton conducting ability of the Nafion[®] film. Ultra-thin Nafion[®] films are of particular importance to understand the catalyst layer in PEFC electrodes. As studies of such films using X-ray techniques becomes more prevalent, quantification and understanding of the damage produced by the X-ray source must be taken into consideration in the data analysis, which otherwise assumes the films remain unaffected during the measurement.

Chapter 9

Conclusions and Recommendations

9.1 Conclusions

This thesis deals with a study of ultrathin Nafion® films. In particular, the focus was to generate films of sub-micron thickness and as thin as 4-10 nm. The original motivation of the work was to probe whether the structure and properties of such thin films, especially 4-10 nm thin films, were different than the well-studied, free-standing membrane form of Nafion®. This motivation arose from the lack of an understanding of structure and properties of Nafion® in the catalyst layer of the polymer electrolyte fuel cells, wherein the ionomer (Nafion®) exists as thin films of thickness 4-10 nm coating the catalyst (Pt/C) aggregates. Several novel contributions have been made through the work undertaken in this experimental thesis.

First novel contribution was the creation of *thinnest, continuous films* of Nafion® (4 nm) ever reported in the literature. To this end, a protocol has been developed for the fabrication of self-assembled ultrathin Nafion® films on planner substrates mimicking the adsorption/self-assembly of ionomer that occurs in the catalyst ink formulation stage. Films of thickness ranging 4-300 nm could be created on SiO₂/Si substrate with high degree of reproducibility by strictly following the developed protocol. The thickness of the films was ascertained with three different techniques that probed three different areal scales – XPS, AFM and Ellipsometry and excellent consistency was obtained. The ability to fabricate 4-10 nm thin Nafion® films has given us a unique opportunity to study the properties of Nafion® at length scales of relevance of PEFC CL. It also led to several successful collaborations with international and Canadian research groups.

New body of knowledge has been created and interesting insights have been gained via extensive characterization of self-assembled ultra-thin Nafion® films on SiO₂ surface. A new finding of this study was the thickness-dependent properties of these films. A surprising and previously unreported observation regarding the wettability of thin Nafion® films was made in this study. Thicker films (>55 nm) demonstrated hydrophobic free surface, consistent with the Nafion® membrane. However, the thinner films (<55nm) had free surface that was demonstrably hydrophilic, clearly indicating the differences between the structure of the sub-55 nm and thicker films. Atomic force microscopy (AFM) was employed to probe any differences in the surfaces of the films. No obvious differences in the surface roughness or height features were noted. On the other hand, differences between the sub-55 nm and thicker films were noted in the phase contrast images. A further evidence of differences in the two classes of films was noted in the protonic conductivity of the films. The self-assembled films of thickness less than 55 nm showed conductivity (at 25 °C) similar to each other, i.e. the conductivity was independent of the film thickness. On the other hand, for higher thickness films (>55nm), conductivity of the film was found to increase with increasing film thickness with 300 nm film exhibiting conductivity similar to that of a freestanding Nafion® membrane. Another important finding was the depressed conductivity of the ultra-thin Nafion® films (<55 nm) compared to the well-studied Nafion® membrane.

To understand the differences in the protonic conductivity of Nafion® membrane and ultra-thin films, complementary measurements on water uptake (by QCM), swelling (by ellipsometry) and ionic domain growth (by GISAXS) was carried out through collaborative work. It may be highlighted that no prior comparable data for 4-10 nm thin Nafion® films are available in the literature and none have reported an integrated set of data on conductivity, water uptake, swelling and ionic domain growth. There are several new and interesting findings arising from

the combined studies. The sub-55 nm thin films were found to have significantly higher water uptake and swelling than the thicker films and Nafion® membranes. This clearly established that the observed suppressed conductivity of the sub-55 nm films is not due to lower content of water, which is a mediator for proton transport. The GISAXS measurements were designed to monitor the time-response of the dry films subjected to humidified environment and growth of ionic domain. Ionic domains were observed in the 55 nm and 160 nm thick films but not in the thinner films. Whereas the 55 nm film showed the presence of the ionic domain, it still had significantly depressed proton conductivity raising the question regarding long-range connectivity of the domains. On the other hand, even in the absence of ionic domains, the 4-30 nm thin films showed reasonable conductivity. These findings highlight the complicated dependency of protonic conductivity on film thickness.

In addition to the extensive characterization of the as-prepared films on SiO₂, several factors expected to influence the film characteristics were investigated including thermal treatment, dispersion medium composition and substrate type.

A systematic study of the effect of thermal treatment on the surface and bulk characteristics of the Nafion® thin films was also completed. The films were heat treated at temperatures well above the glass transition temperature of bulk Nafion®. A new and interesting finding was the switching of the surface wettability of the sub-55 nm films from hydrophilic to hydrophobic surface upon thermal annealing. The wettability switching required higher treatment temperature for lower thickness films, indicating the favorable interaction between SiO₂ substrate and Nafion®. This is the first study pointing towards the thickness-dependence of glass transition temperature of Nafion® thin films and that the glass transition temperature of the ultra-thin Nafion® films (4-10 nm) are significantly higher than that of the bulk Nafion®. Corresponding

with wettability change upon thermal treatment, a change in proton conductivity, a bulk property, was also observed. Thus, a clear evidence of both surface and bulk rearrangements of the thin films occurring simultaneously upon annealing has been observed. Another interesting finding is the dewetting effect of Nafion® on SiO₂ was observed but only for the 4 nm film. Overall, these results have some important implications on the choice for hot-pressing conditions for membrane electrode assembly. The finding of this study indicates that the morphology and property of ionomer thin films and, by extension those in the PEFC CL can be manipulated by appropriate thermal treatment.

Another very interesting finding generated from a rather simple set of experiments was the effect of liquid water exposure on the changes in the surface wettability of the films. These experiments were carried out to simulate the presence of liquid water in the catalyst layer to understand if thermally annealed ionomer films could undergo further reorganization upon exposure to liquid water. Remarkably, upon extended exposure to liquid water, the hydrophobic surface of the ultra-thin annealed films switched back to hydrophilic. Astoundingly, the conductivity of these films, which exhibited highly depressed conductivity after thermal annealing, increased dramatically upon liquid water exposure. The conductivity of these ‘regenerated’ films reached values closer or even exceeded those of the unannealed films. The switchability of the Nafion® film wettability and conductivity upon liquid water exposure is the first such report on these phenomena. Another interesting observation was made that whereas the thinner films required higher temperature, i.e. energy to undergo surface wettability switch, these films were more amenable to reorganization upon liquid water exposure compared to thicker films. These findings may have direct linkage to the enhancement in fuel cell performance upon initial conditioning when liquid water may be produced locally in the catalyst layer.

A study of the effect of dispersion medium composition on the self-assembly of Nafion® was carried out. The morphology of Nafion® on the substrate was examined by AFM and particle size distribution was assessed by dynamic light scattering (DLS) technique. Dispersion media varying in dielectric constant and solubility parameter were generated by changing the IPA/water ratio of the dispersion while keeping a constant Nafion® content (0.1 wt%). Changes in the aggregation state of Nafion® as a function of dispersion medium composition was noted via the changes in the particle size distribution. The influence of dispersion media on Nafion® interaction with the substrate was evident in the differences in the coverage of the films on the substrate. In all cases, the height of the Nafion® self-assembled on the SiO₂ substrate was 3-4 nm, perhaps indicative of a fundamental length scale of the Nafion® aggregate in the dispersion.

The effect of substrate type was also investigated in this thesis. A novel contribution from this work is correlating surface morphology and wettability in terms of the surface energy of the substrates. It was shown that the film morphology, in terms of aggregation behavior and apparent size of the ionic domain, changes significantly with the change in wettability of the substrate from hydrophilic (SiO₂) to hydrophobic (Carbon, Pt and Au). It was discovered that substrates induce the organization of Nafion® in such a way that the thinnest Nafion® films (~4 nm) exhibited hydrophilic free surface on hydrophilic substrate and hydrophobic free surface on hydrophobic substrates. Since the film thickness does not differ much, the differences in the free surface wettability imply that substrate affects the orientation and reorganization of the sulfonic-group containing hydrophilic side-chains. The water uptake was also affected by the substrate type. The water uptake of films on hydrophobic substrates was significantly lower than that of films on hydrophilic SiO₂. On the other hand, dewetting was noted for all of the thinnest films (~4 nm) regardless of the substrate.

Hence, a complete database on the substrate induced structural properties relation might be useful for the fuel cell materials development and selection. Whereas a limited number of substrate has restricted to have the global conclusion how thin film morphology and properties are manipulated by the substrate wetting interaction and surface tensions. Moreover, the measurement of proton transport is limited only on the nonconductive substrate like SiO_2 .

Another contribution arising from the thesis work is the study/quantification of the damage induced by x-ray beam exposure on ultrathin Nafion® film. Using x-ray source of a x-ray photoelectron spectroscopy (XPS) system, the 10 nm films were exposed to different x-ray power and changes in the XPS intensity of the relevant elemental components was followed. At the highest power employed, around 80% sulfur was lost due to 45 min exposure and fluorine to sulfur ratio changes indicated degradation in the side chain at the ether bond. A corresponding dramatic loss in proton conductivity was observed. The findings have an important implication for the researcher utilizing x-ray based techniques for characterization of thin films of Nafion® or similar polymers.

9.2 Recommendations

Although the thesis has generated several insights on the structure and properties of sub-micron thin Nafion® films, many questions still remain unanswered. One of the key questions that need to be resolved through future studies is difference in the thin film conductivity and effective conductivity of ionomer in the catalyst layer. The measured effective ionomer conductivity is significantly higher than those projected using the thin film conductivity but accounting for the CL microstructure. Another related question is why is the protonic conductivity of ultra-thin films (<55nm) low despite the higher water uptake that exceeds those of

the membrane. Solid-state proton NMR may offer some insight by indicating whether the differences are due to local structure and mobility or not. In-situ infra-red techniques may also be helpful. To understand where the water is located in the films, it is recommended that water profile analysis by the Neutron Reflectometry must be carried out.

The thickness-dependent surface and bulk characteristics also demand the need for probing the differences in the internal structure of these films. Since the structure is influenced by the fabrication method, thermal treatment, the nature of the substrate, and the water content in the dispersion media, a systematic approach is needed to delineate the individual effects. In-situ temperature dependent ellipsometry measurement may be applied to determine the thickness-dependent glass transition temperature of the thin films. To generalize the findings, studies with ionomer types varying in side-chain length or equivalent weight is recommended.

Bibliography (or References)

1. More, K.; Borup, R.; Reeves, K. *ECS Trans.* 2006, 3, 717-733.
2. Wagner, F. T.; Lakshmanan, B.; Mathias, M. F. *The Journal of Physical Chemistry Letters* 2010, 1 (14), 2204-2219
3. Kim, S.; Hewlett, S.A.; Roth, C.B.; Torkelson, J.M. *Eur. Phys. J. E* 2009, 30, 83–92.
4. Soles, C. L.; Douglas, J. F.; Wu, W. L.; Dimeo, R. M. *Macromolecules* 2003, 36, 373-379.
5. Soles, C. L.; Lin, E. K.; Lenhart, J. L.; Jones, R. L. *J. Vac. Sci. Technol. B* 2001, 19.6.
6. Frank, C. W.; Rao, V.; Despotopoulou, M. M.; Pease, R. F. W.; Hinsberg, W. D.; Miller, R. D.; Rabolt, J. F. *Science* 1996, 273, 912-915.
7. Vogt, B. D.; Soles, C. L.; Lee, H. J.; Lin, E. K.; Wu, W. L. *Langmuir* 2004, 20 (4), 1453–1458.
8. Dura A. J.; Murthi, S. V.; Hartman, M.; Satija, K.S.; Majkrzak, F. C. *Macromolecules* 2009, 42, 4769-4774.
9. Wood, L. D.; Chlistunoff, J.; Majewski, J.; Borup, L. R. *J. Am. Chem. Soc.* 2009, 131, 18096–18104.
10. Bass, M.; Berman, A.; Singh, A.; Konovalov, O.; Freger, V. *Macromolecules* 2011, 44, 2893–2899.
11. Modestino, A. M.; Kusoglu, A.; Hexemer, A.; Weber, Z. A.; Segalman, A. R. *Macromolecules* 2012, 45, 4681–4688.
12. Kongkanand A. *J. Phys. Chem. C* 2011, 115, 11318–11325.
13. Dishari, K. S.; Hickner, A. M. *ACS Macro Lett.* 2012, 1, 291-295.
14. Siroma, Z.; Kakitsubo, R.; Fujiwara, N.; Ioroi, T.; Yamazaki, S-I.; Yasuda, K. *J. of Power Sources* 2009, 189, 994-998.
15. Eastman, S. A.; Kim, S.; Page, K. A.; Rowe, B. W.; Kang, S.; Soles C. L. *Macromolecules* 2012, 45, 7920–7930.

16. Abuin G. C.; Fuertes, C. M.; Corti, H. R. *J. of Membrane Sci.* 2013, 428, 507-515.
17. Mauritz, K. A.; Moore, R. B. *Chem. Rev.* 2004, 104, 4535-4586.
18. Jacob, T.; Muller, R. P.; Goddanr, W. A. *J of Phy. Chem. B* 2003, 107, 9465-9476.
19. de Morais, R. F.; Sautet, P.; Loffreda, D.; Franco, A. A. *Electrochimica Acta* 2011, 56(28), 10842-10856,
20. Wang, Y. C. *Chem. Rev.* 2004, 104, 4727.
21. Yim, S -D.; Sohn, Y-J.; Park, S-H.; Yoon, Y-G.; Park, G-G.; Yang, T-H.; Kim, C-S. *Electrochimica Acta* 2011, 56(25), 9064-9073,
22. Uchida, M.; Aoyama, Y.; Eda, N.; Ohita, A. *J. Electrochem. Soc.* 1995, 142, 463.
23. Uchida, M.; Fukuoka, Y.; Sugawara, Y.; Ohara, H.; Ohta, A. *J. Electrochem. Soc.* 1998, 145, 3708.
24. Shin, S. J.; Lee, J. K.; Ha, H. Y.; Hong, S. A.; Chun, H. S.; Oh, I. H. *J. Power Sources* 2002, 106, 146.
25. Litster, S.; McLean, G. *Journal of Power Sources* 2004, 130, 61-76.
26. Bolwin, K.; Gulzow, E.; Bevers, D.; Schnumberger, W. *Solid State Ionics* 1995, 77, 324.
27. Ihm, J. W.; Ryu, H.; Bae, J. S.; Choo, W. K.; Choi, D. K. *J. Mater. Sci.* 2004, 39, 4647.
28. Saab, A.P.; Garzon, F.H.; Zawodzinski, T. A. *J. Power Sources* 2002, 149, A1541.
29. Wilson, M.S.; Gottesfeld, S. *J. Appl. Electrochem.* 1992, 22, 1.
30. Wilson, M.S.; Gottesfeld, S. *J. Electrochem. Soc.* 1992, 139, L28.
31. Daud, W. R. W.; Mohamad, A. B.; Kadhum, A. A. H.; Chebbi, R.; Iyuke, S. E. *Energy Convers. Manage.* 2004, 45, 3239.
32. Wang, C. S.; Appleby, A. J. *J. Electrochem. Soc.* 2003, 150, A493.
33. Liang, Z. X.; Zhao, T. S.; Xu, C.; Xu, J. B. *Electrochimica Acta* 2007, 53, 894-902.
34. Zhang, J.; Yin, G-P.; Wang, Z.-B.; Lai, Q-Z.; Cai, K.-D. *J. of Power Sources* 2007, 165, 73-81.

35. Lin, J.-C.; Lai, C.-M.; Ting F.-P.; Chyou, S.-D.; Hsueh, K.-L. *J Appl Electrochem* 2009, 39, 1067–1073.
36. Wilson, M.S.; Valerio, J.A.; Gottesfeld, S. *Electrochim. Acta* 1995, 40, 355.
37. Song, S.Q.; Liang, Z.X.; Zhou, W.J.; Sun, G.Q.; Xin, Q.; Stergiopoulos, V.; Tsiakaras, P.; *J. Power Sources* 2005, 145, 495.
38. Karan, K. *Electrochem Comm.* 2007, 9, 747.
39. Sun, W.; Peppley, B.A.; Karan, K. *Electrochimica Acta* 2005, 50, 3359.
40. Wang, Q.; Eikerling, M.; Song, D.; Liu, Z. *J. Electroanal. Chem.*, 2004, 573, 61.
41. Malek, K.; Eikerling, M.; Wang, Q.; Navessin, T.; Liu, Z. *J. Phys. Chem. C* 2007, 111, 13627–13634.
42. Dai, W.; Wang, H.; Yuan, X.-Z.; Martin, J. J.; Yang, D.; Qiao, J.; Ma, J. *Int. J. of Hydrogen Energy* 2009, 34(23), 9461-9478.
43. Volfkovich, Y. M.; Sosenkin, V. E.; Bagotsky, V. S. *J. Power Sources* 2010, 195, 5429–5441.
44. Vol'fkovich, Y. M.; Sosenkin, V. E.; Nikol'skaya, N. F. *J. Electrochem.* 2010, 46, 438–449.
45. Yu, H. M.; Ziegler, C.; Oszcipok, M.; Zobel, M.; Hebling, C. *Electrochim. Acta* 2006, 51, 1199–1207.
46. Li, X.; Feng, F.; Zhang, K.; Ye, S.; Kwok, D. Y.; Birss, V. *Langmuir* 2012, 28 (16), 6698-6705.
47. Goswami, S.; Klaus, S.; Benziger, J. *Langmuir* 2008, 24, 8627–8633
48. Kinoshita, K.; Wiley-Interscience, 1988.
49. Lee, S. J.; Mukerjee, S.; McBreen, J.; Rho, Y. W.; Kho, Y. T.; Lee, T. H. *Electrochim. Acta* 1998, 43, 3693.
50. Li, G.; Pickup, P. G. *J. of Electrochem. Soc.* 2003, 150 (11) C745-C752.
51. Heitner-Wirguin, C. *J. of Membrane Sci.* 1996, 120, 1-33.
52. Choi, P.; Jalani, H. N.; Datta, R. *J. of Electrochem. Soc.* 2005, 152 , E123-E130.

53. Yeo, S. R.; McBreen, J.; Kissel G.; Kulesa, F.; Srinivasan S. *J. of App. Electrochem.* 1980, 10, 741-747.
54. Grot, W. *Chem. Ing. Tech.* 1978, 50, 299-301.
55. Tailoka, F.; Fray, D. J.; Kumar, R. V. *Solid State Ionics* 2003, 161, 267 - 277.
56. Yakovlev, S.; Wang, X.; Ercius, P.; Balsara, N. P.; Downing, K. H. *J. Am. Chem. Soc.* 2011, 133, 20700.
57. Kang, Y.; Kwan, O.; Xie, X.; Zhu, D. M. *J. Phys. Chem. B* 2009, 113, 15040–15046.
58. Kwon, O.; Kang, Y. H.; Wu, S. J.; Zhu, D. M.; *J. Phys. Chem. B* 2010, 114, 5365.
59. Aleksandrova, E.; Hink, S.; Hiesgen, R.; Roduner, E. *J. Phys.: Condens. Matter*, 2011, 23, 234109.
60. Hsu, W. Y.; Gierke, T. D. *Macromolecules* 1982, 15, 101.
61. Haubold, H. G.; Vad, T.; Jungbluth, H.; Hiller, P. *Electrochim. Acta* 2001, 46, 1559.
62. Rubatat, L.; Rollet, A. L.; Gebel, G.; Diat, O. *Macromolecules* 2002, 35, 4050.
63. Rubatat, L.; Gebel, G.; Diat, O. *Macromolecules* 2004, 37, 7772.
64. Schmidt-Rohr, K.; Chen, Q. *Nat. Mater.* 2008, 7, 75–83.
65. Gebel, G.; Aldebert, P.; Pineri, M. *Macromolecule* 1987, 20(6), 1425-1428.
66. Moore, R. B.; Martin, C. R. *Macromolecules* 1988, 21, 1334-1339.
67. Moore, R. B.; Martin, C. R. *Macromolecules* 1989, 22(9), 3594-3599.
68. Halim, J.; Scherer, G. G. *Macromol. Chem. Phys.* 1994, 195, 3783-3788.
69. Zawodzinski, T. A.; Derouin, C.; Radzinski, S.; Sherman, R. J.; Smith, V. T.; Springer, T. E.; Gottesfeld, S. J. *Electrochem. Soc.* 1993, 140, 1041.
70. Zawodzinski, T. A.; Springer, T. E.; Davey, J.; Jestel, R.; Lopez, C.; Valerio, J.; Gottesfeld, S. J. *Electrochem. Soc.* 1993, 140, 1981.
71. Hinatsu, J. T.; Mizuhata, M.; Takenaka, H. *J. Electrochem. Soc.* 1994, 141, 1493.
72. Morris, D. R.; Sun, X. *J. Appl. Polym. Sci.* 1993, 50, 1445.

73. Skou, E.; Kauranen, P.; Hentschel, J. *Solid State Ionics* 1997, 97, 333.
74. Pushpa, K. K.; Nandan, D.; Iyer, R. M. *J. Chem. Soc., Faraday Trans.* 1988, 84, 2047.
75. Steck, A.; Yeager, H. L. *Anal. Chem.* 1980, 52, 1215.
76. Rivin, D.; Kendrick, C. E.; Gibson, P. W.; Schneider, N. S. *Polymer* 2001, 42, 623.
77. Schroeder, P. V. *Z. Phys. Chem.* 1903, 45, 75.
78. Soboleva, T.; Xie, Z.; Shi, Z.; Tsang, E.; Navessin, T.; Holdcroft, S. *J. Electroanal. Chem.* 2008, 622, 145.
79. Halim, J.; Buchi, F. N.; Haas, O.; Stamm, M.; Scherer, G. G. *Electrochim. Acta* 1994, 39, 1303.
80. Yadav, R.; Fedkiw, P. S. *J. Electrochem. Soc.* 2012, 159 (3), B340-B346.
81. Walsby, N.; Hietala, S.; Maunu, S. L.; Sundholm, F.; Kallio, T.; Sundholm, G. *J. Appl. Polym. Sci.* 2002, 86, 33.
82. Sumner, J. J.; Creager, S. E.; Ma, J. J.; DesMarteau, D. D. *J. Electrochem. Soc.* 1998, 145, 107.
83. Sone, Y.; Ekdunge, P.; Simsonsson, D. *J. Electrochem. Soc.* 1996, 143, 1254.
84. Nouel, K. M.; Fedkiw, P. S. *Electrochim. Acta* 1998, 43, 2381.
85. Park, M. J.; Downing, K. H.; Jackson, A.; Gomez, E. D.; Minor, A. M.; Cookson, D.; Weber, A. Z.; Balsara, N. P. *Nano Lett.* 2007, 7, 3547.
86. Choi, P.; Jalani, N. H.; Datta, R. *J. of Electrochem. Soc.* 2005, 152 (3), E123 E130.
87. Eikerling, M.; Kornyshev, A. A.; Kuznetsov, A.; Ulstrup, M. J.; Walbran, S. *J. Phys. Chem. B* 2001, 105, 3646.
88. Paddison, S. J.; Paul, R. *Phys. Chem. Chem. Phys.* 2002, 4, 1158.
89. Kreuer, K. D.; Paddison, S. J.; Spohr, E.; Schuster, M. *Chem. Rev.* 2004, 104, 4637.
90. Eigen, M. *Angew. Chem.* 1963, 75, 489.
91. Zundel, G.; Metzger, H. *Z. Naturforsch.* 1967, 22a, 1412.

92. Yeo, S. C.; Eisenberg, A. *J. Appl. Polym. Sci.* 1977, 21, 875-98.
93. Zook, L. A.; Leddy, J. *Anal. Chem.*, 1996, 68, 3793.
94. Hensley, J. E.; Way, J. D.; Dec, S. F.; Abney, K. D. *J. of Membrane Sci.*, 2007, 298, 190.
95. Jung, H-Y.; Cho, K.-Y.; Lee, Y. M.; Park, J.-K.; Choi, J.-H.; Sung, Y.-E. *J. of Power Sources*, 2007, 163, 952.
96. Ding, X.; Fuller, T. F.; Harris, T. A. L. *ECS Trans.*, 2011, 41, 1537.
97. Kwon, O.; Wu, S.; Zhu, D.-M. *J. Phys. Chem. B* 2010, 114, 14989.
98. Park, H. B.; Shin, H.-S.; Lee, Y. M.; Rhim, J.-W. *J. of Membrane Sci.* 2005, 247, 103.
99. Aldebert, P. B. D. *J. Phys. France* 1988, 49, 2101-2109.
100. Loppinet, B.; Gebel, G.; Williams, C.E. *J. Phys. Chem. B* 1997, 101, 1884-1892
101. Gebel, G.; Loppinet, B. *J. Molecular Structure* 1996, 383, 43-49.
102. Loppinet, B.; Gebel, G. *Langmuir* 1998, 14, 1977-1983.
103. Rubatat, L.; Gebel, G.; Diat, O. *Macromolecules* 2004, 37, 7772-7783.
104. Szajdzinska-Pietek, E.; Schlick, S.; Plonka, A. *Langmuir* 1994, 10, 2188.
105. Jiang, S.; Xia, K-Q; Xu, G. *Macromolecules* 2001, 34, 7783-7788.
106. Lee, S.-J.; Yu, T. L.; Lin, H.-L.; Liu, W.-H.; Lai, C.-L. *Polymer* 2004, 45, 2853 - 2862.
107. Lin, H-L; Yu, L. T; Huang, C-H; Lin, T-L. *Journal of Polymer Science: Part B: Polymer Physics* 2005, 43, 3044–3057.
108. Moore, R. B.; Martin, C. R., *Macromolecules* 1988, 21, 1334-1339.
109. Ma, C.-H.; Yu, T. L.; Lin, H.-L.; Huang, Y.-T.; Chen, Y.-L.; Jeng, U.-S. *Polymer* 2009, 50, 1764-1777.
110. Ngo, T. T.; Yu, T. L.; Lin, H-L. *J. Power Sources* 2013, 225(1), 293-303.
111. Koestner, R.; Roiter, Y.; Kozhinova, I.; Minko, S. *Langmuir* 2011 27 (16), 10157-10166.
112. Koestner, R.; Roiter, Y.; Kozhinova, I.; Minko, S. *The Journal of Physical Chemistry C* 2011 115 (32), 16019-16026.

113. Masuda, T.; Naohara, H.; Takakusagi, S.; Singh, P.R.; Uosaki, K. *Chem. Lett.*, 2009, 38, 884.
114. Ma, S.; Chen, Q.; Jørgensen, F.H.; Stein, P.C.; Skou, E.M. *Solid State Ionics* 2007, 178, 1568.
115. Li, A.; Han, M.; Chan, S. H.; Nguyen, N. *Electrochimica Acta* 2010, 55 2706-2711.
116. Zeng, J.; Jean, D. Ji, C.; Zou, S. *Langmuir* 2012 28 (1), 957-964.
117. Gebel, G.; Diat, O. *Fuel Cells* 2005, 5, 261-276.
118. Blanchard, R. M.; Nuaao, G. R. *J. Polymer Sci. Part B: Polymer Phy.* 2000, 38, 1512-1520.
119. Krtíl, P.; Troja'nek, A.; Samec, Z. *J. Phys. Chem. B* 2001, 105, 7979-7983.
120. Hill, A. T.; Carroll, L. D.; Czerw, R.; Martin, W. C.; Perahia, D. *J. of Polymer Sci.: Part B: Polymer Phy.* 2003, 41, 149-158.
121. Siroma, Z.; Ioroi, T.; Fujiwara, N.; Yasuda, K. *Electrochem. Comm.* 2002, 4, 143–145.
122. Bertoncello, P.; Ugo, P. *J. Braz. Chem. Soc.* 2003, 14, 517-522.
123. Ugo, P.; Bertoncello, P.; Vezzà, F. *Electrochimica Acta* 2004, 49, 3785–3793.
124. Bertoncello, P.; Ciani, I.; Li, F.; Unwin, R. P. *Langmuir* 2006, 22, 10380-10388.
125. Umemura, K.; Wang, T.; Hara, M.; Kuroda, R.; Uchida, O.; Nagai, M. *Langmuir* 2006, 22, 3306-3312.
126. Murthi, V. S.; Dura, J. A.; Satija, S.; Majkrzak, C. F. *ECS Tran.* 2008, 16, 1471-1485.
127. Noguchi, H.; Taneda, K.; Minowa, H.; Naohara, H.; Uosaki, K. *J. Phys. Chem. C* 2010, 114, 3958–3961.
128. Bass, Maria.; Berman, Amir.; Singh, Amarjeet.; Konovalov, Oleg.; Freger, V. *J. Phys. Chem. B* 2010, 114, 3784-3790.
129. Ahmed, M.; Morgan, D.; Attard, A. G.; Wright, E.; Thompsett, D.; Sharman, J. *Phys. Chem. C* 2011, 115, 17020-17027.

130. Stafford, C. M.; Vogt, B. D.; Harrison, C.; Julthongpiput, D.; Huang, R. *Macromolecules* 2006, 39, 5095-5099.
131. Iden, H.; Ohma, A.; Shinohara, K. *J. Electrochem. Soc.* 2009, 156, B1078-B1084.
132. Krausch, G. *Mat. Sci. and Engg.* 1995, 1-94.
133. Wang, Q.; Nealey, P. F.; Pablo, J. J. *Macromolecules* 2001, 34, 3458-3470.
134. Kim, H-C.; Park, S.-M.; Hinsberg, D. W. *Chem. Rev.* 2010, 110, 146–177
135. Maeda, Y.; Gao, Y.; Nagai, M.; Nakayama, Y.; Ichinose, T.; Kuroda, R.; Umemura, K. *Ultramicroscopy* 2008, 108, 529.
136. Zawodzinski, T. A.; Gottesfeld, S.; Shoichet, S.; McCarthy, T. J. *J. Appl. Electrochem.* 1993, 23, 86–88.
137. Kim, Y-H.; Oblas, D.; Angelopoulos, P. A.; Fossey, S. A.; Matienzo, J. L., *Macromolecules* 2001, 34, 7489.
138. Moore, R. B., 111; Martin, C. R., *Macromolecules* 1988, 21, 1334-1339
139. Jiang, S.; Xia, K-Q; Xu, G. *Macromolecules* 2001, 34, 7783-7788
140. Co., J. W. Ellipsometry Tutorial: Light and Materials.
http://www.jawoollam.com/tutorial_4.html
141. Jalili, N.; Laxminarayana. K. *Mechatronics Journal* 2004, 14, (8), 861.
142. Phase imaging
http://www.eettaiwan.com/ARTICLES/2002MAR/PDF/2002MAR25_AMD_DA_AN116.PDF?SOURCES=DOWNLOAD (accessed June 2013).
143. Chao, S. S.; Takagi, Y.; Lukovsky, G.; Pai, P.; Caster, R. C.; Tyler, J. T.; Keem, J. E. *App. Surf. Sci.* 1986, 26, 575-583.
144. Reichl, R.; Gaukler, K.H. *Surf. Interface Anal.* 1990, 15, 211-214.

145. NIST X-ray Photoelectron Spectroscopy Database, Version 3.5, (National Institute of Standards and Technology, Gaithersburg, 2003), <http://srdata.nist.gov/xps/>, (accessed January 2013).
146. Fairley, N. CASA XPS version 2.3.13 Dev73, 2007.
147. Van Oss, C. J. Marcel Dekker, New York, 1994.
148. Bellon-Fontaine, M. N.; Mozes, N.; Van der, M. H. C.; Sjollem, J.; Cerf, O.; Rouxhet, P. G. *Cell Biophys* 1990, 17, 93-106.
149. Sharma, P. K.; Rao, K. H.; *Adv. Colloids Interface Sci.* 2002, 98, 341-463.
150. Van Oss, C. J. *Colloids Surf B Biointerfaces* 2007, 54, 2-9.
151. Barsoukov, E.; Macdonald, J. R. Impedance Spectroscopy; Theory, Experiment, and Applications, 2nd ed. *Wiley Interscience Publications*, 2005.
152. Basics of Electrochemical Impedance Spectroscopy
<http://www.gamry.com/assets/Application-Notes/Basics-of-EIS.pdf> (accessed July, 2013).
153. Retrieved from http://www.lsinstruments.ch/technology/dynamic_light_scattering_dls/ (accessed July, 2013).
154. Mikhailenko, S. D.; Guiver, M. D.; Kaliaguine, S. *Solid State Ionics* 2008, 179, 619.
155. Prakash, S. S.; Brinker C. J.; Hurd, A. J. *J. of Non-Crystalline Solids* 190, 264 (1995).
156. Rouse, J. H.; Ferguson, G. S. *J. of the Am. Chem. Soc.* 2003, 125, 15529.
157. Tompkins, H. G. *A User's Guide to Ellipsometry*. Dover Publications, Inc. 2006.
158. Zudans, I.; Heineman, W. R.; Seliskar, C. J. *J. of Phys. Chem. B* 2004, 108, 11521.
159. Andrew P.; Leis, S. S. *Appl Environ Microbiol.* 2005, 11 (8), 4801.
160. James, P. J.; Antognozzi, M.; Tamayo, J.; McMaster, T. J.; Newton, J. M.; Miles, M. J. *Langmuir* 2001, 17, 349-360.
161. Surface Energy Data for PTFE: Polytetrafluoroethylene, CAS # 9002-84-0, retrieved on 24th March, 2013 from the website. http://www.accudynetest.com/polymer_surface_data/ptfe.pdf

162. Paul, D. K.; Karan, K.; Giorgi, J.; Docoslis, A.; Pearce, J. *Macromolecules* 2013, 46 (9), 3461–3475
163. Paul, D. K.; Fraser, A.; Pearce, J.; Karan, K. *ECS Trans.* 2011, 41, 1393-1406.
164. Paul, D. K.; Fraser, A.; Karan, K. *Electrochem. Comm.* 2011, 13 (8), 774-777.
165. Modestino, M. A.; Paul, D. K.; Dishari, S.; Petrina, S. A.; Allen, F. I.; Hickner, M. A.; Karan, K.; Segalman, R. A.; Weber, A. Z. *Macromolecules* 2013, 46 (3), pp 867–873, 2013
166. Paul, D. K.; Karan, K. *ECS Trans.* 2013, 50 (2), 951-959.
167. Halim, J.; Buchi, F.N.; Haas, O.; Stamm, M.; Scherer, G.G. *Electrochem. Acta* 1994, 39, 1303.
168. Dimitrova, P.; Friedrich, K.A.; Vogt, B.; Stimming, U. *J. Electroanal. Chem.* 2002, 532, 75.
169. Lee, C. H.; Park, H. B.; Lee, Y. M.; Lee, R. D. *Industrial & Engineering Chemistry Research* 2005, 44 (20), 7617-7626.
170. Reiter, G. *Langmuir* 1993, 9, 1344.
171. Fryer, D. S.; Nealey, P. F.; de Pablo, J. J. *J. Vac. Sci. Technol. B* 2000, 18, 3376-3380.
172. Jiang, X. Q.; Yang, C. Z.; Tanaka, K.; Takahara, A.; Kajiyama, T. *Phys. Lett. A* 2001, 281, 363-367.
173. Kim, J. H.; Jang, J.; Zin, W. C. *Langmuir* 2000, 16, 4064-4067.
174. Tsui, O. K. C.; Russell, T. P.; Hawker, C. J. *Macromolecules* 2001, 34, 5535-5539.
175. Jiang, X. Q.; Yang, C. Z.; Tanaka, K.; Takahara, A.; Kajiyama, T. *Phys. Lett. A* 2001, 281, 363-367.
176. White, C. C.; Migler, K. B.; Wu, W. L. *Polym. Eng. Sci.* 2001, 41, 1497-1505.
177. Feng, Y.; Karim, A.; Weiss, R. A.; Douglas, J. F.; Han, C. C. *Macromolecules* 1998, 31, 484.
178. Sauer, B. B.; McLean, R. S. *Macromolecules* 2000, 33, 7939.
179. Srolovitz, D. J.; Safran, S. A. *J Appl Phys* 1986, 60, 247.

180. Brochard, F.; Dalliant, J. *Can J Phys* 1990, 68, 1084.
181. Innis-Samson, V. A.; Sakurai, K. *J. Phys.: Condens. Matter* 2011, 23, 435010.
182. Vogt, B. D.; Soles, C. L.; Lee, H. J.; Lin, E. K.; Wu, W. *Polymer* 2005, 46 (5), 1635–1642.
183. Wilson, M.S.; Valerio, J.A.; Gottesfeld, S. *Electrochim. Acta* 1995, 40, 355.
184. Song, S.Q.; Liang, Z.X.; Zhou, W.J.; Sun, G.Q.; Xin, Q.; Stergiopoulos, V.; Tsiakaras, P.; J. *Power Sources* 2005, 145, 495.
185. Israelachvili, J. N. *Intermolecular and Surface Forces*; Academic Press: New York, 1992.
186. de Gennes, P. G.; Brochard-Wyart, F.; Quere, D. *Capillarity and Wetting Phenomena: Drops, Bubbles, Pearls, WaVes*; Springer: New York, 2003.
187. [Ohira](#), A.; [Kuroda](#), S.; Mohamed, [H. F. M.](#); Tavernier, [B.](#) *Phys. Chem. Chem. Phys.*, 2013,15, 11494-11500
188. Liu, Y.; Murphy, M. W.; Baker, D. R.; Gu, W.; Ji, C.; Jorne, J.; Gasteiger, H. A. *J. Electrochem. Soc.* 2009, 156, B970.
189. Wheeler, D. R.; Pepper, S. V. *J. Vac. Sci. Technol.* 1982, 20(2), 226.
190. Zhang, L.; Zhang, J.; Wilkinson, D. P.; Wang, H. *Journal of Power Sources* 2006, 156 (2), 171-182.
191. Silberzan, P.; Leger, L.; Ausserre, D.; Benattar, J. J. *Langmuir* 1991 7 (8), 1647-1651
192. Petrina, S. DYNAMIC SWELLING AND CONDUCTIVITY OF ION-CONTAINING BLOCK COPOLYMER THIN FILMS, *Master's Thesis*, 2013
193. Paul, D. K.; Giorgi, J.; Karan, K. *J. of Electrochem. Soc.* 2013, 160 (4), F464-F469
194. Bazylak, A. *Int. J. Hydrogen Energy*, 2009, 34, 3845.
195. Sasabe, T.; Tsushima, S.; Hirai, S. *Int. J. Hydrogen Energy* 2010, 35, 11119.
196. Manke, I.; Hartnig, C.; Gr'unerbel, M.; Lehnert, W.; Kardjilov, N.; Haibel, A.; Hilger, A.; Banhart, J.; Riesemeier, H. *Appl. Phys. Lett.* 2007, 90, 174105.

197. Flückiger, R.; Maroneb, F.; Stampanonib, M.; Wokauna, A.; Büchi, F. N. *Electrochimica Acta*, 2011, 56, 2254.
198. Eller, J.; Ros´en, T.; Marone, F.; Stampanoni, M.; Wokaun, A.; Büchi, F. N. *J. Electrochem. Soc.* 2011, 158, B963.
199. Mukaide, T.; Mogi, S.; Yamamoto, J.; Morita, A.; Koji, S.; Takada, K.; Uesugi, K.; Noma, T. *J. Synchrotron Radiat.* 2008, 15, 329.
200. Schulze, M.; Lorenz, M.; Wagner, N.; Gulzow, E. *Fresenius J. Anal. Chem.* 1999, 365, 106.
201. Chen, C.; Levitin, G.; Hess, D. W.; Fuller, T. F. *J. Power Sources*, 2007, 169, 288.
202. Huang, C.; Tan, K. S.; Lin, J.; Tan, K. L. *Chem. Phy. Lett.* 2003, 371, 80.
203. Schneider, A.; Wieser, C.; Roth, J.; Helfen, L. *J. Power Sources* 2010, 195, 6349..
204. Schulze, M.; Bradke, M. V.; Reissner, R.; Lorenz, M.; Gulzow, E. *Fresenius J. Anal. Chem.* 1999, 365, 123.
205. Militello, M. C.; Gaarenstroom, S. W. *Surf. Sci. Spectra* 2003,10, 117.
206. Roth, J.; Eller J.; Büchi, F. N. *J. Electrochem. Soc.* 2012, 159(8), F449.
207. Hubbell, J. H.; Seltzer, S. M. (2004) Tables of x-ray mass attenuation coefficients and mass energy absorption coefficients (version 1.4) [online] available: <http://physics.nist.gov/xaamdi> [2013, Feb. 15] National Institute of Standards and Technology, Gaithersburg, MD.
208. Gross, T.; Ramm, M.; Sonntag, H.; Unger, W.; Weijers, H. M.; Adem, E. H. *Surf. Interface Anal.* 1992, 18, 59.
209. Clark, D. T.; Feast, W. J.; Kilcast, D.; Musgrave, W. K. R. *J. Polym. Sci. Polym. Chem. Ed.* 1973, 11, 389.
210. Sleight, C.; Pijpers, A. P.; Jaspers, A.; Coussens, B.; Meier, R. J. *J. Electron Spectrosc. Relat. Phenom.* 1996, 77, 41.
211. Lindberg, B. J.; Hamrin, K.; Johansson, G.; Gelius, U.; Fahlmann, A.; Nordling, C.; Siegbahn, K. *Phys. Scripta* 1970, 1, 286..